

Operation and Control of Voltage Source Converters in Transmission Networks for AC System Stability Enhancement

by Tibin Joseph



Energy and Environment
Cardiff University
Cardiff, Wales, United Kingdom

Ynni a'r amgylchedd
Prifysgol Caerdydd
Caerdydd, Cymru, Deyrnas Unedig

Submitted in part fulfilment of the requirements for the degree of
Doctor of Philosophy of Cardiff University

Cardiff, CU, 2017

To My Little Angel Mannya Isa Tibin...

Declaration

This work has not been submitted in substance for any other degree or award at this or any other university or place of learning, nor is being submitted concurrently in candidature for any degree or other award.

Signed(candidate) Date.....

STATEMENT 1

This thesis is being submitted in partial fulfillment of the requirements for the degree of PhD.

Signed(candidate) Date.....

STATEMENT 2

This thesis is the result of my own independent work/investigation, except where otherwise stated, and the thesis has not been edited by a third party beyond what is permitted by Cardiff University's Policy on the Use of Third Party Editors by Research Degree Students. Other sources are acknowledged by explicit references. The views expressed are my own.

Signed(candidate) Date.....

STATEMENT 3

I hereby give consent for my thesis, if accepted, to be available online in the University's Open Access repository and for inter-library loan, and for the title and summary to be made available to outside organisations.

Signed(candidate) Date.....

Acknowledgements

I am deeply thankful to Lord God for His amazing grace, which has kept me from the beginning of my life until now.

I would like to express my gratitude to my supervisors Prof. Jun Liang and Dr. Carlos Ugalde-Loo for their guidance and support throughout the duration of my PhD studies. Especially, to Prof. Jun Liang for allowing me the opportunity to be a part of the international MEDOW consortium. Special thanks to Prof. Nick Jenkins for the time, advice and encouragement received. I would like to thank Dr. Sentooran Balasubramaniam for his time, support and all the pain in setting-up the experimental platform.

In addition, I would like to acknowledge the financial support of the European Commission through the Marie Curie ITN MEDOW project, which gave me the opportunity to explore and develop my career with different training and dissemination activities. In particular, my special thanks to MEDOW colleagues for the interesting and useful discussions we shared during this project and also to Cath and Karolina for their patience dealing with all our issues.

I would like to extend my gratitude and thankfulness to the members of the CIREGS research group of Cardiff University for their valuable advice and instructive discussions. Especially to Gen, Marc, Khadijat, Dantas, Marios, Sara, and Tony for the laughter and the wonderful times we shared during the past years. A special note of thanks to Jorge Gonçalves, for the fruitful discussions and interesting time we had during the secondment period at CEPRI, China, which eventually resulted in one of my chapters.

This acknowledgement would not be complete without thanking my family, especially my wife Minu for her understanding and encouragement during hard times. I would like to also thank my parents for all the love and prayers.

Abstract

The rapid expansion in power transmission for the integration of large-scale renewables is foreseen in the future. This will be complemented by infrastructure reinforcements in the form of series compensation and high-voltage direct current (HVDC) links. These changes will bring forth new operability challenges to grid operators. The stability issues pertained to such reinforcements: potential threat of subsynchronous resonance (SSR) and frequency regulation will be investigated in this thesis. Utilising the existing and future voltage source converters (VSC) based HVDC links to support the AC system by providing ancillary services will be of significant importance in the coming decades.

The research work presented in this thesis is aimed to address these challenges, in particular, the technical barriers associated with AC/DC interaction and to propose measures to avoid any potential instability. The main contributions of this research work comprise of four parts, namely, (1) analysis of interactions in-terms of SSR in AC/DC grids, (2) design of SSR damping (SSRD) controllers, (3) experimental demonstration of SSRD schemes, and (4) assessment and improvement of frequency regulation in a wind-thermal bundled AC/DC grid.

An VSC-HVDC connected series-compensated AC system resembling the Great Britain (GB) power system has been used as the test network to evaluate the operability challenges pertained to the reinforcements. A state-space representation has been formulated and an eigenvalue analysis has been performed to assess the impact of VSC-HVDC on the torsional modes of nearby connected thermal generation plants. This is followed by damping torque investigation for SSR screening with the results compared against time-domain simulations for testing the accuracy of the small-signal models for SSR studies.

A series of SSRD schemes is presented which have been integrated with the VSC-HVDC to damp SSR in the series-compensated GB power system. In addition, this thesis proposes an adaptive SSRD method based on the real-time estimation of the subsynchronous frequency

Abstract

component present in series-compensated transmission lines—key information for the optimal design of HVDC subsynchronous damping controllers. Furthermore, the combined AC/DC GB network has been implemented in a real-time digital simulator and connected to a VSC-HVDC scaled-down test-rig to perform hardware-in-the-loop tests. The efficacy and operational performance of the AC/DC network while providing SSR damping is tested through a series of experiments.

In order to provide frequency support in a wind-thermal bundled AC/DC system a dual-droop control method is presented. The scheme binds the system frequency with the DC voltage of an HVDC network. For completeness, the performance of the proposed method is compared to conventional frequency regulation schemes. Sensitivity studies and eigenvalue analyses are conducted to assess the impact that wind penetration and changes in the dual-droop coefficient have on grid stability. Experimental validation is performed using a real-time hardware-in-the-loop test-rig, with simulation and experimental results showing a good agreement and evidencing the superior performance of the proposed frequency support scheme.

Contents

Declaration	i
Acknowledgements	iii
Abstract	v
List of figures	xiii
List of tables	xix
Abbreviations	xxi
Symbols	xxiii
1 Introduction	1
1.1 Problem Statement and Research Motivation	1
1.2 Reinforcements in the GB Transmission System	2
1.3 Subsynchronous Oscillations in the GB Transmission System	4
1.4 Frequency Regulation in the GB Transmission System	5
1.5 Research Objectives	6
1.6 Thesis Outline	7
2 Literature Review	9
2.1 Introduction	9
2.2 Operation and Control of AC/DC Transmission Systems	9
2.3 HVDC Configurations for Transmission Systems	12
2.3.1 Current Source Converter HVDC	13

vii

Contents

2.3.2	Voltage Source Converter HVDC	13
2.4	Provision of Ancillary Services from HVDC Systems	17
2.5	Series-compensated AC/DC Grids	17
2.6	Subsynchronous Oscillations	18
2.6.1	Subsynchronous Resonance	19
2.6.2	Subsynchronous Control Interactions	21
2.6.3	Subsynchronous Torsional Interactions	22
2.7	Subsynchronous Oscillation Analysis Methods	22
2.7.1	Screening Studies	23
2.7.2	Damping Torque/Perturbation Analysis	24
2.7.3	Electromagnetic Transient Analysis	25
2.7.4	Hardware-in-the-loop Experiments	25
2.8	Subsynchronous Oscillation Mitigation Schemes	26
2.8.1	Network/Transmission Based	26
2.8.2	Generator/User Based	28
2.8.3	Protection Measures against Subsynchronous Oscillations	29
2.9	Frequency Management in AC/DC Grids	30
2.9.1	Frequency Regulation in AC/DC Grids	32
2.10	Summary	33
3	Modelling and Stability Analysis of Series-Compensated AC/DC Network	35
3.1	Introduction	35
3.2	Synchronous Generator Model	35
3.3	Multi-Mass Turbine Modelling	37
3.4	Modelling of Series-compensated Transmission Line	39
3.5	Modelling of VSC HVDC Link	42
3.5.1	Modelling of Voltage Source Converters	43
3.5.2	DC Line	46
3.5.3	State-Space Modelling of the VSC HVDC Link	47
3.6	System Configuration for Subsynchronous Resonance Study	48
3.6.1	Test system 1: IEEE Standard First-benchmark Model	48

3.6.2	Test system 2: Three Machine GB Model	49
3.7	Subsynchronous Resonance Analysis	50
3.7.1	Eigenvalue Analysis	50
3.7.2	Damping Torque Analysis	55
3.8	Validation of the Small-signal AC/DC Models	59
3.8.1	Time-domain Analysis of MFBM Model	60
3.8.2	Time-domain Analysis of 3GB Model	60
3.9	Summary	63
4	Damping of SSR in a Series-Compensated AC/DC Network using VSC HVDC	65
4.1	Introduction	65
4.2	Operation of Series-compensated 3GB AC/DC Network	66
4.2.1	Primary Control Objective	66
4.2.2	Secondary Control Objective	69
4.3	Damping Scheme: 1 Multi-modal Damper Approach	69
4.3.1	Small-signal Analysis	72
4.3.2	Time-domain Simulation and Analysis	73
4.4	Damping Scheme: 2 Wideband Damper Approach	77
4.4.1	Small-signal Analysis	79
4.4.2	Time-domain Simulation and Analysis	80
4.5	Damping Scheme: 3 Real-time Damper Approach	82
4.5.1	Time-domain Simulation and Analysis	85
4.6	Summary	88
5	Hardware-in-the-loop Experimental Tests for SSR Damping Using VSC HVDC	91
5.1	Introduction	91
5.2	Real-time Hardware-in-the-loop Experimental Test Set-Up	91
5.2.1	Real-time Simulator	92
5.2.2	AC Grid Simulator	92
5.2.3	VSC HVDC Test Rig Configuration	93
5.3	Implementation of RT-HiL Test	94
5.4	Experimental Results: Primary Control System Operation	95

Contents

5.5	Experimental Results: SSR Damping Schemes	96
5.5.1	Integrated AC/DC System without Damping Controllers	98
5.5.2	Integrated AC/DC System with Multi-modal Damper	100
5.5.3	Integrated AC/DC System with Wideband Damper	103
5.5.4	Integrated AC/DC System with Real-time Damper	104
5.6	Comparison of Simulation and Experimental Results	108
5.7	Transferability of the proposed SSR damping schemes	109
5.8	Summary	110
6	Control Strategy for Frequency Regulation in a Hybrid AC/DC Network	113
6.1	Introduction	113
6.2	System Configuration and Frequency Regulation	113
6.3	MTDC Grid Operational Scenario	115
6.4	Frequency Support Schemes	116
6.4.1	Conventional Frequency Support Methods	116
6.4.2	Dual-Droop Control	117
6.5	Impact of Wind Penetration	119
6.5.1	Sensitivity of System Parameters to Changes in Inertia	119
6.5.2	Dual-Droop Parameter Design	121
6.5.3	Eigenvalue Analysis	122
6.6	Simulation Results	124
6.7	Experimental Validation	128
6.7.1	RT-HiL Experimental Test Set-Up	128
6.7.2	Experimental Results	130
6.8	Summary	132
7	Conclusions	133
7.1	General Conclusions	133
7.2	Thesis Summary	133
7.2.1	Modelling and Stability analysis of Series-Compensated AC/DC Network .	133
7.2.2	Control of VSC in a Series-Compensated AC/DC Network for SSR Mitigation	135
7.2.3	Control of VSC in a MTDC Network for AC Grid Stability	136

7.3	Thesis Contributions	137
7.4	Publications reported in this thesis	138
7.4.1	Journal Papers	138
7.4.2	Conference Papers	138
7.5	Other publications during PhD	139
7.5.1	Journal Papers	139
7.5.2	Conference Papers	139
7.5.3	International Workshops and Colloquium Presentations	140
7.6	Future Research	140
A	Modelling of Generator, Multi-mass and Series-compensated Transmission Line	145
A.1	Generator Model	145
A.2	Multi-mass Turbine Model	146
A.3	Series-compensated Transmission Line Model	149
B	Dynamic Modelling of VSC-HVDC Link	151
C	Study System Parameters	155
C.1	Modified IEEE First Bench Mark Model	155
C.2	Three GB Model	156
D	Control Parameters	157
D.1	PSCAD Simulation	157
D.2	RT-HiL Experiments	157
E	Simulation and Experiment Models	159
E.1	Simulation Models	159
E.2	RSCAD Model	160
E.3	High level RT-HiL configuration	161
	Bibliography	165

List of Figures

1.1	Reinforcements in the GB transmission network: Present and future [20, 29]. . . .	3
2.1	Classification of power systems stability [50].	12
2.2	HVDC configurations: (a) LCC system; (b) VSC system.	13
2.3	Developments in AC/DC topology v.s. semiconductor technology [122].	15
2.4	Master-Slave control strategy of VSC based HVDC.	16
2.5	MTDC converter control for different Power vs DC voltage characteristics [62]. .	16
2.6	Forms of subsynchronous oscillations in terms of associated components. . . .	20
2.7	Illustration of frequency management [31].	32
3.1	Schematic diagram of a conventional synchronous generator.	36
3.2	Mechanical sections of six masses turbo-generator system.	37
3.3	The one mass model of the i_{th} mass-spring system [27].	38
3.4	Single line diagram of conventional synchronous generator connected to infinite bus.	40
3.5	Vector diagram representation between the terminal voltage of the synchronous generator and the infinite bus in dq frame with respect to Figure 3.4.	40
3.6	VSC HVDC point-to-point link.	42
3.7	Active and reactive power control scheme.	44
3.8	DC Voltage Reactive power control loop.	46
3.9	DC transmission Line.	47
3.10	Modified first-benchmark model for SSR Analysis	49
3.11	GB three-machine system configuration with reinforcements.	50
3.12	Torsional mode stability in terms of series compensation for MFBM system. . .	53

List of Figures

3.13 Torsional mode stability in terms of series compensation for the 3GB system. . .	55
3.14 Electrical damping of MFBM model over the range of series compensation	58
3.15 Electrical damping of GB model over the range of series compensation	59
3.16 Electrical damping for different VSC loading.	59
3.17 Time-domain results of MFBM model at different compensation levels. (a) Mechanical torque LPAB; (b) Electromagnetic torque; (c) Network frequency; (d) Output power of VSC1.	61
3.18 FFT (2 Hz interval) of the IPAB torque section and current of phase a of the synchronous generator of MFBM. (a) at 40 % series compensation(b) 60% series compensation	62
3.19 Time-domain results of 3GB model at different compensation levels. (a) Mechanical torque LPAB; (b) Electromagnetic torque; (c) Network frequency; (d) Output power of VSC1.	63
3.20 FFT (2 Hz interval) of the IPAB torque section and current of phase a of the synchronous generator of 3GB. (a) at 40 % series compensation; (b) 75% series compensation.	64
4.1 Primary control strategy of VSC HVDC link.	67
4.2 Primary control response of 3GB system.	68
4.3 AC line current response to step change in DC power set-points.	69
4.4 Multi-modal filter based injection structure. (a) Band-pass modal filter; (b) Modified VSC1 control loop.	70
4.5 Frequency response of modal filters at different torsional modes	71
4.6 Electrical damping torque profile of 3GB with and without MMD.	73
4.7 Machine dynamics with MMD enabled VSC in operation for Case A. (a) Mechanical Torque HPIP; (b) Mechanical Torque LPAB; (c)Electromagnetic Torque; (d) Frequency.	74
4.8 VSC HVDC dynamics with MMD enabled VSC in operation for Case A. (a) DC-link voltage; (b) Output power at VSC1; (c) magnitude of dq components of subsynchronous currents.	74

4.9 Machine dynamics with MMD enabled VSC in operation for Case B. (a) Mechanical Torque HPIP; (b) Mechanical Torque LPAB; (c) Electromagnetic Torque; (d) Frequency.	75
4.10 VSC HVDC dynamics with MMD enabled VSC in operation for Case B. (a) DC-link voltage; (b) Output power at VSC1; (c) Magnitude of dq components of subsynchronous currents.	75
4.11 FFT (2 Hz interval) of the current of phase a of the synchronous generator when MMD in operation (a) at 40 % series compensation (b) 75% series compensation	76
4.12 Torsional and HVDC dynamics under large-disturbance without and with MMD enabled VSC in operation for Case B. (a) Mechanical Torque HPIP; (b) Mechanical Torque LPAB; (c) Output power at VSC1; (d) DC-link voltage.	77
4.13 Wideband filter based VSC1 control structure.	78
4.14 Frequency response of band pass filter for the WBD at different values of Q and at $\omega_c=150.72$ rad/s.	79
4.15 Electrical damping torque profile for the 3GB system with and without WBD. . .	80
4.16 Machine dynamics with WBD enabled VSC in operation. (a) Mechanical Torque HPIP; (b) Mechanical Torque LPAB; (c) Electromagnetic Torque; (d) Frequency. .	81
4.17 HVDC link dynamics with WBD enabled VSC in operation. (a) DC link voltage; (b) Output power at VSC1; (c) Magnitude of dq components of subsynchronous currents.	81
4.18 Block diagram of SSFDC: (a) SSFT (b) SSFD.	84
4.19 Rectifier VSC with main and auxiliary control loops.	85
4.20 Machine dynamics with SSFDC enabled VSC in operation for Case A. (a) Mechanical Torque HPIP; (b) Mechanical Torque LPAB; (c) Electromagnetic Torque; (d) Frequency.	86
4.21 Machine dynamics with RTD enabled VSC in operation for Case B. (a) Mechanical Torque HPIP; (b) Mechanical Torque LPAB; (c) Electromagnetic Torque; (d) Frequency.	86
4.22 SSFDC enabled VSC operation for Case A. (a) DC-link voltage; (b) Output power at VSC1; (c) Performance of tracking network oscillation frequency (f_{osc}); (d) Magnitude of dq components of subsynchronous currents.	88

List of Figures

4.23 SSFDC enabled VSC operation for Case B. (a) DC-link voltage; (b) Output power at VSC1; (c) Performance of tracking network oscillation frequency (f_{osc}); (d) Magnitude of dq components of subsynchronous currents.	88
5.1 RT-HiL general diagram.	92
5.2 Real-time set-up. (a) RTDS; (b) Grid simulator.	93
5.3 VSC HVDC test rig configuration. (a) VSC HVDC set-up; (b) VSC's and dSPACE unit,	94
5.4 RT-HiL implementation diagram.	94
5.5 RTDS and VSC test rig interface.	95
5.6 HiL response to primary control of VSC HVDC link.	97
5.7 Experimental results (RTDS signals) without SSR dampers. (a) Line current measured at Bus1 for Case A; (b) Line current measured at Bus1 for Case B; (c) Spectrum of a-phase output current for Case A; (d) Spectrum of a-phase output current for Case B.	98
5.8 Experimental results (RTDS signals) of 3GB system without SSR dampers for Case A. (a) Frequency of phase a current of the Northern Scotland generator; (b)-(c) selected torque interactions in the multi-mass shaft of the Northern Scotland generator.	99
5.9 Experimental results (HVDC rig signals) for Case A. (a) Output power at VSC1; (b) DC-link voltage.	100
5.10 Experimental results (RTDS signals) with MMD enabled VSC in operation for Case A. (a) Frequency of phase a current of the Northern Scotland generator; (b)-(d) selected torque interactions in the multi-mass shaft of the Northern Scotland generator.	101
5.11 Experimental results (HVDC rig signals) with MMD enabled VSC in operation for Case A. (a) Output power at VSC1; (b) DC-link voltage.	101
5.12 Experimental results (RTDS signals) with MMD enabled VSC in operation for Case B. (a) Frequency of phase a current of the Northern Scotland generator; (b)-(d) selected torque interactions in the multi-mass shaft of the Northern Scotland generator.	102

5.13 Experimental results (HVDC rig signals) with MMD enabled VSC in operation for Case B. (a) Output power at VSC1; (b) DC-link voltage.	102
5.14 Experimental results (RTDS signals) with WBD enabled VSC in operation. (a) Frequency of phase a current of the Northern Scotland generator; (b)-(d) selected torque interactions in the multi-mass shaft of the Northern Scotland generator. .	103
5.15 Experimental results (HVDC rig signals) with WBD enabled VSC in operation. (a) Output power at VSC1; (b) DC-link voltage.	104
5.16 Performance of tracking network oscillation frequency (f_{osc}). (a) at around 20 Hz (Case A); (b) at around 27 Hz (Case B).	105
5.17 Experimental results (RTDS signals) SSFDC in operation. (a) Line current measured at Bus1 for Case A; (b) Line current measured at Bus1 for Case B; (c) Spectrum of a-phase output current for Case A; (d) Spectrum of a-phase output current for Case B.	106
5.18 Experimental results (RTDS signals) with SSFDC enabled VSC in operation. . . .	107
5.19 Experimental results (HVDC rig signals) with SSFDC enabled VSC in operation. .	108
5.20 Comparison of simulation and real-time results.	109
6.1 Hybrid wind-thermal system.	114
6.2 Primary frequency regulation including a speed governor and a steam turbine: (a) Grid 1 (b) Grids 2 and 3.	115
6.3 Conventional VSC operation modes in an MTDC grid: (a) Constant power injection; (b) DC voltage - active power droop.	116
6.4 Active power modulation strategies in response to power imbalances: (a) frequency deviation; (b) frequency derivative; (c) dual-droop.	117
6.5 Effect of parametric changes in H : (a) Frequency of Grid 1; (b) Frequency of Grids 2 and 3; (c) DC voltage.	120
6.6 Variation of frequency in Grid 1 to changes in k_{DC} and H for selection of: (a) Operating region; (b) Operational limit.	121
6.7 Loci of eigenvalues for Cases 1 to 4 when inertia in Grid 1 is changed: (a) Eigenvalues of the full system; (b) Dominant eigenvalues; (c) Magnified view of critical eigenvalues.	123

List of Figures

6.8	Eigenvalues when H changes from 0.2 to 2 p.u. for different values of k_{DC} : (a) 1 p.u.; (b) 0.1 p.u.; (c) 1.5 p.u.; (d) 2 p.u.	124
6.9	Trajectory of dominant eigenvalues for $H = 1$ p.u. = 5 s and different values of k_{DC} . 124	
6.10	Simulation results: (a) Wind power injection; (b) Frequency profile of Grid 1; (c) Injected power of Grid 1; (d) Absorbed power by Grid 2 and 3; (e) DC voltage; (f) Frequency of Grids 2 and 3.	126
6.11	RT-HiL configuration: (a) Connection diagram; (b) Set-up.	129
6.12	RT-HiL results. (a) Wind power injection; (b) Frequency profile of Grid 1; (c) Injected power of Grid 1; (d) Absorbed power by Grid 2 and 3; (e) DC voltage. . .	131
E.1	MFBM AC/DC system model implemented in PSCAD/EMTDC.	159
E.2	3GB AC/DC system model implemented in PSCAD/EMTDC.	160
E.3	VSC HVDC control system implemented in PSCAD/EMTDC.	160
E.4	3GB AC system model implemented in RSCAD/RTDS.	161
E.5	High-level diagram of RT-HiL set-up for SSR damping.	163

List of Tables

2.1	The GB transmission system reinforcements [30]	11
2.2	Subsynchronous Oscillation Matrix	21
2.3	Recent SSO events	22
2.4	SSO mitigation schemes: adopted from [30].	27
2.5	Subsynchronous oscillation countermeasures	30
3.1	Torsional Modes of the Modified FBM System	52
3.2	Torsional Modes of the 3GB System	54
5.1	Specifications and parameters of the RT-HiL test-rig	95
6.1	Base parameters used in simulation and experiment	127
6.2	Specifications and parameters of the system	127
C.1	Modified IEEE First Bench Mark Model: System parameters	155
C.2	Three GB model: System parameters	156
C.3	Synchronous Generator: Electrical parameters	156
C.4	Multi-mass parameters:Inertias (in MWs/MVA)	156
C.5	Multi-mass parameters:Self and mutual damping coefficients (in p.u. T/p.u. speed dev.)	156
C.6	Multi-mass parameters:Torsional stiffness (in p.u. T/rad)	156
D.1	Controller Parameters: PSCAD SSR Simulations	157
D.2	Controller Parameters: RT-HiL Tests	157

Abbreviations

2L-VSC	Two-Level Voltage Source Converter
3L-VSC	Three-Level Voltage Source Converter
ENTSOE	European Network of Transmission System Operators for Electricity
EMT	Electromagnetic Transient
FBM	First Benchmark Model
FACTS	Flexible Alternating Current Transmission System
FFT	Fast Fourier Transform
GB	Great Britain
GTAI	Analogue Input
GTAO	Analogue Output
HVDC	High Voltage Direct Current
HiL	Hardware-in-the-Loop
IGBT	Insulated-Gate Bipolar Transistor
LCC	Line Commutated Converter
MMC	Multi-modular Converter
MTDC	Multi-terminal Direct Current
NGET	National Grid Electricity Transmission
PI	Proportional-Integral
PSCAD	Power System Computer Aided Design
p.u.	Per-Unit
PWM	Pulse Width Modulation
RTDS	Real Time Digital Simulator
SSRD	Subsynchronous Resonance Damping

Acknowledgements

SSF	Subsynchronous Frequency
SSCI	Subsynchronous Control Interaction
SSO	Subsynchronous Oscillations
SSTI	Subsynchronous Torsional Interaction
SUB	Subsynchronous Mode
TSO	Transmission System Operator
TCSC	Thyristor Controlled Series Capacitor
TM	Torsional Mode
VSC	Voltage Source Converter
WPP	Wind Power Plant

Symbols

δ	The electrical angle in electrical radians (load angle in rad/s)
Δ	The prefix denotes a small deviation about the initial operating point
σ	Real-part of eigenvalue
ω	Frequency in rad/s
ω_{cn}	Centre frequency of filter in rad/s
ϕ_1, ϕ_2	Phase angle of perturbation and modulated signals
D_e	Damping factor
f_{tm}	Torsional mode frequency
f_n	Network frequency
f_m	Generator rotor frequency
f_{mf}	Modulated frequency
f_{osc}	Subsynchronous frequency component
H_s	Power system inertia constant
I_{dSUB}	SSR damping current in d-axis
I_{qSUB}	SSR damping current in q-axis
I_d	Generator d-axis current
I_q	Generator q-axis current
i_d, i_q	Current in the dq-axis
I_d^{ref}	Reference current in the d-axis
I_q^{ref}	Reference current in the q-axis

Symbols

i_f	Generator field winding current
i_{kd}	Generator d-axis damper winding current
i_{kq1}	Generator q-axis damper winding current 1
i_{kq2}	Generator q-axis damper winding current 2
k_d	d-axis damper winding
k_{q1}	q-axis damper winding 1
k_{q2}	q-axis damper winding 2
K	Series compensation level
k_{MMD}	Multi-modal damper gain
k_{WBD}	Wideband damper gain
k_{DC}	Dual droop coefficient
P_e	Electrical power
P_1	VSC1 output active power
Q_1	VSC1 output reactive power
T_e	Electromagnetic torque
T_S	Synchronizing torque
T_d	Damping torque
T_{LPAB}	Mechanical LPAB section torque
V_{dc}	DC voltage
V_{dssr}	SSR damping voltage in the d-axis
V_{qssr}	SSR damping voltage in the q-axis
v_d	Voltage in the d-axis
v_q	Voltage in the q-axis
X_c	Series-capacitive reactance
X_L	Inductive reactance

1 Introduction

1.1 Problem Statement and Research Motivation

The electric power grid is evolving towards a cleaner, affordable and secure energy network with more non-fossil fuel generation supported by power electronic converters. The integration of low-carbon grid-friendly renewable resources is expected to rise dramatically in the near future. Several countries have increased their renewable share to up to 20% of their total generation capacity [1, 2, 3]. If this trend is sustained, a power grid with more than 30% of renewable penetration will be achieved by 2030 and foreseen to reach 50% by 2050 [3, 4]. A substantial contribution is expected from wind power [3, 4, 5]. Wind power plants are normally located far away from the main load centres, where the resources are plentiful. Their large-scale integration into transmission grids has been accompanied by AC line reinforcements and technological advancements in power electronics [6]. The line reinforcements include the installation of series compensation, complemented by high-voltage direct-current (HVDC) lines [7, 10]. It is expected that the future transmission network will be a hybrid AC/DC structure with many HVDC lines operating in parallel with compensated or uncompensated AC lines [10].

HVDC links which draw no reactive current compared to their high-voltage alternating-current (HVAC) counterpart have been successfully adopted worldwide for long distance bulk power transmission and wind integration [8, 9]. In Europe, it is estimated that within a decade over 25,000 km of HVDC transmission lines will be built and operated in parallel with over 300,000 km of HVAC transmission lines [10]. Hybrid AC/DC operation, control and interaction are

expected to be key challenges in the coming years for a stable and reliable system operation and development [10]. On the other hand, transmission network reinforcement using series-compensation is a well-established alternative to HVDC links. Series-compensation is a well-known method for enhancing the thermal and stability limits of long transmission lines and is economic in installation and operation [11, 12]. Moreover, it provides additional capacity to already constrained transmission line power corridors, thereby reducing the cost associated with building new lines [15]. An example of this case is the Great Britain (GB) transmission network, which is currently undergoing restructuring including HVDC and series compensation installations [7, 13, 14, 15].

1.2 Reinforcements in the GB Transmission System

The United Kingdom (UK) government has set a target of increasing the renewable generation share in the GB energy mix to 15% by 2020 and foreseen to reach 30% by 2030 [16]. Wind energy with nearly 35 GW will account for a major share in this energy mix [17, 18]. The majority of these wind resources are located in the North of the UK (Scotland), but the major load centres are situated in the South of England (London). To accommodate and transmit power from North to South, substantial line reinforcements and introduction of new technologies are required [13, 19]. The existing Anglo-Scottish boundary (known as the B6 boundary) consists of two 400 kV double-circuit AC lines. It has a thermal capability of 4.5 GW, but the power transfer is limited to 3.5 GW because of angle stability constraints [14, 20]. To overcome these limitations, the use of onshore and offshore network reinforcements are planned and adopted [14, 21]. Onshore reinforcements are in the form of fixed series capacitors (FSC) and thyristor controlled series compensator (TCSC), where offshore reinforcements will be achieved through submarine HVDC links (see Figure 1.1) [15, 21].

Besides the reinforcements in the national transmission network, DC interconnection with other grids in Europe and offshore wind power resources, as depicted in Figure 1.1 has been recognised as a key enabler to fulfil GB environmental targets [15, 18]. HVDC technology has been selected as the preferred solution to transfer these clean energy to shore and to develop an integrated North Sea grid [32, 24, 23]. Two alternative technologies are available for HVDC, namely line commutated converter (LCC) and voltage source converter (VSC) [8]. LCC HVDC is

1.2. Reinforcements in the GB Transmission System

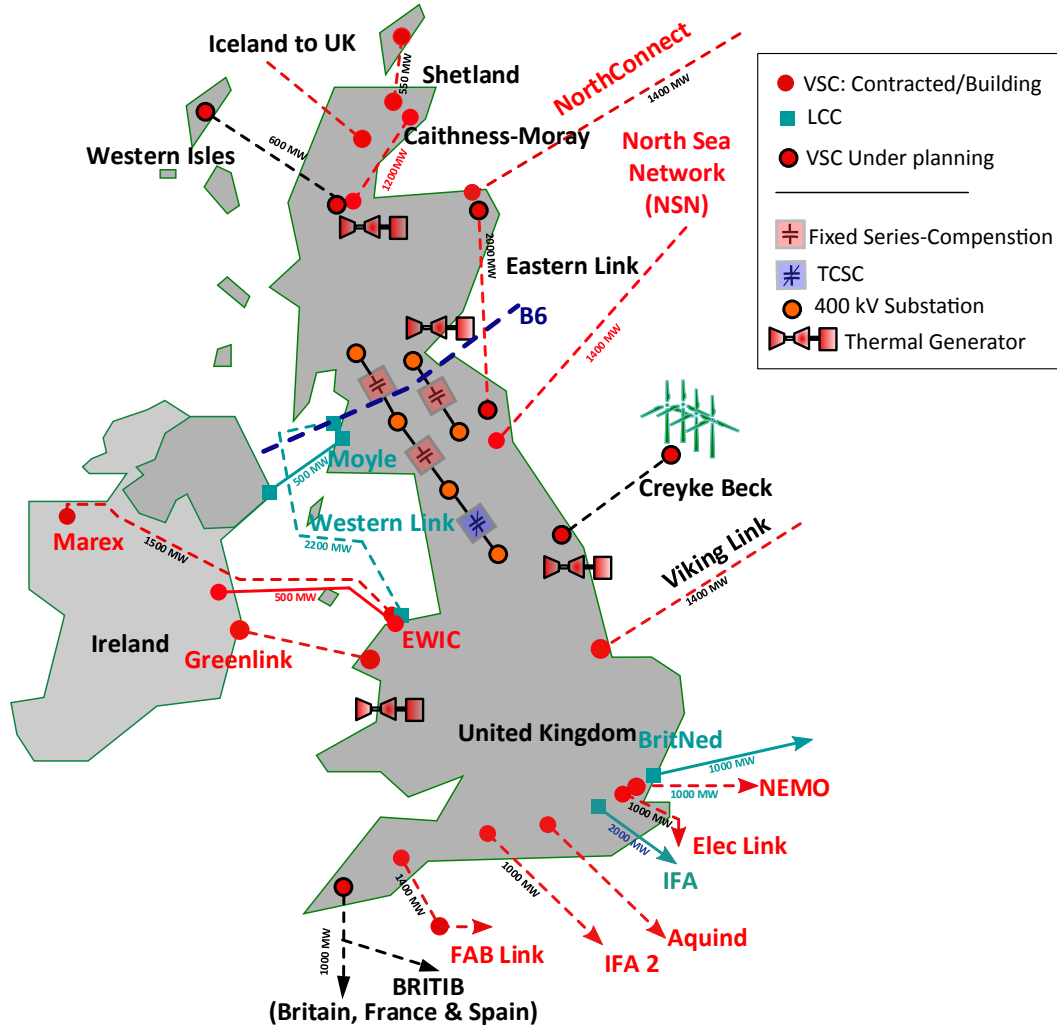


Figure 1.1: Reinforcements in the GB transmission network: Present and future [20, 29].

a well developed and mature technology that has been conventionally employed for bulk power transfer [9]. However, they are susceptible to commutation failure, torsional interaction and do not have black-start and fault-ride-through-capability [22]. On the other hand, VSC HVDC offers independent control of active and reactive power and black-start capability. Due to its inherent advantage of reversing the power flow without reversing the DC voltage polarity, it is expected that multi-terminal DC (MTDC) grids based on VSC technology will be the key enabler for the North Sea grid [6, 22, 24]. Substantial AC line reinforcements have been planned for the GB system to accommodate the North Sea offshore wind developments and increasing the DC link interconnections [20, 21]. To this end, the introduction of HVDC and series compensation will introduce new attributes and challenges in the GB transmission system.

1.3 Subsynchronous Oscillations in the GB Transmission System

The installation of new technologies and services like series-compensator and HVDC has shifted the centralised generation structure of GB power system with new operability challenges which were not present before [15]. Series compensation alters the characteristics of the AC line and its transient behaviour. In addition to enhancing the power transmission capability, series compensation installation is also accompanied by a form of transient and dynamic instability termed sub-synchronous resonance (SSR) [15, 25]. SSR is a condition where the series-compensated transmission line exchanges energy with the turbo-generator at one or more shaft natural frequencies [26, 27]. The interaction causes shaft oscillations resulting in stress, fatigue, failure and damage of the mechanical sections [15, 26].

The potential risk of SSR in the GB system needs to be evaluated in this context due to the proximity of large thermal and nuclear generations near the Anglo-Scottish border to series-compensated lines [21, 15, 29]. Moreover, an effective system-wide SSR analysis in the GB network has been hindered by the parameter uncertainty of the masses representing the shaft. Such information as inertia constant, torsional stiffness and damping coefficients are usually not available which limits the scope of the analysis and design of proper mitigation measures due to the lack of reliable plant data [21]. The challenges related to SSR is expected to be further escalated by the installation of new HVDC links [15, 29].

In the case of HVDC technology, there is a possibility of similar interaction called sub-synchronous torsional interaction (SSTI), seen in LCC installations confined to the interaction between HVDC control systems and the nearby turbine-generator [15, 27]. In addition, with the increased penetration of VSC based devices in applications such as HVDC, wind and photovoltaic inverters a new form of interaction called subsynchronous control interaction (SSCI) has been recently reported [15, 28]. It has been attributed to the interaction of electric network modes of series-compensated transmission lines with the power electronic control systems used in flexible AC transmission system (FACTS) devices, VSC HVDC and wind turbines. SSCI can result in current distortions, overvoltage and potential damage to the control system itself [15, 28].

An increased integration of highly sophisticated control system in close proximity has been identified in the GB system, which is related to the connection of new VSC HVDC interconnecti-

ons, large wind farms, series capacitors, and FACTS devices [15, 29, 30]. The National Electricity Transmission System Security and Quality of Supply Standards (NETS SQSS) have been working on this aspect from the GB point of view and has recently published the revised Grid Code (GC) including sub-synchronous oscillations (SSO) related provisions [30]. The major modifications include the phenomenon (SSR, SSTI, and SSCI) that needed to be considered, the potential risk of SSO events under steady state and transient operating conditions and an assessment of acceptable and unacceptable SSO events and their mitigation measures [30].

Within this context, the impact of VSC systems on SSO and their interaction with neighbouring synchronous generators and series-compensated AC lines is an important research topic with great practical significance, which received a little attention until now.

1.4 Frequency Regulation in the GB Transmission System

With the landing of more HVDC technologies and wind farms to minimise the carbon footprint of GB power system, the future grid will be dominated by power electronic interfaced generations. Such a scenario will bring on a number of challenges for AC system operation such as frequency instability, voltage instability, and reduced system strength [31, 32]. An imminent risk to the GB electricity system due to this high converter penetration has been identified as the reduction in system inertia attributed to the gradual phasing out of synchronous generators [31]. The natural inertia support provided by the synchronous generators to maintain the system frequency will be displaced by generators that are not sensitive to frequency changes, which could results in frequency instability [31]. Frequency regulation schemes and enhanced frequency support provision has thus become a research topic of substantial interest and attention in recent days [33, 35, 36].

Most of the research in this context has been focused only on events such as frequency containment and frequency recovery after a severe disturbance such as generation or demand loss and less attention has been given to the steady state frequency regulation [34, 33]. As number of large wind resources, especially offshore wind farms is expected to be connected through MTDC schemes, the temporary fluctuations of loads and uncontrollable sources have become a relevant issue [33, 35]. Although the impact of such class of events is expected to be smaller, they

occur more often [34]. For analysis purpose, such persistent disturbances need to be considered on the bus where renewable and thermal generators are connected, as the latter still satisfy the base load in current power system and are gradually replaced by the former [34, 37]. In such a scenario, the power grid is expected to operate as a wind-thermal bundled grid with AC/DC connections at low system inertia [38, 39]. Frequency management of such a system through fast active power injection has been considered by National Grid (GB transmission operator) in their recent operability report [31]. Fast power delivery and controllability of converters especially that of VSC based devices can be utilised in such a case for providing flexible frequency support [31, 32].

1.5 Research Objectives

This thesis investigates the operation and control aspects of AC/DC grids with focus on measures to enhance the AC system stability utilising the control flexibility provided by VSC technology. The main objectives of this research work are summarised as:

- To develop mathematical models of hybrid AC/DC grid including the multi-mass model of turbo-generators, VSC HVDC link with associated controllers and series-compensated transmission line to perform small-signal stability assessment.
- To design and test different multi-modal subsynchronous resonance dampers (SSRD) in the reinforced hybrid AC/DC GB model through VSC control loop modification.
- To develop an adaptive SSRD which can identify, track and damp multiple network modes irrespective of power system configurations and turbine generator shaft parameter uncertainty using VSC HVDC in the GB system.
- To design and build a real-time hardware-in-the-loop (RT-HiL) experimental set-up to validate the VSC's capability to damp multiple torsional modes and provide the basic functionality of power transfer utilising the proposed SSRD schemes.
- To implement a new control scheme for primary frequency regulation and frequency stability enhancement in a wind-thermal bundled hybrid AC/DC network.

- To experimentally validate the proposed controller performance in maintaining wind-thermal bundled hybrid AC/DC system frequency under high wind penetration levels.

1.6 Thesis Outline

- **Chapter 2** address the challenges in AC/DC grids of the future with a focus on SSO and frequency regulation and provides a review on the existing research on SSO and frequency regulation analysis, schemes and control methodologies.
- **Chapter 3** presents the modelling approaches and analysis suitable for performing the small-signal stability studies for SSO quantification in the 3GB system with series compensation and VSC HVDC link. Two approaches namely eigenvalue analysis and damping torque analysis have been used. The small-signal models are further utilised in Chapter 6 for analysing the frequency stability. The developed models are validated against time-domain simulations in PSCAD/EMTDC package and RT-HiL platform.
- **Chapter 4** introduces, formulates and evaluates different SSO damping schemes based on supplementary control of VSC HVDC link embedded in the 3GB system. Three damping schemes were discussed: the first one based on the multi-modal filter; second one based on the wideband filter; and the third one, an adaptive damper which can identify, track and damp multiple modes (frequencies) irrespective of power system configuration and mechanical mass uncertainty of turbine-generators. The robustness of the controller to different operating conditions is tested through small and large disturbances like three-phase faults. The performance of the dampers on damping multiple modes using VSC is tested through PSCAD time-domain simulations.
- **Chapter 5** describes an RT-HiL design to test and validate the SSRD schemes devised in Chapter 3. The 3GB network is modelled in Real-Time Digital Simulator (RTDS), whilst a physical VSC HVDC test rig is used to represent the DC link. A power amplifier is used to close the loop to perform the HiL tests. The damper schemes introduced in Chapter 4 is implemented in VSC and various tests are performed by changing the series compensation levels to validate the adaptability of the controllers. The experimental results show good agreement with the simulations performed in Chapter 4.

- **Chapter 6** introduces the frequency stability and regulation issues associated with wind-thermal bundled AC/DC system under high wind penetration levels. A control scheme named dual-droop is introduced and implemented as a supplementary control in a three-terminal VSC MTDC scheme. The performance of the proposed method is compared to conventional frequency regulation schemes via sensitivity studies, eigenvalue analysis and time-domain simulations for different wind penetration levels. Finally, the performance of the proposed controller is experimentally validated through RT-HiL platform. The experimental results show good agreement with theoretical analysis and simulation results.
- **Chapter 7** outlines the summary of major findings and contributions of this thesis. Future scope of work pertained to SSO and frequency stability challenges in hybrid AC/DC grids are discussed.

2 Literature Review

2.1 Introduction

This chapter presents the background review of network configuration, operation, stability and control of AC/DC grids. A brief review of the operational challenges of the AC/DC grids is introduced followed by the discussion on the AC/DC transmission configurations. Introduction of series compensation and the potential risk of sub-synchronous oscillations (SSO) has been discussed in detail. The state-of-the-art models, concepts, analysis and tools for SSO detection and mitigation are discussed within the context of compensated AC/DC grids. Finally, the issues pertained to frequency stability and frequency regulation in a hybrid AC/DC grid with a high level of renewable penetration is formulated. This is followed by a detailed review of the methods, schemes and control approaches for primary frequency regulation in AC/DC grids.

2.2 Operation and Control of AC/DC Transmission Systems

The nature of electricity transmission network has evolved over the last 20-30 years due to the technological advances and increased environmental concerns [43]. This has fuelled interest in the development of cost-effective, reliable and environment-friendly technologies which can fundamentally change the behaviour of the power systems [40]. HVDC technology is one these new component, which is seen as a key enabler for a sustainable and competitive energy supply and can operate alongside traditional AC grids to form an AC/DC transmission network [40, 41, 43]. This change is foreseen not only in Europe but around the globe as evidenced by the profound need to replace or upgrade the ageing and constrained transmission assets to expedite the renewable integration [40, 41]. Moreover, the difficulties such as public

resistance, environmental concerns and long permitting process associated with building new AC transmission lines has fuelled the interest in HVDC, which are considered to replace AC lines [45, 46]. To complement the HVDC transmission, existing AC line upgrade using series compensation is also considered [14]. These reinforcements will improve the power transfer through restricted transmission corridors without building new lines and structures, thereby reducing the impact on the environment [14, 15].

Many researchers have worked on the potential benefits of AC/DC system operation in terms of design complexities, power transfer capability, economic value and the impact on climate change [45, 46, 47]. The process of converting AC transmission lines to DC operation were reported in the early twentieth century. These retrofit was mainly based on the transformers ability to increase the voltage level, to achieve low loss power transmission [44, 48, 49]. Faster economic growth and industrialization in the 1990s demanded the need for long transmission lines impacting the existing AC lines, as they start saturating to their critical ampacity limit [48]. Further to that, as the distance gets longer, the active power transfer capability of AC lines was constrained by the reactive power limits of overhead lines and cable technologies. This required the installation of reactive power compensation at short intervals along transmission lines [44, 48, 49]. However, the absence of reactive power in HVDC systems makes them suitable for long distance power transmission [44]. Moreover, they provide additional services like asynchronous AC systems connection, active power flow control and reduced requirement for right-of-way [40].

To complement the HVDC developments further efforts are being made to extend the AC line capacity through shunt and series compensations, variable transmission frequency for AC cables and different operating voltages [46, 47]. To this end, over a century after the war of currents when AC won over DC, application of HVDC in the transmission system is progressing to reach in parity with AC. This might take a few more years, however, the transmission network is foreseen to operate as a hybrid AC/DC electrical power network [40, 41, 43].

From the Great Britain (GB) power systems perspective, the transmission network reinforcement plans for the next ten years are outlined in Table. 2.2 [30]. The main drivers for the GB network upgrade with HVDC and series-compensated transmission lines are the proliferation of

2.2. Operation and Control of AC/DC Transmission Systems

Table 2.1: The GB transmission system reinforcements [30]

Project	Technology	Transmission Licensee	Need Case	ETYS 2014 EISD*
Harker-Hutton Series Compensation	Thyristor Controlled Series Capacitor (TCSC)	NGET	Increasing the stability limit of the AC interconnection between NGET and SPT	Already in service
Gretna-Harker / Moffat-Harker Series Compensation	Fixed Series Capacitor with Passive SSR Damping Filter	SPT	Increasing the stability limit of the AC interconnection between NGET and SPT	2015
Eccles-Stella West Series Compensation	Fixed Series Capacitor with Passive SSR Damping Filter	SPT	Increasing the stability limit of the AC interconnection between NGET and SPT	2015
Western HVDC Link	CSC HVDC Submarine Cable	NGET / SPT	Primary boundary capability increase	2017
Caithness Moray HVDC Link	VSC HVDC Link (with multi-terminal capability)	SHET	Primary boundary capability increase	2018
Shetland Connection	VSC HVDC Link (to be connected to the Caithness Moray Link)	SHET	Generation connections	2020
Western Isles	VSC HVDC Link	SHET	Generation connections	2020
Orkney	VSC HVDC Link	SHET	Generation connections	2021
Eastern HVDC Link(s)	VSC HVDC Link	NGET / SPT / SHET	Primary boundary capability increase	Post 2024

renewables, ageing power system assets which need retrofit, deregulation of power market and the growing load demand which are located far away from the generation [15, 30]. Another key driving force is the provision to balance generation through cross-border electricity trading and the offshore renewable potential in the North Sea [31].

The landing of new technologies brings new system operation and control challenges, such as potential AC/DC interactions and instabilities which are associated with traditional power systems operation, as shown in Figure 2.1 [50]. Instabilities in a hybrid AC/DC grids may be manifested in a different way and/or in the traditional way which requires thorough analysis and control measures [45]. To this end, in this we discuss the power system stability, in particular, rotor angle and frequency stability associated with compensated or uncompensated hybrid

AC/DC grid, highlighted as green in Figure 2.1.

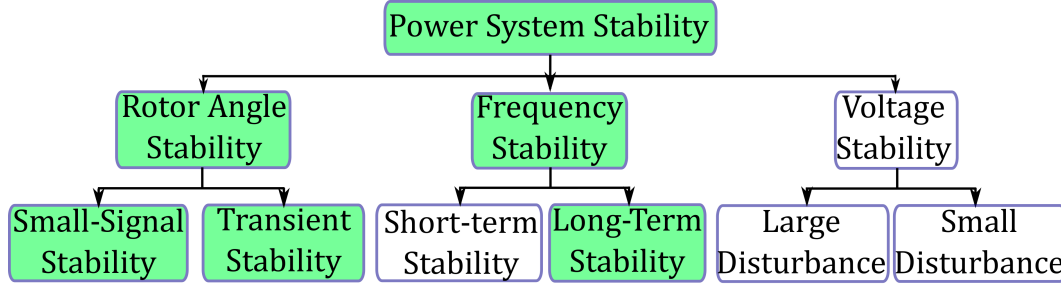


Figure 2.1: Classification of power systems stability [50].

2.3 HVDC Configurations for Transmission Systems

With the availability of mercury arc valves in the early 1930's, HVDC transmission reached certain parity with AC transmission. Such a major development in semiconductor technology paved the way for the construction of the first DC link. This was a 3 MW, 45 kV link between Germany and Switzerland [9]. However, by 1970's, the use of mercury arc valves in HVDC applications lost ground due to the unavailability of spare parts and the concurrent progress in thyristor valves. Once thyristors started to take over the HVDC regime from mercury valves, the availability of HVDC projects increased significantly from 83 to 98% and since then they have been substantially deployed in transmission networks [51, 52, 53].

However, in 1997, HVDC converters employing transistor technology has been introduced in power transmission. Such voltage controlled devices, such as voltage source converters (VSC) with self-turn-off capability, together with an independent control of active and reactive power added more value proposition for HVDC systems [51, 52]. Until now, the VSC-based transmission has paralleled thyristor-based converter assets wherever possible [43]. To this end, irrespective of technology, depending upon the location and function of the converter stations, different HVDC system configurations can be identified and are entirely project and application dependent. The typical HVDC configurations are back-to-back, monopolar, bipolar and multi-terminal scheme [42, 43].

2.3.1 Current Source Converter HVDC

Current Source Converter or Line Commutated Converter (LCC) HVDC systems use thyristor valves. The key performance addition from thyristor-based converters compared to mercury arc valve was the ability to bring together control and conversion operations into one device, leading to substantial savings in space and weight [8, 42, 43]. However, current reversal is not possible in LCC systems due to the limited two-quadrant operation of the thyristor switches. Moreover, LCC can only control active power and not the reactive power which prerequisite additional filters for reactive power compensation that can reach up to 50-60% of the rated load [42, 43]. The main elements of an LCC station are shown in Figure 2.2 (a), which consists of valve bridge with an array of valves, smoothing reactor (L_s) in the DC side and the converter transformer which interfaces the LCC to the AC grid through phase reactor and filters [52, 54]. The LCC systems operate as constant current controlled devices to limit the over-current and the AC voltage fluctuations which can damage the converter bridges [52, 54]. Until now around 50 LCC HVDC projects have been constructed with power rating reaching up to 10.5 GW and voltages reaching ± 1100 kV with a DC line of 2600 km [55]. However, even after years of research and practical experience in LCC technology, due to their large volume are unattractive for weak grid connections especially offshore applications [24]. In addition, they are susceptible to commutation failure, torsional interaction and do not have black start capability [42, 43].

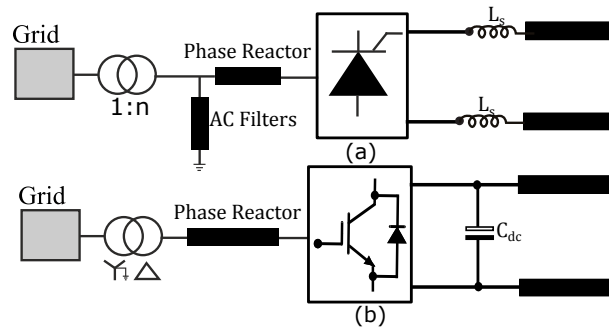


Figure 2.2: HVDC configurations: (a) LCC system; (b) VSC system.

2.3.2 Voltage Source Converter HVDC

Voltage-controlled transistor-based semiconductor devices like insulated-gate bipolar transistor (IGBT) developed during the late 1970's, have found their place in the lower end of the power

range for HVDC applications [51]. Their self-turn-off capability, together with an independent control of active and reactive power, leads to a smaller footprint when employed in VSC stations [42, 43, 51]. In addition, the four-quadrant operation enables them to achieve power flow reversal in HVDC applications by changing the direction of current while keeping constant DC voltage. This service made them attractive for niche applications like weak grid connection and/or the construction of dc grids for the integration of large-scale renewables—such as offshore wind farms [55, 56]. The main elements of a VSC station are shown in Figure 2.2(b), which consists of converter bridge with an array of IGBT modules, DC link capacitor (C_{dc}). A converter transformer is used to interface the VSC to the AC grid through the phase reactor [57, 58, 59]. Independent control of active and reactive power in VSC is achieved by controlling the current flowing through the phase reactor. The DC link capacitor will behave as a DC voltage source to the converter while filtering out the ripples in the DC voltage caused by converter switching [57, 58, 59]. Earlier design of VSC HVDC converters based on two-level topology necessitates the AC filters for wave form smoothing and harmonic elimination [58, 59].

As of now, VSC-based high voltage transmission assets are in their fourth generation, with modular multilevel-based converter topologies suitable for high power and high voltage applications due to their low power losses and minimal filter requirements (see Figure 2.3) [56, 60]. Until now, the VSC-based transmission has paralleled thyristor-based converter assets wherever possible [56, 60]. With the increased demand for renewables to meet climate change challenges and the increasing interconnections among countries, further development of transistor-based power converter topologies are imperative. As of now, the VSC HVDC transmission reached the voltage rating of ± 515 kV for a power exchange of 1400 MW through a 720 km DC cable line, which is being built between the GB and Norway [61].

2.3.2.1 Topology and Control of Voltage Source Converter based HVDC

The high voltage AC/DC topology developments in concurrent to semiconductor technology advancements are depicted in Figure 2.3. The common VSC topologies for HVDC systems are two-level (2LVSC), three-level (3LVSC) and multi-level converter (MLC) topologies [56, 60]. A 2LVSC operates between two voltage levels: either V_{dc} and *zero* or $V_{dc}/2$ and $-V_{dc}/2$ [59, 60]. The 3LVSC provides a third voltage level due to the neutral point clamping: $V_{dc}/2$, *zero*, $-V_{dc}/2$

2.3. HVDC Configurations for Transmission Systems

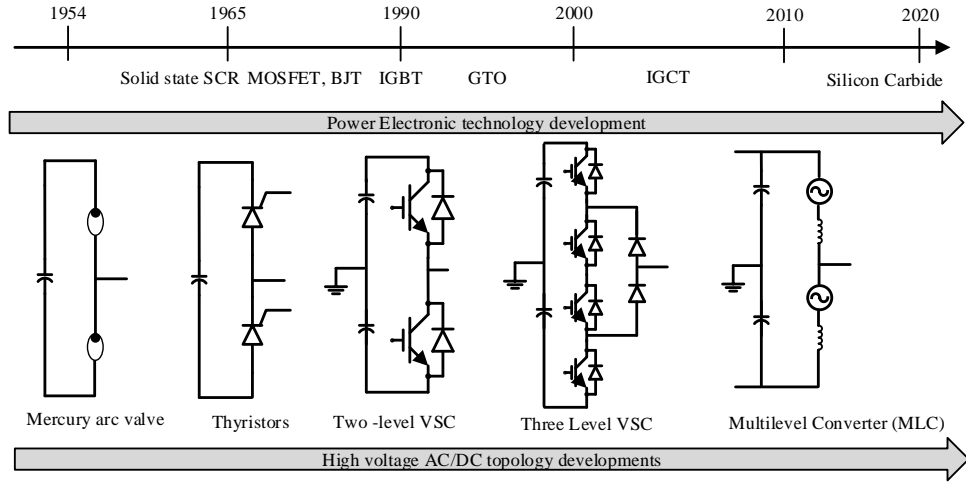


Figure 2.3: Developments in AC/DC topology v.s. semiconductor technology [122].

[56, 60]. In an MLC, there are hundreds of series connected bi-directional cell of IGBTs called sub-modules which can switch in a large number of time-steps between $V_{dc}/2$ and $-V_{dc}/2$ [56, 60]. Therefore for MLC, the output voltage is close to the sinusoidal waveform with only higher order harmonics because of a large number of small steps. This resulted in less or almost no filtering required for MLC compared to other topologies [56, 60].

Irrespective of topologies the typical control strategy opted for VSC HVDC link is master-slave control as shown in Figure 2.4, where one terminal regulates the DC voltage (see Figure 2.4(a)), while the other terminal controls the active power flow in the link (see Figure 2.4(b)) [58, 59]. The VSC's can control the power flow through the DC lines through voltage magnitude and angle control with AC systems or alternatively through direct and quadrature (dq) control mode, as depicted in Figure 2.4 [58, 59]. In the dq control scheme, an outer controller is used to set the operation mode of the VSC which provides current orders to the inner control loop, where the measured currents are controlled to match the reference value set by the outer controller [59]. In addition to the primary control objectives secondary system control functions such as AC voltage, reactive power and frequency control can be employed for grid support [58, 59].

For multi-terminal DC (MTDC) connected converters there are different control options proposed by a number of authors. Motivated from the traditional point-to-point HVDC control, master-slave control is the frontrunner among them, a modified version of master-slave control

Figure 2.5: MTDC converter control for different Power vs DC voltage characteristics [62].

2.4 Provision of Ancillary Services from HVDC Systems

The provision of ancillary services such as supplementary modulation of the active power of HVDC links to damp low-frequency oscillation has been implemented by system operators such as WECC since the 1970s [63]. With an increasing number of HVDC installations around the globe, there has been a renewed interest in this area [64]. To this end, an increasing amount of research has been conducted on the provision of ancillary services from HVDC's, such as frequency and inertia support, power oscillation damping, subsynchronous oscillation damping and AC voltage support [64, 65, 66, 67]. However, most of the work in this direction has primarily focussed on LCC HVDC technology [64, 67]. With independent active and reactive power provisions, the VSC HVDC technology offers more flexibility than LCC where only active power modulation can be utilised for this purpose [68].

Taking this into account, the European Network of Transmission System Operators for Electricity (ENTSO-E) recently published the Network Code on High Voltage Direct Current Connections (NC HVDC) [69]. The key requirements for network interconnection of HVDC systems (both HVDC and MTDC) and dc-connected power plants are specified in this document. Ancillary service provisions to host and connected AC grids is stated as one of the key requirements in the grid code [69]. This includes frequency and active power control, voltage and reactive power control, provision of power oscillation and subsynchronous torsional interaction damping [69]. It is expected that transmission system operators (TSOs) associated with ENTSO-E will integrate NC HVDC guidelines into their own respective network codes [30, 69]. The GB power system network operator National Grid (NG) has identified the urgency of this issue and recently updated the National Electricity Transmission System Security and Quality of Supply Standards (NETS SQSS) and Grid Code related to SSO in the light of increasing network reinforcements through HVDC and series compensation [30].

2.5 Series-compensated AC/DC Grids

Enhancing the transmission boundary power flows using existing assets is always a challenging task for TSO's, as they have to rely on new technologies which bring forth important operational challenges [7, 15, 30]. To this end, installation of series compensation is an effective and econo-

mical way of improving asset utilisation which in turn improves the investors return and reduces consumers cost [7, 15, 30]. It is also seen as an alternative to capital-intensive AC transmission line addition and/or HVDC installations for easing the power flow bottle-necks [70, 71]. Series compensation comprises of either fixed series capacitor (FSC's) or thyristor controlled series capacitor (TCSC). Their installation into the AC/DC grid is becoming widespread, with the GB system landing its first series compensation in 2015 [30, 71]. These reinforcements, especially those of ABB's TCSC installation are aimed to enhance the transmission corridor between North and South [70, 71]. In addition to improving the power flow management of the network, they help with transient stability, voltage stability, and reactive power management of the network [70, 71].

However, the use of series capacitors brings the risk of subsynchronous resonance (SSR), where the electrical modes of the series-compensated transmission line interact with their mechanical counterparts from nearby thermal generation plants, evidenced by the Mohave SSR events in 1970 and 1971 [72]. After these events, a number of significant efforts and research studies have been made by utilities and equipment suppliers to tackle any such undesirable interactions as reported by IEEE SSR Working Group [73]-[79]. However, in 2009, a new form of interaction occurred in Texas, the US. This phenomenon was attributed by the interaction of electric network modes of series-compensated transmission lines with the power electronic control systems used in Type-3 wind turbines [28, 80]. This event caused the re-emergence of SSR and fuelled the interest among power converter manufacturers and system operators realising the importance of analysis and control schemes needed to identify and mitigate any such interactions [15, 81, 82]. A number of research contributions have been made in this directions focussing on the phenomenon, screening and mitigation schemes associate with any of these undesirable interactions [81, 82, 83, 84] and will be detailed in the following sections.

2.6 Subsynchronous Oscillations

The IEEE committee report defines SSR as the electric power systems condition where the electrical modes of the series-compensated transmission line exchange energy with their mechanical counterparts of nearby thermal generation plants [78]. This was used as the bottom-line for analysis and control design until new forms of interactions and negative energy exchange emer-

ged in the power systems domain [78, 79]. The terminologies associated with the oscillations occurring at subsynchronous frequency has been redefined due to the incorporation of new technologies and new forms of interactions [84]. To this end, the Office of Gas and Electricity Market (Ofgem) in the UK defines SSO as the power system oscillations attributed by the interaction between certain equipment on the National Electricity Transmission System (NETS) below the power frequency, 50 Hz [30]. The SSO incorporates all the oscillations occurring at subsynchronous frequencies, as a result of the interactions between the different types of equipment connected to the NETS [30, 84]. The interactions may occur between: series compensation and generating units; generating units and HVDC converters; or between different converter control systems and series compensation [30, 84]. To clearly understand the interactions between different components and equipment in the power systems domain, a classification of different SSO phenomenon is presented in the next section. The SSO can be mainly classified into three categories as illustrated in Figure 2.6 [15, 30, 84]. The interactions between different components in the power systems and the resulted phenomenon are also highlighted in Figure 2.6.

2.6.1 Subsynchronous Resonance

Subsynchronous resonance (SSR) is the condition of the power systems, typically when a series-compensated AC line, exchanges energy with a turbine-generator at one or more natural frequencies below the fundamental 50/60hz frequency. SSR, if left unattended could have a significant implication by causing damage or failure to the generator shafts; and cause health and safety risks on personnel [30, 84]. Typically there are three aspects of SSR:

2.6.1.1 Torsional Oscillation:

Subsynchronous torsional oscillations (SSR-TO) is the classical SSR condition and is attributed by rotor oscillations at torsional mode frequency (f_{tm}) induced by the voltage in the armature at a frequency $f_m = f_n \pm f_{tm}$ due to small-disturbances [74, 75]. When f_m is close to or equal to the network frequency (f_n), introduced by the series-compensated transmission line below, f_n , there will be a sustained oscillation in the mechanical torque produced by the subsynchronous voltage components [74, 75]. SSR-TO is associated with both mechanical (turbine-generator shafts)

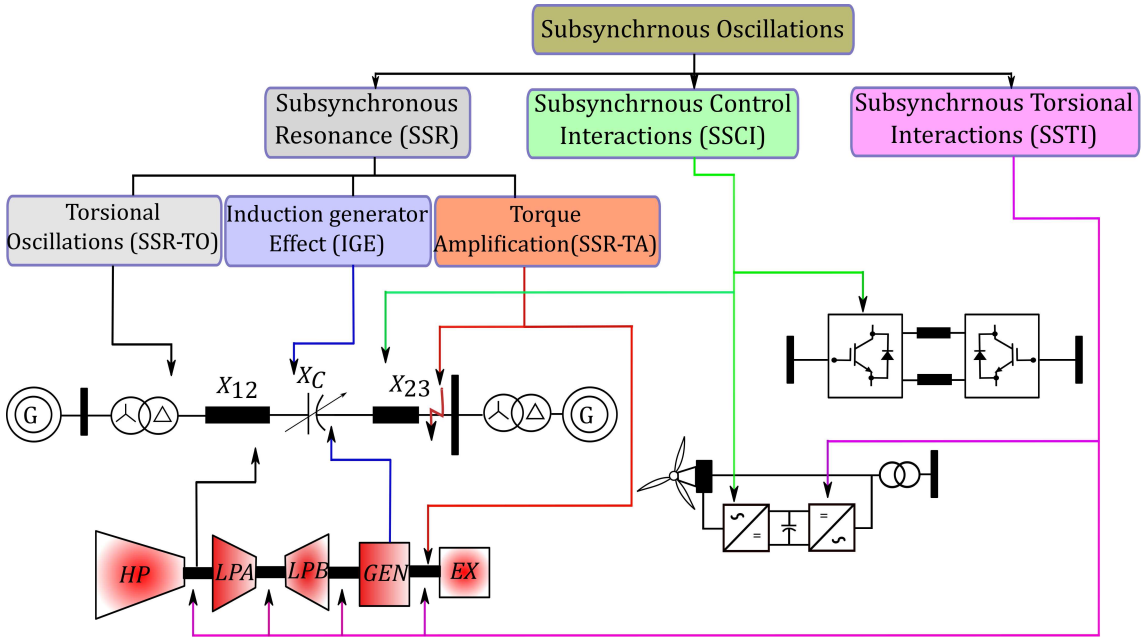


Figure 2.6: Forms of subsynchronous oscillations in terms of associated components.

and electrical (series-capacitors) components as traced by black lines in Figure 2.6 [74, 75]. The SSR-TO event is accompanied by extreme heating due to the excessive field currents, and results in low cycle fatigue vibrations and eventually shaft damage [15, 85].

2.6.1.2 Induction Generator Effect:

The induction generator effect (IGE) is purely an electric resonance condition attributed by the interaction between series-compensated AC lines and the generator rotor electrical dynamics and is independent of the generator shaft torsional modes as traced by blue lines in Figure 2.6 [15, 84]. The subsynchronous frequency component (f_n) will produce a rotating magnetomotive force (MMF) in the armature air-gap, which will interact with the main field air-gap MMF to produce torques at the sub and supersynchronous frequencies $f \pm f_n$ [84, 85]. When the generator rotor frequency f_m differs from $f - f_n$, the generator rotor will turn more rapidly than the rotating MMF and as a result the resistance of the rotor at subsynchronous frequencies viewed from armature terminals is negative since the slip of the machine viewed as an induction generator is negative [85]. This condition is known as self-excitation and is accompanied by sustained armature currents and voltage oscillations enough to damage the equipment connected [84, 85].

Table 2.2: Subsynchronous Oscillation Matrix

Device	Series Capacitor	Power Electronics	Turbine Shafts	Weak AC Grids
Series Capacitor	–	SSCI	SSR	–
Power Electronics	SSCI	SSCI	SSTI	New SSO
Turbine Shafts	SSR	SSTI	–	–
Weak AC grids	–	New SSO	–	–

2.6.1.3 Torque Amplification:

Subsynchronous torsional amplification (SSR-TA) is attributed to a large system disturbance, such as faults in a series-compensated AC line as traced by red lines in Figure 2.6, leaving high amplitude transient torques on the generator rotors and mechanical shafts [84, 85]. The shaft response contains typically contributions from non-sinusoidal uni-directional components which decays exponentially with subsynchronous and multiple frequency components [84, 85]. However, due to SSR-TA, the subsynchronous component will be predominant following the large disturbance and may take a longer time to damp out. The occurrence of such high amplitude torque may lead to cyclic fatigue of the mechanical shaft system [15, 84].

2.6.2 Subsynchronous Control Interactions

Subsynchronous control interactions (SSCI), is a condition where a power electronic device (HVDC, SVC, STATCOM, Wind turbine control, etc.) interacts with the subsynchronous modes of the nearby series-compensated transmission line, as illustrated by green lines in Figure 2.6 [15, 84]. The SSCI events are attributed to the control system interactions and can be more pronounced in networks with low short circuit ratios [15, 84]. There is no mechanical components involved in this event and is associated with overvoltage, current distortions and potential damage to control systems of the power electronic interface. The potential risk of SSCI events has been recently explored by a number of work which is predominately related to the interactions from non-synchronous generators, HVDC converters, FACTS devices and series-compensated transmission lines [81, 84].

Table 2.3: Recent SSO events

Events	Year	Contributors	Type
Texas SSCI Event	2009	Type-III Wind Turbine and Series Compensation	SSCI
North Dakota SSO Event	2010	Type-III Wind Turbine and Series Compensation	SSR
Oklahoma SSO Event	2011	Type-III Wind Turbine and Series Compensation	SSR
China Jibei SSO Events	2014	Turbine-generator and Series Compensation	SSCI
SSR Event in India	2014	Turbine-generator and Series Compensation	SSR
Xinjiang, China	2015	Type-IV Wind Turbine and Weak Grid	SSCI
China South Grid	2016	Power electronic devices and Weak Grid	SSTI

2.6.3 Subsynchronous Torsional Interactions

Subsynchronous torsional interaction (SSTI) is a condition attributed to the interaction between power electronic devices and the mechanical mass system of a turbine-generator as portrayed by the purple line in Figure 2.6 [15, 84]. To emphasise, SSTI does not involve interaction with series compensation and the likely sources are HVDC, SVC, STATCOM and variable speed drives [15, 84, 85]. The known incidents associated with SSTI is the Square Butte USA event, in which the HVDC terminals interacted with the modes of turbine-generator shafts resulting in the destabilization of the control modes of the HVDC system [72]. The interdependency of different power system components and the interactions arising from them in the subsynchronous frequency range is summarised in the subsynchronous oscillation matrix, Table. 2.2 [73]-[84].

The recent SSO events and the phenomenon attributed to the incidents are summarised in Table. 2.3 [80]-[84].

2.7 Subsynchronous Oscillation Analysis Methods

There is a vast amount of techniques available in the literature for the study of SSO in electric power systems [73]-[84]. Depending upon the applications and requirements the most common techniques adopted are:

2.7.1 Screening Studies

The increased interest from the power systems equipment suppliers and system operators in the light of new SSO events paved the way for the developments in SSO screening studies as reported in [30, 81, 85]. The recent advancements in this direction can be summarised under the three categories:

2.7.1.1 Eigenvalue Analysis:

Eigenvalue analysis or modal analysis is identified as one of the most matured and detailed screening technique for SSO identification [81, 85]. It is based on the mathematical representation of electrical network, generators and power electronic devices of interest in a common linearised system of differential equations [27, 85]. Eigenvalue analysis can be used to predict the system state behaviours under small-disturbances and are suitable for SSR, SSCI and SSTI analysis. Moreover, the detailed information on the system performance beyond the normal frequency scanning can be achieved for each modes of oscillation [27, 85]. Another key advantage of this method is that it can be combined with well known linear control schemes and can be used to design SSO damping methods [85, 86]. However, this method is computationally intensive and complex, which requires detailed mechanical and electrical system representation, with a separate linear model required for each network configuration [83, 85].

2.7.1.2 Frequency Scan/Harmonic Impedance Analysis:

Frequency scan analysis introduced in late 1970's is used to determine the network impedance as a function of frequency viewed from behind the generator equivalent impedance [87]. Furthermore, it can be used to determine the approximate electrical resonance frequency and can be also used to recognise those sections in the system that is not influenced by SSR [27, 87]. The technique is a common tool in industry for SSR, SSCI and SSTI screening of a large system during the design stages [27, 47, 79]. Resonance points and damping of the system can be deduced from frequency scans to assess the possibility of SSO's [27, 47, 79]. The main limitations of this technique is associated with the representation of the power electronic devices in the network and do not take into account system contingencies and transient events [47, 85].

2.7.1.3 Unit Interaction Factor Analysis:

The influence of HVDC converter control on the torsional oscillations and damping of a generator under study can be quantified by the Unit Interaction Factor (UIF) which was developed by Electric Power Research Institute (EPRI), US [88]. It is widely used as a screening level indicator for SSTI identification, so as to determine the level of risk [27, 88]. In general, UIF can be defined as:

$$UIF = \frac{MVA_{HVDC}}{MVA_{Gi}} \cdot \left[1 - \frac{SC_{Gi}}{SC_{TOT}}\right]^2 \quad (2.1)$$

where MVA_{HVDC} , MVA_{Gi} , are the rating of the HVDC and generator under study; SC_{Gi} , SC_{TOT} are the system short-circuit capacity at the HVDC bus with generator under study in-service and without service [27, 88]. A UIF value of less than 0.1, indicates less possibility of interactions and is recommended. The UIF is performed with different AC network configurations and contingencies so as to evaluate the SSTI condition when the system configuration changes [27, 88]. As this is routinely carried out before HVDC installations, once SSO risk is identified ($UIF > 0.1$), a detailed Electromagnetic Transient (EMT) analysis is required for further evaluation and control design [27].

2.7.2 Damping Torque/Perturbation Analysis

A damping torque analysis can be used to determine the contribution made by the power systems towards the electrical damping of the generator unit of interest [27, 89]. It is a useful tool for SSR, SSCI and SSTI analysis which received much interest due to the simple representation of the mechanical characteristics [90]. This analysis can be carried out only with electrical representation of power system components in an EMT type simulation with a non-linear representation and detailed control system of associated power electronic device [27, 89]. This avoids the limitations associated with eigenvalue screening method. The damping torque analysis is carried out by perturbing the generator speed and correspondingly calculating the electric torque of the generator unit of interest [89, 90]. Further, this torque response is used to calculate the electric damping for all the subsynchronous frequency range by varying the perturbation signal frequency from zero to the fundamental value [89, 90]. To generalise, the real

part of the network transfer function (or network equivalent impedance) between speed change and the electrical torque indicates the electrical damping factor. If the resultant damping torque is negative the torsional oscillation is unstable [89, 90]. However, this method is computationally intensive and time-consuming.

2.7.3 Electromagnetic Transient Analysis

To overcome the modelling challenges associated with SSO screening techniques, detailed time-domain analysis in an EMT type digital software platform or real-time simulator is a proven alternative [26, 90]. The key advantage of this kind of solver is the identification of SSR-TA phenomenon instigated by a large system disturbance [90, 85]. Detailed models of both mechanical and electrical systems can be simulated for a large transient case and can also test corrective actions [26, 27]. Off-line simulation becomes handy when the overall system response needs to be simulated in response to an SSO event and to analyse the performance of necessary control actions and protection settings [26, 27]. Moreover, this approach is essential to analyse multiple network configurations and system topologies. Real-time simulation on the other hand, shows the closest realistic dynamic performance of a power system and is widely used by utilities and suppliers [6, 91, 92]. Moreover, they form the basic building block for hardware-in-the loop (HiL) analysis for system stability studies such as SSO [6].

2.7.4 Hardware-in-the-loop Experiments

To take a further step in the SSO analysis and control design HiL experiments can be conducted. The HiL simulations can be performed as a complementary test for off-line and real-time simulations, which can be considered as a final stage before implementing the device or solution in real-systems. Moreover, the HiL allows the tests to be performed in a safe and controlled environment without risking the real power system equipments and can represent the natural characteristics such as uncertainties, interferences, noises and practical limits of the real-system [6]. Research advancements in this direction have been recently reported in the literature. This includes different options to replicate the dynamics of multi-mass enabled synchronous generators, HVDC and series-compensated AC lines [93, 94, 95]. However, a full scale series-compensated AC/DC grid representation with detailed power system models is still missing

from the literature.

2.8 Subsynchronous Oscillation Mitigation Schemes

The function of the SSO mitigation scheme is to prevent any instabilities or interactions in the power systems, which results in equipment damage and personal injury. A number of SSO countermeasures have been studied and reported in the literature, however only a handful of them have been implemented in real-systems. To this end, the SSO mitigation measures can be generally classified into two as depicted in Table. 2.4 [30]:

2.8.1 Network/Transmission Based

The mitigation measures applied at the network or transmission level such as damping schemes or blocking filters installed with series capacitors, would come under this category [30]. Typically the decision for such countermeasures will be undertaken by the operators which is beyond the asset owners boundary [30]. The commonly employed network side mitigation schemes are:

2.8.1.1 Network Reconfiguration Procedures:

This involves restricting the operation of the generator under certain contingencies through system reconfiguration so as to deal with SSO events [30, 85]. An alternative approach is to by-pass the series compensation when there is a potential risk of SSO condition. It is widely considered as an acceptable and cost-effective process for a simple system protection [30, 85].

2.8.1.2 Passive Filter Schemes:

This scheme involves the installation of an additional passive element to the network with equivalent impedance, as a function of frequency to counter the resonant condition in a series capacitor compensation [30, 47]. The installation of fundamental frequency blocking filter in parallel with the series capacitor is a type of passive filtering scheme. However, this method is expensive due to the high ratings of the elements required to withstand short-circuit events, see Table. 2.4 [30].

2.8.1.3 Active Filter Schemes:

This approach involves use of network connected power electronic converters based FACTS devices such as SVC, STATCOM or HVDC for SSO mitigation. The device control systems can be designed and tuned to actively mitigate SSO through the use of auxiliary damping controllers [47, 85]. These kind of devices will provide support in SSO mitigation irrespective of system configuration and series compensation levels. A number of schemes have been discussed in the literature in this direction [30, 47, 85]. The addition of supplementary damping controller to an existing SVC, STATCOM or an HVDC link is an extra value proposition to the assets as it provides the cost effective solution for SSO mitigation compared to any other schemes, see Table. 2.4 [30].

2.8.1.4 Active Series Compensation Schemes:

The use of TCSC instead of FSC is an alternative way of increasing the power transfer capability and a proven way for SSO mitigation [70, 71]. By incorporating specific thyristor angle control methods, the effective TCSC reactance can be made capacitive, there by reducing the risk of SSO [70, 71]. The prospective use of this device in SSO mitigation and proposal for different control schemes to do so are reported in the literature [47, 96, 97]. As compared to series capacitors the TCSC includes several additional components such as control systems, thyristor cooling and a series reactor, which makes them capital and maintenance intensive, compared to its counterpart. An approximate evaluation of the cost can be found out from the National Grid report as shown in Table. 2.4 [30].

Table 2.4: SSO mitigation schemes: adopted from [30].

	Mitigation Measure	Indicative Cost
Network	Thyristor Controlled Series Capacitor (TCSC)	2x the price of FSC
	Fixed Series Compensation (FSC) with Damping Filters	1.5x the price of FSC
	Damping Control Systems on HVDC Converter	<£250k
	Auto bypass and/or Intertipping Schemes	<£5m
User	Blocking Filters	£10m/Generating Unit
	Damping Control Systems	<2m/Generating Unit
	Windfarm protection	<£250k/Power Park Module

2.8.2 Generator/User Based

This category includes the countermeasures applied at the generator or at the generator bus. The asset owner will be the responsible party to install such devices and provide support whenever required by the system owner [30, 79]. The common generator side mitigation schemes employed are:

2.8.2.1 Passive Filter Schemes:

This approach involves the use of static blocking filter tuned at specific subsynchronous frequencies in series with generator to provide a firewall against SSO events [79]. The blocking filter creates a parallel resonance or a high impedance to prevent the subsynchronous current from entering the generator stator thereby effectively mitigate the potential SSR and SSTI conditions [98]. However, the filter design is independent of system current and future conditions, therefore less reliable and adaptive [98]. The scheme is expensive while compared to active network side countermeasures as each generator units needs separate filter banks [30, 98].

2.8.2.2 Active Filter Schemes:

This approach involves use of generator terminal or step-up transformer connected shunt devices such as thyristor-controlled reactors (TCR) much like a SVC or STATCOM for SSO mitigation [85, 93, 99]. This approach is more practical as the devices do not have to be rated to carry the full current of the generator as would be required in series blocking filter [93, 99]. Moreover, they can effectively damp SSO using the generator speed as the control input and are substantially immune to network configuration and series compensation levels [85, 99].

2.8.2.3 Supplementary Excitation Damping Control:

The use of Supplementary Excitation Damping Control (SEDC) for SSO mitigation involves the modulation of synchronous generator excitation voltage to damp SSR and SSTI [85, 100]. SEDC's use the shaft speed as an input signal and can be implemented through active voltage regulators (AVRs) or power system stabilizers (PSS) [85, 100]. Their installation in practical system dated

back to 1970's, which demonstrates the SEDCs adequacy in SSO damping [79]. The current work on SEDC focus on developing advanced control techniques considering different types of excitation systems and PSS [100, 101]. It is an alternative cost-effective solution compared to blocking filter schemes since no high voltage equipment are required [100, 101]. However, they cannot be integrated with all type of exciters as the time constant of exciters are higher compared to the subsynchronous frequency range. The possible benefits of SEDC can be obtained when operated in conjunction with other mitigation measures as reported in [85, 101].

2.8.2.4 Wind Turbine Control:

The proliferated application of wind turbines in the close vicinity of series-compensated network has resulted in the occurrence of new forms of SSO phenomenon as reported in Section. 2.6.2. The wind turbines use VSC topology for variable speed and AC voltage control. After the first occurrence of the SSCI event in 2009, there has been a number of studies focussed on the control measures through turbine converter design and tuning [86, 102, 104]. Major wind turbine manufacturers have considered the consequence of SSO events, especially SSCI and have proposed mitigation measures as reported in [102, 103, 104].

2.8.3 Protection Measures against Subsynchronous Oscillations

Apart from implementing the network and generator based countermeasures, the use of protection measures provide an alternative solution for SSO mitigation [85, 92]. The main element of such a scheme is the relay which may take several forms: solid-state or microprocessor based [47, 85]. Further, they can detect the level and duration of SSO events using the terminal voltage and armature current measurements at the generator terminals and can trip the units during an incident [47, 85]. Their application for SSO control dated back to 1970's in response to the first SSR event [103]. Out of these, the torsional stress relay (TSR) has been widely employed in generator units to measure any SSO event due to the proximity of series-compensated lines and HVDC converters [85, 103]. A summary of the most commonly applied SSO countermeasures is provided in Table. 2.5 [30, 85, 92, 103] .

In general, an in-depth understanding of the different forms of SSO with the interdependencies

Table 2.5: Subsynchronous oscillation countermeasures

Description	SSR-TO	IGE	SSR-TA	SSCI	SSTI
Design damping controllers	X	X	X	X	X
Generator transformer filter	X	X	X	–	X
Series capacitor bypass Filters	X	X	X	X	–
Shunt compensation	X	X	X	X	X
FACTS devices	X	X	X	X	X
Operational procedure	X	X	X	X	X
Torsional relays	X	–	X	X	X
Reduced compensation	X	X	X	X	–

of associated equipment and the knowledge of necessary tools is vital for the design of suitable countermeasures. To this end, the work in this thesis focuses on the implementation of an active filter schemes based on the VSC HVDC control modification for SSO mitigation, which is identified as the most cost-effective solution in the GB context.

From the GB power system operation perspective, the SSO phenomenons which will be analysed, studied and detailed in this thesis will be SSR, especially SSR-TI and SST-TA forms. Before implementing the SSR damping schemes, a thorough analysis on the contribution of VSC HVDC link to SSR in a hybrid AC/DC grid has been made using eigenvalue and damping torque screening methods. These analysis are used to design the proper control schemes for SSR damping, which will be introduced and discussed in the following chapters.

2.9 Frequency Management in AC/DC Grids

The unbundling of the transmission network to incorporate more power electronic converter (PEC) interfaced sources such as wind turbines, HVDC and decentralised generation has changed the structure of the traditional power systems [105]. As a consequence, the frequency stability as well as small-signal and voltage stability, are of increasing importance to large interconnected power systems [105, 106]. Moreover, the increased penetration of PEC replacing synchronous generators places immense pressure on the stable and secure operation of the interconnected power systems which are already operating close to the stability limits [105, 106].

The increased deployment of HVDC connections to support the constrained corridors not only relieves the AC congestion but also provide a fast control response and are capable of contributing to AC system stability characteristics [107]. An example of such a service is the HVDC involvement in frequency management by responding to a frequency event in an interconnected AC systems through the fast delivery and/or reversal of power through the DC link [106, 107, 108].

As the generation mix becomes more diverse and further distanced from the main load centres, the interconnection of HVDC links to form an MTDC grid interfacing generation and consumption becomes attractive. Such a configuration facilitates power flow management and operational reliability [109, 110, 111]. However, as thermal generation still satisfies the base load in current power systems, the large-scale integration of wind presents an operational challenge [37]. For instance, significant power mismatches and frequency deviations may occur due to the intermittent nature of the wind and arguably the slow primary frequency control from thermal power plants [37, 110]. As wind integration progresses, this may bring system stability and reliability issues [112].

The GB system operator National Grid has identified this scenario in their annual system operability framework (SOF) and describes frequency management as one of their top priority in the future AC/DC grids [31]. According to SOF, frequency management is described as the operational requirements needed to govern the regulation and control of frequency, an illustration of which is provided in Figure 2.7 [31]. The three main areas under frequency management are frequency regulation, frequency containment and frequency recovery, which are related to system inertia, the rate of change of frequency and fast active power injection [31]. There are a number of works in the literature focusing on the frequency containment and frequency recovery issues and provision of support using HVDC links, wind power plants both offshore and onshore and other devices [108, 113, 114]. To this end, the frequency regulation has become a relevant issue due to the rapid growth in power generation from renewables and fluctuating power demand [31, 108].

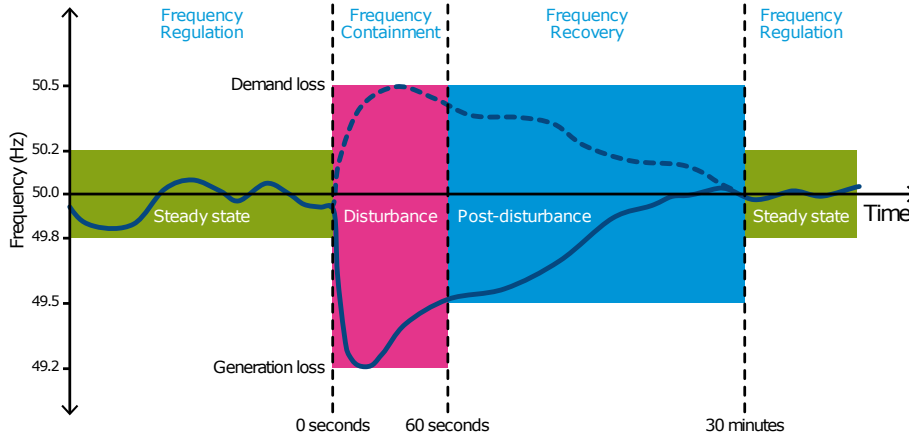


Figure 2.7: Illustration of frequency management [31].

2.9.1 Frequency Regulation in AC/DC Grids

Frequency regulation or steady-state frequency operation is defined as the second-by-second variation in frequency caused by the difference between generation and demand in the power systems and is balanced by the frequency response services that act to regulate frequency in normal or a pre-fault operation [31, 108]. However, with the integration of highly intermittent grid decoupled renewable generation, the persistent small disturbances caused by their fluctuating nature has become a worry for stable system operations [31, 108]. An alternative solution to this dilemma is to use the fast controllability of PEC's for frequency stabilization [108, 114]. Such a scenario is foreseen in many countries, an example of which is the case in China where the wind and coal generations are located far away from the load centres, where the resources are plentiful [38, 115]. However, to transport the abundant wind resources over long distances HVDC links are preferred over AC line [38, 110, 116]. But considering the intermittency of wind, transmitting wind power alone through these HVDC links will be an ineffective and costly method and this could jeopardize the system stability [38, 39, 110]. As such, the wind power plants will be bundled with thermal generators and the power will be transmitted through HVDC links to form a hybrid wind-thermal AC/DC grid [38, 39, 110].

Such scenarios are foreseen in the GB power systems as the plans for onshore wind installations is expected to rise from the current capacity and thermal generations will act as base load provider with HVDC converters in the close proximity [31, 29]. Frequency regulation and stability of such a hybrid AC/DC grid will be of prime importance as the declining system inertia

and higher wind penetration will result in higher steady state frequency disturbances [108, 114]. A number of studies have been done in the literature to address these issues associated with the wind-thermal hybrid AC/DC system [110, 112, 117, 118]. A wind-thermal bundled system with a three-terminal MTDC scheme for fast power delivery has been reported in [110]. The provision of using LCC HVDC fast power routing to enhance the system stability in a hybrid wind-thermal AC/DC grid has been proposed in [117]. Fast frequency support from PEC's is another potential option that could be explored in this context [118]. The impact of declining system inertia corresponding to an increased wind penetration in such a network has to be evaluated so as to quantify the frequency stability of the hybrid AC/DC systems.

2.10 Summary

The state-of-the-art system operability challenges and potential technical solutions associated with compensated or uncompensated AC/DC grids has been discussed in this chapter. The traditional stability issues pertained to AC systems such as angular stability in terms of SSO and frequency stability related to frequency regulation have been addressed with regards to AC/DC grid structure.

The reinforcements in the GB transmission network and the potential risk of SSO associated with it has been identified followed by a detailed classification of different forms of SSO events. The SSO analysis and mitigation measures were introduced with a detailed description of each analysis and mitigation methods.

Finally in the context of changing grid structure and increasing power electronic converter integration, the frequency management issues, especially the frequency regulation and stability issues associated with a wind-thermal hybrid AC/DC grid were outlined with a discussion on the problems and existing control schemes.

3 Modelling and Stability Analysis of Series-Compensated AC/DC Network

3.1 Introduction

Modelling of network parameters incorporating AC and DC components are essential for establishing a stable operation and control of AC/DC grid. To this end, this chapter discusses the mathematical modelling of different network parameters. This includes synchronous generator, multi-mass turbine, AC transmission line, and VSC HVDC link with its associated controllers. The test systems for SSR studies are introduced with a detailed explanation of its associated components. The linearisation of these dynamic components and the adequacy of them for SSR screening are discussed with the help of eigenvalue analysis. This is followed by damping torque investigation for SSR screening in the test systems under study. The results of eigenvalue and damping torque analysis were compared against electromagnetic (EMT) simulations in PSCAD/EMTDC for testing the accuracy of the linearised models for SSR studies. A series of time-domain simulations were performed to identify the range of series- compensation levels where there is potential risk of SSR in the test systems under investigation.

3.2 Synchronous Generator Model

The schematic of synchronous generator model is depicted in Figure 3.1, which consists of stator and rotor circuits [27, 119]. The stator circuit carries alternating currents and is modelled as three-phase armature windings, while the rotor circuits which comprise field and damper

windings are excited by a DC voltage [119]. The currents flowing through the damper windings can be assumed to flow in a closed circuit: one whose flux is aligned with the d-axis or the field axis and the second aligned with q-axis which is at right angles to the field axis. The damper windings are represented with three equivalent damper circuits: one on the d-axis (k_d) and two on the q-axis (k_{q1}, k_{q2}) [27, 119].

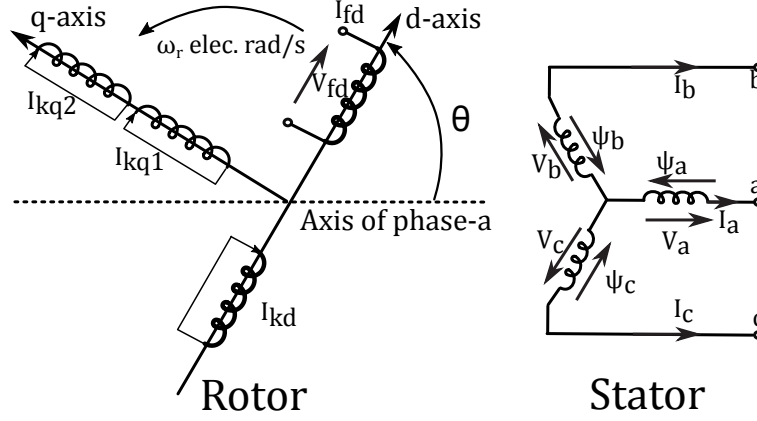


Figure 3.1: Schematic diagram of a conventional synchronous generator.

In-order to perform small-signal studies, the generator currents are considered as state variables instead of flux linkages [26]. The sixth order generator voltage model in the linearised form can be written as:

$$\begin{aligned} \frac{1}{\omega_b} [-x_d \Delta \dot{i}_d + x_{md} \Delta \dot{i}_f + x_{md} \Delta \dot{i}_{kd}] &= \Delta v_{td} + r_a \Delta i_d - x_q \Delta i_q + x_{mq} \Delta i_{kq1} + x_{mq} \Delta i_{kq2} + \phi_{q0} \Delta \omega \\ \frac{1}{\omega_b} [-x_{md} \Delta \dot{i}_d + x_f \Delta \dot{i}_f + x_{md} \Delta \dot{i}_{kd}] &= \Delta v_f - r_f \Delta i_f \\ \frac{1}{\omega_b} [-x_{md} \Delta \dot{i}_d + x_{md} \Delta \dot{i}_f + x_{kd} \Delta \dot{i}_{kd}] &= r_{kd} \Delta i_{kd} \end{aligned} \quad (3.1)$$

$$\begin{aligned} \frac{1}{\omega_b} [-x_q \Delta \dot{i}_q + x_{mq} \Delta \dot{i}_{kq1} + x_{md} \Delta \dot{i}_{kq2}] &= \Delta v_{tq} + r_a \Delta i_q + x_d \Delta i_d - x_{md} \Delta i_f - x_{md} \Delta i_{kd} - \phi_{d0} \Delta \omega \\ \frac{1}{\omega_b} [-x_{mq} \Delta \dot{i}_q + x_{kq1} \Delta \dot{i}_{kq1} + x_{kq2} \Delta \dot{i}_{kq2}] &= r_{kq1} \Delta i_{kq1} \\ \frac{1}{\omega_b} [-x_{mq} \Delta \dot{i}_q + x_{mq} \Delta \dot{i}_{kq1} + x_{kq2} \Delta \dot{i}_{kq2}] &= r_{kq2} \Delta i_{kq2} \end{aligned} \quad (3.2)$$

Equations. 3.1 and 3.2 represents the linearised voltage equation of the d-axis and q-axis circuit; v_{td} and v_{tq} are the synchronous generator terminal voltages in d-q reference frame; v_f represents the field voltage and is defined in equation 3.3. The superscript "·" represents the

differential operator and subscript "o" represents initial operating condition.

$$v_f = \frac{r_f}{x_{md}} E_{fd} \quad (3.3)$$

The corresponding detailed state-space model of the synchronous machines including equations 3.1 - 3.3 in the linearised form can be written as:

$$\Delta[\dot{X}_{GE}] = [A_{GE}][\Delta X_{GE}] + [B_{GE}][\Delta U_{GE}] \quad (3.4)$$

with X_{GE} and U_{GE} contains the vector of state and input variables represented by equations. 3.5 and 3.6 and A_{GE} , B_{GE} are the state and input matrix.

$$\Delta X_{GE} = [\Delta i_d, \Delta i_q, \Delta i_f, \Delta i_{kd}, \Delta i_{kq1}, \Delta i_{kq2}]^T \quad (3.5)$$

$$\Delta U_{GE} = [\Delta \omega, \Delta E_{fd}, \Delta v_{td}, \Delta v_{tq}]^T \quad (3.6)$$

The detailed linearised model of the generator and associated parameters are provided in Appendix. A.1.

3.3 Multi-Mass Turbine Modelling

The six-mass mechanical system for a turbo-generator including high-pressure(HP), intermediate-pressure (IP), low pressure (LPA and LPB) turbine sections, a generator (GEN) and its rotating exciter (EX) coupled to a common shaft as depicted in Figure 3.2 is used for performing small-signal stability studies [27, 26]. The individual sections of the shaft behave like springs and together they constitute a linear six-mass-spring system which is adequate for SSR studies as reported in [27].

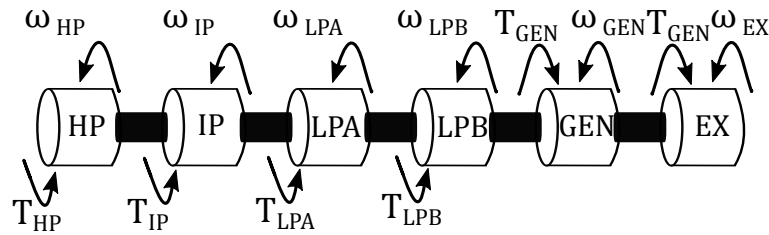


Figure 3.2: Mechanical sections of six masses turbo-generator system.

For clarity of the dynamic expressions, the one mass model as shown in Figure 3.3 is used, which represents the relation of torques of the i^{th} mass-spring system [27]. The external torque input ($K_{i-1,i}(\theta_{i-1} - \theta_i)$) is acting in the same direction as the shaft torque (T_i), with the output torque ($K_{i,i+1}(\theta_i - \theta_{i+1})$), damping torque ($D_i\omega_i$) and accelerating torque (M_i) acting in tandem in the opposite direction [26, 27].

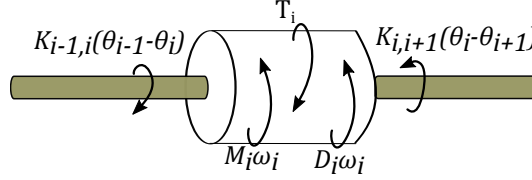


Figure 3.3: The one mass model of the i^{th} mass-spring system [27].

Therefore, the linearised model of the multi-mass shaft system that describes the torque equilibrium and the motion of the i^{th} mass can be written as [26, 27].

$$\begin{aligned} \frac{M_i}{\omega_0} \Delta \dot{\omega}_i &= K_{i-1,i}(\Delta \theta_{i-1} - \Delta \theta_i) - \Delta T_i - K_{i,i+1}(\Delta \theta_i - \Delta \theta_{i+1} - D_i \Delta \omega_i) \\ \Delta \dot{\theta}_i &= \omega_0 \Delta \omega_i \\ K_{i-1,i}|_{i=1} &= 0; K_{i,i+1}|_{i=n} = 0, i = 1, 2, \dots, n \end{aligned} \quad (3.7)$$

Where, $K_{i,i}$ is the shaft stiffness in p.u. torque/rad; θ_i is the mechanical angle in rad/s; M_i is the inertia constant of i^{th} mass in seconds; D_i is the damping coefficient of each mass in p.u. torque/p.u.; ω_i the speed of the i^{th} mass in p.u. and ω_0 is the base speed of the machine. The linearised shaft model consists of the rotor angle and speed of each masses as the state variables and is of 12^{th} order represented by the following state-space equation:

$$\Delta[\dot{X}_{MM}] = [A_{MM}][\Delta X_{MM}] + [B_{MM}][\Delta U_{MM}] \quad (3.8)$$

with X_{MM} and U_{MM} contains the vector of state and input variables represented by equations. 3.9 and 3.10 and A_{MM} , B_{MM} are the state and input matrix.

$$\Delta X_{MM} = [\Delta \omega_{HP}, \Delta \theta_{HP}, \Delta \omega_{IP}, \Delta \theta_{IP}, \Delta \omega_{LPA}, \Delta \theta_{LPA}, \Delta \omega_{LPB}, \Delta \theta_{LPB}, \Delta \omega, \Delta \delta, \Delta \omega_{EX}, \Delta \theta_{EX}]^T \quad (3.9)$$

$$\Delta U_{MM} = [\Delta T_H, \Delta T_{IP}, \Delta T_{LPA}, \Delta T_{LPB}, \Delta T_e]^T \quad (3.10)$$

The detailed linearised model representation of the multi-mass is provided in Appendix. A.2.

3.4 Modelling of Series-compensated Transmission Line

In small-signal stability studies, representation of transmission system components plays a critical part. In the conventional modelling and assessment tools used for small-signal studies, the AC network is represented as admittance matrix. However, this method can be accurate only for studies involving low-frequency oscillations (0-3 Hz) [120]. For high frequency stability studies such as SSR the dynamic models of the AC system components, such as transmission lines, transformers are necessary [27, 120]. The equivalent single line representation of a series-compensated transmission line is depicted in Figure 3.4 [26, 27]. Where the network components R_L , X_L and X_C represents the total resistance, reactance and series-capacitive reactance, E and V_b represents the generator terminal and infinite bus voltage. With respect to Figure 3.4, the effective impedance of the transmission line including series compensation can be written as:

$$X_{L_{eff}} = X_L - X_C \quad (3.11)$$

If we define the degree of series compensation or the series compensation level (K) as:

$$K = \frac{X_C}{X_L}; \quad 0 \leq K < 1 \text{ or } 0\% \leq K < 100\% \quad (3.12)$$

If we substitute Eq: 3.12 in 3.11 the effective transmission line impedance in terms of series compensation level can be obtained as:

$$X_{L_{eff}} = (1 - K)X_L \quad (3.13)$$

In the Figure 3.4, if we assume $E = V_b$, the infinite bus voltage then the real power and line current relation can be derived as [121]:

$$P = \frac{P_M}{(1 - K)} \sin \delta; \text{ with, } P_M = \frac{V^2}{X_L} \quad (3.14)$$

$$i_L = \frac{2V}{(1 - K)X_L} \sin \frac{\delta}{2}$$

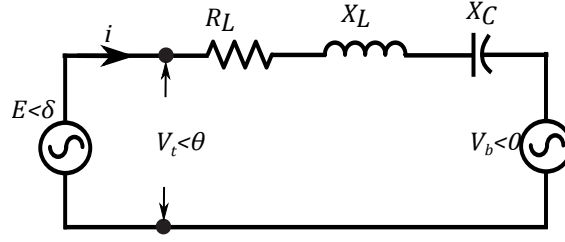


Figure 3.4: Single line diagram of conventional synchronous generator connected to infinite bus.

Correspondingly the reactive power injection by the series-compensated transmission line can be represented as [119, 121]:

$$Q = 2P_M \frac{K}{(1-K)^2} (1 - \cos \delta) \quad (3.15)$$

It is evident from equations (3.14 and 3.15) that the real power transmission in an AC line increases with an increase in K, likewise the reactive power by cancelling out the inductive impedance through the series capacitor. This is the basic ideas behind series compensation. However for understanding its impact on the system stability, dynamic modelling is needed, and to make modelling simpler the transformation of AC abc variables into dq variables is performed by applying Park's transformation [119]. The voltage phasor representation of the synchronous generator in dq frame is depicted in Figure 3.5.

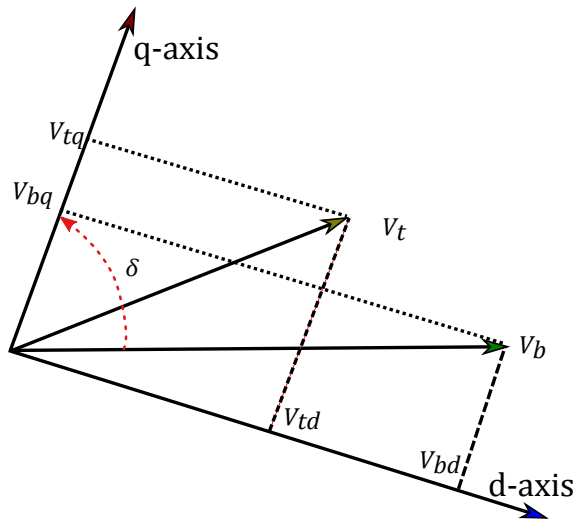


Figure 3.5: Vector diagram representation between the terminal voltage of the synchronous generator and the infinite bus in dq frame with respect to Figure 3.4.

3.4. Modelling of Series-compensated Transmission Line

The q-axis leads the reference bus voltage by δ , which is the rotor angle of the generator and V_t is generator terminal voltage. Therefore we can state the differential equations of the series-compensated transmission lines in dq reference frame as:

$$V_{td} = R_L i_{Ld} - X_L i_{Lq} + \frac{X_L}{\omega_b} \frac{di_{Ld}}{dt} + e_{cd} + V_{bd} \quad (3.16)$$

$$V_{tq} = X_L i_{Lq} + R_L i_{Ld} + \frac{X_L}{\omega_b} \frac{di_{Lq}}{dt} + e_{cq} + V_{bq}$$

$$i_{Ld} = \frac{1}{\omega_b X_C} \frac{de_{cd}}{dt} - \frac{1}{X_C} e_{cq} \quad (3.17)$$

$$i_{Lq} = \frac{1}{\omega_b X_C} \frac{de_{cq}}{dt} + \frac{1}{X_C} e_{cd}$$

Where e_{cd} and e_{cq} are the dq variables of the voltage across series-capacitor. From Figure 3.5, the dq components of the reference bus voltage can be written as:

$$V_{bd} = V_{b0} \sin(\delta); V_{bq} = V_{b0} \cos(\delta); \quad (3.18)$$

By substituting eq: 3.18 in eq: 3.16 and eq: 3.17, the linearised transmission line equations can be formed as:

$$\begin{aligned} \Delta V_{td} &= R_L \Delta i_{Ld} - X_L \Delta i_{Lq} + \frac{X_L}{\omega_b} \Delta \dot{i}_{Ld} + \Delta e_{cd} + V_{bd} \cos(\delta_0) \Delta \delta \\ \Delta V_{tq} &= X_L \Delta i_{Ld} + R_L \Delta i_{Lq} + \frac{X_L}{\omega_b} \Delta \dot{i}_{Lq} + \Delta e_{cq} + V_{bq} \sin(\delta_0) \Delta \delta \end{aligned} \quad (3.19)$$

$$\begin{aligned} \Delta i_{Ld} &= \frac{1}{\omega_b X_C} \Delta \dot{e}_{cd} - \frac{1}{X_C} \Delta e_{cq} \\ \Delta i_{Lq} &= \frac{1}{\omega_b X_C} \Delta \dot{e}_{cq} + \frac{1}{X_C} \Delta e_{cd} \end{aligned} \quad (3.20)$$

The linearised transmission line model consists of the voltages and current as state variable and in state-space format it can be expressed as:

$$\Delta \dot{X}_{TN} = [A_{TN}] [\Delta X_{TN}] + [B_{TN}] [\Delta U_{TN}] \quad (3.21)$$

with X_{TN} and U_{TN} contains the vector of state and input variables represented by 3.22 and 3.23 and A_{TN} , B_{TN} are the state and input matrix.

$$\Delta X_{TN} = [\Delta i_{Ld}, \Delta i_{Lq}, \Delta V_{td}, \Delta V_{tq}, \Delta e_{cd}, \Delta e_{cq}]^T \quad (3.22)$$

$$\Delta U_{MM} = [\Delta i_d, \Delta i_q, \Delta V_{td}, \Delta V_{tq}]^T \quad (3.23)$$

The detailed linearised model representation of the series-compensated transmission line are provided in Appendix. A.3.

3.5 Modelling of VSC HVDC Link

This section outlines the modelling of a point-to-point VSC HVDC link and its associated controllers as depicted in Figure 3.6 in a synchronous reference frame (SRF) [122]. Ideal lossless average representations are assumed for the converters [122]. As shown in Figure 3.6, R_1 , L_1 and R_2 , L_2 are the grid resistance and inductance at converter-1 (VSC1) and 2 (VSC2) respectively; C_1 , C_2 are the dc link capacitors, C_{dc} is the dc line capacitor. To simplify the modelling approach for small-signal stability assessment, the HVDC link is split into three generic building blocks: one for each converter station with its control and one for the DC line as depicted in Figure 3.6. Finally to form the state-space representation the three subsystems are gathered.

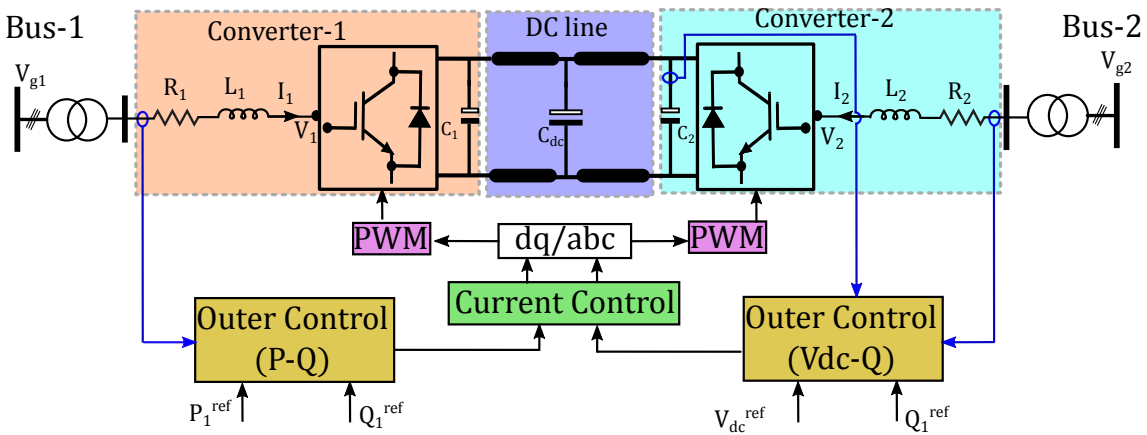


Figure 3.6: VSC HVDC point-to-point link.

3.5.1 Modelling of Voltage Source Converters

The modelling of VSC connected to Bus-1 and 2 follows the SRF approach based on the amplitude-invariant Park transformation for voltage and current equations [122, 123]. For simplifying the analytical derivation the converter grid interface reactance and resistance (including transformer reactance) at both terminals are assumed to be similar, ($R_1 = R_2 = R_f$ and $L_1 = L_2 = L_f$).

3.5.1.1 Grid Interface Model

The three-phase voltage and current are transformed to dq reference frame based on the amplitude-invariant Park transformation, with the d-axis aligned with the voltage and q-axis leading the d-axis by 90° . A cascaded structure with proportional-integral (PI) controllers is used. The following equations can be obtained for the voltage relations:

$$\begin{aligned} V_{d1} &= V_{gd1} + R_f I_{d1} + L_f \frac{dI_{d1}}{dt} - \omega_s L_f I_{q1}, \\ V_{q1} &= V_{gq1} + R_f I_{q1} + L_f \frac{dI_{q1}}{dt} + \omega_s L_f I_{d1}, \\ \frac{dV_{dc1}}{dt} &= \frac{(V_{d1} I_{d1} + V_{q1} I_{q1})}{C_1 V_{dc1}} + \frac{I_{dc1}}{C_1} \end{aligned} \quad (3.24)$$

where V_{d1} , V_{q1} , V_{gd1} , V_{gq1} are the converter AC side and grid voltages; I_{d1} , I_{q1} the converter AC side currents in dq frame; V_{dc1} , I_{dc1} are the DC link capacitor voltage and current at VSC1 terminal; ω_s is the grid frequency. After linearising the equation. 3.24, the grid connected converter model can be written as:

$$\begin{aligned} \Delta \dot{I}_{d1} &= \frac{-R_f}{L_f} \Delta I_{d1} + \frac{\omega L_f \Delta I_{q1}}{L_f} + \frac{\Delta V_{d1}}{L_f} - \frac{\Delta V_{gd1}}{L_f} \\ \Delta \dot{I}_{q1} &= \frac{-R_f}{L_f} \Delta I_{q1} - \frac{\omega L_f \Delta I_{d1}}{L_f} + \frac{\Delta V_{q1}}{L_f} - \frac{\Delta V_{gq1}}{L_f} \\ \Delta \dot{V}_{dc1} &= \frac{-V_{d1}}{C_1 V_{dc1}} \Delta I_{d1} - \frac{V_{q1}}{C_1 V_{dc1}} \Delta I_{q1} + \frac{(V_{d1} I_{d1} + V_{q1} I_{q1})}{C_1 V_{dc1}} \Delta V_{dc1} - \frac{I_{d1}}{C_1 V_{dc1}} \Delta V_{d1} \\ &\quad - \frac{I_{q1}}{C_1 V_{dc1}} \Delta V_{q1} + \frac{\Delta I_{dc1}}{C_1} \end{aligned} \quad (3.25)$$

3.5.1.2 Inner Current Loop

The design of inner current loop is assumed to be in SRF with proportional and integral controller as shown in Figure 3.7 expressed as [122, 123]:

$$\begin{aligned} V_{d1} &= k_{pd1}(I_{d1}^{ref} - I_{d1}) + k_{id1} \int (I_{d1}^{ref} - I_{d1}) dt, \\ V_{q1} &= k_{pq1}(I_{q1}^{ref} - I_{q1}) + k_{iq1} \int (I_{q1}^{ref} - I_{q1}) dt, \end{aligned} \quad (3.26)$$

where I_{d1}^{ref} , I_{q1}^{ref} are the reference currents; k_{pd1} , k_{id1} the d-axis proportional and integral gains of the controller; and k_{pq1} , k_{iq1} the q-axis proportional and integral gains of the controller. To further simplify the differential equations two variables are introduced for the integral terms, $\alpha_{1d} = k_{id1} \int (I_{d1}^{ref} - I_{d1}) dt$ and $\alpha_{1q} = k_{iq1} \int (I_{q1}^{ref} - I_{q1}) dt$.

Therefore the linearised current control loop for the converter can be realised as

$$\begin{aligned} \Delta V_{d1} &= k_{pd1}(\Delta I_{d1}^{ref} - \Delta I_{d1}) + \Delta \alpha_{1d}, \\ \Delta V_{q1} &= k_{pq1}(\Delta I_{q1}^{ref} - \Delta I_{q1}) + \Delta \alpha_{1q}, \end{aligned} \quad (3.27)$$

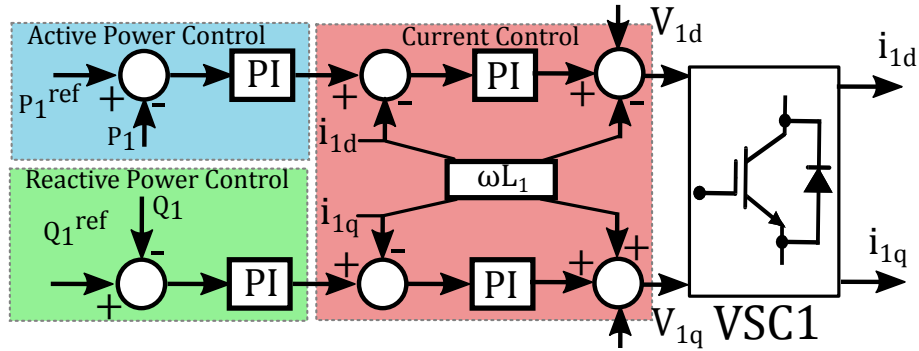


Figure 3.7: Active and reactive power control scheme.

3.5.1.3 Active and Reactive Power Loop

The VSC1 connected to Bus-1 is operating in active and reactive power control mode (PQ), which forms the outer control loop of the converter, as shown in Figure 3.7 [122, 123]. The current references for the inner loop can be obtained using a PI controller as:

$$\begin{aligned} I_{d1}^{ref} &= k_{pp1}(P_1^{ref} - P_1) + k_{ip1} \int (P_1^{ref} - P_1) dt, \\ I_{q1}^{ref} &= k_{pq1}(Q_1^{ref} - Q_1) + k_{iq1} \int (Q_1^{ref} - Q_1) dt, \end{aligned} \quad (3.28)$$

where P_1^{ref} , Q_1^{ref} , P_1 , Q_1 are the reference and measured active and reactive power; k_{pp1} , k_{ip1} the d-axis proportional and integral gains of the controller (active power); and k_{pq1} , k_{iq1} the q-axis proportional and integral gains (reactive power). The general equation for the active and reactive power flow from the converter to the DC link can be represented as:

$$\begin{aligned} P_1 &= V_{gd1} I_{d1} + V_{gq1} I_{q1}, \\ Q_1 &= V_{gq1} I_{d1} - V_{gd1} I_{q1}, \end{aligned} \quad (3.29)$$

To further simplify the differential equations two variables are introduced for the integral terms, $\alpha_p = k_{ip1} \int (P_1^{ref} - P_1) dt$ and $\alpha_{q1} = k_{iq1} \int (Q_1^{ref} - Q_1) dt$. Therefore linearised active/reactive power control loop for the converter can be realised as:

$$\begin{aligned} \Delta I_{d1}^{ref} &= k_{pp1}(P_1^{ref} - V_{gd1} \Delta I_{d1}) + \Delta \alpha_p, \\ \Delta I_{q1}^{ref} &= k_{pq1} Q_1^{ref} - k_{pq1} V_{gd1} \Delta I_{q1} + \Delta \alpha_{q1} \end{aligned} \quad (3.30)$$

3.5.1.4 DC Voltage and Reactive Power Loop

The main control objective of VSC2 connected to Bus2 (see Figure 3.6) is to regulate the DC voltage and reactive power ($V_{dc}Q$) as shown in Figure 3.8. Similar control structure as in converter-1 is used here with cascaded PI control, expressed by [122, 123]:

$$\begin{aligned} I_{d2}^{ref} &= k_{pdc}(V_{DC}^{ref} - V_{DC}) + k_{idc} \int (V_{DC}^{ref} - V_{DC}) dt, \\ I_{q2}^{ref} &= k_{pq2}(Q_2^{ref} - Q_2) + k_{iq2} \int (Q_2^{ref} - Q_2) dt, \end{aligned} \quad (3.31)$$

where I_{d2}^{ref} , I_{q2}^{ref} , are the reference currents; k_{pdc} , k_{idc} , the d-axis proportional and integral gains; k_{pq2} , k_{iq2} , the q-axis proportional and integral gains; Q_2^{ref} , Q_2 , the reference and measured reactive powers of VSC2; and V_{DC}^{ref} , V_{DC} , the reference and measured DC voltage at the terminal

of VSC2 all at converter-2 terminals. To further simplify the differential equations two variables are introduced for the integral terms, $\alpha_{dc} = k_{idc} \int (V_{DC}^{ref} - V_{DC}) dt$ and $\alpha_{q2} = k_{iq2} \int (Q_2^{ref} - Q_2) dt$.

Therefore linearised DC voltage/reactive power control loop for the converter-2 can be realised as:

$$\begin{aligned}\Delta I_{d2}^{ref} &= k_{pdc}(V_{DC}^{ref} - \Delta V_{DC}) + \Delta \alpha_{dc}, \\ \Delta I_{q2}^{ref} &= k_{pq2}Q^{ref} - k_{pq2}V_{gd2}\Delta I_{q2} + \Delta \alpha_{q2},\end{aligned}\tag{3.32}$$

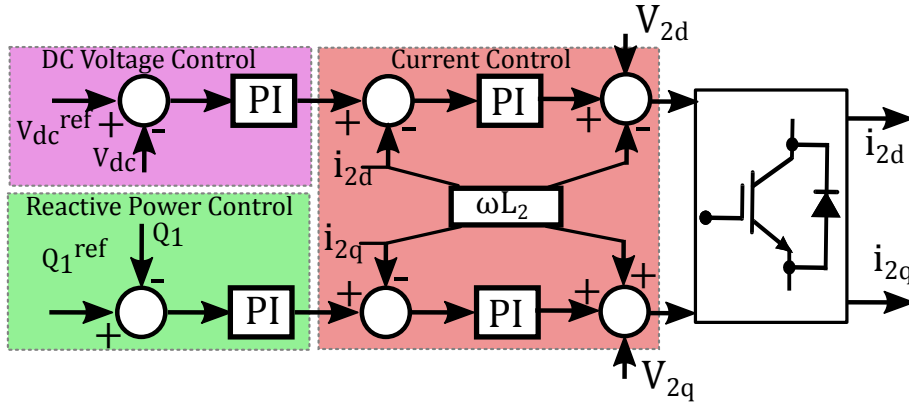


Figure 3.8: DC Voltage Reactive power control loop.

3.5.2 DC Line

The DC cable model adopted in this work consisting of a T-equivalent circuit with lumped parameters uniformly distributed along the line is shown in the Figure 3.9. This is the common cable model used for dynamic AC/DC studies with series resistance, inductance and shunt capacitance. However, the simplified cable model presented here does not indicate the relative stability of the DC cable modes [124]. But for SSO studies these modes are irrelevant since their frequency range is higher than the subsynchronous frequency. Furthermore, in this work we used the lumped cable model to replicate the physical DC network available in the laboratory. The dynamics of the DC branch can be represented by [122, 123]:

$$\begin{aligned}\frac{dI_{dc1}}{dt} &= \frac{1}{L_{dc}}[V_{dc1} - V_{dc} - R_{dc}I_{dc1}], \\ \frac{dI_{dc2}}{dt} &= \frac{1}{L_{dc}}[V_{dc2} - V_{dc} - R_{dc}I_{dc2}], \\ \frac{dV_{dc}}{dt} &= \frac{1}{C_{dc}}[I_{dc1} - I_{dc2}]\end{aligned}\tag{3.33}$$

where I_{dc1} , I_{dc2} , and V_{dc1} , V_{dc2} are the DC line currents and voltages at the converter 1 and 2 terminals; V_{DC} , the mid point capacitor voltage; C_{dc} , R_{dc} and L_{dc} , are the DC line capacitance, resistance and inductance respectively. The linearised DC line equations can be expressed :

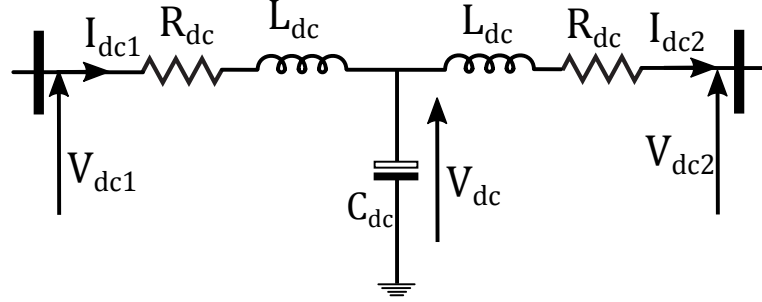


Figure 3.9: DC transmission Line.

$$\begin{aligned}\Delta \dot{I}_{dc1} &= \frac{1}{L_{dc}} [\Delta V_{dc1} - \Delta V_{dc} - R_{dc} \Delta I_{dc1}], \\ \Delta \dot{I}_{dc2} &= \frac{1}{L_{dc}} [\Delta V_{dc2} - \Delta V_{dc} - R_{dc} \Delta I_{dc2}], \\ \Delta \dot{V}_{dc} &= \frac{1}{C_{dc}} [\Delta I_{dc1} - \Delta I_{dc2}]\end{aligned}\tag{3.34}$$

3.5.3 State-Space Modelling of the VSC HVDC Link

To assess the small-signal stability, state-space representation of the VSC HVDC link is used. After rewriting the equations. 3.24 to 3.34 and changes of variable, the final linearised relation of VSC HVDC link in state-space format can be written as:

$$\Delta \dot{X}_{HVDC} = [A_{HVDC}] [\Delta X_{HVDC}] + [B_{HVDC}] [\Delta U_{HVDC}]\tag{3.35}$$

with ΔX_{HVDC} and ΔU_{HVDC} containing the vector of state and input variables represented by 3.36 and 3.37 and A_{HVDC} , and B_{HVDC} are the state and input matrix.

$$\Delta X_{HVDC} = [\Delta X_{PQ}, \Delta X_{DCt}, \Delta X_{DCQ}]^T\tag{3.36}$$

$$\Delta U_{HVDC} = [\Delta U_{PQ}, \Delta U_{DCt}, \Delta U_{DCQ}]^T\tag{3.37}$$

Where $\Delta X_{PQ}, \Delta X_{DCt}, \Delta X_{DCQ}$ are the vector of state variables and $\Delta U_{PQ}, \Delta U_{DCt}, \Delta U_{DCQ}$ are the vector of input variables of PQ controlled VSC1, DC line and $V_{dc}Q$ controlled VSC2. The detailed linearised model representation of the VSC HVDC link with control systems are provided in Appendix. B.

3.6 System Configuration for Subsynchronous Resonance Study

To perform a formal analysis on SSR, two test systems are introduced in this section. The first one consists of the IEEE First Benchmark Model (FBM) for SSR studies which have been upgraded with a point-to-point VSC HVDC link [125]. The second system represents a simplified Great Britain (GB) power system [127]. The GB system has been upgraded for future (2025 scenario), with reinforcements considered through onshore series compensation and offshore submarine VSC HVDC transmission [30, 94].

3.6.1 Test system 1: IEEE Standard First-benchmark Model

The IEEE FBM model is a standard system used to study different forms of SSO such as SSR and SSTI effects [125]. In this work a modified FBM (MFBM), through the inclusion of a VSC HVDC link connected in parallel with the AC line as shown in Figure 3.10 is used. The test system consists of a synchronous generator connected to an infinite bus via a series-compensated 539 kV transmission line. The transmission line is represented by a resistance (R_L) a reactance (X_L) including the transformer reactance, and a series capacitor (X_C) (whose value depends on the compensation level).

The shaft of the generator has been modelled as a linear six mass-spring system that considers a four-stage steam turbine, the generator and its rotating exciter; all of these masses are mounted on the same shaft [125]. The output real power of the generator is 0.9 p.u. with a power factor of 0.9 (lagging). The HVDC transmission system consists of two six-pulse VSCs. A DC line is connected between two converter stations. Typical PI controllers have been used at the VSC HVDC stations for power flow and DC voltage control, as explained in Section. 3.5 and the control parameters are provided in Appendix. D. The MFBM system parameters used in thesis are provided in Appendix. C.1

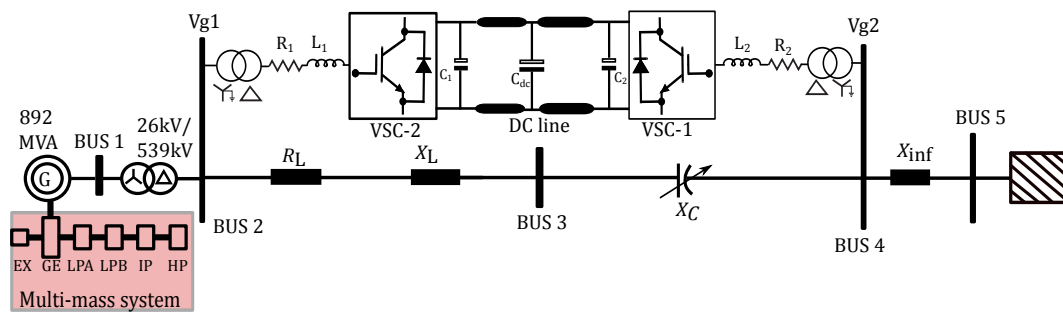


Figure 3.10: Modified first-benchmark model for SSR Analysis

3.6.2 Test system 2: Three Machine GB Model

IEEE First and Second Benchmark Models (FBM and SBM) have been traditionally used to obtain a good understanding of SSR [125, 126]. As such, they are suitable for designing (SSDCs) [95, 128]. However, in order to assess the impact of VSC HVDC links in a multi-machine system, the models have been extended to the three machine GB network (3GB) shown in Figure 3.11. The system resembles a simplified GB mainland system splitting into three major generation areas: England and Wales (E&W), Southern Scotland (SS) and Northern Scotland (NS), with respective ratings of 21000, 2800 and 2400 MVA [127]. The NS generator has been modelled to include a multi-mass shaft with four turbine masses. The remaining two machines were modelled as single mass turbo-generators [129].

The system under study has been previously employed for SSR studies in a reinforced GB system [94, 129, 130]. Network infrastructure upgrades are in line with those proposed by National Grid (the UK Transmission System Operator) –aiming to facilitate the transmission of additional wind power from Scotland to major load centres in the South without the construction of new onshore overhead lines. These consist of series compensation in the onshore network and submarine HVDC interconnections between England and Scotland [14, 15, 68]. Although it could be argued that the adopted network is a rather simplified version of the GB system, it provides enough information to study, understand and test SSO events such as SSR and SSTI in a multi-machine AC/DC system. The selection of technology and location for series compensation and HVDC link reflects the GB system future scenario (2025) [14, 15, 29, 30]. Moreover the test system was modelled to emulate the parallel operation and damping performance of AC/DC grid in simulation and experimental environment. The HVDC transmission system model is detailed

in Section. 3.5 with the control parameters outlined in Appendix. D.1. The 3GB AC/DC system parameters used in thesis are provided in Appendix. C.2

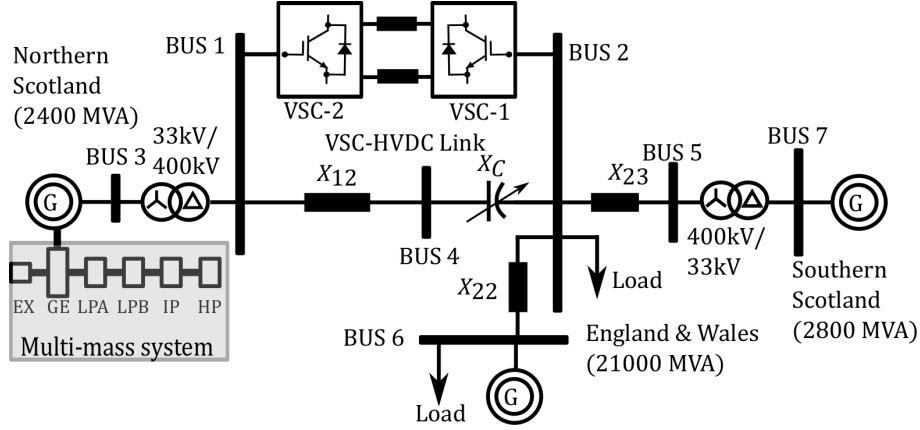


Figure 3.11: GB three-machine system configuration with reinforcements.

3.7 Subsynchronous Resonance Analysis

The SSR characteristics of the test systems introduced in the previous section are evaluated using small-signal stability analysis methods. The SSR characteristics of VSC HVDC for various operating cases are reported in [131]. Since the use of this technology may sometimes destabilize the torsional dynamics [132, 133], its impact on the torsional modes has to be evaluated in detail before exploring the capability for damping. The work presented here furthers the results obtained in [94] by presenting a complete state-space representation of the integrated AC/DC system –suitable for small-signal stability assessments. The analysis starts with the FBM for SSR studies, where the impact of VSC HVDC links is assessed. This initial approach is then extended to the 3GB system. SSR is examined in the integrated AC/DC systems both through eigenvalue analysis (performed in MATLAB), perturbation/damping torque analysis (performed in PSCAD/EMTDC) and time-domain simulations to validate the theoretical analysis (also carried out in PSCAD/EMTDC).

3.7.1 Eigenvalue Analysis

The linearised equations of the multi-mass shaft, generator, AC transmission line and VSC HVDC links from Sections: 3.2 to 3.5 are aggregated to formulate the final state-space model of the

two test systems presented in the previous section. The '*eig*' function in MATLAB is used to perform the calculations of the eigenvalues. The small-signal stability characteristics of the system are evaluated from the eigenvalues to understand the SSR phenomenon with respect to the different level of series compensation in the AC line and the contribution of VSC HVDC to the system damping.

3.7.1.1 Eigenvalue Analysis of MFBM System

The IEEE FBM may be represented as a system of 20 differential equations. The detailed modelling and state-space representation of FBM can be found in [129, 130]. The upgraded IEEE FBM with a point-to-point VSC HVDC link as shown in Figure 3.10 can be represented by a set of 39 differential equations. Following a linearisation exercise, a state-space representation as in equation. 3.38 and the system state matrix A_{sys1} consist of the aggregated state matrices of each elements as introduced in equations 3.4, 3.18, 3.21 and 3.35 are used in screening the SSR through eigenvalue calculations. The system state matrix A_{sys1} and associated states are provided in Appendix. A and B

$$\begin{aligned}\Delta \dot{X}_{sys1} &= A_{sys1} \Delta X_{sys1} \\ \Delta X_{sys1} &= [X_{GE}, X_{MM}, X_{TN}, X_{HVDC}]^T\end{aligned}\tag{3.38}$$

where, X_{GE} , X_{MM} , constitute the states associated with the synchronous generator and multi-mass shaft model; X_{TN} the series-compensated transmission line; and X_{HVDC} the VSC HVDC link.

The multi-mass shaft has associated with five torsional modes (TM1-TM5) and one electro-mechanical mode (TM0). Each TM has its largest SSR interaction at a certain value of series compensation. Table 3.1 summarises the relevant eigenvalues for 30, 40 and 60% series compensation of the transmission line connecting the multi-mass enabled turbine-generator of the MFBM system. The MFBM is characterised by four unstable torsional modes (TM1-TM4) associated with the multi-mass shaft of the NS generator which may be excited at different levels of compensation. TM5 is stable over the whole range of series compensation as its modal inertia is high. The SUB and SUPER mode indicates the subsynchronous and supersynchronous frequencies of MFBM (see Table 3.1).

Table 3.1: Torsional Modes of the Modified FBM System

Torsional Modes	30% Compensation $\sigma \pm j\omega$	40% Compensation $\sigma \pm j\omega$	60% Compensation $\sigma \pm j\omega$
TM5	-1.173 ± 298.104	-1.173 ± 298.104	-1.173 ± 298.104
TM4	-0.011 ± 202.110	$+0.089 \pm 202.115$	-0.089 ± 202.121
TM3	-0.22 ± 160.752	-0.222 ± 160.76	$+0.225 \pm 160.785$
TM2	-0.021 ± 127.104	-0.022 ± 127.101	-0.024 ± 127.990
TM1	-0.142 ± 99.305	-0.1475 ± 99.311	-0.123 ± 99.313
TM0	-0.552 ± 9.572	-0.581 ± 9.87	-0.583 ± 9.881
SUB	-6.312 ± 216.272	-7.674 ± 197.35	-15.82 ± 155.904
SUPER	-10.06 ± 560.701	-10.26 ± 560.751	-10.62 ± 560.771

When 30% of compensation is employed the system is stable. However, for 40% the SUB mode ≈ 31.42 Hz ($\omega = 197.35$ rad/s) interacts with TM4 of the shaft, ≈ 32.18 Hz ($\omega = 202.115$ rad/s). As a consequence, SSR arises and TM4 becomes unstable, evidenced by its positive real part. Similarly, for 60% the SUB mode ≈ 24.82 ($\omega = 155.90$ rad/s) interacts with TM3 of the shaft, ≈ 25.47 Hz ($\omega = 160.78$ rad/s), resulting in unstable oscillations in the system evidenced by the positive real part of TM3. For these operating conditions, any small disturbance, fault or load change would trigger SSR.

A comparison between the FBM system with and without the VSC HVDC link over a wide range of series compensation levels is shown in Figure 3.12. It is noted that until 30% compensation, the frequency of mode SUB is far from the natural frequency of any TM; thus there is no SSR present. By increasing the series compensation levels, the risk for SSR rises as the subsynchronous frequency becomes close or in the near vicinity of any of the TM frequencies as shown. It is noticeable from Figure 3.12 that the excitation of the TMs leading to instability and oscillation for a system with an HVDC link occurs at a lower series compensation level than that for the FBM alone. This shifting is due to the reduction of the frequency of the SUB mode for the FBM with a VSC HVDC link. Although connecting the VSC HVDC link attenuates the amplitude of the torsional oscillations, it does not contribute much to the damping of SSR.

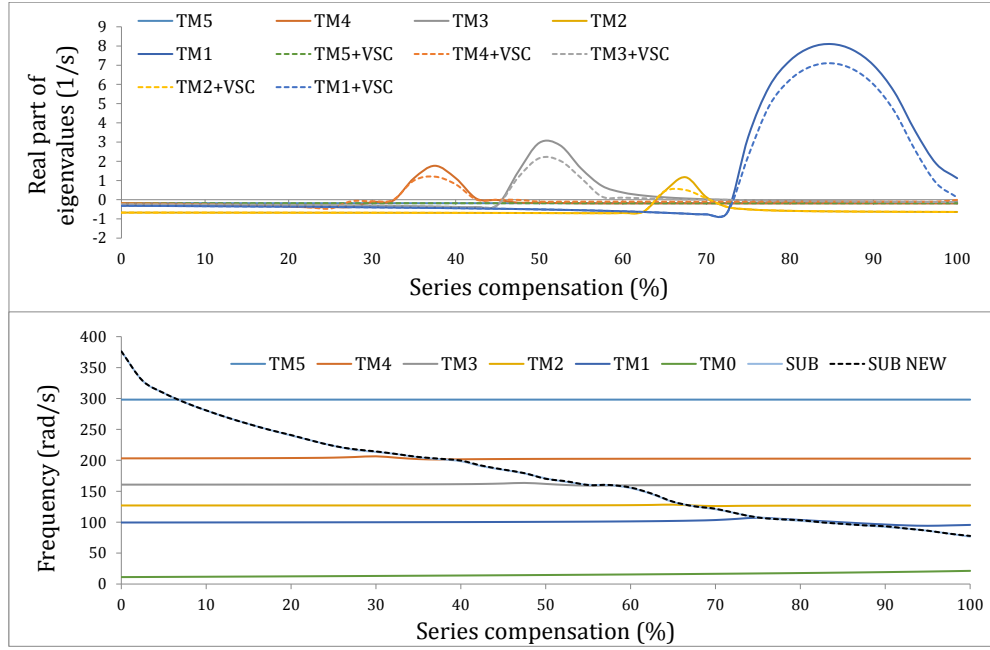


Figure 3.12: Torsional mode stability in terms of series compensation for MFBM system.

3.7.1.2 Eigenvalue Analysis of 3GB Model

A detailed state-space model of the system with the dynamic equations of the synchronous machines, transmission lines and the HVDC link with its controllers has been developed for the 3GB model as in Figure 3.11. This is a system of 77 differential equations linearised around an operating point (ref Appendix. A and B), given by:

$$\begin{aligned} \Delta \dot{X}_{sys2} &= A_{sys2} \Delta X_{sys2} \\ \Delta X_{sys2} &= [X_{NG}, X_{N\omega}, X_{N\theta}, X_{SG}, X_{EWG}, X_{TN}, X_{HVDC}] \end{aligned} \quad (3.39)$$

where, X_{NG} , $X_{N\omega}$, $X_{N\theta}$ constitute the states associated with the NS synchronous generator; X_{TN} the series-compensated transmission line; X_{SG} , X_{EWG} the SS and E&W generators; and X_{HVDC} the VSC HVDC link.

As shown in Figure 3.11, the transmission line connecting NS generator has been upgraded with series compensation. The VSC HVDC link is connected between buses 1 and 2. The system

Table 3.2: Torsional Modes of the 3GB System

TM	30% Compensation $\sigma \pm j\omega$	40% Compensation $\sigma \pm j\omega$	75% Compensation $\sigma \pm j\omega$
TM5	-1.173 \pm 272.193	-1.173 \pm 272.183	-1.173 \pm 272.1935
TM4	-0.2078 \pm 185.488	+0.097 \pm 187.925	-0.185 \pm 185.099
TM3	-0.3839 \pm 146.666	-0.3792 \pm 146.56	+0.2974 \pm 146.825
TM2	-0.0587 \pm 115.970	-0.0584 \pm 114.75	-0.051 \pm 116.012
TM1	-0.1492 \pm 90.574	-0.1475 \pm 91.123	-0.128 \pm 90.868
SUB	-7.4436 \pm 209.289	-7.674 \pm 191.574	-7.735 \pm 148.310
SUPER	-8.5183 \pm 418.520	-8.665 \pm 432.55	-9.11 \pm 479.435

in equation 3.39 has been constructed in MATLAB in order to perform eigenanalysis. The three-machine series-compensated AC/DC system shown in Figure 3.11 is characterised by four unstable torsional modes (TM1-TM4) associated with the multi-mass shaft of the NS generator which may be excited at different levels of compensation. TM5 is stable over the whole range of series compensation as its modal inertia is high.

Table 3.2 summarises the relevant eigenvalues for 30, 40 and 75% series compensation of the transmission line connecting the NS generator. As it can be observed, when 30% of compensation is employed the system is stable. However, when the compensation is increased to 40% the SUB mode (≈ 30.7 Hz) interacts with TM4 of the multi-mass shaft (≈ 29.6 Hz). As a consequence, SSR emerges and TM4 becomes unstable, evidenced by its positive real part. Similarly, for 75% the SUB mode (≈ 23.61 Hz) interacts with TM3 of the shaft (≈ 23.37 Hz), resulting in unstable oscillations in the system evidenced by the positive real part of TM3. For these operating conditions, any small disturbance or load change would trigger SSR.

Figure 3.13 shows the ranges of series compensation levels for which torsional instability arises. System stability is directly related to the subsynchronous mode of the HVDC-connected series-compensated transmission line linked to the NS generator (termed SUB). Potential instability occurs whenever the SUB mode is in the vicinity of a torsional mode frequency, as illustrated by the real part of the eigenvalues of the torsional modes (TM1-TM4).

As seen from the FBM case, in the GB system as well the VSC by itself does not affect the stability

of the AC/DC system neither it contributes much for damping. However, their controllability can, therefore, explored for better damping.

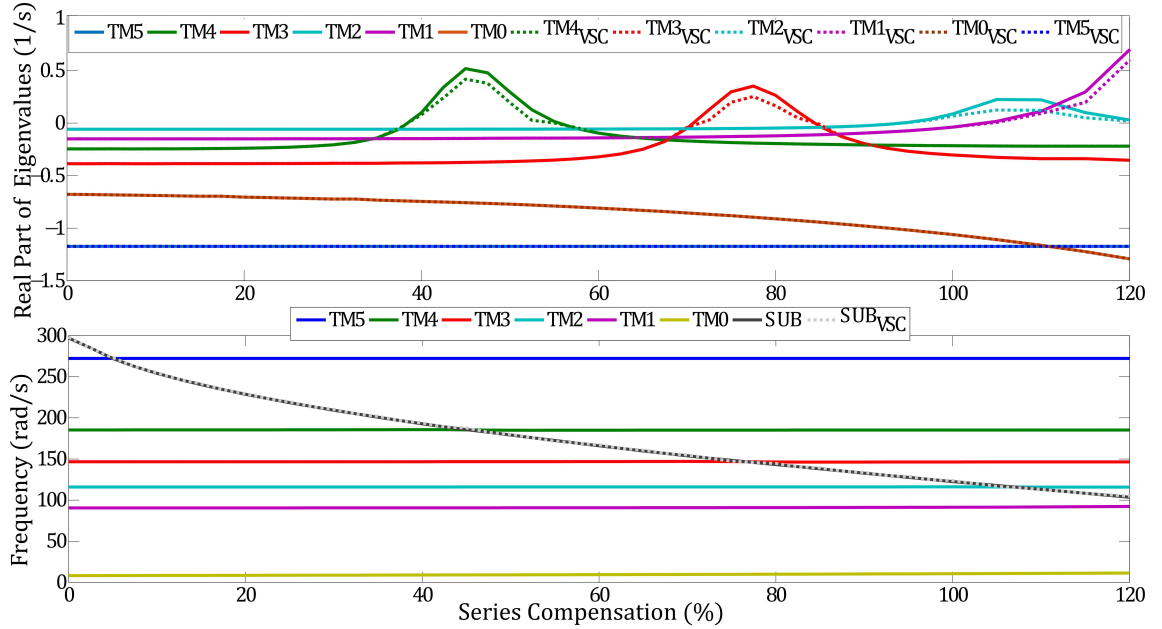


Figure 3.13: Torsional mode stability in terms of series compensation for the 3GB system.

3.7.2 Damping Torque Analysis

To confirm the validity of the eigenvalue analysis, EMT based electrical damping analysis performed in PSCAD/EMTDC for the two test systems are adopted in this section [89, 90]. The advantage of this method over eigenvalue analysis exist in the representation of the detailed switches and associated delays with the valves as VSC is explicitly modelled with all its associated components.

Depending on the apparent network impedance (viewing the network from the generator location) and the action of the nearby VSC and other network elements, a small-disturbance in machine speed will result in a certain perturbation in terminal voltage and, thus, on the generator current. This is then translated into a change in electrical power and, thus, the electrical torque. This electrical torque will suffice to demonstrate the SSR characteristics [89, 90, 134].

The electrical damping torque screening is used in this section to complement and validate the eigenvalue analysis. Moreover, it is used to assess the contribution made by the VSC HVDC link

towards the electrical damping of the nearby generator unit. In general, the electromagnetic torque of the generator is given by:

$$T_e = P_e / \omega_r = T_{e0} + \Delta T_e \quad (3.40)$$

where P_e is the electrical power, and T_{e0} is a constant torque that depicts generator output power at the fundamental frequency. ΔT_e is the perturbed electromagnetic torque, from torsional oscillations and plays the fluctuating role on the rotor, which is divided into two components as:

$$\Delta T_e = T_S \Delta \theta + T_D \Delta \omega \quad (3.41)$$

where the synchronizing torque component $T_S \Delta \theta$ will act as an auxiliary spring on the rotor and is in phase with angular displacement. The damping torque component $T_D \Delta \omega$, acts as a damping element and is in phase with the angular velocity.

Substituting $\Delta \theta = \Delta \omega / j\omega$ yields

$$\Delta T_e = \left(\frac{T_{se}}{j\omega} + T_{de} \right) \Delta \omega \quad (3.42)$$

Equation 3.42 shows that the state of the electrical torque and the machine speed can be exploited to calculate the electrical damping factor. A small-signal fluctuation in the turbine speed $\Delta \omega$ is achieved by injecting a perturbation signal and thereby the electrical damping is evaluated by the resulting perturbation in electrical torque ΔT_e . Consider a small speed modulation at frequency f_{mf} given by:

$$\omega(f_{mf}) = A_1 \sin(2\pi f_{mf} + \phi_1) \quad (3.43)$$

where A_1 and ϕ_1 is the magnitude and phase angle of the injected signal component of frequency f_{mf} . The selection A_1 should be made carefully in such a way as not to impact the steady-state operation of the test system under investigation [90, 134]. For the study presented here A_1 is set to be 0.001 p.u. The corresponding electrical torque component for the modulated signal

frequency f_{mf} , $T_e(f_{mf})$ can be described as

$$-T_e(f_{mf}) = B_1 \sin(2\pi f_{mf} + \phi_2) \quad (3.44)$$

where B_1 and ϕ_2 is the magnitude and phase angle by which T_e is modulated by f_{mf} .

Thus the Damping Factor (T_{de} or D_e) can be computed as

$$D_e = \frac{B_1 \cos(\phi_2 - \phi_1)}{A_1} \quad (3.45)$$

The SSR screening for the two test systems were carried out using the electrical damping equation presented in the 3.45. To compute the damping profile for all subsynchronous frequencies of interest, the excitation frequency fluctuates between zero and the fundamental value. If D_e have positive values for all the subsynchronous range for the entire series compensation level there is low-risk SSR. However, if D_e having negative values in the subsynchronous range, that indicates the potential risk of SSR [89, 95, 134].

3.7.2.1 Damping Analysis of MFBM Model

To compute the electrical damping for all subsynchronous frequencies of interest in the MFBM model, the perturbation frequency is varied from zero and 60 Hz, as shown in Figure 3.14. The analysis is performed with the multi-mass model of the generator disabled and using the *multi-run* and Fast Fourier Transform (FFT) tools in PSCAD/EMTDC [89, 90, 134]. The MFBM system built in PSCAD/EMTDC with associated VSC HVDC control systems for damping analysis is provided in Appendix. E.1.

The results are plotted in Figure 3.14, showing the damping profile for the modified FBM model when the series compensation is varied from 0 to 90%. The red circle on the plots represents the mechanical torsional modes (TM1-TM4) of the FBM system, TM5 is neglected because of its high modal inertia and less participation in SSR, as evidenced by eigenvalue analysis (see Figure 3.12). The results reveal that for low series compensation levels there is a low risk of SSR. However, when the series compensation level goes beyond 40% the risk of SSR increases as evidenced by the increased negative peaks in the damping torque. The maximum negative peaks

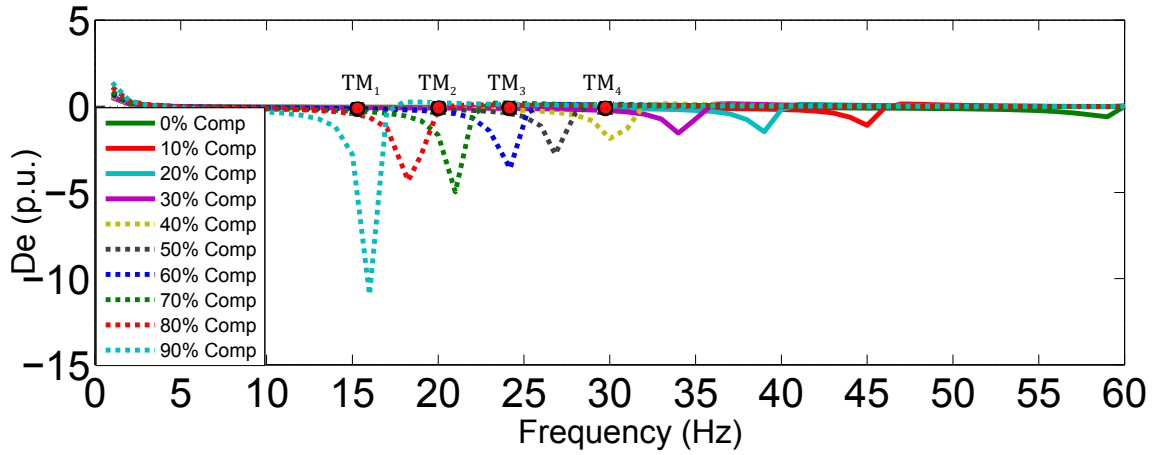


Figure 3.14: Electrical damping of MFBM model over the range of series compensation

occur at frequencies close to the mechanical modes corresponding to series compensation levels of 40%, 60% and 90%. This analysis agrees well with the eigenvalue method indicating the accuracy of the damping torque screening scheme.

3.7.2.2 Damping Analysis of 3GB Model

The same set-up as explained in Section 3.7.2.1 for damping torque evaluation is repeated for the 3GB model. The perturbation is applied for all subsynchronous frequencies of interest in the 3GB model with frequency varied from zero and 50 Hz and is plotted in Figure 3.15. The torsional modes (TM1-TM4) of the NS generator in the 3GB system as identified from eigenvalue analysis is shown as red circles on the plot. Series compensation levels of the line between NS and E&W is varied from 0 to 90%. The damping torque traces of the NS generator reveals the levels of series compensation in which the maximum interaction occurs when the frequencies are in the vicinity mechanical modes. The identified series compensation levels are 40%, 75% and above 90%. Moreover, it can be evidenced by the damping plots that there is a high risk of SSR associated with higher compensation levels.

To further evaluate the impact of VSC on the electric damping and SSR, the damping profile of the 3GB network for three different cases at 40% series compensation level is evaluated and plotted in Figure 3.16. The test cases correspond to the 3GB model: without VSC; with VSC connected and operated at no-load and with VSC at full-load. The results agree well with the eigenvalue analysis as the negative peak of torque diminishes when VSC is connected. However,

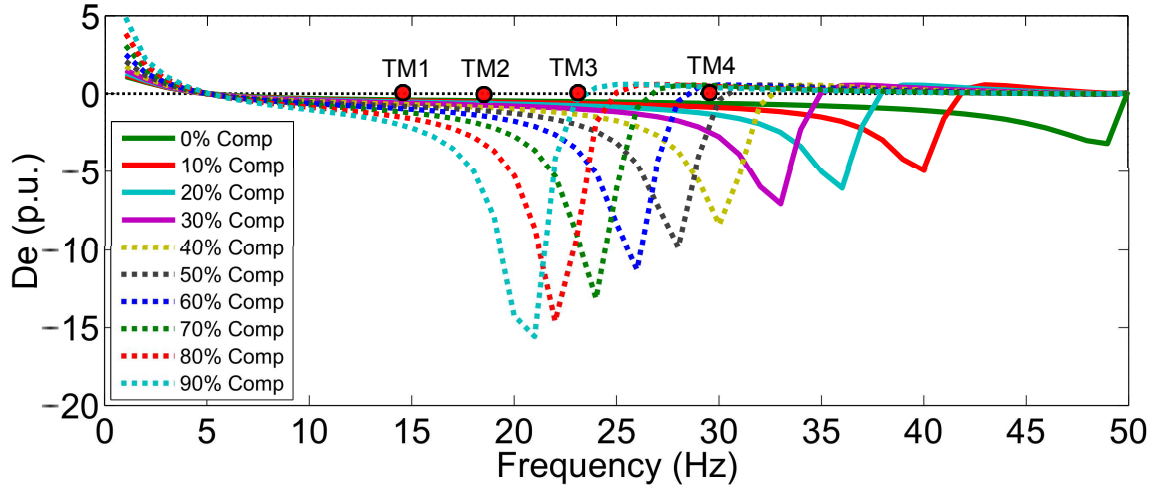


Figure 3.15: Electrical damping of GB model over the range of series compensation

VSC by itself cannot substantially increase the network damping under maximum torsional interactions. Moreover, the impact of loading condition is also evident with the no-loaded VSC contributing slightly to damping degradation. For completeness the 3GB system built in PSCAD/EMTDC with associated VSC HVDC control systems for damping analysis is provided in Appendix. E.1.

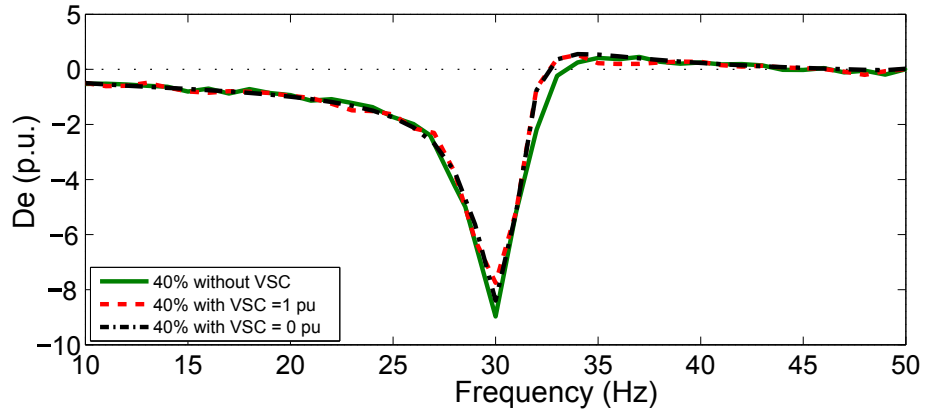


Figure 3.16: Electrical damping for different VSC loading.

3.8 Validation of the Small-signal AC/DC Models

To validate the small-signal models and findings, a time-domain simulation is carried out for the two test systems using the electromagnetic transient program PSCAD/EMTDC. The validation is essential to see the impact of torsional amplification under an SSR event, which cannot be

achieved through analytical calculations such as eigenvalue and damping torque screening studies. The AC/DC systems (MFBM and 3GB) built in PSCAD/EMTDC with associated VSC HVDC control systems for simulation tests is provided in Appendix. E.1.

3.8.1 Time-domain Analysis of MFBM Model

The validation of the developed small-signal models of the FBM system is performed through a small disturbance in time-domain achieved by a change in series compensation levels from 20% to 30%, 40% and finally 60%, at time $t = 6s$ with the results plotted in Figure 3.17. As it can be observed, the system exhibits SSR –reflected by the growing oscillations in the mechanical shaft and electrical torques for series-compensation levels at 40% and 60%, and remains stable for 30%, as shown in Figure 3.17(a) and Figure 3.17(b). The oscillations are due to vicinity of the frequency of the torsional oscillations near one of the mechanical shaft modes (i.e. ≈ 32 Hz), which coincides with the complement of the subsynchronous frequency component (≈ 28 Hz) for 40% and the mechanical shaft modes (i.e. ≈ 25 Hz), which coincides with the complement of the subsynchronous frequency component (≈ 35 Hz) for 60%. This is shown by the FFT of the mechanical shaft and current of phase-a in Figure 3.18(a) for 40% compensation level and from Figure 3.18(b) for 60% compensation level which results in the deviation of frequency from 60 Hz observed in Figure 3.17(c).

Figure 3.17(d) depicts the output power (P_1) of VSC1 at Bus 2 (see Figure 3.10). The results reveal that the converter power is building up in magnitude due to SSR for 40% and 60% compensation level and if no corrective measures are taken these oscillations will surpass the converter limits.

The time-domain results agree well with the analytical studies, showing the contributors and the subsynchronous frequency of interest for different series-compensation levels. This is achieved through transient torque and FFT analysis in PSCAD.

3.8.2 Time-domain Analysis of 3GB Model

The investigation of the 3GB system stability is further extended and validated through time-domain simulations. The series-compensated 3GB system with a VSC HVDC link in Figure 3.11 has been constructed in PSCAD.

3.8. Validation of the Small-signal AC/DC Models

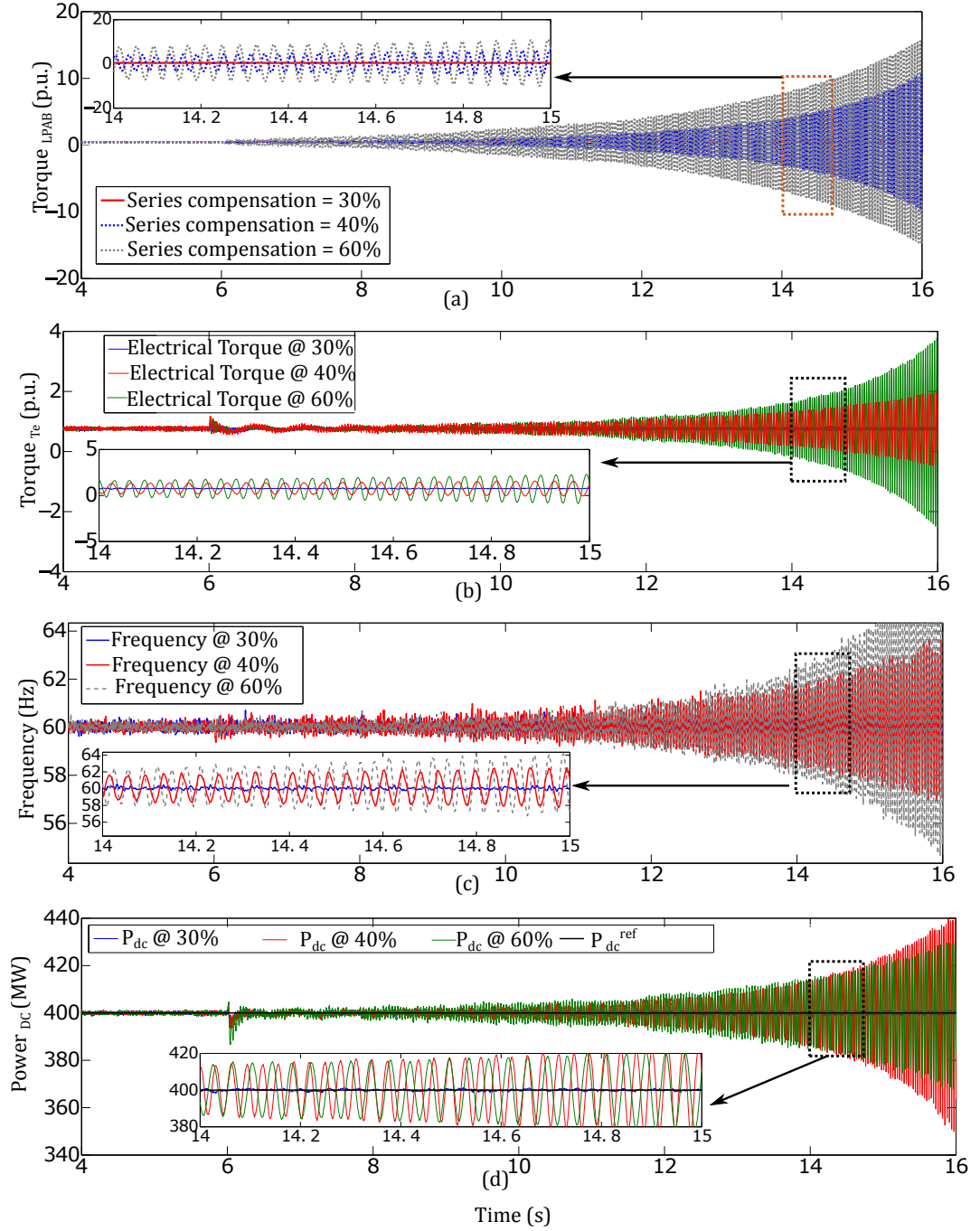


Figure 3.17: Time-domain results of MFBM model at different compensation levels. (a) Mechanical torque LPAB; (b) Electromagnetic torque; (c) Network frequency; (d) Output power of VSC1.

The simulation starts at a 20% series compensation level; as it can be seen the system is in steady-state and is stable. To evaluate the system response to small-signal changes, at 6 s the compensation level is increased to 30%, 40% and 75% respectively. It can be observed that

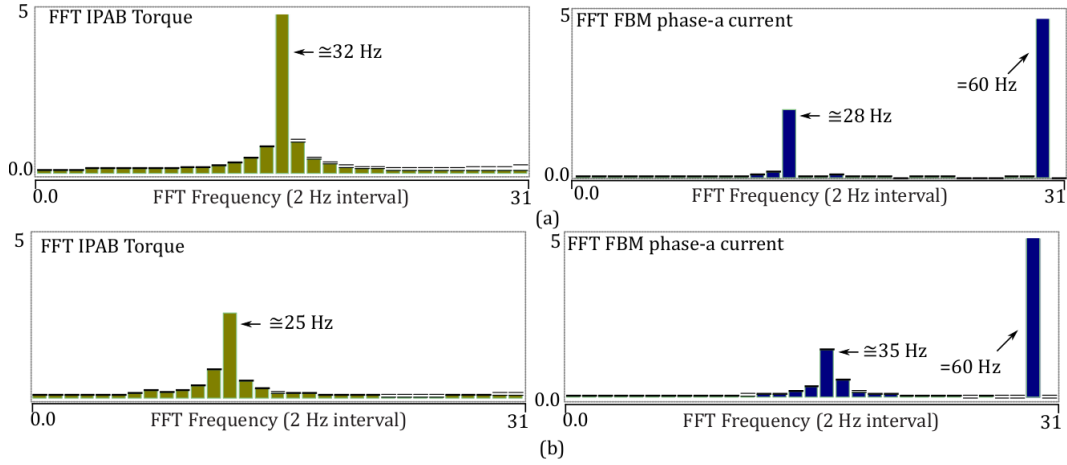


Figure 3.18: FFT (2 Hz interval) of the IPAB torque section and current of phase a of the synchronous generator of MFBM. (a) at 40 % series compensation (b) 60% series compensation

such a disturbance renders the system unstable, as shown by the growing oscillations of the turbine torques in Figure 3.19 (a)-(b) for 40% and 75% and remains stable for 30% as expected. In practice, the oscillating torque responses would eventually damage the turbine shaft if corrective measures are not taken.

Figure 3.19(c) shows the frequency of the current in the phase of the NS generator, which deviates from the nominal 50 Hz. Following an FFT analysis Figure 3.20 of this current, it can be seen that it has a component at subsynchronous frequency (20 Hz) and (26 Hz) for 40% and 75% series-compensation levels, which is the complement of the TM4 frequency ($\approx 30\text{Hz}$) for 40% and TM3 frequency ($\approx 24\text{Hz}$) for 75%. These results are consistent with the eigenanalysis summarised in Table. 3.2 and damping profile in Figure 3.15.

The impact of the SSR oscillations on the HVDC link power due to small-disturbance under different series compensation levels are illustrated in Figure 3.19(d). The results are consistent with the theoretical analysis as evidenced by the building up in oscillation magnitudes after the disturbance at 6s in the test network for 40% and 75% compensation levels.

The theoretical analysis and time-domain exercise for the MFBM and the 3GB test systems complements each other and thus it can be concluded that the 3GB test system can be used for SSR studies and damping scheme implementation. Therefore, in the following chapters only the 3GB system will be considered for further analysis.

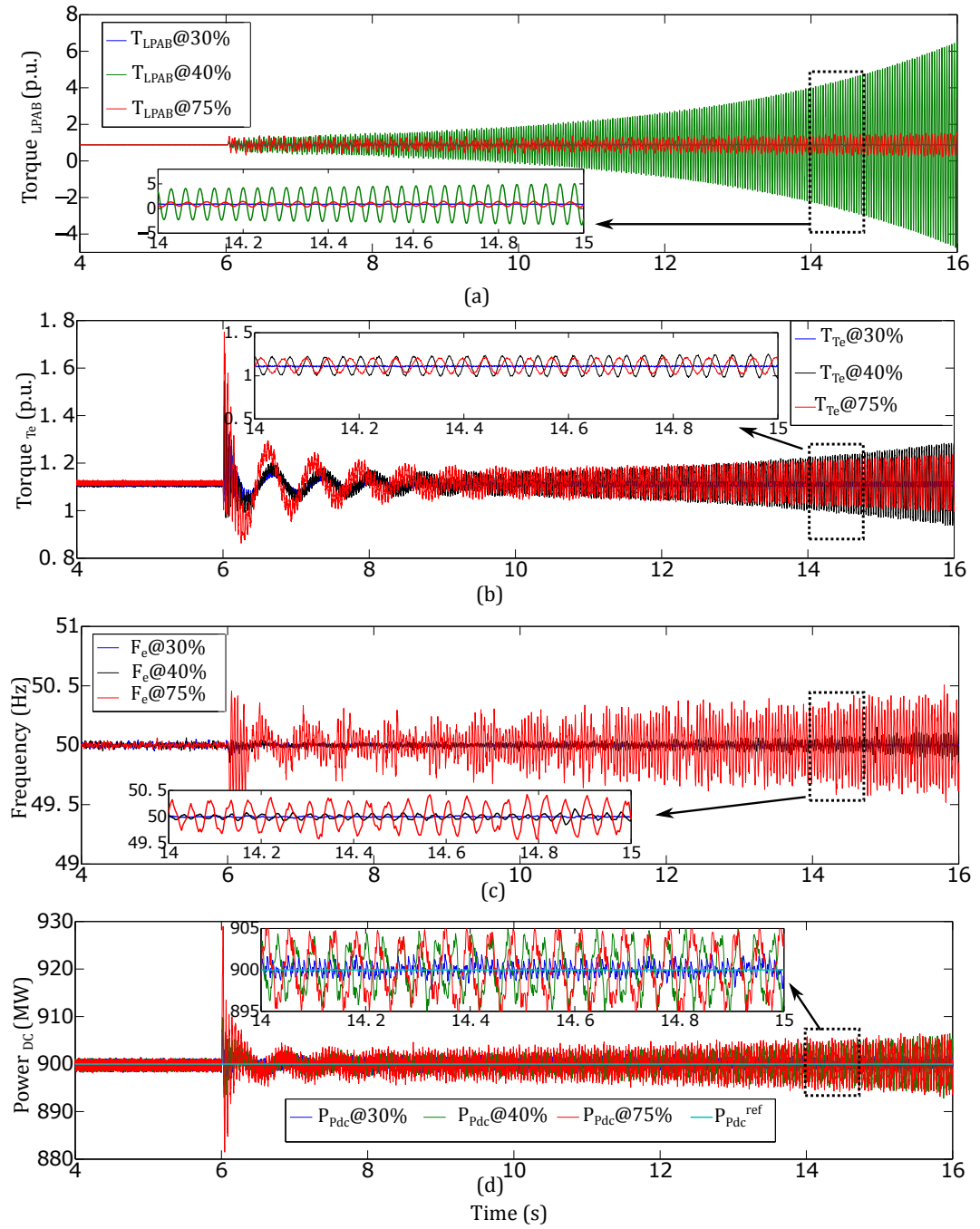


Figure 3.19: Time-domain results of 3GB model at different compensation levels. (a) Mechanical torque LPAB; (b) Electromagnetic torque; (c) Network frequency; (d) Output power of VSC1.

3.9 Summary

This chapter presented two integrated AC/DC systems which are dynamically modelled, constructed and simulated for small-signal stability studies. The first system under study consists

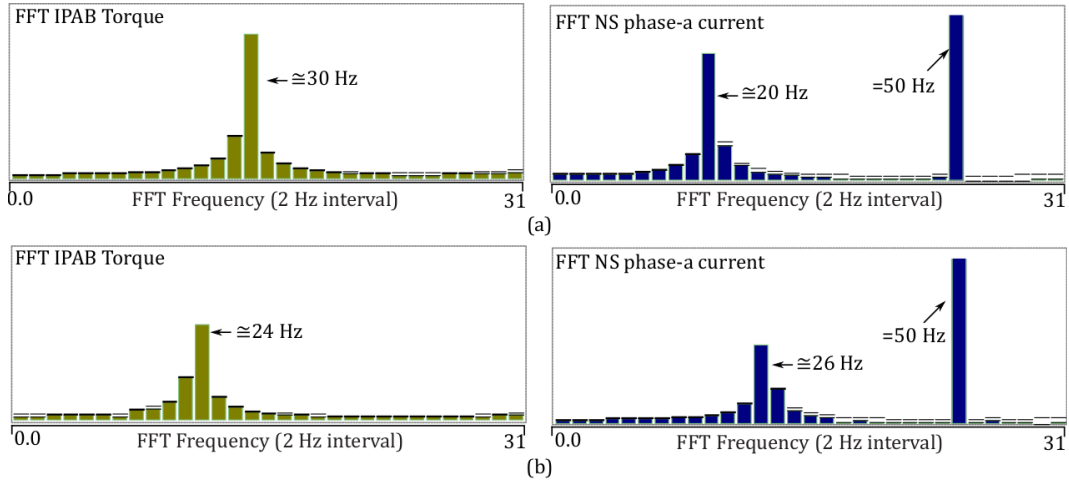


Figure 3.20: FFT (2 Hz interval) of the IPAB torque section and current of phase a of the synchronous generator of 3GB. (a) at 40 % series compensation; (b) 75% series compensation.

ted of the IEEE FBM upgraded with a point-to-point VSC HVDC link. A series-compensated three-machine network featuring a point-to-point VSC HVDC link representing the operating conditions of the reinforced GB system in 2020 was then constructed. Both models were built in MATLAB to perform small-signal stability assessments through eigenvalue analysis. As it has been shown through eigenvalue analyses, the use of series compensation nearby synchronous machines employing thermal turbines may result in SSR. Such undesirable phenomenon may be characterised by unstable regions of operation throughout the series compensation range. Upon such conditions, system faults and scheduled/ unexpected switching actions may render the system unstable. The results are then validated with damping torque analysis and PSCAD time-domain simulations.

The dynamic modelling and formal approach adopted in this work are amenable to a detailed understanding of subsynchronous oscillations arising in integrated AC/DC networks. Moreover, the models developed in this chapter could be used for other stability studies such as frequency stability and controller implementation. The modelling has been performed in such a way that the proposed models are easily scalable to build more complex and detailed networks and also for implementing and testing different SSR damping schemes.

4 Damping of SSR in a Series-Compensated AC/DC Network using VSC HVDC

4.1 Introduction

The illustration of SSR phenomenon in the previous chapter using the reduced GB transmission network incorporating series compensation and VSC HVDC link clearly highlights the need for additional countermeasures so as to keep the quality and security of the network. This scenario has brought forth the need for a remedial action that has to be implemented to avoid any negative interactions introduced by the reinforcements and avoid possible instability. To this end, this chapter introduces the supplementary damping capability of the proposed VSC HVDC link, which has been identified as the most economical and efficient active filtering solution to avoid SSR.

The primary control system of the VSC HVDC link was implemented initially to examine the operation of the compensated AC/DC grid and its contribution to SSR characteristics. This is followed by the design and implementation of three active filtering schemes which are integrated as supplementary controllers into the VSC. The capability of each control schemes in providing SSR damping has been evaluated through damping torque analysis and time-domain simulations in PSCAD/EMTDC.

4.2 Operation of Series-compensated 3GB AC/DC Network

The operation of the series-compensated 3GB AC/DC network as depicted in Figure 3.11 will be discussed with focus been made on the VSC control schemes for steady-state and SSR events. The main objective of the proposed VSC HVDC link is active power transfer, identified as the primary control function. However, the provision of ancillary services requirement such as power oscillation and SSR damping capability from system operators prerequisites a supplementary/secondary control that has to be embedded with the VSC control system [69]. This section provides an insight into both control schemes with their operational characteristics.

4.2.1 Primary Control Objective

The primary control objective of the VSC HVDC link connected in parallel with the series-compensated 3GB system as shown in Figure 3.11 is to control the active power flow between Bus 1 and Bus 2. Moreover, the VSC's are also used to regulate the AC voltage at both ends through reactive power control. Thus the VSC parameters which were controlled are the active and reactive power (PQ) at Bus 1 and DC voltage and reactive power ($V_{dc}Q$) at Bus 2. For completeness the control systems associated with VSC HVDC built in PSCAD/EMTDC and used in this chapter is provided in Appendix. E.1.

The control system block diagrams for primary control mode operation is illustrated in Figure 4.1. The design of the controllers follows the same approach as discussed in Section. 3.5 [122, 123]. As depicted in Figure 4.1(a), the VSC1 regulates the active power flow by controlling the current reference I_{d1}^{ref} achieved by cascaded PI controllers in dq reference frame. The VSC2 terminal is used for DC voltage regulation by controlling the current reference I_{d2}^{ref} as shown in Figure 4.1(b). Reactive power control is achieved in both ends through controlling the current reference I_q^{ref} using PI controllers as shown in Figure 4.1 .

To test the primary control objectives of the VSC HVDC link, the control schemes as in Figure 4.1 were implemented and simulated in PSCAD/EMTDC. The response of the HVDC link to power (active and reactive power) set-point change is simulated to ensure system stability under parallel operation with AC lines. The results in this section are expressed in per unit (p.u.)

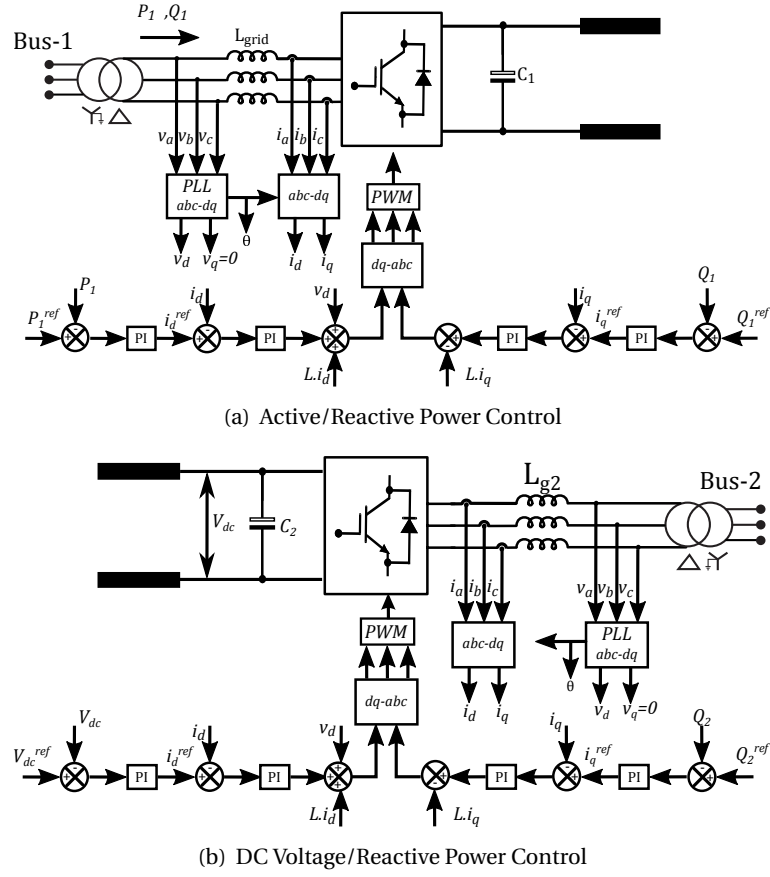
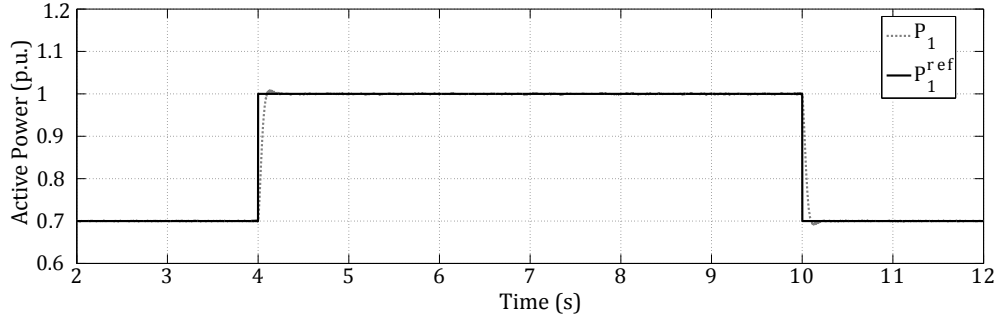


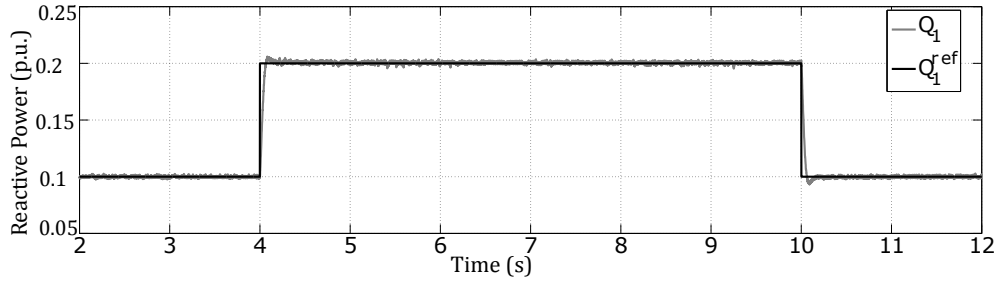
Figure 4.1: Primary control strategy of VSC HVDC link.

considering the following DC power, DC voltage and AC current bases: 1000 MW, ± 320 kV, and 4 kA. VSC1 is initially set to inject 0.7 p.u. active power and 0.1 p.u. reactive power, whereas VSC2 has been designated as a slack converter that maintains the grid power balance (*i.e.*, maintains a constant DC voltage).

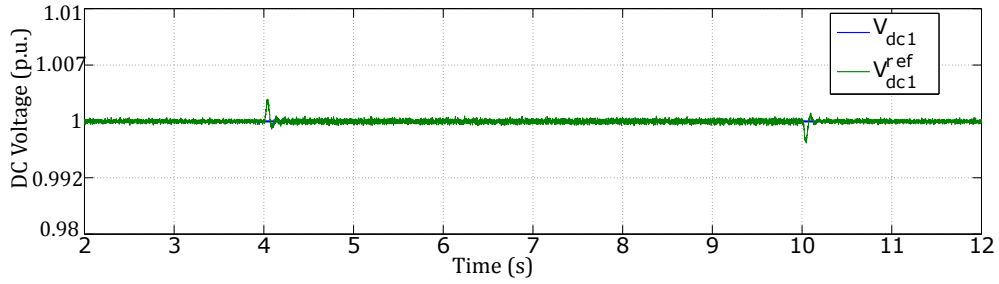
The results plotted in Figure 4.2 demonstrates the performance of the 3GB hybrid AC/DC network when there is a step change from 0.7 p.u. to 1 p.u. at $t = 4$ s and back to 0.7 p.u. at $t = 10$ s in the active power (Figure 4.2(a)) and from 0.1 p.u. to 0.2 p.u. in reactive power (Figure 4.2(b)) with 40% series compensation in the AC line. Variations in the DC voltage characteristics for the power set-point changes are evident in Figure 4.2(c). The impact of such a small-disturbance in the machine dynamics and AC line current response under series-compensated case has been evaluated by the shaft torque (T_{LPAB}), the electric torque (T_E) and current responses plotted in Figure 4.2(d) and Figure 4.3. The torques start to oscillate after the events and suddenly settles down to their initial operating conditions, which shows the stable operation of the network



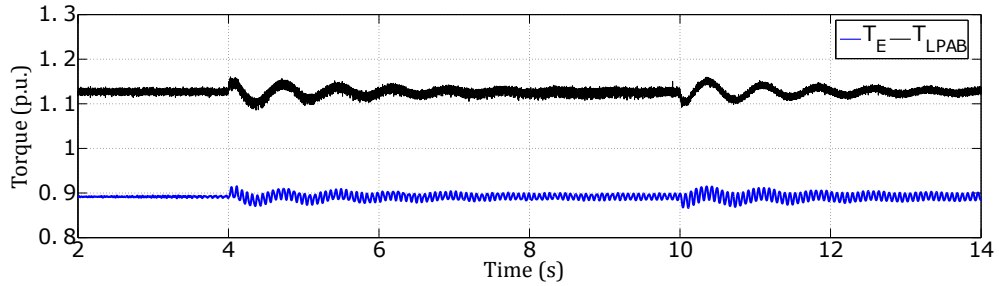
(a) Active Power Response to a step change at 4s and 10s.



(b) Reactive Power Response to a step change at 4s and 10s.



(c) DC Voltage Response to the step change at 4s and 10s.



(d) Torque Responses to the step change at 4s and 10s of HVDC Link.

Figure 4.2: Primary control response of 3GB system.

and the sensitivity of torsional responses to the small-disturbance such as the power set-point change. The AC line current plots clearly show the changes in power flow when the DC link is ordering more power at $t = 4$ s and reducing its power level at $t = 10$ s.

4.3. Damping Scheme: 1 Multi-modal Damper Approach

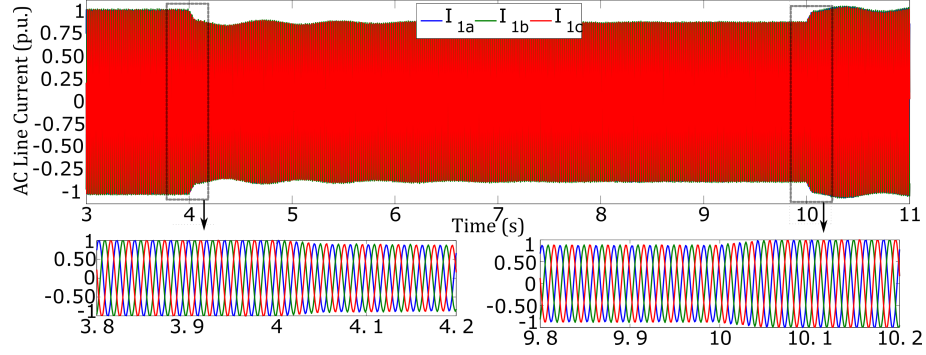


Figure 4.3: AC line current response to step change in DC power set-points.

4.2.2 Secondary Control Objective

Operation of the AC/DC network could be compromised due to the SSR events and the need for necessary countermeasures are at high. Utilising existing HVDC links rather than building new devices is always a better utilisation of assets. To damp SSR upon occurrence, a supplementary controller has been designed and integrated with the control loop of VSC1. Its main objective is to increase the network damping at those frequencies that are critical for the turbo-generator shafts and this is achieved by suppressing the line current component at the subsynchronous frequency (SSF). Three damping schemes were implemented and will be detailed in the following sections.

4.3 Damping Scheme: 1 Multi-modal Damper Approach

The damping scheme discussed in this section utilises a real-time system that injects subsynchronous currents at the point of connection to the AC system (in this case, near the stator terminals of the synchronous generator) to mitigate SSR upon occurrence.

The work presented in this section builds on an SSR damping scheme originally reported in the literature, where SSR is mitigated for a specific value of series compensation following the excitation of a single torsional mode of a turbo-generator [94]. However, in this case the damping is ensured through all the series compensation range. This is achieved through the adoption of a method based on active filters which upon an SSR condition extracts subsynchronous components of the current flowing in a transmission line. By employing the filtering structures proposed in [128] and [135], components at SSF's are extracted and then injected into the AC

system in such a way that damping is performed.

Motivated from the existing filtering schemes, in order to accommodate the multiple torsional modes (TM) associated with the series-compensated 3GB system as identified through eigenvalue analysis (see Section. 3.7.1.2) a multi-modal filter based damper (MMD) embedded in the VSC1 control system is used. The structure of the SSR damping loop is shown in Figure 4.4.

As it can be seen from Figure 4.4(a) the line current (in dq reference frame) is used as the input signal which then follow separate paths (in this case two), each of which targets different subsynchronous modes along the frequency range of interest and comprises an additional band-pass modal filter (B_{TMn}) as presented in equation 4.1. The outputs are then summed to form the SSR damping signal, which is injected into the summation point before the inner current control loops of the VSC1. Fast injection of the active damping signal can be achieved by the selection of this injection point due to the high bandwidth of inner current control loop [95]. The current components I_{dSUB} and I_{qSUB} are used to modulate real (I_{d1}^{ref}) and reactive current (I_{q1}^{ref}) references of VSC1 as shown in Figure 4.4(b).

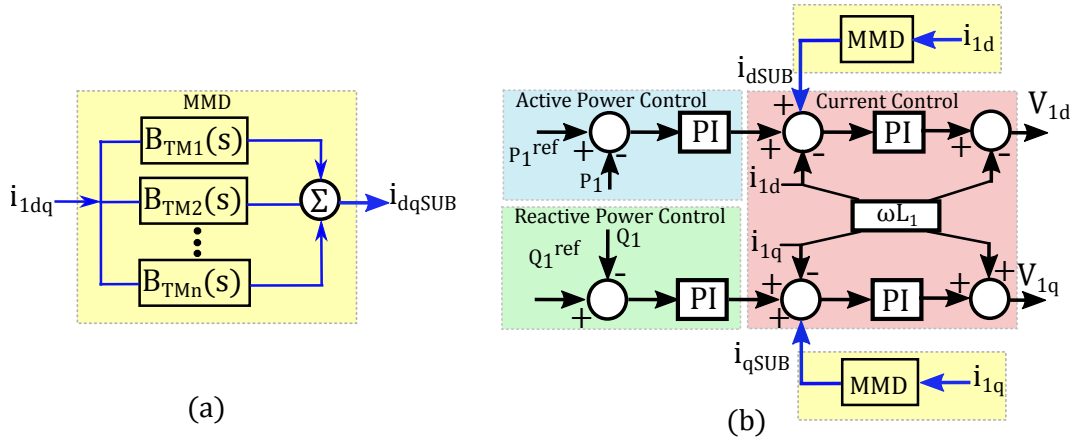


Figure 4.4: Multi-modal filter based injection structure. (a) Band-pass modal filter; (b) Modified VSC1 control loop.

For this work, prior knowledge of the multi-mass shaft torsional modes following an eigenvalue analysis (see. Section 3.7.1) has been used to accurately tune the modal filters. This allows for an adequate extraction of subsynchronous components upon SSR. The critical torsional modes associated with the 3GB system for 40 and 75% of series compensation levels, (*i.e.* TM3 (26 Hz) and TM4 (20 Hz)) has been taken as the centre frequency (ω_{cn}) for the modal filters. Each

4.3. Damping Scheme: 1 Multi-modal Damper Approach

modal filter will be effective only for their corresponding TM frequency and act upon to provide damping to the respective modes by reducing the negative damping region. The modal filter is a series combination of a 2nd order band-pass filter which is then combined with a gain (k_{MMD}) to form the final MMD structure. The final transfer function of the MMD is expressed as:

$$B_{TM}(s) = k_{MMD} \frac{\frac{s}{\omega_{cn}}}{1 + 2z \frac{s}{(\omega_{cn})} + (\frac{s}{\omega_{cn}})^2} \quad (4.1)$$

$$B_{TM}(s) = B_{TM1}(s) + B_{TM2}(s) + \dots + B_{TMn}(s)$$

where ω_{cn} is the centre frequency of the filter, z the damping factor and k_{MMD} denotes the gain coefficient. The frequency response of the designed modal filters is shown in Figure 4.5. As seen, the gain of the targeted modes are maximum at the corresponding SSF modes and decreases for other frequencies. Moreover, the phase shift introduced by the MMD is equal to zero at the selected frequencies. The observations conclude that by providing individual paths for the SSF modes, it is possible to achieve selective damping-subjected to the knowledge of the TM of turbine-generator. Using the expressions in 4.1 and for achieving satisfactory damping of the

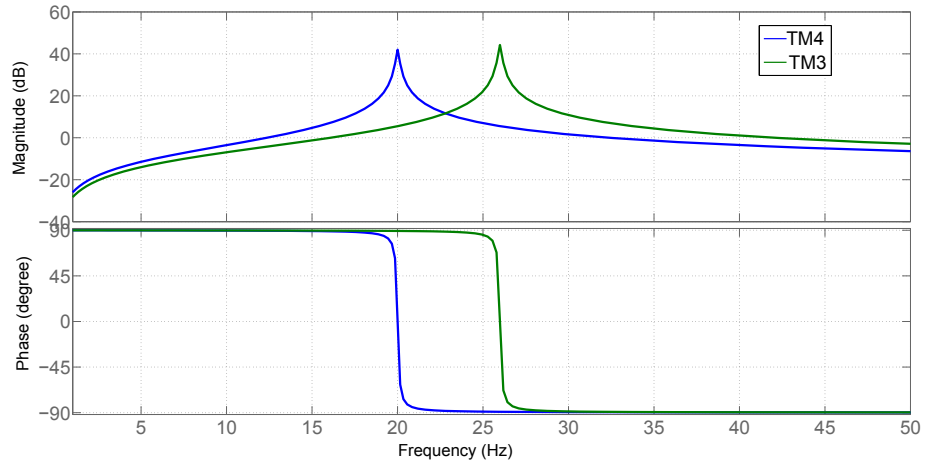


Figure 4.5: Frequency response of modal filters at different torsional modes

3GB system at 40 and 75% compensation levels, the design parameters of the MMD are:

$$B_{TM4}: z=0.5, \omega_{c4}=125 \text{ rad/s } (2.\pi.20 \text{ Hz}), k_{MMD} = 1;$$

$$B_{TM3}: z=0.5, \omega_{c3}=169 \text{ rad/s } (2.\pi.26 \text{ Hz}), k_{MMD} = 1.$$

The transfer function of individual filters used in this study with design parameters discussed above are presented in 4.2 and 4.3.

$$B_{TM4}(s) = \frac{0.008s}{1 + 0.008s + 0.00006s^2} \quad (4.2)$$

$$B_{TM3}(s) = \frac{0.006s}{1 + 0.006s + 0.00003s^2} \quad (4.3)$$

Since the SSR of interest in this study is SSR-TI the MMD approach is valid for any network configuration. A notion for this explanation is that, the contributor for SSR-TI phenomenon, the SSF component in the line current will be controlled and suppressed upon an SSR event using MMD enabled VSC close to the generator. This will block the subsynchronous current from entering the generator shaft thereby preventing TI phenomenon.

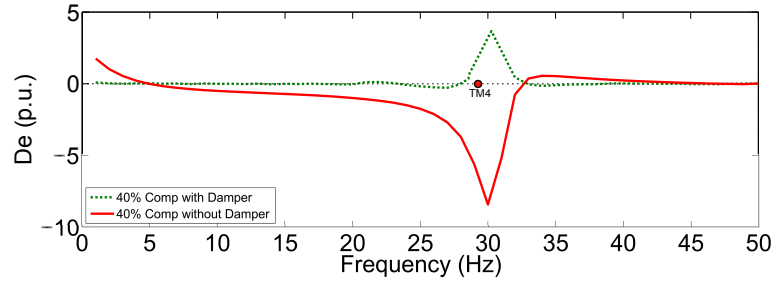
The results reported in this section are for the operational characteristics of the series-compensated AC/DC 3GB system under two network reconfiguration scenarios:

- Case A: Change in series compensation level from 30 to 40% at $t = 4$ s.
- Case B: Change in series compensation level from 30 to 75% at $t = 4$ s.

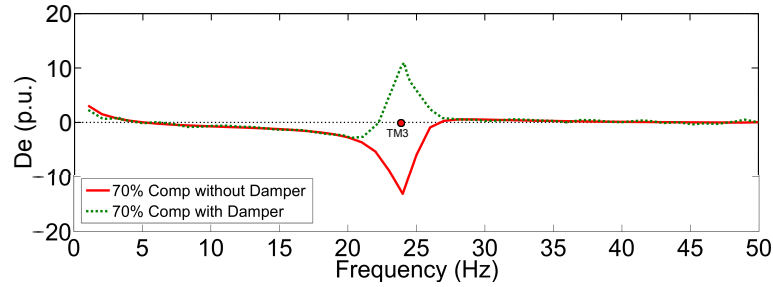
4.3.1 Small-signal Analysis

To investigate the impact of MMD enabled VSC HVDC on the SSR characteristics of the 3GB model, small-signal stability studies in the form of damping torque analysis were undertaken. The overall system electrical damping profile is obtained with and without MMD compensation for both Cases A and B as shown in Figure 4.6. It can be observed that for Case A (see Figure 4.6(a)) and Case B (see Figure 4.6(b)) with MMD the damping profile is considerably improved by acting upon the targeted modes compared to the system without MMD. The modal-filters are designed to stabilise the target torsional modes by introducing positive electrical damping at their frequency modes.

4.3. Damping Scheme: 1 Multi-modal Damper Approach



(a) For 40% series compensation



(b) For 75% series compensation

Figure 4.6: Electrical damping torque profile of 3GB with and without MMD.

4.3.2 Time-domain Simulation and Analysis

To validate the results of the damping torque analysis and subsequent design of the MMD, time-domain simulations of the system shown in Figure 3.11 have been carried out in PSCAD/EMTDC for both Case A and B respectively. These have been performed with and without the MMD enabled VSC controller being active for a small and large disturbances.

4.3.2.1 Small-disturbance Analysis

A small-disturbance is achieved by suitably modifying values of X_c for the 3GB system (see Figure 3.11). Relevant results for such an interference are plotted in Figure 4.7 and Figure 4.8. For Case A, the simulation results for the mechanical shaft torques are plotted in Figure 4.7(a) and (b), with the corresponding electrical torque and network frequency (see Figure 4.7 (c) and (d)). The additional compensation at $t = 4$ s is observed as a small-disturbance, which could initiate SSR as reported in Section. 3.8.2 of Chapter. 3. However, with MMD enabled VSC in operation, this condition does not produce SSR, as evidenced by the decaying torque and frequency responses.

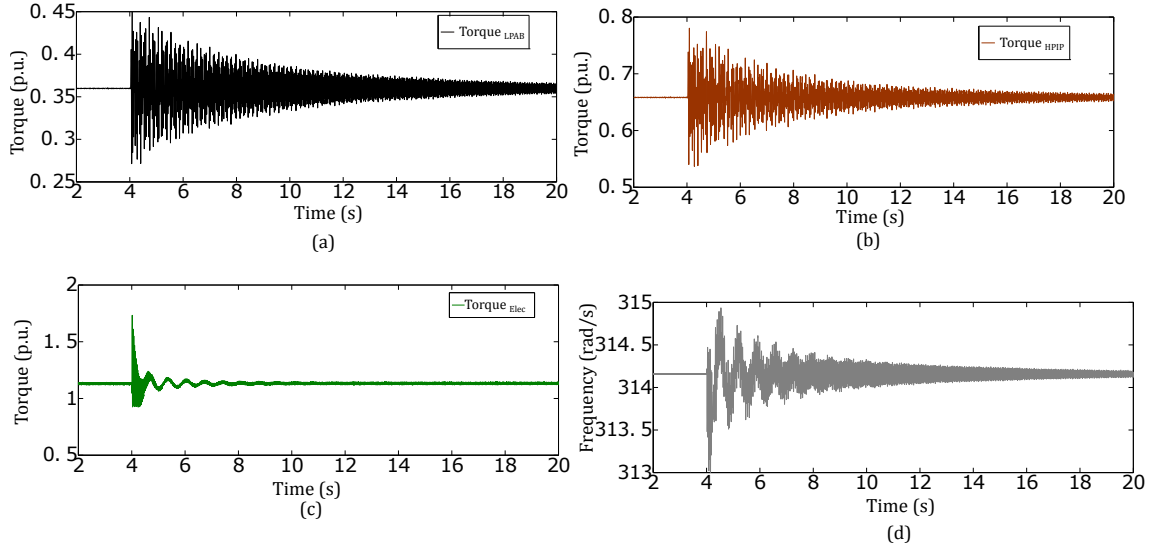


Figure 4.7: Machine dynamics with MMD enabled VSC in operation for Case A. (a) Mechanical Torque LPAB; (b) Mechanical Torque HPIP; (c) Electromagnetic Torque; (d) Frequency.

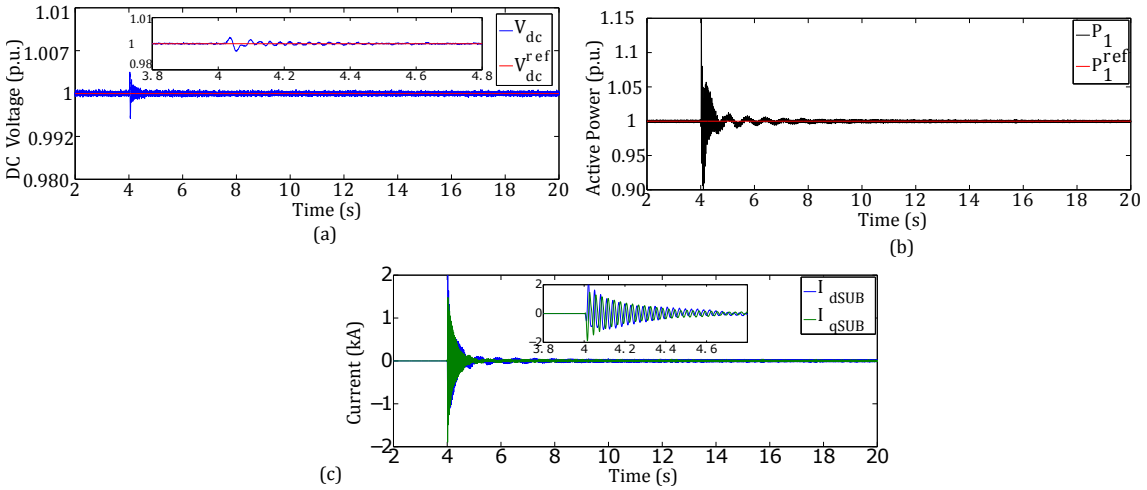


Figure 4.8: VSC HVDC dynamics with MMD enabled VSC in operation for Case A. (a) DC-link voltage; (b) Output power at VSC1; (c) magnitude of dq components of subsynchronous currents.

The VSC output power, DC link voltage and the subsequent current injections have been monitored to evaluate the performance of the MMD enabled VSC and to demonstrate its capability to damp SSR. When the VSC starts injecting upon an SSR event, the DC voltage fluctuates by a lower magnitude, less than 1% from the steady state value (≈ 0.005 p.u.), (see Figure 4.8(a)). However, the active power is modulated around 15% to achieve satisfactory damping as observed in Figure 4.8 (b). The modulation of the active and reactive power components for SSR damping is achieved at same magnitude demonstrated by the SUB current components (I_{dSUB} and I_{qSUB})

4.3. Damping Scheme: 1 Multi-modal Damper Approach

as depicted in Figure 4.8(c)). Moreover, it is to be emphasised that the injected SUB current components before the small-disturbance is zero and as the event happens the component rises to 2 kA (0.5 p.u.), which is then controlled back to zero by MMD enabled VSC.

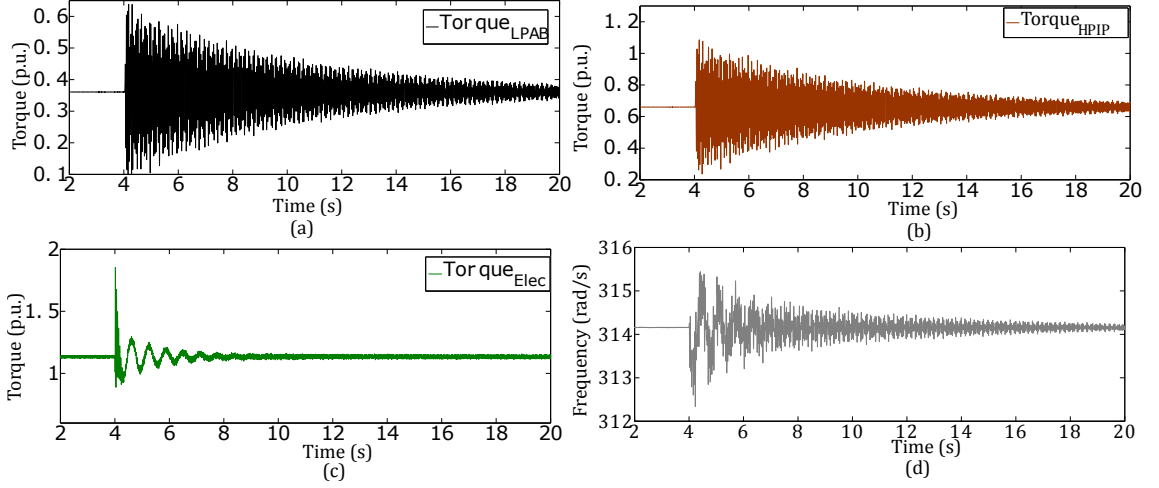


Figure 4.9: Machine dynamics with MMD enabled VSC in operation for Case B. (a) Mechanical Torque HPIP; (b) Mechanical Torque LPAB; (c) Electromagnetic Torque; (d) Frequency.

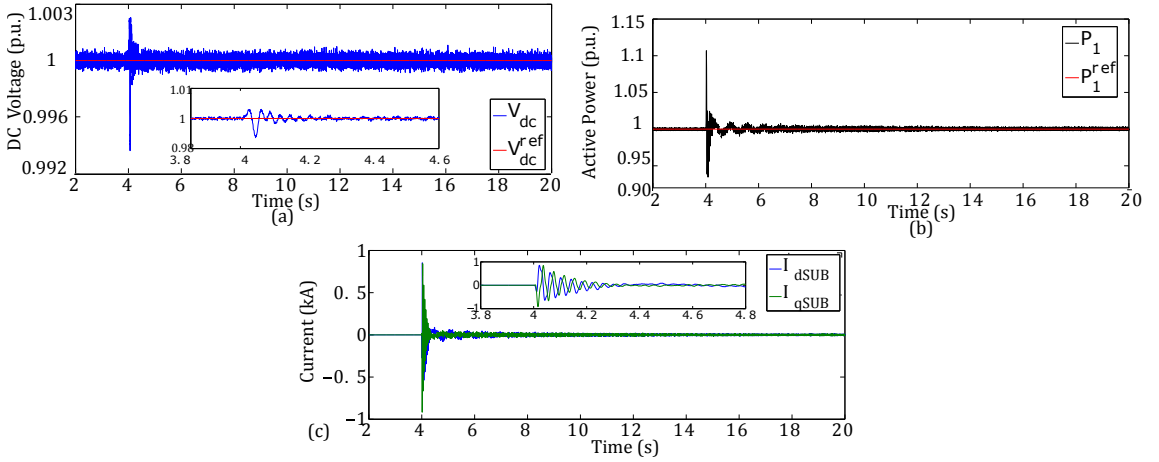


Figure 4.10: VSC HVDC dynamics with MMD enabled VSC in operation for Case B. (a) DC-link voltage; (b) Output power at VSC1; (c) Magnitude of dq components of subsynchronous currents.

The simulation plots for Case B show the same pattern as in Case A as seen from Figures 4.9 to 4.10 apart for the injected current components magnitude and the corresponding modulation of DC power. The VSC active power modulation required to achieve satisfactory SSR damping for Case B is around 10% compared the 15% for Case A (see Figure 4.10(b)) and thus the SUB current magnitude reduces correspondingly (see Figure 4.10(d)). This difference is attributed to the rate at which the mechanical torque oscillations grow subjected to an SSR events (see Figure

3.19).

For completeness, an FFT analysis has been performed to complement the time-domain results for Case A and B. The SSR components for the two cases can be observed from the FFT plots in Figure 4.11. Following the activation of the MMD scheme, only the fundamental frequency is observed with all other components being cancelled out (Figure 4.11(a)-(b)).

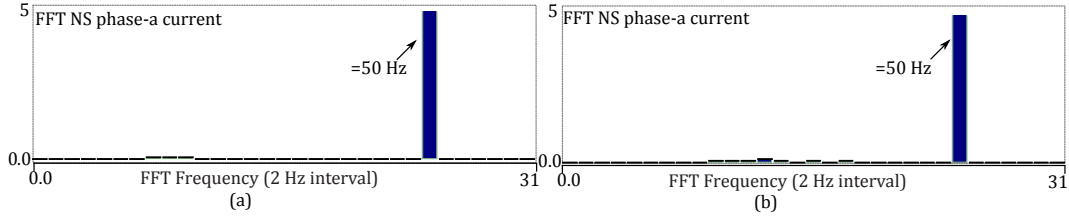


Figure 4.11: FFT (2 Hz interval) of the current of phase a of the synchronous generator when MMD in operation (a) at 40 % series compensation(b) 75% series compensation

4.3.2.2 Large-disturbance Analysis

The operation of the MMD scheme under a large-disturbance is evaluated by exerting a three-phase to ground fault on the series-compensated AC line at $t = 4$ s with a duration of 0.075 s. The compensation level is considered as 75% for the studies performed. Performance of the network without MMD in operation after the fault-clearance shows the existence of SSR evidenced by the fluctuations in torque and DC link variables as depicted in Figure 4.12. However, after the fault-clearance and when the MMD is enabled in VSC1, the rate of convergence of the mechanical torque oscillations improved significantly compared with no MMD as evidenced by Figure 4.12(a)-(b). The DC link voltage and active power follow the same trend as seen from Figure 4.12(c)-(d). This analysis confirms the ability of MMD in achieving satisfactory damping in the event of SSR triggered by transient phenomenon such as three phase-to-ground fault. Moreover, the operational characteristics of the VSC HVDC link under such a scenario are evaluated and the damping performance is achieved successfully using MMD enabled VSC operation.

To conclude, time-domain simulations are consistent with the results obtained from small-signal stability studies and SSR damping using active filters embedded in a VSC HVDC link is a promising, efficient and economical solution compared to other mitigation schemes, whenever a power electronic converter is available as discussed in Table 2.2 [30]. However, to minimise the

4.4. Damping Scheme: 2 Wideband Damper Approach

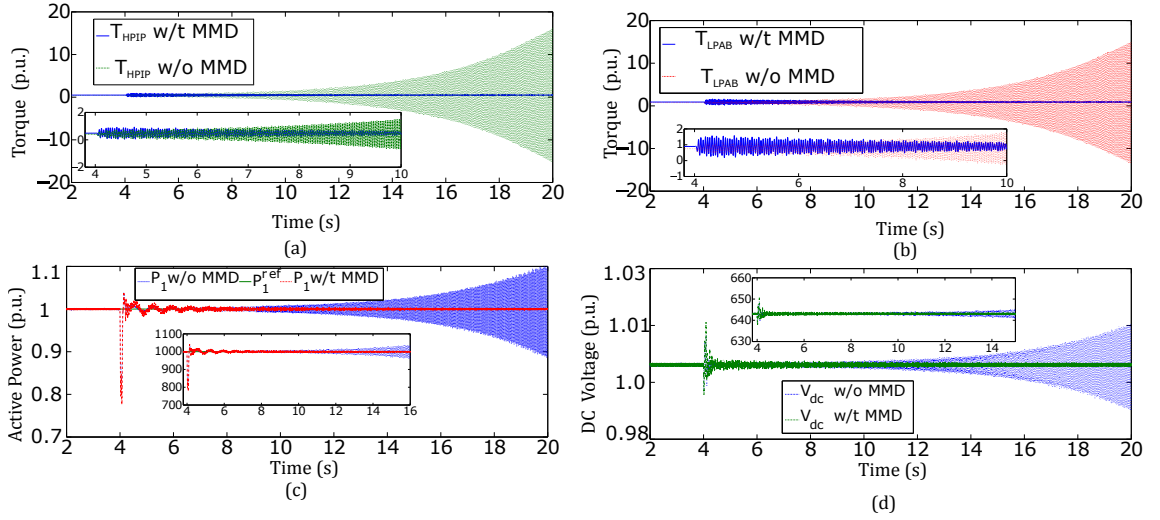


Figure 4.12: Torsional and HVDC dynamics under large-disturbance without and with MMD enabled VSC in operation for Case B. (a) Mechanical Torque HPIP; (b) Mechanical Torque LPAB; (c) Output power at VSC1; (d) DC-link voltage.

impact of multiple filtering stages and thereby reducing the complexity associated with them a wideband filter based damping scheme is introduced in the next section.

4.4 Damping Scheme: 2 Wideband Damper Approach

As evidenced in the preceding section that in addition to the provision of bulk power transfer, an auxiliary control loop embedded in the VSC station can be successfully designed and utilised to damp SSR. To this end, utilising the active filter with the VSC control loops will provide a adequate mitigation of SSR phenomenon in series-compensated AC/DC grids. However, the multi-modal filter presented in the previous section prerequisites the knowledge of the multiple TM frequencies for the effective design and damping. In order to avoid the control complexity associated with the multiple filters and to make the damping process easier and simpler a wideband filter based damper (WBD) is introduced and implemented with the VSC control.

The structure and implementation of the WBD in the VSC current control loop are illustrated in Figure 4.13. As it can be seen the injection point for the damping signal is selected in such way as to achieve a faster mitigation of the negative damping associated with the SSF components of interest upon an SSR event. This is achieved by processing the line current (in dq reference frame) through a wideband compensator ($G_d(s)$) to generate current components I_{dSUB} and

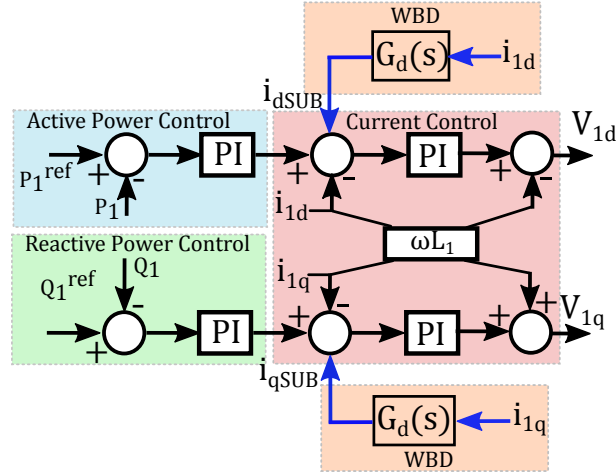


Figure 4.13: Wideband filter based VSC1 control structure.

I_{qSUB} which are used to modulate the real (I_{d1}^{ref}) and reactive current (I_{q1}^{ref}) references of VSC1 as shown in Figure 4.13.

To achieve wideband compensation we utilise a simple second order bandpass filter with transfer function 4.4:

$$G_d(s) = k_{WBD} \frac{s(\frac{\omega_c}{Q})}{s^2 + (\frac{\omega_c}{Q}) + \omega_c^2} \quad (4.4)$$

Where ω_c is the centre frequency of the filter, Q the quality factor and k_{WBD} denotes the filter gain coefficient. For the WBD design when the centre frequency remains fixed the passband range is determined by the quality factor. Thus a higher value of Q leads to narrowband for frequencies and vice versa. This has to be taken into consideration while selecting ($G_d(s)$) for SSR damping and there will be a compromise between the filtering effects and the passband frequencies.

For the 3GB system under investigation, the frequency response of the bandpass filter for different values of Q is shown in Figure 4.14. The centre frequency (ω_c) for WBD should follow the concerned modes and allow zero phase shift around the centre frequency. An assumption for the selection of ω_c is that the SSR modes are identifiable or known in this case TM3 (26 Hz) and TM4 (20 Hz) corresponding to 75 and 40% of series compensation levels. Another notion is that the natural frequencies of the turbine-generators system are constants and are

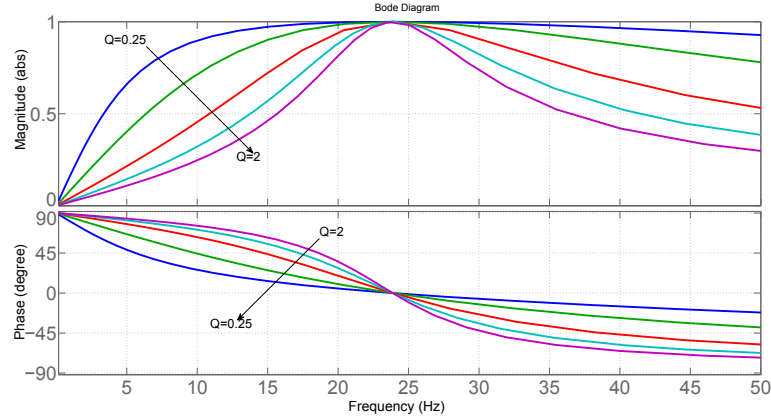


Figure 4.14: Frequency response of band pass filter for the WBD at different values of Q and at $\omega_c=150.72$ rad/s.

typically in the range of 15 to 30 Hz (94 to 188 rad/s), so a middle frequency could be selected as the centre frequency of the WBD. Moreover, the selection of a higher value of Q results in the deviation from the identified modes, or in other terms the desired phase required for damping multiple modes is different at different Q values. This might trigger other TM associated with the turbine-generator when both high Q and high gain k_{WBD} are employed. So in order to maintain a robust damping performance smaller Q and k_{WBD} values are selected.

Using the expressions in 4.4 and according to previous discussions, for achieving satisfactory damping of the 3GB system at 40 and 75% compensation levels, the design parameters of the WBD are chosen as: $Q = 1$, $\omega_c = 150.72$ rad/s ($2\pi \cdot 24$ Hz), $k_{MMD} = 1.5$.

4.4.1 Small-signal Analysis

The overall electrical damping profile with and without WBD enabled VSC in operation for 40% and 75% series compensation levels are shown in Figure 4.15. It can be observed from Figure 4.15(a) that for 40% the negative peak of the electrical torque is compensated over the entire SSF range and also at the critical mode *i.e.* TM4. The corresponding damping profile for 75% of series compensation is plotted in Figure 4.15(b), reveals the successful mitigation of the critical torsional mode *i.e.* TM3 by creating a positive electrical damping. The results verify that the WBD approach is robust enough to stabilize multiple torsional modes associated with the 3GB model by acting upon the entire subsynchronous range.

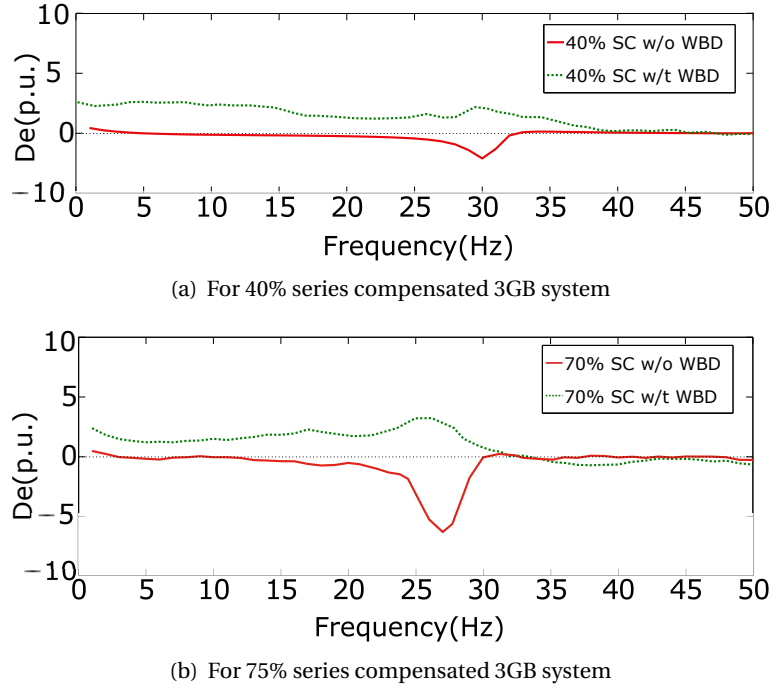


Figure 4.15: Electrical damping torque profile for the 3GB system with and without WBD.

4.4.2 Time-domain Simulation and Analysis

To validate the results of the damping torque analysis and subsequent design of the WBD, time-domain simulations of the 3GB system shown in Figure 3.11 have been carried out in PSCAD/EMTDC. These have been performed with and without the WBD enabled VSC controller being active. The simulation starts in the steady-state with 30% series compensation. This condition does not create SSR, as evidenced by Figure 3.7.1.2 and Figure 4.16. At $t = 4$ s the value of series compensation is modified to 40%, such a disturbance could trigger the SSR if the damping controller is not active (see Figure 3.19). This is consistent with Figure 3.7.1.2, as for 40% compensation the real part of TM4 becomes positive – hence representing an unstable condition. The WBD operation under different power system configurations is investigated by instigating two changes in the compensation levels. The simulation has been repeated with the proposed controller being active, at $t = 4$ s the series compensation level is modified to 40%. Subsequently, the level of series compensation is modified to 75% at 18 s.

As it can be observed from Figures 4.16 and 4.17, since the damping controller is active the change in series compensation is detected and oscillations due to SSR are damped. It can

4.4. Damping Scheme: 2 Wideband Damper Approach

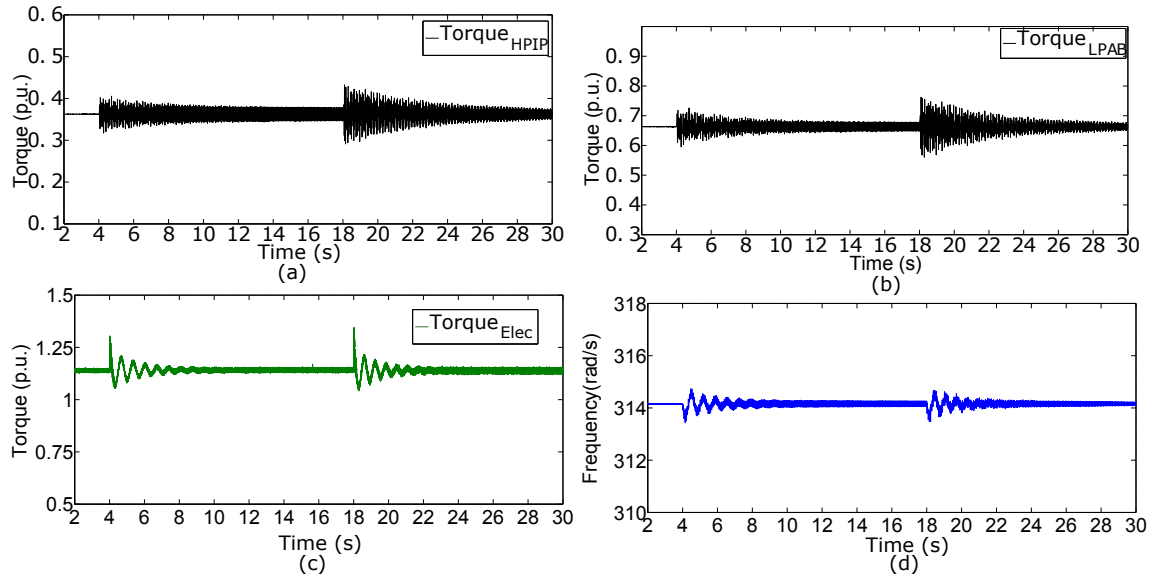


Figure 4.16: Machine dynamics with WBD enabled VSC in operation. (a) Mechanical Torque HPIP; (b) Mechanical Torque LPAB; (c) Electromagnetic Torque; (d) Frequency.

be noticed that mechanical shaft and electrical torque oscillations (Figures 4.16(a) to (c)) and oscillations in the frequency of the phase-a current of the transmission line (Figure 4.16(d)) decay with time. This behaviour demonstrates the effectiveness of the proposed control method.

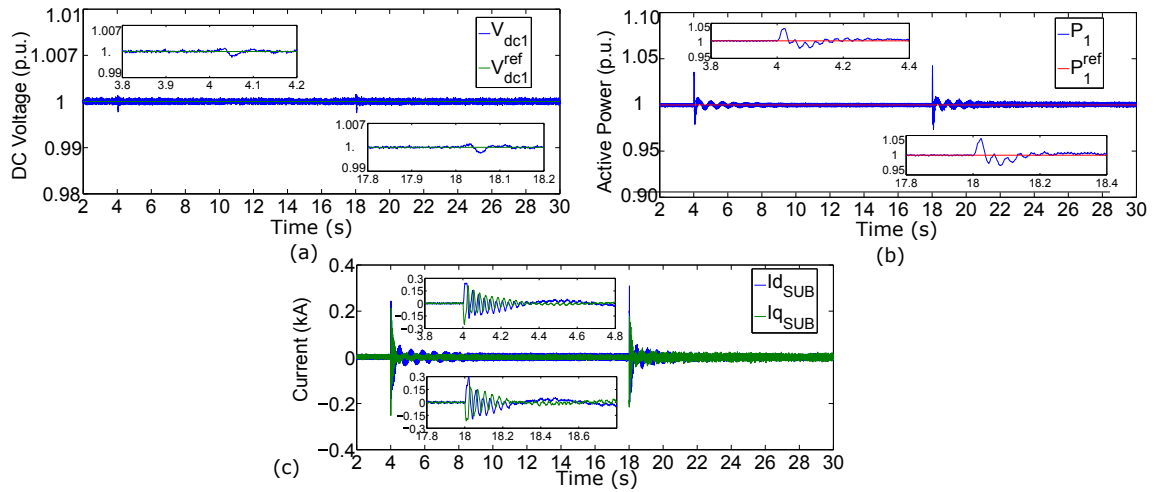


Figure 4.17: HVDC link dynamics with WBD enabled VSC in operation. (a) DC link voltage; (b) Output power at VSC1; (c) Magnitude of dq components of subsynchronous currents.

The VSC output power, DC link voltage and the subsequent current injections are monitored in Figures 4.17(a-c), to evaluate the performance of the WBD enabled VSC capability in providing

the additional service of SSR damping. For the multiple changes in series compensation levels the VSC adapts well by injecting the damping signal upon an SSR event, the fluctuations in DC voltage is less than 0.5% (*i.e.* ≈ 0.004 p.u.) from the steady state value (see Figure 4.17(a)). The active power is modulated around 5% to achieve satisfactory damping as observed in Figure 4.17(b) for both cases. The modulation of the active and reactive power components for SSR damping is achieved at same magnitude demonstrated by the SUB current components (I_{dSUB} and I_{qSUB}) as depicted in Figure 4.17(c)). Moreover, it is to be emphasised that the injected current components before the small-disturbance is zero and as the event happens the component rises to 0.25 kA (0.12 p.u.), which is then controlled back to zero by WBD enabled VSC. Using this method the modulations in the DC powers and subsequent DC voltage fluctuations are reduced substantially as compared to MMD approach, resulting in a satisfactory damping within converters capability.

As discussed the active filtering schemes utilising VSC's controllability is proven to be effective, simple and easier to implement damping solutions for SSR mitigation. However, the design of filters prerequisites the knowledge of natural frequencies of the turbine-generator shaft system and thus a real-time damping in response to system changes is not viable. To address these shortcomings a real-time frequency estimation and damping approach are introduced and discussed in the next section.

4.5 Damping Scheme: 3 Real-time Damper Approach

The filter-based SSR damping schemes discussed in the previous sections are effective only for the operating point where the design of filter is optimized and its response could be compromised by the multiple modes of frequencies such as in the case for SSR. Another aspect which demands attention is the uncertainty in the mechanical modes of turbo-generator shafts and associated information such as inertia constants, damping coefficients and torsional stiffness. These data are usually not available or missing, affecting the effectiveness of the filter approach and limits the adaptability of previously proposed damping schemes to multiple modes of oscillations [21]. Real-time estimation and tracking can overcome this uncertainty by identifying the subsynchronous electrical mode at any series compensation level and act on it to avoid interactions with the mechanical shaft modes irrespective of their values. To contribute to this

effort, in this section we propose a real-time damper (RTD) or an adaptive subsynchronous frequency damping controller (SSFDC), capable of estimating and damping the SSF component regardless of the configuration of the power system.

To achieve this, the SSFDC shown in Figure 4.18 is proposed. It is formed by a SSF tracker (SSFT), which estimates and tracks the real-time frequency component in the line current upon an SSR event and by a SSF damper (SSFD), which utilises the tracked frequency component to generate a 180° anti-phase signal at the point of common coupling (PCC) with the VSC station. In general, the voltage signal with subsynchronous components can be represented as :

$$\begin{aligned}
 s(t) &= A_1 \sin(2\pi f t + \theta_1) + \sum_{k=2}^m A_k \sin(2\pi f_k t + \theta_k) \\
 &= A_1 \sin(2\pi f t + \theta_1) + \sum_{k=2}^m [A_k \sin(2\pi f_k t) \cos(\theta_k) + A_k \cos(2\pi f_k t) \sin(\theta_k)] \\
 &= A_1 \sin(2\pi f t + \theta_1) + \sum_{k=2}^m [A_{k1} \sin(2\pi f_k t) + A_{k2} \cos(2\pi f_k t)] \\
 &= x(t) + g(t).
 \end{aligned} \tag{4.5}$$

where f is the fundamental frequency of the voltage signal, A_k and θ_k are the amplitude and phase angle of the k -th component, which includes subsynchronous (SUB) and super-synchronous (SUPER) components, and m is the total number of torsional modes. In 4.5, $x(t)$ is the fundamental frequency signal and $g(t)$ encapsulates the SSF component of $s(t)$. As explained in [136], the network exhibits a small positive damping for frequencies above the fundamental. Therefore, the SUPER component is not of interest.

The SSFDC aims to cancel $g(t)$ from $s(t)$ to obtain $x(t)$. In the proposed method, the frequency component of $g(t)$ is first detected and tracked upon occurrence of SSR. Then a compensation signal $g'(t)$ is generated to cancel $g(t)$.

4.5.0.1 Subsynchronous Frequency Tracker

During an SSR event, the frequency of the line current will deviate from its nominal value and will begin to oscillate. The deviation in line current upon an SSR event occurs in a faster rate as compared to other local signals (voltage, power) which makes it a suitable candidate for input signal. When the frequency of oscillation (f_{osc}) coincides with the complement of the frequency

of a generator shaft torsional mode (f_{tm}), the oscillations will be sustained [26, 27]. An SSFT can be designed to identify and track f_{osc} .

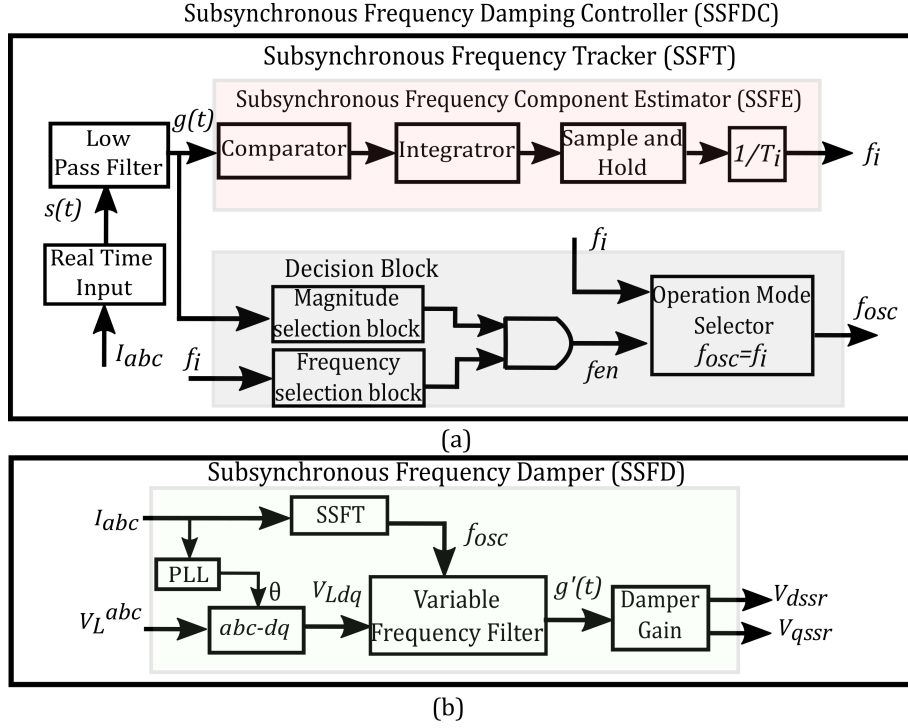


Figure 4.18: Block diagram of SSFDC: (a) SSFT (b) SSFD.

As seen from Figure 4.18(a), the SSFT is comprised mainly of an SSF component estimator (SSFE) and a decision block. The line current is fed to the SSFE through a low pass filter, which isolates $g(t)$ and eliminates the voltage driving frequency component $x(t)$ at (50 Hz). This is the input signal to the SSFT block, which through a series of transformations (see Figure 4.18(a)) identifies the SSF component f_i to avoid a tracking operation when no oscillation is observed. An operating mode selector is utilised to enable the output of SSFT, which is the tracked oscillation frequency f_{osc} . It should be emphasised that the tracking of f_{osc} could be done regardless of the configuration of the power system since the natural frequencies of a turbo-generator shaft can be considered as constant [26].

4.5.0.2 Subsynchronous Frequency Damper

The second stage in the SSFDC design process is to generate signal $g'(t)$ to eliminate the SSF component (f_{osc}). To serve this purpose, the SSFD shown in Figure 4.18(b) has been designed

and implemented. It is formed by a variable frequency filter and a damper gain. The output of the SSFT is used as the central frequency of the filter which has a basic second-order resonant filter structure, whose input is the dq voltage at the PCC - obtained using a suitable reference frame transformation block and synchronized using a phase-locked loop (PLL). The filter outputs the target signal fed to the damper gain block to produce a 180° phase shift to create $g'(t)$. Following a coordinate transformation, damping components (v_{dssr}) and (v_{qssr}) are generated. These are added to the primary control voltage reference signals v_{d1} and v_{q1} of VSC1 (see Figure 4.19). The resultant voltage at the converter terminal will damp SSR in the AC network by effectively eliminating $g(t)$ in $s(t)$.

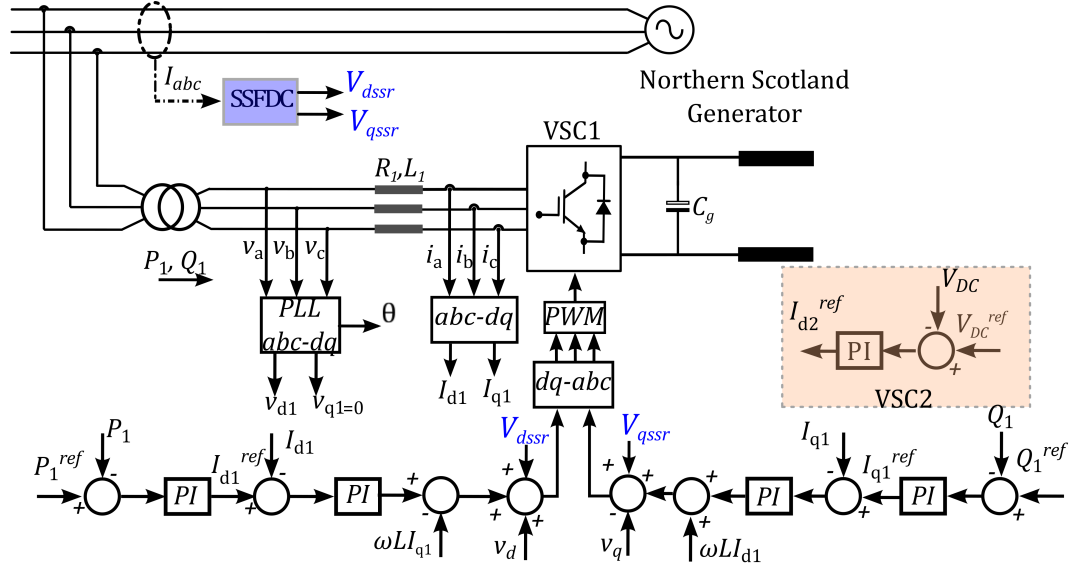


Figure 4.19: Rectifier VSC with main and auxiliary control loops.

4.5.1 Time-domain Simulation and Analysis

Time-domain simulations were carried out on the test system to validate the effectiveness of the SSFDC to provide damping at selected SSFs and to assess its impact on the converter performance. For comparison purposes, the performance of the integrated 3GB AC/DC system shown in Figure 3.11 was evaluated with and without the use of an SSFDC. To assess system stability, two scenarios have been considered:

- Case A: Change in series compensation level from 30 to 40%.

- Case B: Change in series compensation level from 30 to 75%.

In both cases, the change in series compensation occurs at $t = 4$ s into the simulation. This is achieved by suitably modifying the value of X_C .

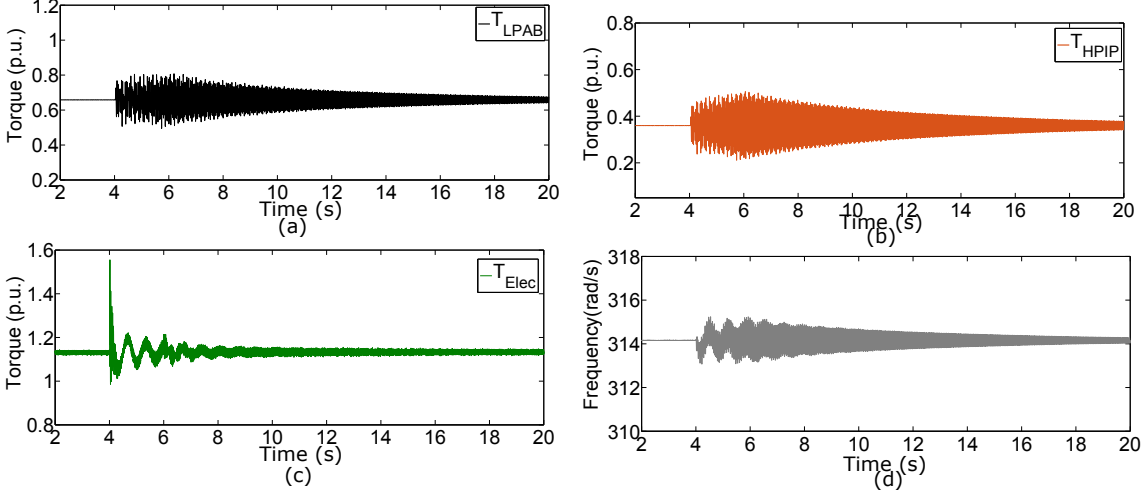


Figure 4.20: Machine dynamics with SSFDC enabled VSC in operation for Case A. (a) Mechanical Torque HPIP; (b) Mechanical Torque LPAB; (c) Electromagnetic Torque; (d) Frequency.

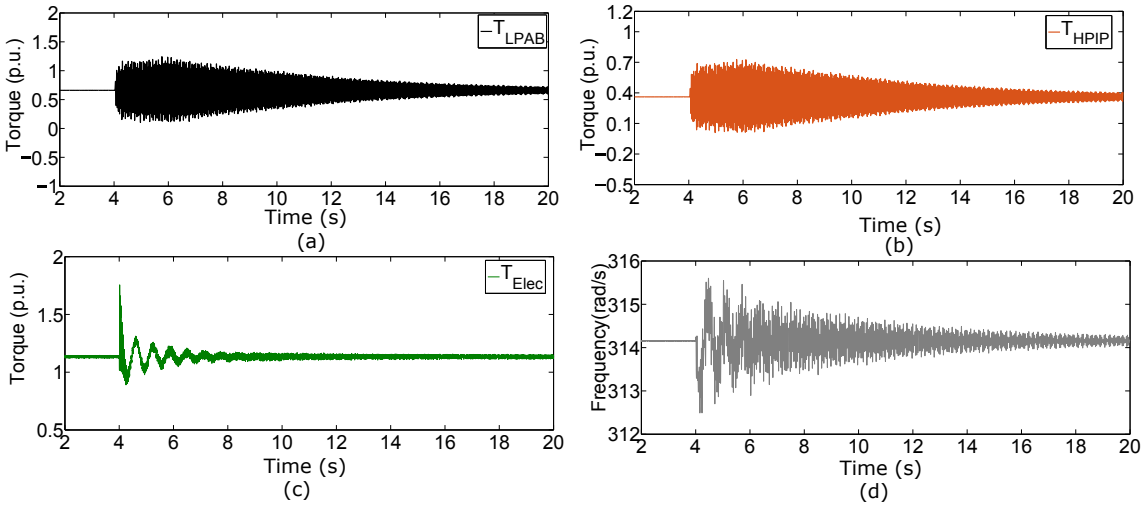


Figure 4.21: Machine dynamics with RTD enabled VSC in operation for Case B. (a) Mechanical Torque HPIP; (b) Mechanical Torque LPAB; (c) Electromagnetic Torque; (d) Frequency.

The relevant plots for the 3GB system with the control loop of VSC1 upgraded with SSFDC is shown in Figures 4.20 to 4.23. The network SSF component f_{osc} for Cases A and B is successfully identified as shown in Figures 4.22(c) and 4.23(c). The dominant modes for Cases A (≈ 20 Hz) and B (≈ 26 Hz) are tracked in less than ≈ 2 s using the SSFT. Figures 4.20 and 4.21 show

the selected torque responses of the NS generator and frequency of the phase a current. An initial transient caused by the change in series compensation results in a frequency deviation from its nominal value and an increase in torque oscillations. Once the SSFDC operates, the shaft oscillations are damped out and steady-state operation is reached. These plots reveal the successful damping of multiple torsional modes—afforded by a correct SSF component tracking.

Figures 4.22 and 4.23 show the responses of the VSC. The contribution of the SSFDC is evident and the stable performance of the converter is reflected in the DC voltage and power plots (see Figures 4.22(a-b) and 4.23(a-b)). Initially, DC voltage (V_{dc}) and active power (P) deviate from their nominal values, but once the SSFDC operates the oscillations disappear and steady-state is reached within seconds. The results reveal the satisfactory damping performance of the SSFDC enabled VSC where the network SSF components interacting with the mechanical modes are identified, tracked and damped in less than 3s.

The modulation of the active and reactive power for SSR damping is achieved at same magnitude demonstrated by the SUB current components (I_{dSUB} and I_{qSUB}) as depicted in Figure 4.22(d) and 4.23(d). Moreover, it is to be emphasised that the injected current components before the small-disturbance is zero and as the event happens the component reaches 1 kA (0.25 p.u.) and starts to increase, but once the SSFDC starts operating the current begins to settle down and reaches zero within seconds.

The results presented in this section show that the active damping compensation afforded by the proposed SSFDC stabilizes the system. A good performance is achieved for different modes of oscillation. Moreover, the additional support provided by VSC1 is within the converter capability and thus does not affect the normal operation of the HVDC link.

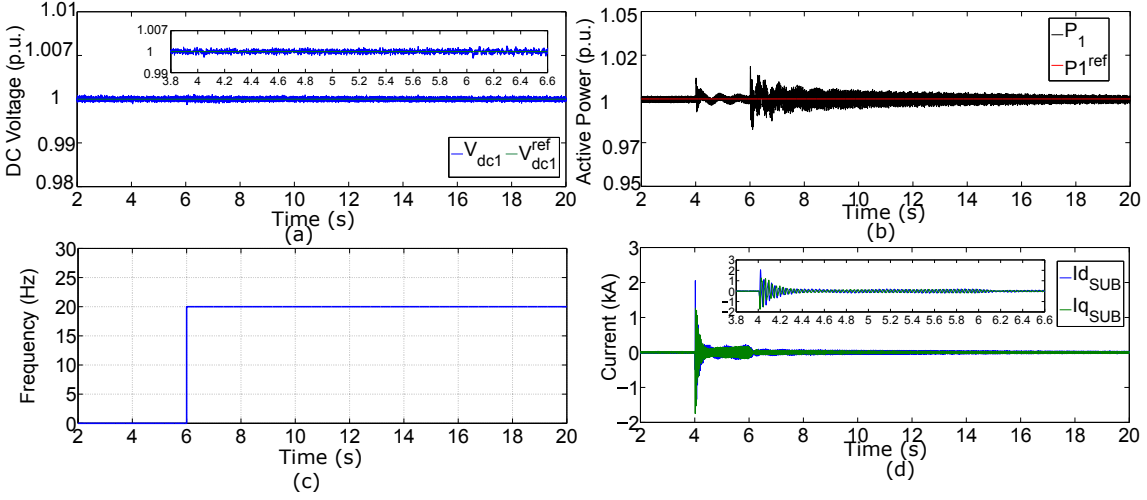


Figure 4.22: SSFDC enabled VSC operation for Case A. (a) DC-link voltage; (b) Output power at VSC1; (c) Performance of tracking network oscillation frequency (f_{osc}); (d) Magnitude of dq components of subsynchronous currents.

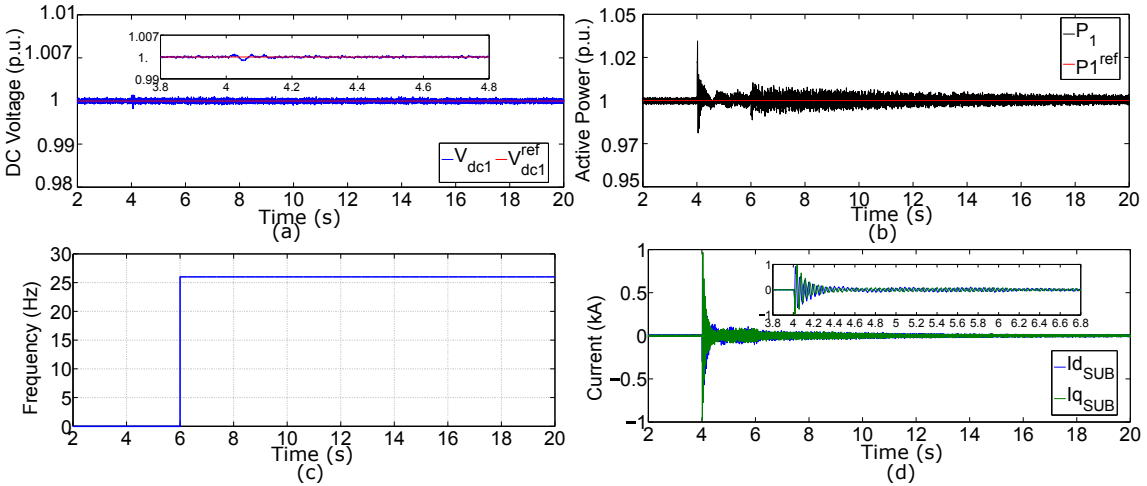


Figure 4.23: SSFDC enabled VSC operation for Case B. (a) DC-link voltage; (b) Output power at VSC1; (c) Performance of tracking network oscillation frequency (f_{osc}); (d) Magnitude of dq components of subsynchronous currents.

4.6 Summary

Methods for extracting the subsynchronous components of the current flowing in a transmission line at different series compensation levels has been presented in this chapter. This has been embedded in a VSC HVDC station as a supplementary control loop to damp SSR upon occurrence. As it has been evidenced, if the shaft torsional modes of the synchronous generators are known, the design of the proposed active filter based damping scheme can be easily carried

out. However, to account for the uncertainties pertained with the mechanical shaft data an adaptive network frequency estimation and damping schemes based on it has been proposed and implemented. This can be extended to any transmission topology. The effectiveness of the scheme has been assessed in the 3GB system, which has been upgraded with a point-to-point VSC HVDC link. This AC/DC system has been assessed through damping torque analysis for small signal-stability assessment with and without the proposed active filter schemes .

The test system, together with the SSR damping controller, have been implemented in PS-CAD/EMTDC to perform time-domain simulations. The damping torque analysis and the results obtained through simulations agree on well. More importantly, the SSR damping controller proposed in this work is effective for a broad series compensation range. Experimental validation of the proposed methods will be devised and implemented in the next chapter.

5 Hardware-in-the-loop Experimental Tests for SSR Damping Using VSC HVDC

5.1 Introduction

This chapter presents a real-time experiment platform to test and validate the SSR damping schemes developed in Chapter 4. The experimental test set-up consists of a Real-time Digital Simulator (RTDS), where the 3GB series-compensated AC system is modelled. The VSC HVDC link was implemented on a physical test-rig, with the VSC controllers being realised in a dSPACE DS1005 unit. The data exchange between the two platforms (RTDS and dSPACE) were achieved using analogue and digital signals to form a real-time hardware-in-the-loop (RT-HiL) configuration.

The active filtering schemes for SSR damping proposed in Chapter 4 were implemented with the physical VSC controllers and a series of experimental tests were performed with and without the controllers in operation. Finally, a comparison is drawn between the simulation and experimental results.

5.2 Real-time Hardware-in-the-loop Experimental Test Set-Up

The main components of the RT-HiL experimental platform are shown in Figure 5.1. These comprise of a real-time digital simulator (RTDS), a grid simulator (GS), DC network cabinet and an VSC test-rig. The DC network cabinet and the physical VSC test-rig represents the scaled down model of the simulated VSC HVDC link.

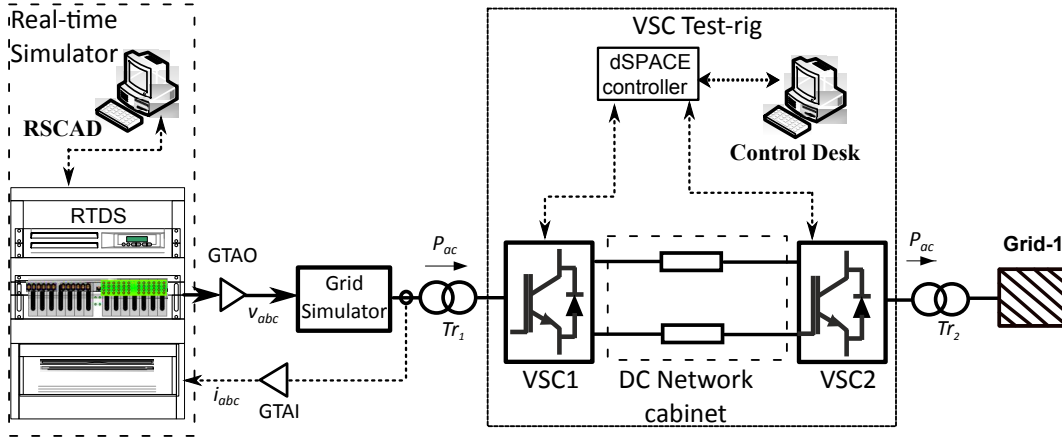


Figure 5.1: RT-HiL general diagram.

5.2.1 Real-time Simulator

As shown in Figure 5.2(a), the RTDS is used for real-time and digital electromagnetic transient power system simulations. The power system components can be modelled in the RTDS using the graphical user interface RSCAD. In this chapter for performing the RT-HiL tests, the 3GB system were modelled using the RSCAD software of the RTDS. The model incorporates the three machine AC system with the multi-mass turbine-generator and series-compensated transmission line modelled in RSCAD platform of the RTDS. This network can be easily expanded to represent generators, loads, transformers and transmission lines of more complex AC systems. The high voltage value was converted to a low voltage suitable for the GS (and the HVDC test rig) through Analogue Output (GTAO) cards of the RTDS. A controlled current source is connected at Bus 1 (see Figure 5.4) and the GS outputs were used to control the current injection through the Analogue Input (GTAI) cards of the RTDS firmware. The technical parameters of the RTDS used in this work are included in Table 5.1. The 3GB AC system model built in RSCAD is provided in Appendix. E.2.

5.2.2 AC Grid Simulator

The main function of the grid simulator (GS), as shown in Figure 5.2(b) is to produce a three-phase mains supply voltage from the GTAOs of the RTDS. This is achieved using a four-quadrant amplifier rated 2 kVA and 270 V (L-G rms). For this study, the output of the GS is connected to VSC1 of the HVDC test rig. To close the loop between RTDS and HVDC rig, the three-phase

5.2. Real-time Hardware-in-the-loop Experimental Test Set-Up

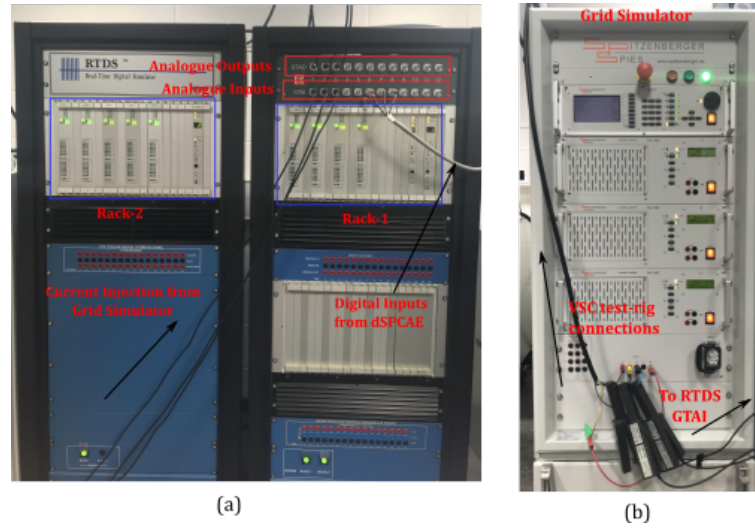


Figure 5.2: Real-time set-up. (a) RTDS; (b) Grid simulator.

line current is tapped and fed to the GTAI of the RTDS. The technical parameters of the GS are provided in Table. 5.1.

5.2.3 VSC HVDC Test Rig Configuration

The HVDC test-rig is formed by two 2-level VSCs, two transformers, DC network cabinet and a dSPACE controller as shown in Figure 5.3. The VSC's are operated at a rated power of 1 kW, 140 V AC and 250 V DC (see Figure 6.11). Through the GS, a conversion ratio of 400 kV / 140 V is achieved, which means that an AC voltage of 140 V in the test-rig represents 400 kV in the high voltage system. The output voltage of the GS was controlled using an autotransformer and is connected to VSC1, while VSC2 is charged from the laboratory 400 V grid through a 400/140 V transformer (see Figure 5.3 (a)). The DC network cabinet uses a scaled down DC cable parameters, which includes DC inductors and capacitors and distributed π models of the DC cables. Its main purpose is to connect the two VSC's to form the VSC HVDC link configuration, for the study presented here the DC lines are represented using DC inductors.

The dSPACE unit acquires data and monitors system states of the rig and is also used to control each VSC. The digital signals are transmitted to and from the RTDS through the interface board as shown in Figure 5.3(b). Hardware parameters for the VSC HVDC rig can be found in Table. 5.1.

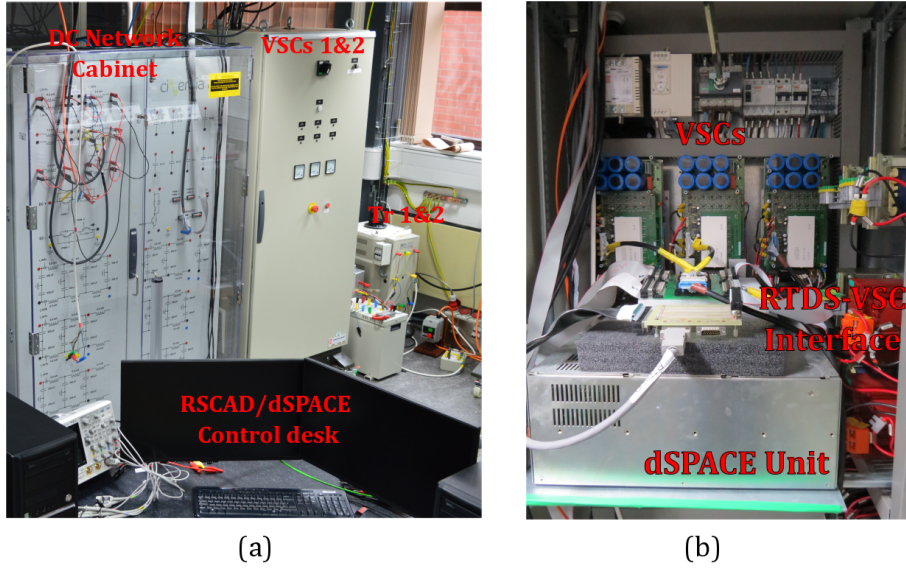


Figure 5.3: VSC HVDC test rig configuration. (a) VSC HVDC set-up; (b) VSC's and dSPACE unit,

5.3 Implementation of RT-HiL Test

The connection of different components to form the final RT-HiL configuration to test and validate the SSR damping schemes developed in Chapter 4 is depicted as a block diagram in Figure 5.4. The 3GB series-compensated AC/DC system, without the VSC HVDC link in high voltage (400 kV) is model in RSCAD solver and is represented as AC grid 2. The PI control parameters used for the RT-HiL tests are provided in Appendix. D.2

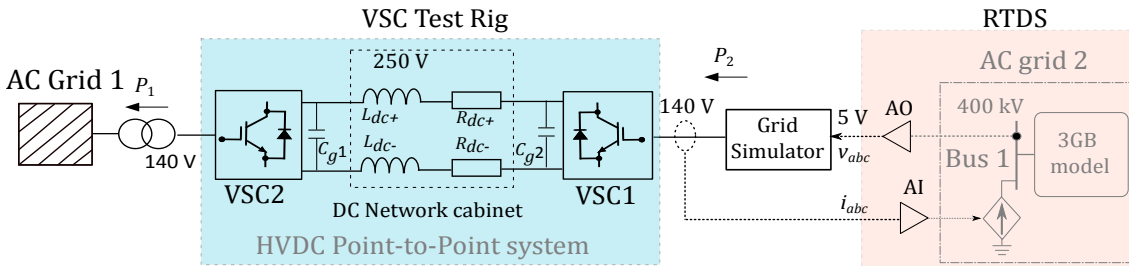


Figure 5.4: RT-HiL implementation diagram.

The voltage at Bus 1 (400 kV) is fed as analogue signals to the GS through the GTAO (see Figure 5.5(a)) and receives the current measurements from VSC1 as analogue signals through the GTAI (see Figure 5.5(b)) card of the RTDS firmware. A lead-lag compensator is designed and implemented in RTDS to avoid the transmission delay in the current measurements. Two VSCs were used in this work with VSC1 operating in active and reactive power control mode and VSC2

5.4. Experimental Results: Primary Control System Operation

Table 5.1: Specifications and parameters of the RT-HiL test-rig

Devices	Specifications	Rating
Converters	Rated power	1 kW (1 p.u.)
	Rated ac voltage	140 V
	Rated dc voltage	250 V (1 p.u.)
	Topology	two-level, symmetrical monopole
AC inductors	L_{g1}, L_{g2}	2.2 mH
DC lines	L_{dc}	2.4 mH
	R_{dc}	0.26 Ω
DC capacitors	C_{g1}, C_{g2}	1020 μF
Control system	dSPACE DS 1005/ControlDesk 3.2 (SIMULINK interface)	
Real-time simulator	RTDS/RSCAD, Racks: 2. Cards: 2 GTWIE, 4 PB5 (2 GTDI, 2 GTDO, 2 GTAI, 2 GTAO, 2 GTNET)	

in DC voltage and reactive power control mode, same as the simulation study. The SSR damping controllers were implemented with VSC1 and the current measurements from the GS terminal (i_{abcinj}) are fed back into a controllable current source in the RSCAD model, as shown in Figure 5.4 to close the loop. For completeness on the hardware implementation the detailed high-level RT-HiL set-up diagram (see Figure E.5) with connection configuration for the tests presented in this chapter is provided in the Appendix E.3.

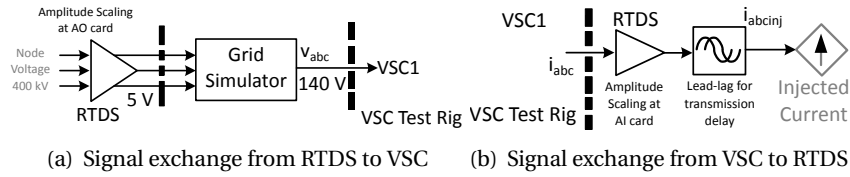


Figure 5.5: RTDS and VSC test rig interface.

5.4 Experimental Results: Primary Control System Operation

To validate the primary control functions of the VSC HVDC link, the RT-HiL test platform developed and implemented in Sections. 5.2 and 5.3 were tested through time-domain experiments. The relevant AC and DC network results are shown in Figure 5.6. An HVDC power (P_{dc}) set-point change is order at $t = 3.5$ s from 0.8 to 1 p.u. as shown in Figure 5.6(a). The DC voltage (V_{dc})

fluctuation during such a transition is depicted in Figure 5.6(b). The mechanical shaft torque and the AC line current responses to the HVDC power set-point change are plotted in Figures 5.6(c) and 5.6(d). The variation of DC power flow is reflected in the AC network however, causing a modest change and the system remains stable evidenced by the plots in Figure 5.6. The experiment results (see Figure 5.6) shows good agreement with the simulation results in Figure 4.2 both in performance and dynamics of the measured variables. The experiment test exercised in this section demonstrated the efficacy and ability of the RT-HiL platform for AC/DC system dynamic studies.

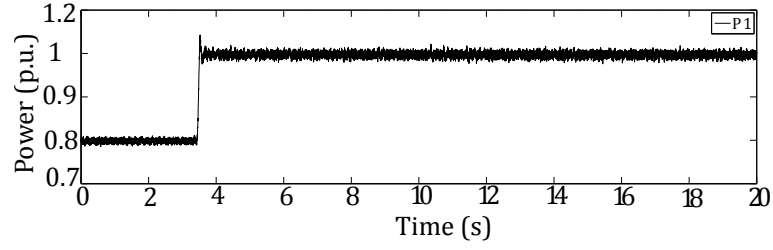
5.5 Experimental Results: SSR Damping Schemes

To investigate the robustness and performance characteristics of the proposed SSR damping schemes, experiments were carried out on the RT-HiL platform. The tests aim to validate the effectiveness of the proposed controllers to provide positive damping at the selected and whole range of subsynchronous frequencies (SSFs). Furthermore, it helps to validate the controller implementation and its impact on the converter performance. The data for RT-HiL tests is acquired from RSCAD and the dSPACE controller and are plotted in MATLAB. Four cases were tested:

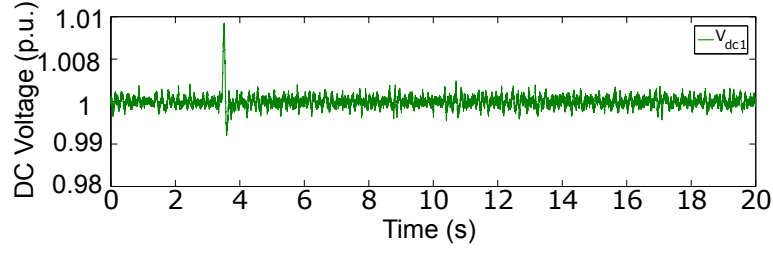
- Integrated AC/DC system without dampers.
- Integrated AC/DC system with Multi-modal Damper.
- Integrated AC/DC system with Wideband Damper.
- Integrated AC/DC system with Real-time Damper.

The results reported in the following sections are for the operational characteristics of the series-compensated AC/DC 3GB system under two network reconfiguration scenarios:

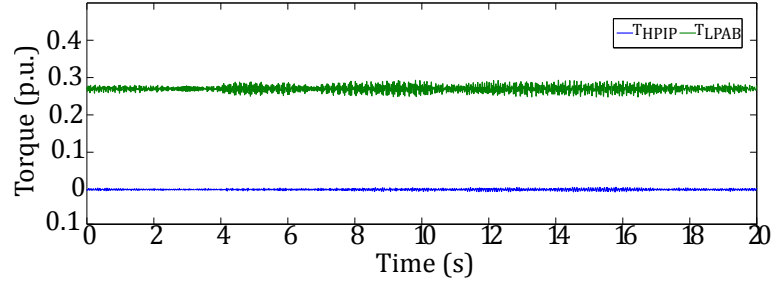
- Case A: Change in series compensation level from 30 to 40%.
- Case B: Change in series compensation level from 30 to 75%



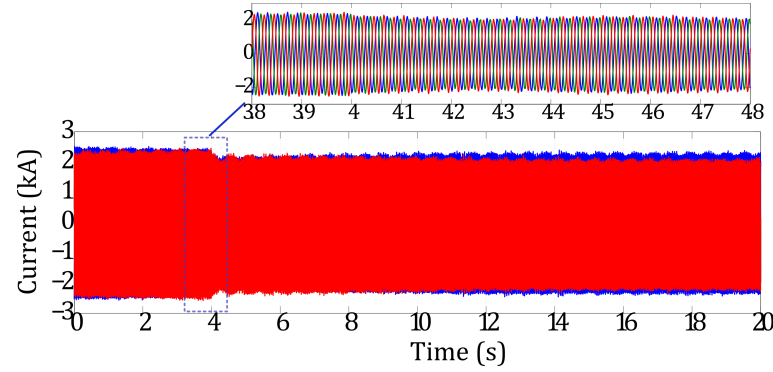
(a) DC link power response to a step change.



(b) DC voltage variation to a step change.



(c) Mechanical torque dynamics.



(d) AC current response to a step change of DC power.

Figure 5.6: HiL response to primary control of VSC HVDC link.

In both cases, the change in series compensation occurs at $t = 4$ s in the real-time simulation. This is achieved by suitably modifying the value of series compensation X_c of the AC transmission line modelled in RTDS.

For all cases, the damper schemes have been implemented with the Simulink based VSC control system and is updated into the physical VSC through the dSPACE controller.

5.5.1 Integrated AC/DC System without Damping Controllers

The operation of the AC/DC network is tested to see the effect of series compensation levels on the system stability. Figures 5.7 to 5.9 show the operational characteristics of the network for Cases A and B without the SSR dampers in operation.

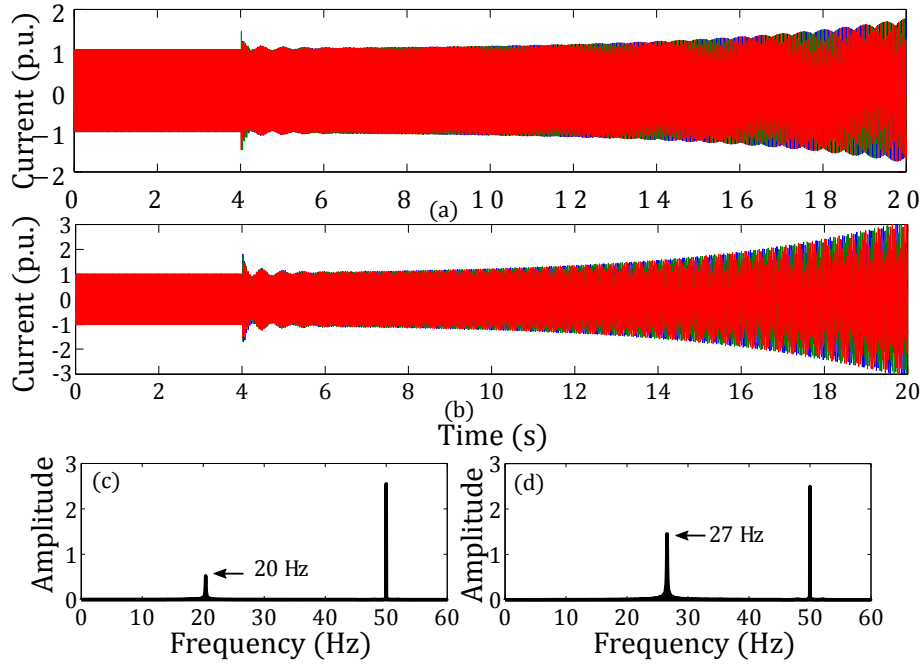


Figure 5.7: Experimental results (RTDS signals) without SSR dampers. (a) Line current measured at Bus1 for Case A; (b) Line current measured at Bus1 for Case B; (c) Spectrum of a-phase output current for Case A; (d) Spectrum of a-phase output current for Case B.

The occurrence of SSR is evidenced in Figure 5.7(a) and (b) by the rise in line current measured at Bus 1 of the 3GB system (see Figure 3.11) from its rated value. The dominant frequency component for the new compensation values (i.e. (≈ 20 Hz) for 40% and (≈ 27 Hz) for 75% compensation) are evidenced in Figures 5.7(c) and (d) obtained following a Fast Fourier Transform (FFT) spectrum analysis. The information provided by Figure 5.7 agrees well with the eigenvalue analysis presented in Section 3.7.1.2, that 40% compensation level excites torsional mode TM4 (≈ 30 Hz), which is the complement of the network mode (≈ 20 Hz), and 75% compensation interacts with torsional mode TM3 (≈ 23 Hz), which is the complement of the network mode (\approx

27 Hz). Furthermore, it is clear from the plots that without proper control methods the network subsynchronous frequency (SSF) component increases in magnitude and the system becomes unstable.

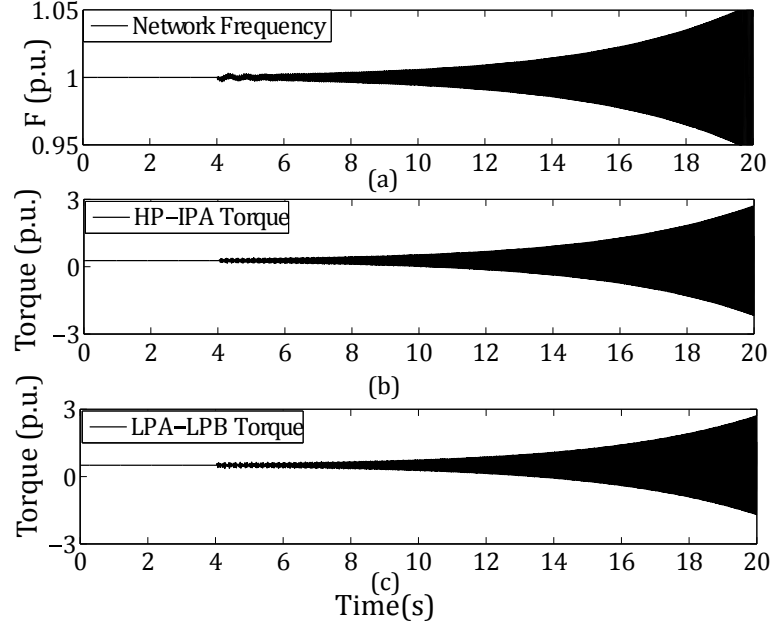


Figure 5.8: Experimental results (RTDS signals) of 3GB system without SSR dampers for Case A. (a) Frequency of phase a current of the Northern Scotland generator; (b)-(c) selected torque interactions in the multi-mass shaft of the Northern Scotland generator.

Figure 5.8 shows the frequency and torque responses for Case A only. Since the plots for Case B exhibit a similar behaviour no further discussion is warranted. Figure 5.8(a) shows the network frequency, which has a nominal value before the SSR event but starts deviating from 1 p.u. (50 Hz) due to SSR following the change in series compensation. Figures 5.8(b)-(d) depict selected torque responses in the shaft of the NS generator.

Figure 5.9 shows the relevant measured DC parameters, V_{dc} , and P_{dc} of VSC1 at Bus 1. The results reveal that these converter variables are building up in magnitude. If no corrective measures are taken these oscillations will surpass the converter limits. The converter instability is reflected in V_{dc} and P_{dc} , indicated by building oscillations, (see Figure 5.9(a)-(b)). In all cases, the oscillations build up over a long period (≈ 16 s), attributed by the natural result of the low-frequency instability associated with SSFs [95].

As seen, the AC/DC system is unstable as predicted by the analysis summarised by Figures

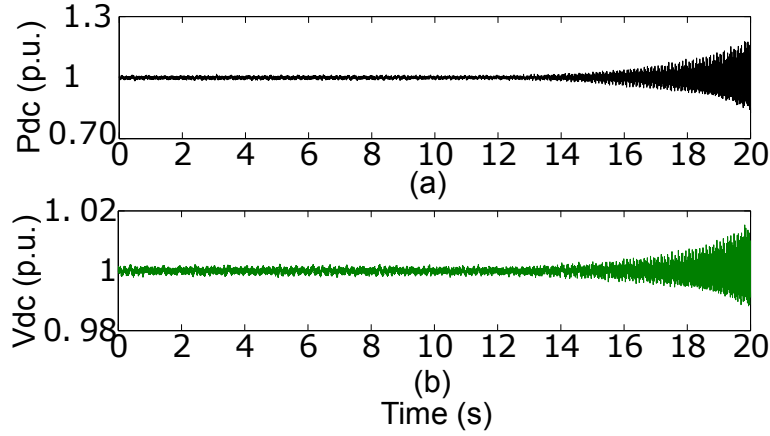


Figure 5.9: Experimental results (HVDC rig signals) for Case A. (a) Output power at VSC1; (b) DC-link voltage.

3.13 and 3.16 and the time-domain simulation tests. The VSC without the supplementary controllers does not have a significant contribution to SSR damping. Furthermore, without proper countermeasures, the HVDC link operation could be compromised.

5.5.2 Integrated AC/DC System with Multi-modal Damper

To validate the time-domain simulation results of the multi-modal damper (MMD) enabled VSC operation during SSR damping, an RT-HiL test is performed. The experimental tests aim to evaluate the converter performance and capacity in achieving adequate damping at selected subsynchronous frequencies.

To create a small-disturbance in the 3GB test system, the series capacitor X_c value is modified as described in Section. 5.5. The relevant results for such an interference are plotted in Figures 5.10 and 5.11. For Case A, the simulation results for the mechanical shaft torques are plotted in Figure 5.10(a) and (b), with the corresponding electrical torque and network frequency plots in Figure 5.10(c) and (d). The additional compensation at $t = 4$ s is observed as a small-disturbance, which initiates SSR as reported in Section. 3.8.2 of Chapter. 3. However, with MMD enabled VSC in operation, this condition does not produce SSR, evidenced by the decaying torque and frequency responses

The relevant DC link results have been plotted in Figure 5.11, to evaluate the real-time operational characteristics of the MMD enabled VSC. When the VSC starts injecting upon an SSR

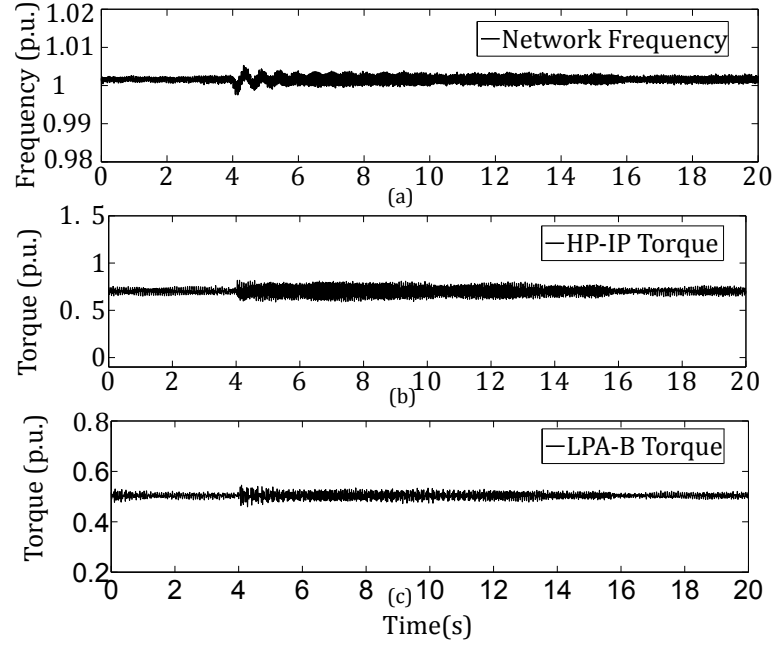


Figure 5.10: Experimental results (RTDS signals) with MMD enabled VSC in operation for Case A. (a) Frequency of phase a current of the Northern Scotland generator; (b)-(d) selected torque interactions in the multi-mass shaft of the Northern Scotland generator.

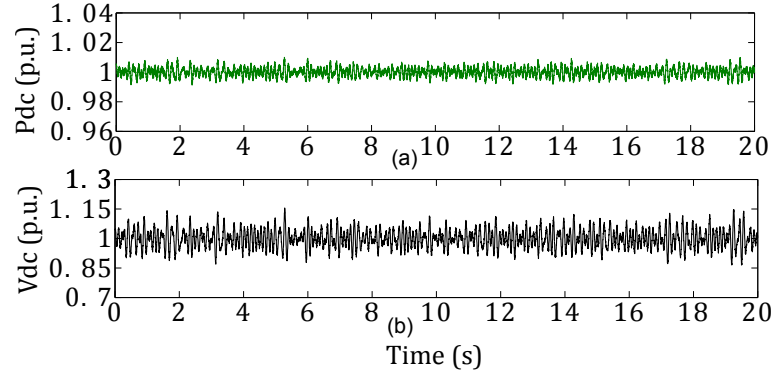


Figure 5.11: Experimental results (HVDC rig signals) with MMD enabled VSC in operation for Case A. (a) Output power at VSC1; (b) DC-link voltage.

event, the changes monitored in both V_{dc} and P_{dc} is by very little magnitude as shown in Figure 5.11(a) and (b). For Case A, the occurrence of SSR at $t = 4$ s can be observed more evidently in P_{dc} measurement.

However, when the SSF injection is applied at $t \approx 5$ s, the oscillations are controlled back to steady-state by MMD enabled VSC (see Figure 5.11(b)).

The real-time experimental plots for Case B show the same pattern as in Case A, as seen from

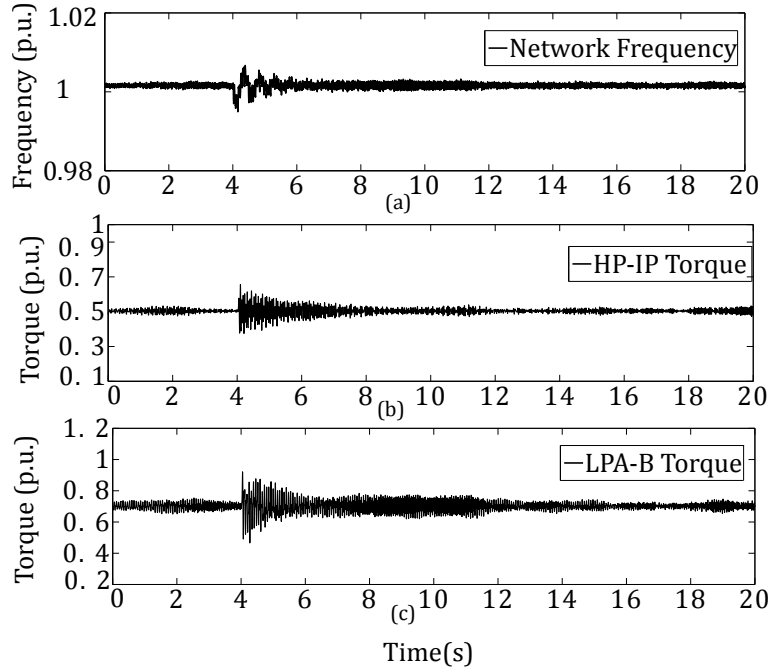


Figure 5.12: Experimental results (RTDS signals) with MMD enabled VSC in operation for Case B. (a) Frequency of phase a current of the Northern Scotland generator; (b)-(d) selected torque interactions in the multi-mass shaft of the Northern Scotland generator.

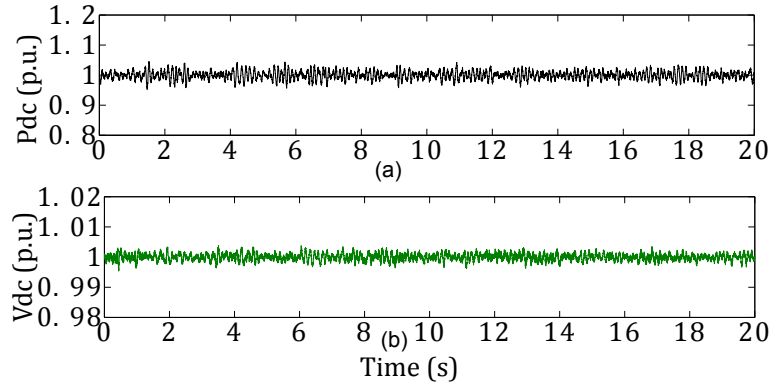


Figure 5.13: Experimental results (HVDC rig signals) with MMD enabled VSC in operation for Case B. (a) Output power at VSC1; (b) DC-link voltage.

Figures 5.12 to 5.13, apart for the injected current components magnitude and the corresponding modulation of P_{dc} is almost undetectable from the real measurements. The experimental results agree well with the time-domain findings proving the validity of MMD based filter enabled VSC's capability for SSR damping.

5.5.3 Integrated AC/DC System with Wideband Damper

To validate the time-domain results of the wideband damper (WBD) enabled VSC operation during SSR, the RT-HiL tests were performed. The experimental tests aim to evaluate the converter performance and capacity in achieving adequate damping for the whole range of subsynchronous frequencies. The RT-HiL tests were performed with the VSC controller embedded with

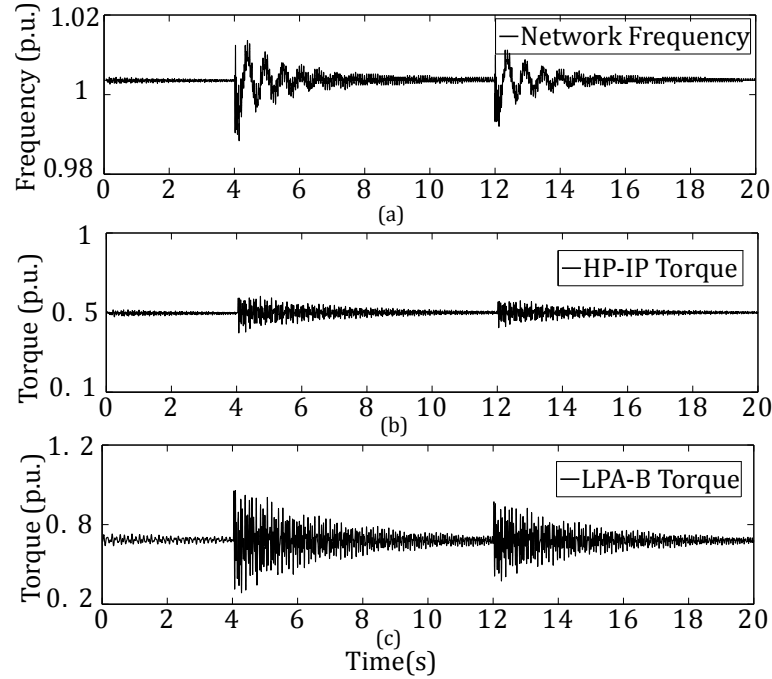


Figure 5.14: Experimental results (RTDS signals) with WBD enabled VSC in operation. (a) Frequency of phase a current of the Northern Scotland generator; (b)-(d) selected torque interactions in the multi-mass shaft of the Northern Scotland generator.

the WBD. The real-time simulation starts in the steady state with 30% series compensation. This condition does not produce SSR. At $t = 4$ s the value of series compensation is modified to 40%. Subsequently, the level of series compensation is modified to 75% at 12 s. As shown in Figure 3.19, such conditions would normally create SSR. After such a disturbance, the system develops SSR if the damping controller is not active (see Figure 5.8). However, as it can be seen from Figures 5.14 and 5.15, since the damping controller is active the change in series compensation is detected and oscillations due to SSR are damped. It can be noticed that shaft torque oscillations (Figures 5.14 (b) and (c)) and oscillations in the frequency of the current of the transmission line (Figures 5.14 (a)) converge to the steady-state with time. This behaviour demonstrates the effectiveness of the proposed control method.

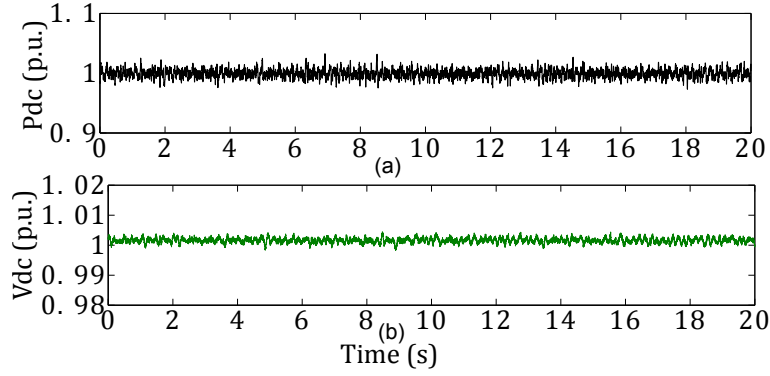


Figure 5.15: Experimental results (HVDC rig signals) with WBD enabled VSC in operation. (a) Output power at VSC1; (b) DC-link voltage.

DC link variables are monitored and are plotted in Figure 5.15, to evaluate the real-time operational characteristics of the WBD enabled VSC. The WBD is enabled in the VSC from the start and upon the change in the series compensation level at $t = 4$ s and 12 s, the injected SUB currents from the SSF components will act on the active and reactive powers to achieve damping of SSR oscillations. The resultant fluctuations in both P_{dc} and V_{dc} is barely evident, such that it cannot be observed from the waveform. This is because of the overlap of the impact of SSR Current injection with the switching disturbances attributed by the real-time operations of the VSC's and associated noise interferences. It can be concluded that, the experimental results complements well with the time-domain findings proving the validity of WBD filter enabled VSC's capability for SSR damping.

5.5.4 Integrated AC/DC System with Real-time Damper

Experimental results to validate the results obtained via the time-domain PSCAD simulations for the SSR damping using the real-time damper or the adaptive subsynchronous frequency damping controller (SSFDC) enabled VSC HVDC will be presented in this section. Operation of the series-compensated AC/DC 3GB network for two cases (see Section. 5.5) were evaluated. Making use of existing HVDC links rather than building new devices is always a better utilisation of assets and the experimental tests provides the final step before the practical implementation of the device or control system. In this regard, we test the performance of the SSFDC enabled VSC's capability to damp SSR using the RT-HiL platform (see Figure 5.4) and the results are plotted in Figures 5.16 to 5.19.

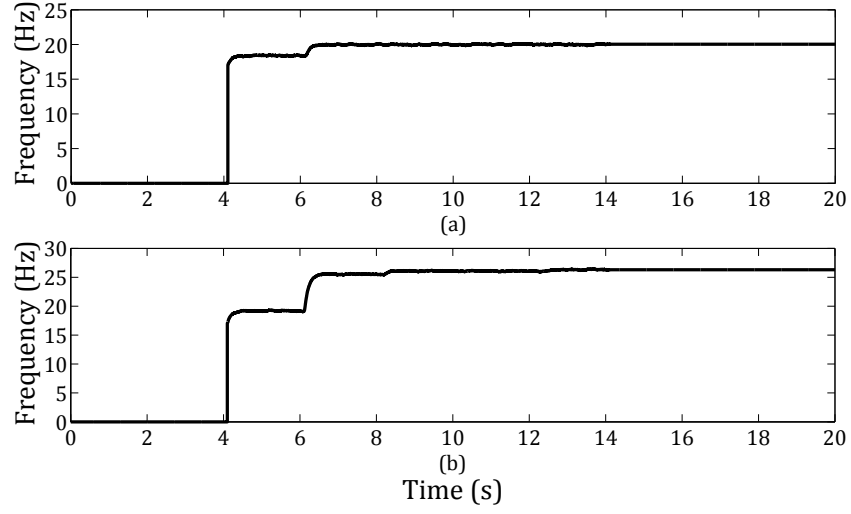


Figure 5.16: Performance of tracking network oscillation frequency (f_{osc}). (a) at around 20 Hz (Case A); (b) at around 27 Hz (Case B).

Using the SSFE and SSFT described in Section. 4.5, the network SSF component (f_{osc}) for the two cases has been evaluated and is shown in Figure 5.16. For Case A, the SSFT is able to track the dominant frequency component (≈ 20 Hz) in less than ≈ 2.5 s (see Figure 5.16(a)). Similar response can be observed for Case B, where the dominant mode (≈ 27 Hz) is tracked and estimated (see Figure 5.16(b)). These findings agree well with the FFT spectrum results shown in Figures 5.7(c)-(d), complementing the eigenvalues summarised in Table. 3.2.

The line current plot and corresponding spectrum can be seen in Figure 5.17. The additional series compensation for Cases A and B has triggered the oscillations as seen from the increasing current magnitude. Once the SSFT identifies and tracks the exact network mode, SSFDC starts injecting the anti-phase signal through the VSC at around $t \approx 7$ s and is able to damp the rise in current (see Figures 5.17(a) and 5.17(b)). The network SSF component which interacts with the mechanical modes are identified, tracked and mitigated in less than 3.5 s and is evidenced by the spectrum results Figures 5.17(c) and 5.17(d) respectively.

The frequency and torque interactions are evaluated with the SSFDC in operation for Cases A and B respectively. Figure 5.18(a) shows the plots for Case A, initial transient caused by switching in the additional compensation results in the deviation of frequency from its nominal value and an increase in the torque oscillations. To estimate the impact of damping on the multiple modes the test is repeated for Case B, the same pattern can be seen here as well, (see Figure 5.18(b)).

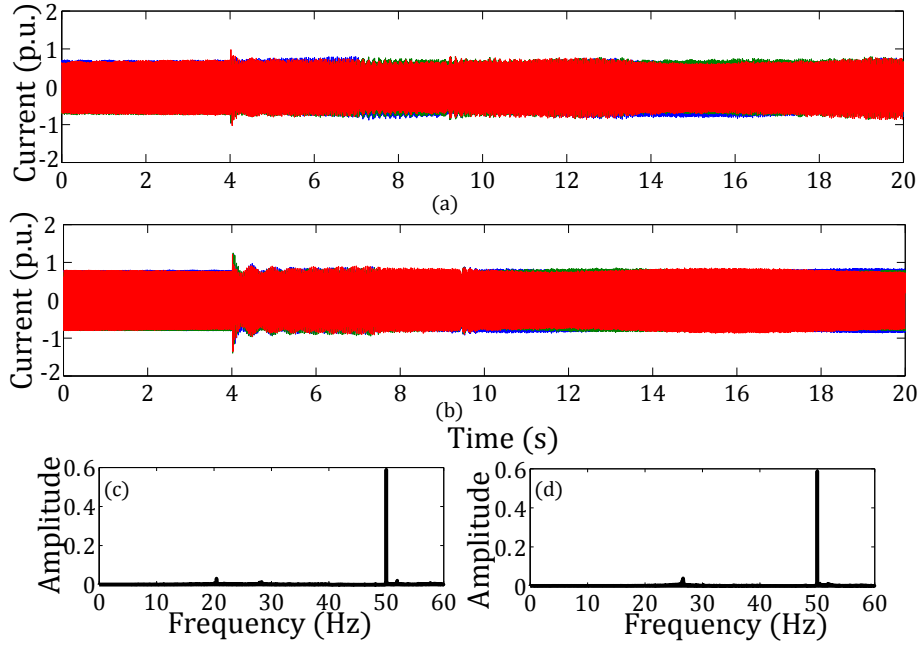
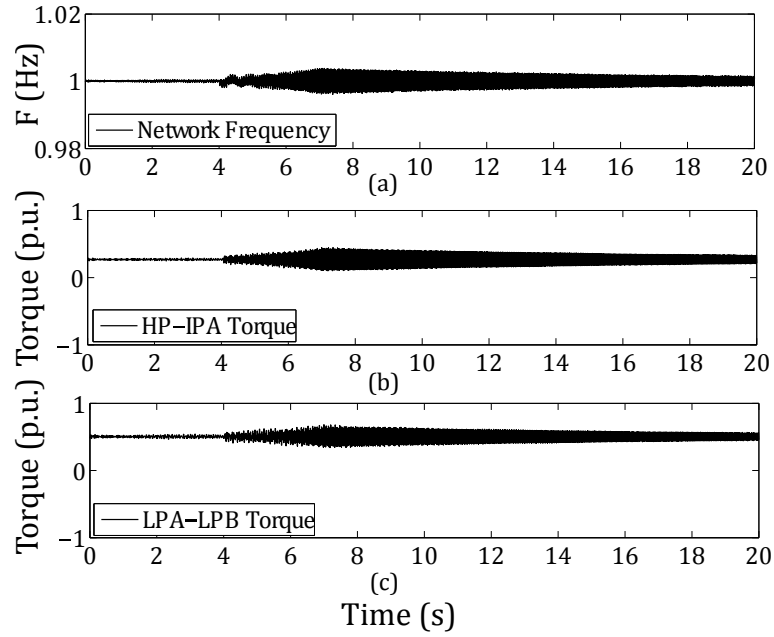


Figure 5.17: Experimental results (RTDS signals) SSFDC in operation. (a) Line current measured at Bus1 for Case A; (b) Line current measured at Bus1 for Case B; (c) Spectrum of a-phase output current for Case A; (d) Spectrum of a-phase output current for Case B.

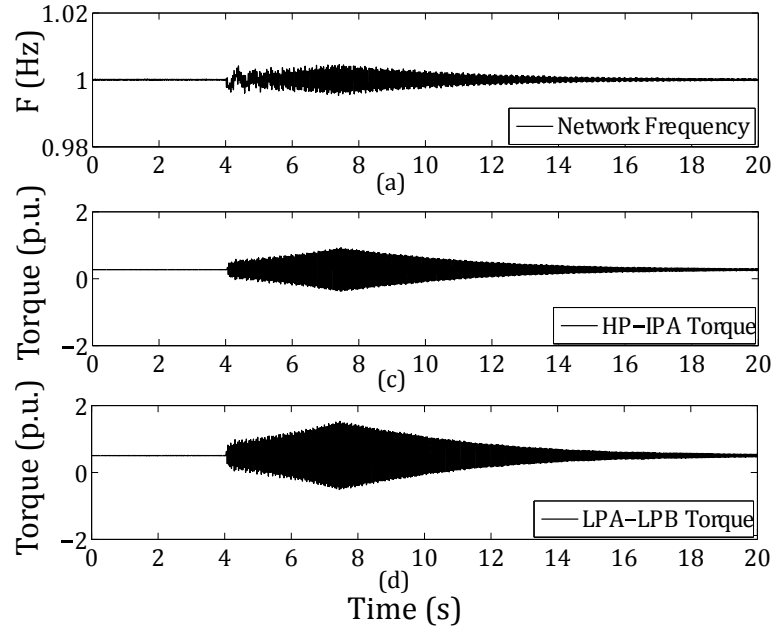
Once the SSFDC starts operating (at $t \simeq 7$ s) the shaft oscillations begin to die out and return to the steady state operating condition evidenced by the stable frequency and torque plots. This reveals the successful mitigation of multiple torsional modes by the effective injection of network modes tracked in real-time.

Figure 5.19 show the experimental results for the physical VSC with the proposed SSFDC for Cases A and B respectively. As evidenced in Section. 5.5.1, without proper mitigation measures the SSR, initiated oscillations can be transferred to DC side and can cause DC voltage oscillations. Thus the need for an effective damping scheme within the capacity of the existing VSC HVDC link and operational performance while providing SSR damping is of high importance and is not yet analysed fully in an experimental platform. Furthermore, the damping provided should not interfere the power transfer capability or the stability of the HVDC link.

Figure 5.19(a) shows the VSC analogue results for Case A. The impact of damping is clearly evident in P_{dc} and V_{dc} plots, followed by the SSFDC operation. Initially V_{dc} and P_{dc} starts to oscillate from their nominal value, once the SSFDC starts operating at ($t \simeq 6.2$ s) the oscillation settles down and reaches the initial condition within seconds.



(a) Frequency and selected torque interactions for Case A



(b) Frequency and selected torque interactions for Case B

Figure 5.18: Experimental results (RTDS signals) with SSFDC enabled VSC in operation.

The performance is tested for Case B, the impact of SSR is clearly mitigated in this case as well, evidenced by the damped converter voltage and power waveforms, (see Figure 5.19(b)). Furthermore, the impact of injection after detecting the frequency of oscillation (f_{osc}), is evident in both Figures 5.19.

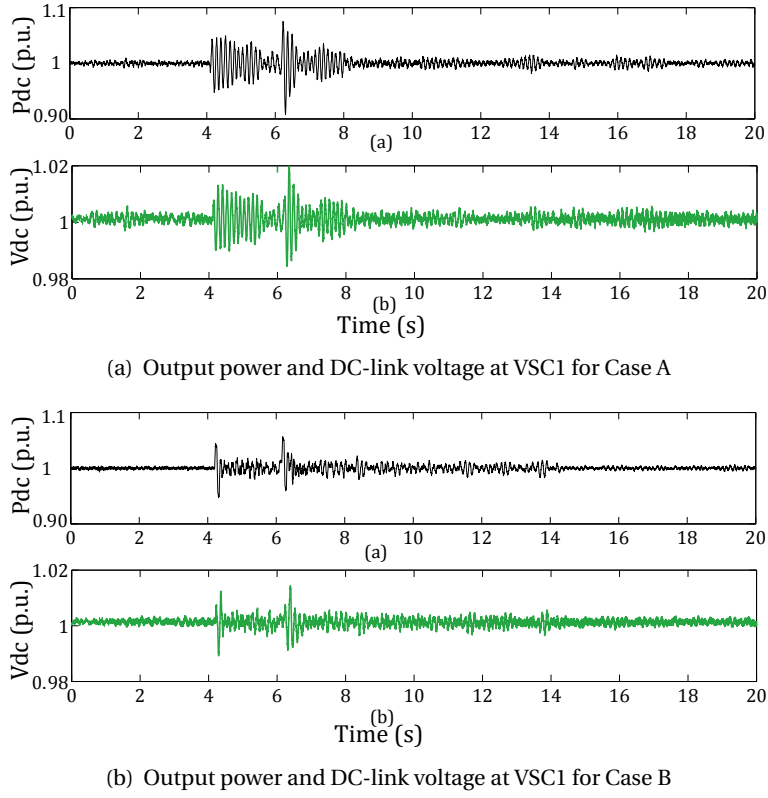


Figure 5.19: Experimental results (HVDC rig signals) with SSFDC enabled VSC in operation.

5.6 Comparison of Simulation and Experimental Results

This section provides a comparison between the results obtained from time-domain PSCAD simulations and the RT-HiL experimental tests. The proposed adaptive SSR damping scheme based on SSFDC is selected for fulfilling this task. To create a small-disturbance in the 3GB test system, the series capacitor X_c value is modified from 30 to 40% at $t = 4$ s. The AC network response is represented by the mechanical mass torque between HP-IP sections and the DC link dynamics are compared using active power signals P_{dc} as shown in Figure 5.20.

The undamped and damped cases for the torque interactions are compared with the results depicted in Figure 5.20(a) and Figure 5.20(b) with both showing good agreement in-terms of transient and steady-state performance. Similarly, the active power signals for the undamped and damped cases are shown in Figure 5.20(c) and Figure 5.20(d), with both results showing good correlation. The difference in the magnitude of SSF component for active power modulation in the real-time experiment is attributed to the scaled down VSC capacity, compared to the

5.7. Transferability of the proposed SSR damping schemes

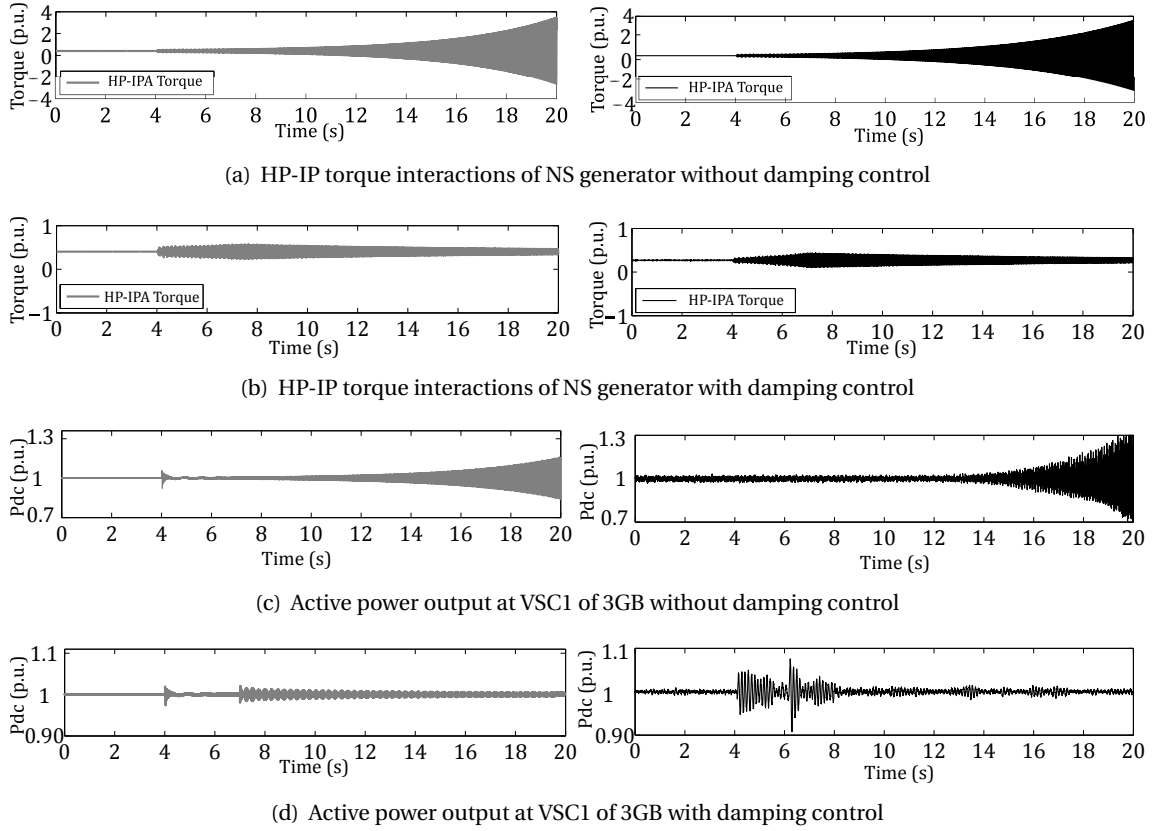


Figure 5.20: Comparison of simulation and real-time results.

high power simulation model. In simulations, both the AC and DC systems are represented in high-voltage, however, in the RT-HiL tests, the physical VSC is connected to low-voltage causing the impact of SSR damping to be more severe than simulation.

5.7 Transferability of the proposed SSR damping schemes

In this section a discussion is provided on the transferability of different SSR damping schemes introduced in this thesis for practical applications. The comparison results drawn from the simulation and experimental tests performed for the 3GB AC/DC system demonstrates the transferability of SSR damping schemes in two platforms with uncertainty and different environment (see Section 5.6). Moreover, the MMD and WBD based damping schemes utilise filters, which are robust and simplistic in implementation and operation. This is a key aspect for transferability since the knowledge of filters and their execution is a familiar task for field engineers [137]. For RTD approach the key aspect which makes it transferable is the ability to track SSF component

at any series compensation level irrespective of power system configurations and uncertainty in the mechanical modes of turbo-generator shafts.

Furthermore, local measurements (voltage and current) are used as input signals for the dampers and current injection is carried out by the VSC closest to the generator. Since local signals are used as damper inputs, in the case that a VSC HVDC station is not available, the SSR damping controllers devised in this work could be implemented in a nearby power electronic based controller (for instance, with the service being rendered by FACTS devices such as a static VAR compensator, thyristor-controller series compensator or a STATCOM).

However, some real-world challenges can be identified, which could hinder the full transferability of the proposed damping schemes. The MMD and WBD approach prerequisites the knowledge of the multiple TM frequencies (mechanical shaft data) for the effective design and damping. The RTD approach, on the other hand, can overcome these limitations, however, the SSF estimation and damping could be impacted by the time delay brought forward by measurement uncertainties. A robust design of SSFT with time delay compensation can overcome this drawback.

5.8 Summary

An experimental platform was developed and implemented through RT-HiL configuration to assess the capability of VSC enabled with three active filter based SSR damping schemes described in Chapter. 4. The connection of different physical components to form the RT-HiL configuration has been used in this chapter for experimental testing of the primary and supplementary control services of the VSC HVDC link connected in parallel to the series-compensated 3GB network. The ability of the experimental test-rig for SSR damping has been demonstrated by implementing the different damping schemes devised in Chapter 4.

Another important aspect of experimental tests is the assessment of the VSC HVDC link capability to damp SSR upon occurrence utilising its existing capacity. The experimental results validate the time-domain evaluation that the damping provided by the proposed schemes does not interfere with the power transfer capability or the stability of the HVDC link.

Finally, the time-domain from Chapter 4 and the real-time experimental results of the proposed adaptive SSR damping scheme embedded VSC control system were compared, with both results complementing each other in performance and wave form shape.

6 Control Strategy for Frequency Regulation in a Hybrid AC/DC Network

6.1 Introduction

This chapter examines the capability of VSC-based multi-terminal DC (MTDC) grids to provide ancillary services to power systems with a large penetration of wind generation. In particular, the dual-droop scheme is presented. This is a flexible frequency support scheme that binds the system frequency and the DC grid voltage. A small-signal model of the hybrid AC/DC network is constructed and its dynamics were assessed when the dual-droop scheme is used for primary frequency regulation. System performance considering high wind penetration is evaluated through sensitivity studies and eigenanalysis. For completeness, time-domain simulations are carried out in MATLAB/Simulink to compare the proposed method with conventional frequency support schemes. To validate the small-signal model and the simulation results, a real-time hardware-in-the-loop (RT-HiL) experimental test-rig is used..

6.2 System Configuration and Frequency Regulation

The system shown in Figure 6.1 is used in this work. It consists of three AC grids connected through a three-terminal VSC-based MTDC network and supported by frequency regulation schemes. Such a configuration resembles China's future power grid with proposed transmission reinforcements for 2030 [39, 110]. Grid 1 is a power injection model of a mixed power park consisting of a coal-fired thermal power plant and a doubly-fed induction generator based

wind farm. Thermal generation is twice as large as wind generation—a feasible and foreseeable generation ratio highlighting the importance of an effective frequency regulation upon large power injection from wind farms [38, 112]. The synchronous generator production is 500 MW and the wind farm generates 250 MW at nominal wind speed (11 m/s). A nominal power of 750 MW is transmitted from Grid 1 and shared equally by Grids 2 and 3, which represent load centres. The MTDC grid has a nominal voltage of 400 kV and each DC transmission line has a length of 500 km .

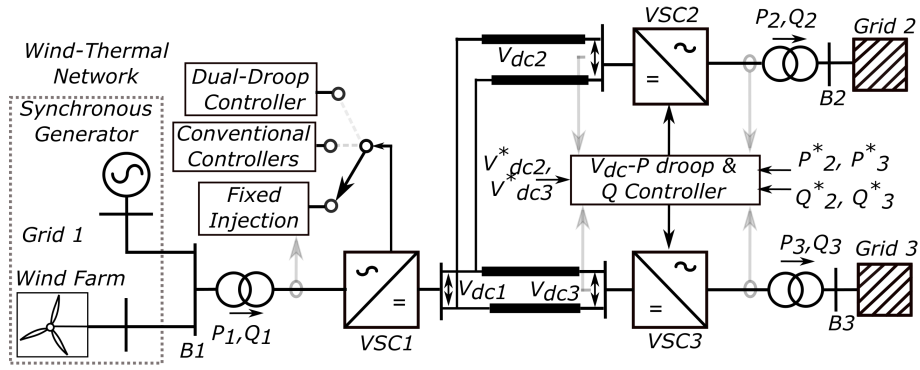


Figure 6.1: Hybrid wind-thermal system.

Grid 1 considers a complete representation of the primary frequency regulation scheme for a synchronous machine-based power plant, as shown in Figure 6.2(a). It includes a speed governor and a steam turbine [37]. An automatic generator control was not included as its response is considerably slower than the inertial and primary responses [118, 138]. Deviation in grid frequency $\Delta\omega$ can be expressed as a function of system inertia H_s and injected/absorbed power as:

$$2H_s \frac{dw}{dt} = P_m + P_{WF} - P_{conv}, \quad (6.1)$$

where P_m denotes the prime mover power of the thermal plant, P_{WF} the active power of the wind farm, and P_{conv} the power of VSC1. The power absorbed by VSC1 is injected into the MTDC grid, binding AC and DC power balances; *i.e.*, AC power fluctuations are routed to the MTDC grid. This exploits the fast power routing capabilities of VSCs to retain system stability.

The frequency regulation scheme for Grids 2 and 3 is illustrated in Figure 6.2(b). For simplicity,

it is assumed that they have similar electrical parameters as Grid 1. Therefore,

$$2H_s \frac{dw}{dt} = P_m + P_{conv} - P_{load}, \quad (6.2)$$

where P_{load} aggregates the active power load in Grids 2 and 3. A nominal value $P_{load} = 375$ MW is assumed.

6.3 MTDC Grid Operational Scenario

Droop control is a method employed to regulate the DC voltage in an MTDC grid. Its application is borrowed from conventional power systems using frequency-power droop schemes [111, 139]. Droop control is considered to be more reliable than master-slave or improved voltage margin methods mainly due to its robustness and the ease of power sharing between different terminals [111, 140]. However, unlike frequency in traditional AC systems, voltage is not a universal measurement in a DC network. A DC voltage droop control may cause deviations from the nominal value, resulting in power losses in the transmission line—a scenario detrimental to the seamless integration of HVDC grids. Thus, droop settings should be carefully designed to prevent mismatches [141, 142].

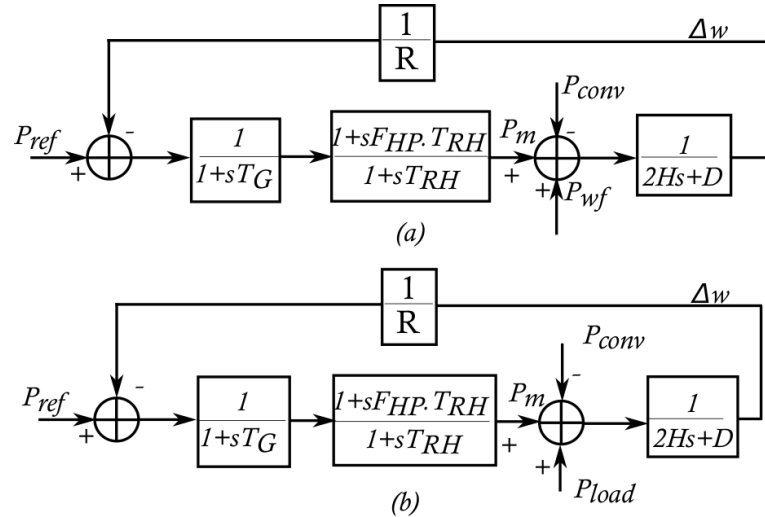


Figure 6.2: Primary frequency regulation including a speed governor and a steam turbine: (a) Grid 1 (b) Grids 2 and 3.

In the MTDC grid of Figure 6.1, the sending-end converter (VSC1) operates in a constant power

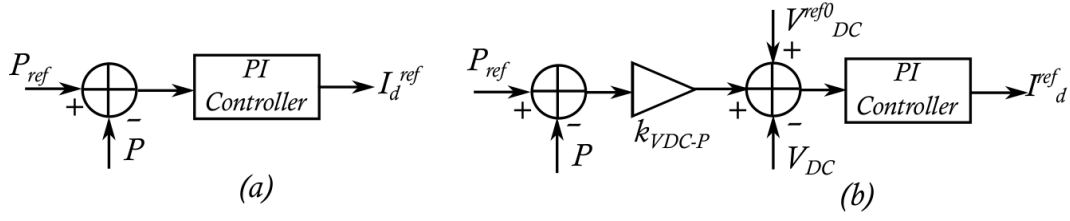


Figure 6.3: Conventional VSC operation modes in an MTDC grid: (a) Constant power injection; (b) DC voltage - active power droop.

injection mode (see Figure 6.3(a)). VSCs2 and 3 work in droop control mode, as depicted in Figure 6.3(b). The control law for VSCs2 and 3 can be written as:

$$V_{DC}^{ref} = V_{DC}^{ref0} + k_{VDC-P}(P_{inj}^{ref} - P_{inj}), \quad (6.3)$$

where V_{DC}^{ref} is the DC voltage reference and V_{DC}^{ref0} is the reference when there is no power deviation between the injected power P_{inj} and its reference value P_{inj}^{ref} . The droop coefficient k_{VDC-P} binds the power deviations in the MTDC grid to the DC voltage reference.

6.4 Frequency Support Schemes

For the system under study and as shown by Figure 6.1, active power injection at VSC1 is directly related to the power balance in Grid 1. Therefore, the converter power absorption can be used for frequency regulation [117, 118].

6.4.1 Conventional Frequency Support Methods

Methods based on the measurement of frequency derivatives and deviations have been proposed to provide frequency and inertia support using HVDC-connected wind farms [117, 143]. To this end, active power modulation through the HVDC links is employed. However, DC grid dynamics, especially DC voltage variations, have not been considered. This is a critical shortcoming since DC voltage is regarded as a global parameter indicating the power balance in MTDC systems. The control-level implementation is illustrated in Figure 6.4, with:

$$P_{Conv}^{ref} = P_{Conv}^{ref0} + k_{pf}(f_0 - f), \quad (6.4)$$

$$P_{Conv}^{ref} = P_{Conv}^{ref0} + k_{p\frac{df}{dt}} \cdot \frac{df}{dt}, \quad (6.5)$$

where f and f_0 are the measured and nominal frequencies of Grid 1, k_{pf} is the gain for the frequency deviation scheme and $k_{p\frac{df}{dt}}$ is the gain for the frequency derivative scheme.

Similar methods for frequency support in offshore wind power delivery have been proposed [33, 143]. A VSC HVDC link incorporating ancillary DC voltage control has been used to exploit the DC capacitor bank characteristics to absorb and release energy, thereby regulating frequency. However, the influence of k_{pf} and $k_{p\frac{df}{dt}}$ on frequency regulation has not been addressed for varying system inertia conditions and, to the knowledge of the authors, an experimental validation of the aforementioned methods using real converters is missing.

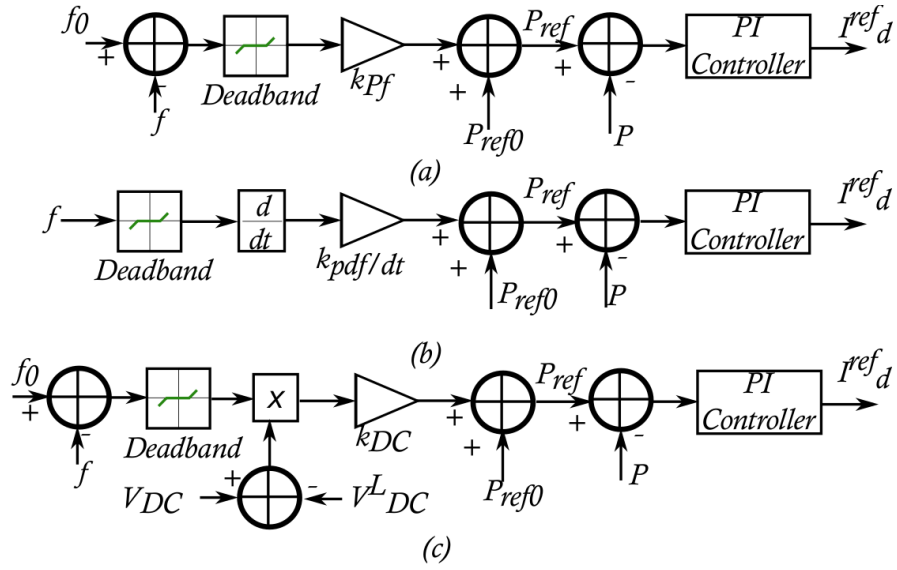


Figure 6.4: Active power modulation strategies in response to power imbalances: (a) frequency deviation; (b) frequency derivative; (c) dual-droop.

6.4.2 Dual-Droop Control

To overcome the limitations of conventional methods, a dual-droop control scheme is proposed. It uses the frequency and the DC voltage as feedback signals, as shown in Figure 6.4(c). Consider that it is desired to provide frequency regulation to Grid 1. The following control law for VSC1 is

defined:

$$P_{Conv}^{ref} = P_{Conv}^{ref0} + k_{DC}(V_{DC} - V_{DC}^L)(f_0 - f). \quad (6.6)$$

P_{Conv}^{ref} is the active power injection reference and P_{Conv}^{ref0} the reference without frequency deviations (*i.e.* $f_0 = f$) and when the dc voltage V_{DC} is above a threshold value V_{DC}^L (included for the safe operation of the DC grid). Parameter k_{DC} is the DC voltage-AC frequency droop or dual-droop coefficient.

Reference [144] had previously proposed the binding of DC voltage and frequency droops for AC grid support. However, the control law includes an interaction term that may cause adverse coupling between control loops; thus, care should be exercised for the adequate selection of droop parameters. Conversely, the control law given by eq. 6.6 avoids such shortcomings, with VSC1 acting as an "active frequency-dependent load" that modulates power in response to frequency variations. For instance, if a lower than expected wind farm power output due to low wind speeds results in a negative power imbalance, the frequency deviation will be negative and the converter will decrease the active power injection accordingly. This would translate into a small and slow frequency deviation.

Since VSCs2 and 3 operate under a DC voltage droop given by eq. 6.3, the change in the injected active power in Grids 2 and 3 will cause a reduction in DC voltage. Given that DC voltage is a mean to transmit information in an MTDC grid without communications [33, 143], it should only vary within a very narrow range. This is taken into account in eq. 6.6, by including the deviation between V_{DC} and the security margin V_{DC}^L .

The dual-droop concept can be seen as a variable/adaptive scheme accounting for changes in the injected power and thus frequency, but simultaneously regulating converter action. This is the key element of eq. 6.6, allowing the binding of AC and DC dynamics without compromising any of them and supporting AC grid frequency stability without risking the DC grid voltage. The superior performance of the dual-droop approach under different wind penetration levels will be examined in the next section through sensitivity and eigenvalue analyses.

6.5 Impact of Wind Penetration

One of the main advantages of the dual-droop scheme is its capability to accommodate high wind power penetration (WPP) by utilising the fast controllability of a VSC-based MTDC scheme. The performance of the grid controller will be mainly influenced by the DC voltage-AC frequency droop coefficient k_{DC} and the inertia (H) of the network. To obtain the optimal control effect, these parameters should be factored carefully. WPP is considered to be 33% of the total generation capacity of Grid 1 (see Section. 6.2). The performance of the test system in Figure 6.1 is assessed for the following cases:

- Case 1: WPP without any contribution from MTDC grid converters (Fixed injection).
- Case 2: WPP with frequency deviation control implemented in VSC1 (F_{dev}).
- Case 3: WPP with frequency derivative control implemented in VSC1 (F_{dfdt}).
- Case 4: WPP with dual-droop control implemented in VSC1 (Dual-Droop).

6.5.1 Sensitivity of System Parameters to Changes in Inertia

The nominal inertia constant of the electrical machines directly coupled with Grid 1 is $H = 5$ s (1 p.u.). H will decrease as WPP increases if the number of committed synchronous units is assumed to decrease accordingly. To assess the impact of a higher WPP, Cases 1 to 4 are evaluated as inertia changes. Three vital variables are considered for the analysis: frequency of Grid 1, frequency of Grids 2 and 3, and DC voltage.

Figure 6.5(a) shows the changes in frequency of Grid 1. Cases 1 (fixed injection) and 3 (frequency derivative) yield the lowest frequency for all values of H , with the statutory limit of 49.5 Hz being breached for low inertia values. As expected, the worst performance is exhibited when VSC1 is not upgraded with a frequency support scheme (Case 1). The frequency deviation control (Case 2) outperforms the frequency derivative scheme, but leads to frequency regulation below the operational limit of 49.8 Hz. Dual-droop control (Case 4) exhibits the smallest deviation, with frequency values always lying above 49.8 Hz independently of the system inertia.

The frequency in Grids 2 and 3 remains above 49.8 Hz for all cases, as shown in Figure 6.5(b).

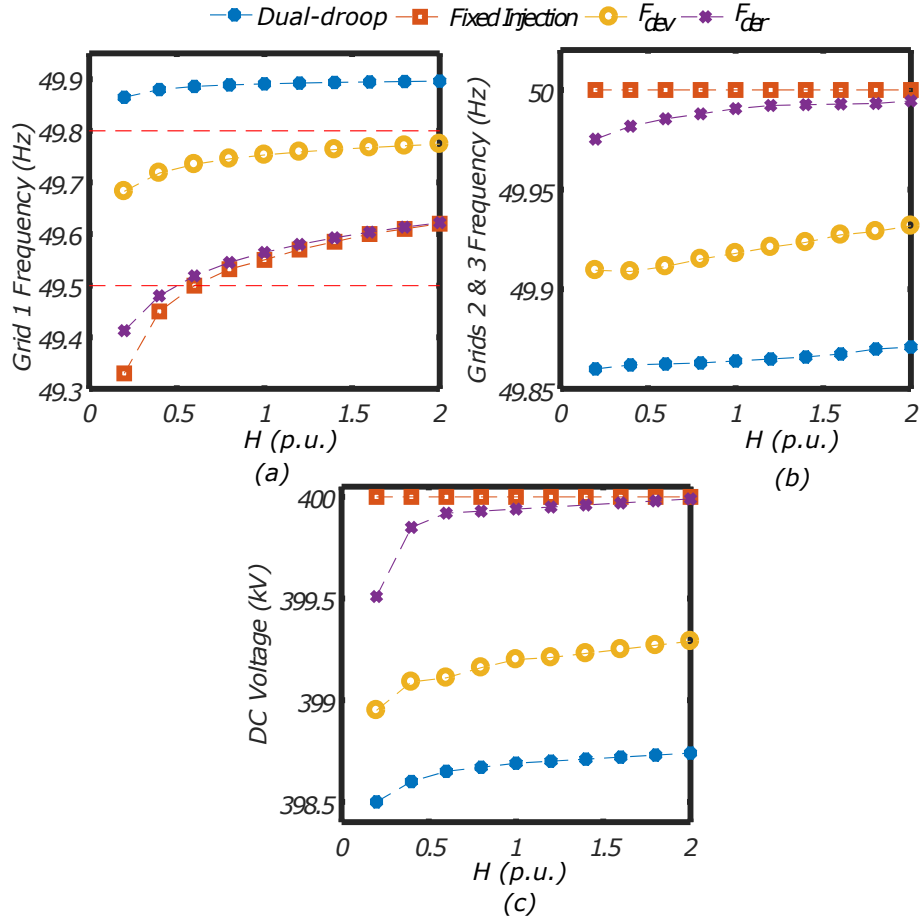


Figure 6.5: Effect of parametric changes in H : (a) Frequency of Grid 1; (b) Frequency of Grids 2 and 3; (c) DC voltage.

However, the frequency of Grid 1 (see Figure 6.5(a)) substantially improves from 49.55 to 49.891 Hz for the nominal inertia when the dual-droop method is adopted (Case 4) compared to the fixed injection scenario (Case 1). This occurs at the expense of a small deviation in the receiving grids (from 50 to 49.865 Hz). This shared correction of power imbalances is a result of the collaborative nature of the ac and dc grids when the dual-droop control is used, which is achieved without significant changes in DC voltage. As shown in Figure 6.5(c)), the maximum deviation from 400 kV (1 p.u.) occurs when $H = 0.1$ p.u. (with $V_{DC} = 398.5$ kV). Although this value (0.4%) is larger than in the other cases, it leads to the lowest combined frequency deviations in all grids. Given that dc voltage deviations are reasonably small with the dual-droop control, dc voltage can be still used to communicate the state of power balance in the MTDC system.

It can be observed that the higher the penetration of wind is, the larger the frequency deviations and DC voltage variations are in all AC grids for all frequency support cases. However, the key improvement afforded by the dual-droop strategy is to ensure that frequency of Grid 1 remains within operational limits while leading to the smallest frequency deviations: for instance, frequency is 49.865 Hz for the nominal inertia and 49.8963 Hz when $H = 2$ p.u. (corresponding to a deviation from the nominal frequency by 0.06% only). This characteristic leads to a better overall system operation.

6.5.2 Dual-Droop Parameter Design

The selection of parameters is critical for the effective operation of the dual-droop scheme. Figure 6.6 shows the impact that droop gains have on the frequency deviation of Grid 1 for different inertia values. The dual-droop gain k_{DC} is varied from 0.125 to 1.625 p.u. while inertia H is changed from 0.2 to 2 p.u. As observed in Figure 6.6(a), $k_{DC} = 1$ p.u. enables satisfactory frequency regulation irrespective of system inertia. The selection of k_{DC} is made in such a way that the wind-thermal system can accommodate large variations in power injection without violating operational limits. The variation of droop gains in terms of the system operational limit is depicted in Figure 6.6(b). As it can be observed, frequency regulation can be effectively achieved during very high wind penetration ($H=0.5$ p.u.) when higher droop gains are employed while ensuring that operational limits are not violated.

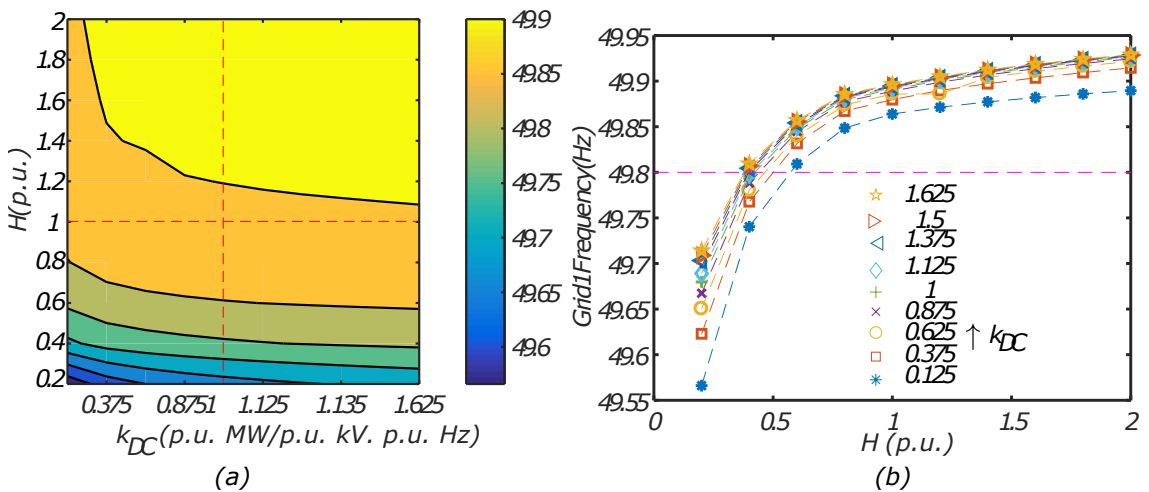


Figure 6.6: Variation of frequency in Grid 1 to changes in k_{DC} and H for selection of: (a) Operating region; (b) Operational limit.

The dual-droop scheme can be used to mitigate frequency deviations following power imbalances in systems with reduced inertia. Thus, it constitutes an effective method to cope with present and future uncertainties in the power generation mix where a significant penetration of renewables is expected.

6.5.3 Eigenvalue Analysis

Detailed small-signal models of the test system for Cases 1 to 4 have been developed to perform eigenanalysis and to determine the optimum values of control parameters for an MTDC grid which enables frequency regulation. These include the dynamic equations of the AC grids, transmission lines and the HVDC converters with their controllers as given described in Chapter. 3 . Following linearisation around an operating point, a state-space representation is constructed, with

$$\begin{aligned}\Delta \dot{X}_{sys} &= A_{sys} \Delta X_{sys}, \\ \Delta X_{sys} &= [X_{ACG}, X_{VSC1}, X_{VSC2}, X_{VSC3}]^T.\end{aligned}\tag{6.7}$$

X_{ACG} considers the state variables of the AC grids and X_{VSC1} , X_{VSC2} , X_{VSC3} the state variables of VSCs1, 2 and 3 and their controllers. System eq. 6.7 has been implemented in MATLAB to assess the effects that wind penetration and changes in the droop coefficient have on system stability.

The loci of system eigenvalues for Cases 1 to 4 when the inertia of Grid 1 is modified from 2 to 0.1 p.u. are shown in Figure 6.7. All eigenvalues lie at the left hand s-plane, which indicates a stable system operation in all cases (see Figure 6.7(a)). However, Figure 6.7(b) shows the movement of poles and zeros towards the origin as wind penetration increases. A closer look into the critical eigenvalues for low inertia values reveals that for Cases 1 and 3 a similar pattern occurs (see Figure 6.7(c)). The movement towards the origin is restricted when the dual-droop controller (Case 4) is implemented. This behaviour is consistent with the sensitivity analysis from Section. 6.5.1.

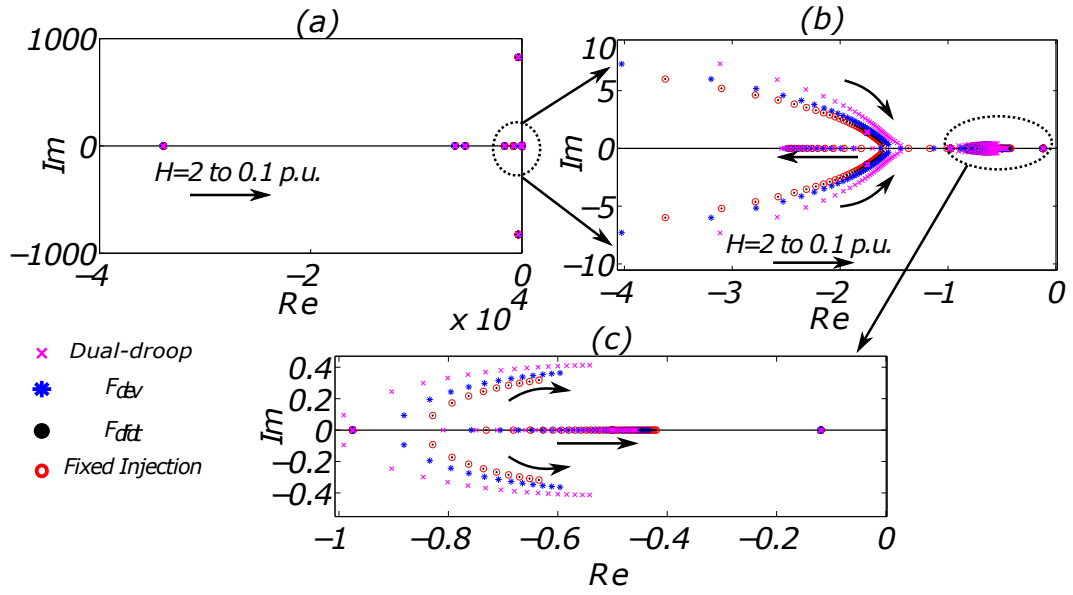


Figure 6.7: Loci of eigenvalues for Cases 1 to 4 when inertia in Grid 1 is changed: (a) Eigenvalues of the full system; (b) Dominant eigenvalues; (c) Magnified view of critical eigenvalues.

The combined effect of the dual-droop gain k_{DC} and H is shown in Figure 6.8, where the position of the critical eigenvalues is depicted when the dual-droop scheme is implemented (Case 4). The inertia of Grid 1 changes from 0.2 to 2 p.u. while k_{DC} is kept at 1, 0.1, 1.5 and 2 p.u. In particular, Figure 6.8(b) shows that a combination of a reduced inertia and small droop gain moves some poles to the right hand s -plane, indicating potential system instability. This is consistent with the analysis in Section 6.5.2: in a system with high wind penetration, effective frequency support cannot be provided with small droop gain values. Figures. 6.8(c) and 6.8(d) show that the higher the value of k_{DC} is the farther apart from the origin the eigenvalues lie. Such an effect in system stability demonstrates the additional grid support afforded by the dual-droop scheme for cases of high wind penetration.

The trajectory of the most critical eigenvalues is magnified in Figure 6.9 for the nominal inertia and different values of k_{DC} . As it can be observed, damping increases when the droop coefficient is in the range of 1 to 1.6 p.u. When it is smaller than 0.5 p.u., damping decreases instead. It can be concluded that the droop coefficient not only impacts system stability, but also the speed in which grid frequency can be regulated.

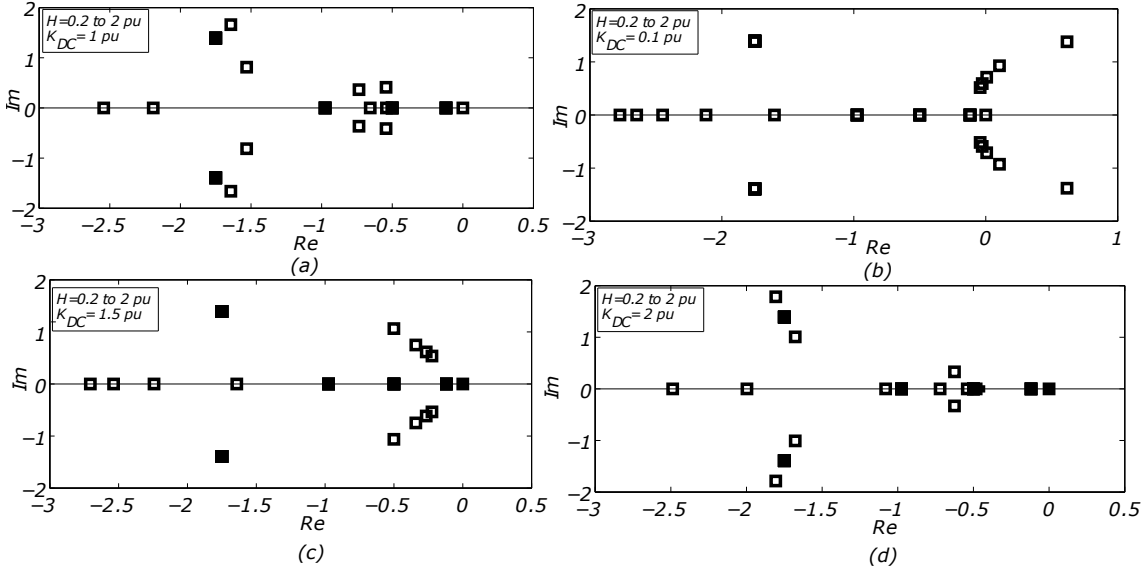


Figure 6.8: Eigenvalues when H changes from 0.2 to 2 p.u. for different values of k_{DC} : (a) 1 p.u.; (b) 0.1 p.u.; (c) 1.5 p.u.; (d) 2 p.u.

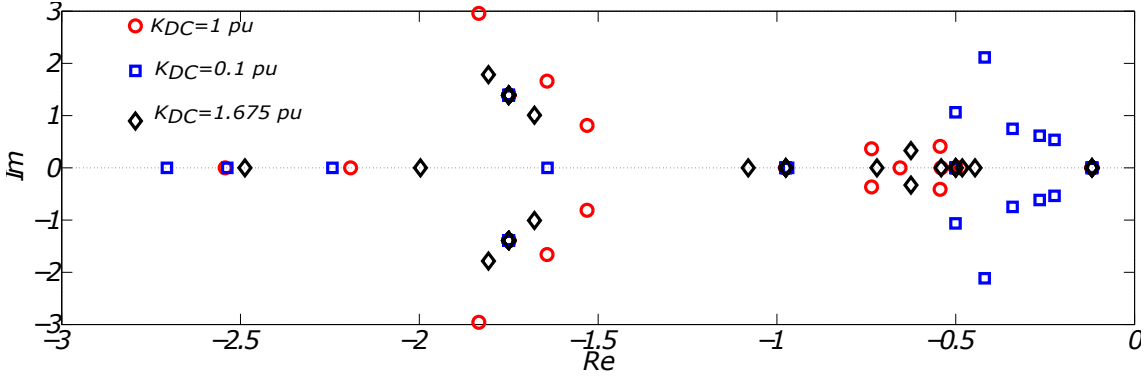


Figure 6.9: Trajectory of dominant eigenvalues for $H = 1$ p.u. = 5 s and different values of k_{DC} .

6.6 Simulation Results

The test system under study was implemented in MATLAB/Simulink to carry out time-domain simulations. All frequency support methods were implemented in VSC1. Grids 2 and 3 are assumed to be similar and share the power injection equally; *i.e.* they are operated in V_{dc} - P droop control mode with similar droop values for VSCs2 and 3. A dead-band of (± 200 mHz) is included for all schemes. The parameters and specifications of the system are given in Tables 6.1 and 6.2.

Simulation results are provided in Figure 6.10. The wind profile shown in Figure 6.10(a) has

been employed to ensure a similar wind farm power injection for all cases. The frequency of Grid 1 and its injected power are shown in Figures. 6.10(b) and 6.10(c), respectively. The DC voltage at the terminals of VSC1 is given in Figure 6.10(d); the injected power into Grids 2 and 3 and their frequency are shown in Figure 6.10(e) and 6.10(f), respectively. The first 25 seconds of the simulations have been omitted in the graphs as these corresponds to initial simulation transients.

In Case 1, a fixed power injection from VSC1 into the DC grid is considered in spite of changes in the wind farm output. DC voltage is not affected and, consequently, power injection into Grids 2 and 3 and their frequency remain unchanged. It is important to mention that a communication-free operation of an MTDC grid is frequently envisaged as a means to cope with loss of communication or transmission of erroneous information or with a significant delay. As the DC voltage does not change, the variation on the wind farm output is accommodated completely by Grid 1. As shown in Figure 6.10(b), the frequency follows the variation pattern of power injection.

The use of the frequency derivative (Case 3) to improve the inertial response does not provide significantly better results when compared with a fixed injection scenario. As shown in Figure 6.10(b), the smooth frequency variation in Grid 1 leads to a limited modulation of the injected power and an equally limited variation of the dc voltage, leading to a small effect in the injected power of Grids 2 and 3. This in turn results in a minimal frequency deviation (see Figures. 6.10(c)-6.10(f)).

For the frequency deviation method (Case 2), the injected power from VSC1 responds to the frequency deviation from its nominal value in Grid 1. As it can be observed, the variation of the injected power into Grids 2 and 3 leads to the modulation of the DC voltage, which in turn is used to control the injected power by VSC1 and its grid frequency. As Grids 2 and 3 absorb the fluctuations of the wind farm output, the frequency deviation in Grid 1 is much smaller than for Cases 1 and 3.

It should be highlighted that if the frequency deviation method is employed (Case 2), the frequency at Grid 1 varies significantly less when compared to the derivative method (Case 3) or when no support is provided (Case 1) and remains within ± 0.2 Hz of the nominal value (50 Hz).

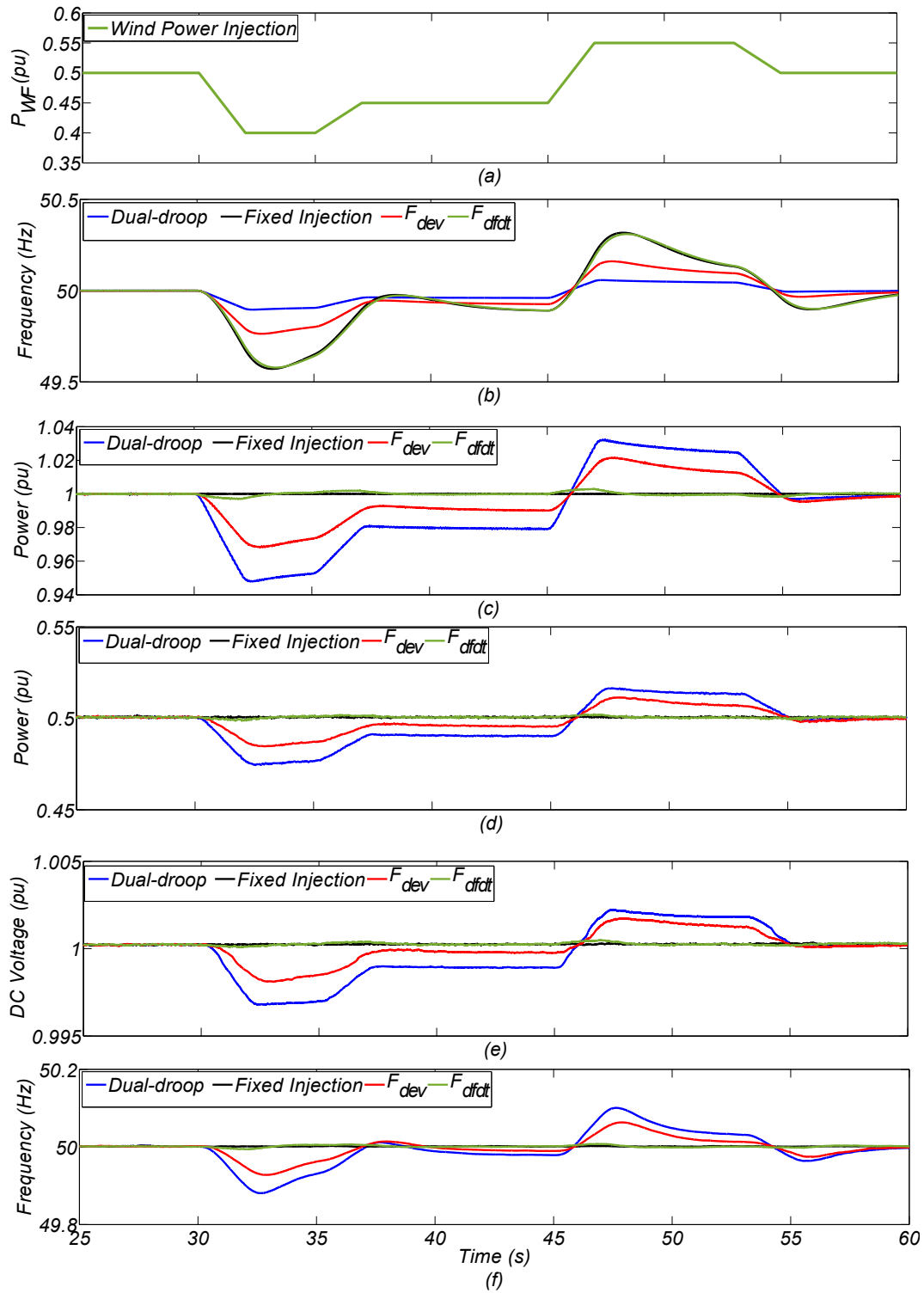


Figure 6.10: Simulation results: (a) Wind power injection; (b) Frequency profile of Grid 1; (c) Injected power of Grid 1; (d) Absorbed power by Grid 2 and 3; (e) DC voltage; (f) Frequency of Grids 2 and 3.

Table 6.1: Base parameters used in simulation and experiment

Parameter	Simulation	Experiment
AC Voltage ($V_{ac,b}$)	220 kV	140 V
DC Voltage ($V_{dc,b}$)	400 kV	250 V
Active Power (P_b)	750 MW	1500 W

Table 6.2: Specifications and parameters of the system

Devices	Specifications	Simulation	Experiment
Converters	Grid 1 Power	750 MW	1500 W
	AC voltage	400 kV	140 V
	DC voltage	400 kV	250 V
	AC inductors	11.35 mH	2.2 mH
	Grids 2 and 3 Power	350 MW	750 W
Control	k_{VDC-P}	0.5	0.01
	k_{p-f}	100	500
	$k_{Pdf/dt}$	10	200
	k_{DC}	20000	100
DC lines	L_{13}	43.12 mH	11.8 mH
	L_{23}	11.01 mH	2.4 mH
	R_{13}	1.075 Ω	0.98 Ω
	R_{23}	0.204 Ω	0.26 Ω
DC capacitors	C_{g1}, C_{g2}, C_{g3}	1050 μF	1020 μF
Control system	dSPACE DS 1005 / ControlDesk 3.2 (SIMULINK interface)		
Simulator	RTDS/RSCAD, Racks: 3. Cards: 3 (GTWIF, 4 PB5) (2 GTDI, 2 GTDO, 2 GTAI, 2 GTAO, 2 GTNET)		

Given that Grids 2 and 3 share power equally, their frequency variation is approximately half of the variation in Grid 1. Globally, the sum of the maximum values of frequency variation in the three grids corresponds to the maximum frequency deviation in Grid 1 when the fixed or frequency derivative-based injection methods are used. The cooperative nature of the MTDC grid does not alter the magnitude of the overall frequency deviation, but allows it to be shared by the different AC grids it interfaces. This contributes to a better operation of the system. It is worth noticing that the DC grid voltage only varies by less than 1 kV (*i.e.* 0.25%) if the frequency deviation scheme is employed.

Case 4 corresponds to the dual-droop control method. As with the frequency deviation method (Case 2), the injected power into Grids 2 and 3 is actively modulated—although by a higher

amount. As a consequence, a slightly higher frequency variation is achieved (by little more than 0.1 Hz). Similarly, DC voltage is modulated at a higher magnitude (marginally more than 0.05 p.u. \approx 1 kV). The notable benefit of the proposed control method can be observed in Figures. 6.10(b) and 6.10(c): as VSC1 responds to frequency and DC voltage deviations, the power injection is significantly higher than for the other cases, leading in turn to a very small frequency deviation of about 0.1 Hz in Grid 1. As it can be noticed, such deviation is similar in all AC grids. This demonstrates that the primary frequency regulation of the integrated system has been significantly improved when the dual-droop control scheme is employed. It should be highlighted that this has been achieved without considerably modulating the DC voltage: its deviation is very small (less than 0.5%) even when the DC grid power flow is modified to incorporate the variation in the wind power.

6.7 Experimental Validation

To investigate the real-time operational characteristics of the dual-droop scheme in a mixed AC/DC grid, experimental tests have been carried out on the multi-platform network shown in Figure 6.11. The tests aim to validate the effectiveness of the proposed frequency support controller against conventional ones and to validate the controller implementation and its impact on the converter performance. The data for real-time hardware-in-the-loop (RT-HiL) tests is acquired in RSCAD and the dSPACE controller, with results plotted in MATLAB.

6.7.1 RT-HiL Experimental Test Set-Up

The RT-HiL platform consists of a real-time digital simulator (RTDS), a grid simulator (GS), and an HVDC test-rig. The connection of different components to form the HiL configuration is depicted in Figure 6.11(a). To perform the RT-HiL tests, the system shown in Figure 6.1 was modelled using the RSCAD software of the RTDS. This network can be easily expanded to represent generators, loads, transformers and transmission lines of more complex AC systems. High voltages were converted to a low voltage suitable for the GS and the HVDC test-rig through analogue output (GTAO) cards of the RTDS firmware. The technical parameters of the RTDS used in this work are included in Table 6.2.

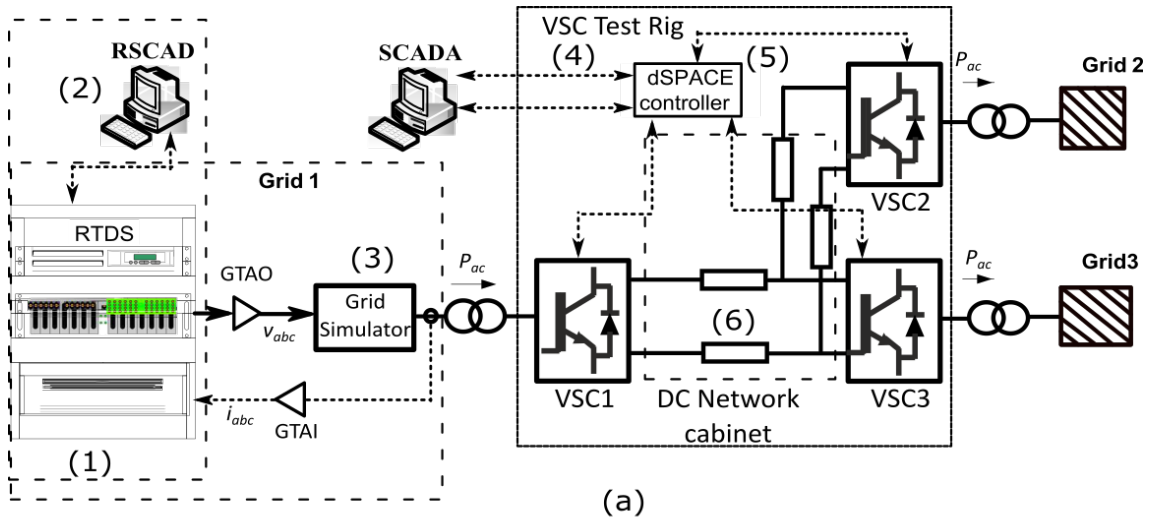


Figure 6.11: RT-HiL configuration: (a) Connection diagram; (b) Set-up.

The GS produces a three-phase mains supply voltage from the GTAO cards of the RTDS. This is achieved by using a four-quadrant amplifier rated at 2 kVA and 270 V (line-to-ground rms). To close the loop between the RTDS and the HVDC rig, the three-phase line current is tapped and fed to the analogue input (GTAI) card of the RTDS (see Figure 6.11(a)).

The HVDC test-rig is formed by three VSCs, three transformers, a DC network cabinet and a dSPACE DS1105 controller. The VSCs are operated at a rated power of 1.5 kW, 140 V AC and ± 125 V DC (see Table 6.1). Through the GS, a conversion ratio of 400 kV / 140 V is achieved, which means that an AC voltage of 140 V in the test-rig represents 400 kV of the high voltage system. The output voltage of the GS is controlled using an autotransformer. The dSPACE platform acquires data and monitors system states of the test-rig and controls each VSC. The hardware set-up is shown in Figure 6.11(b) and the parameters for the VSC HVDC rig can be found in Table 6.2.

6.7.2 Experimental Results

Experimental tests were carried out for Cases 1 to 4, with results shown in Figure 6.12. The wind power profile employed for the experiments is slightly different from that in the simulations. In this case, step changes in wind are considered as opposed to ramp changes (see Figure 6.12(a)).

The frequency of Grid 1 is shown in Figure 6.12(b) and the power injection through VSC1 in Figure 6.12(c). The injected power into Grids 2 and 3 and the DC link voltage variations are plotted in Figures 6.12(d) and 6.12(e). DC voltage traces show a deviation of less than 0.05 p.u. while providing frequency support when the dual-droop scheme is implemented in VSC1. This variation in DC voltage is a result of the additional 0.5 p.u. of power injection into the MTDC grid (see Figure 6.12(c)) to accommodate the power variation in the wind-thermal bundled Grid 1. These deviations are accommodated by the power injection of Grids 2 and 3 (see Figure 6.12(d)). This agrees well with the simulation studies, with results well within operational limits for the satisfactory operation of the MTDC grid.

The experimental results show that the dual-droop scheme outperforms the conventional frequency support schemes, which validates its effectiveness to accommodate high wind penetration without violating AC and DC operational limits.

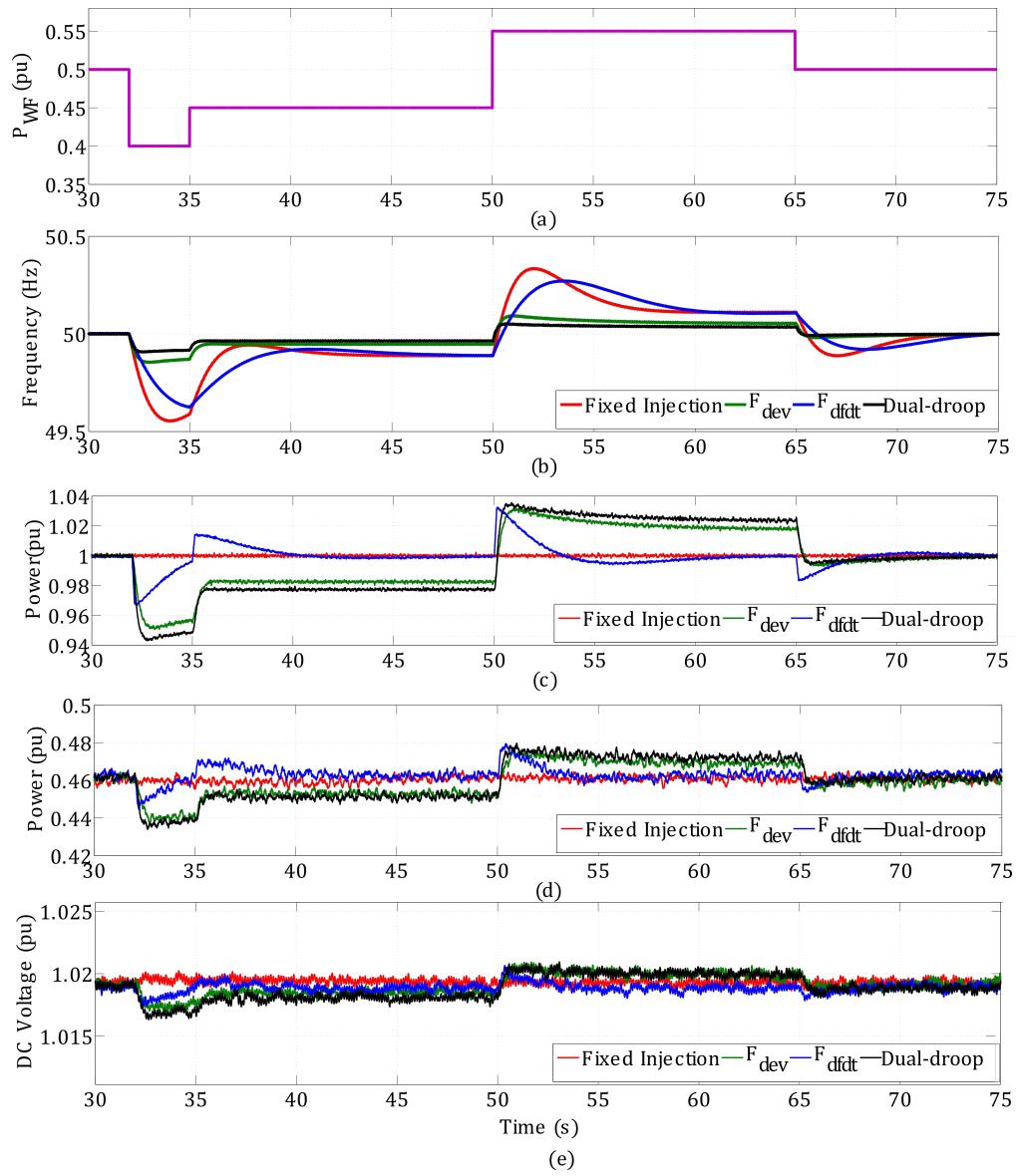


Figure 6.12: RT-HiL results. (a) Wind power injection; (b) Frequency profile of Grid 1; (c) Injected power of Grid 1; (d) Absorbed power by Grid 2 and 3; (e) DC voltage.

6.8 Summary

The effect of high wind penetration on power system frequency regulation and stability has been studied in this chapter using a wind-thermal MTDC bundled network. To this end, a control scheme named dual-droop that binds system frequency with the DC voltage of a VSC-based MTDC grid has been proposed. The dual-droop scheme is capable of providing frequency support, generation balancing, and reduction of wind power curtailment.

To show the effectiveness of the dual-droop control scheme, the stability issues arising from wind power fluctuations and the relatively slow primary frequency response of thermal power plants have been analyzed. The sensitivity studies and eigenvalue analysis performed in this work have elucidated the capabilities of the proposed scheme to accommodate large-scale wind power penetration and enhance system stability.

Simulation and experimental results have shown that the frequency stability issues caused by wind power variations can be addressed and, more importantly, mitigated when the proposed method is employed. Results have shown that the dual-droop scheme outperforms conventional frequency regulation schemes while keeping the DC voltage within a narrow range regardless of significant power flow changes. This enables an enhanced performance of the wind-thermal bundled AC system without compromising the DC grid operational constraints.

7 Conclusions

7.1 General Conclusions

Increased application of VSC based power electronic devices is foreseen in the future transmission grids, which will operate in parity with the existing compensated or uncompensated AC lines. Power converters based on VSC technology provides a cost-effective and reliable solution for transmission network reinforcements and sustainable energy integration. Utilizing VSC's to provide AC system operation and stability support can add more value proposition to the asset. To achieve these services the technical barriers associated with the VSC's integration into the existing AC transmission asset base have to be addressed.

To this end, this thesis investigated the contributions of VSC based HVDC connections to AC system stability enhancement, through their control flexibility and fast power injection capability. In particular, how the inclusion of the proposed VSC HVDC link in the GB system contributes to SSR damping and frequency management.

7.2 Thesis Summary

7.2.1 Modelling and Stability analysis of Series-Compensated AC/DC Network

This study contributes to the field by deriving the small-signal models suitable for evaluating the AC/DC interactions in a series-compensated hybrid AC/DC network. Two test systems, the

Chapter 7. Conclusions

IEEE standard first benchmark and the reinforced GB model have been introduced for AC/DC interaction studies, in particular, SSR-TI and SSR-TA. In order to perform the small-signal studies, a detailed state-space model of the two AC/DC test systems were developed. It includes the dynamic equations of the synchronous machines, turbo-generators, transmission lines and the VSC HVDC link with its controllers, as discussed in Chapter 3.

Following a linearisation exercise, the eigenvalues were computed in order to quantify the torsional instability between the series-compensated power system with turbine-generator and the VSC HVDC line. The eigenvalues indicated the range of compensation levels for which torsional instability arises and the relation of the SUB mode of the HVDC-connected series-compensated transmission line linked to the multi-mass TM frequency. Four torsional mode frequencies were identified for the test systems which may be excited at the different level of series-compensations and potentially cause SSR. In addition, it has been identified that for both test systems, the VSC by itself does not degrade the stability neither it contributes much for damping.

To validate the eigenvalue findings and to estimate the damping contributions from VSCs, perturbation based damping torque analysis is performed on both test systems. Through this approach, the detailed switches and associated delays with the valves of VSCs can be explicitly modelled with all its associated components. The damping torque traces of the turbo-generator revealed the levels of series compensation at which the maximum interaction occurs when the network frequencies are in the vicinity of mechanical modes. In addition, the study has revealed the contribution made by the VSC HVDC link towards the electrical damping of the nearby generator unit.

The small-signal models were compared against detailed EMT simulations to validate the findings through theoretical analysis and to conclude on the modelling fidelity essential to display meaningful results. Study cases are presented to show the impact of different series compensation levels on the AC/DC system stability. The time-domain results agree well with small-signal findings for both tests systems. Time domain-based screening of SSR reveals the amplification of torsional dynamics and oscillations in DC link components under an SSR event.

Through theoretical small-signal based and numerical EMT based simulations, it has been

identified that for low series compensation levels there is a low risk of SSR. However, when the series compensation level goes beyond 40% the risk of SSR increases as evidenced by the negative real part of eigenvalues, increased negative peaks in the damping torque and the sustained growth of oscillations in the AC/DC network variables.

7.2.2 Control of VSC in a Series-Compensated AC/DC Network for SSR Mitigation

The illustration of SSR phenomenon using the reduced GB transmission network incorporating series compensation and VSC HVDC link clearly highlights the need for additional counter-measures so as to keep the quality and security of the network. The results demonstrate the criticality of network sections under different series compensation levels. Hence to account for multiple network modes under different series compensation levels SSRD controllers and adaptation strategies has been implemented.

In this thesis, three types of SSRD controllers (MMD, WBD and RTD) have been introduced and embedded with VSC to mitigate the negative interactions between HVDC connected series-compensated AC line and turbine-generators. Each variant shares the same fundamental characteristic but offers unique advantages for deployment. Among the proposed schemes, the RTD provides the better solution in terms adaptability, frequency selectivity and sensitivity. Conversely, MMD and WBD provide better damping compare to RTD where the frequency and mechanical shaft modes of the turbine-generators are known. However, the real-time SSF identification scheme proposed in this thesis is applicable to any power system and is capable of addressing the uncertainties in mechanical parameters of turbo-generators which limits the adaptability of SSRD controllers to multiple torsional modes.

The effectiveness of the proposed SSRD enabled VSC HVDC to damp multiple torsional modes and providing the basic functionality of power transfer has been validated through damping torque analysis and time-domain simulations, as presented in Chapter 4.

In Chapter 5, an RT-HiL experiment test has been performed to validate the operational performance of the proposed schemes in the 3GB system. Through experimental tests, three cases of the VSC HVDC link operations were evaluated: normal, during an SSR event and while proving the additional service of damping. It has been shown that without proper mitigation schemes

the oscillations initiated by SSR can pass through to the DC side and can jeopardise the HVDC link operation. However, with the proposed schemes the VSC is able to damp SSR upon occurrence utilizing its existing capacity. The provision of active power transfer and SSR damping using the same link has been tested and validated successfully through experiment platforms.

Results obtained from computational simulations and experimental tests do not only show a good correlation but also demonstrate the capability of the developed RT-HiL platform for SSO, AC/DC interaction studies and control system testing. In addition, from numerical EMT and real-time tests results it has been proved that the damping services from VSC HVDC links can be achieved without overrating the capacity of the converters.

7.2.3 Control of VSC in a MTDC Network for AC Grid Stability

The AC grid operations with wind-thermal generations bundled with multi-terminal dc (MTDC) grids under high wind penetrations has been tested and evaluated in Chapter 6. The frequency regulation and stability issues which might arise due to the intermittency of the wind has been presented here. Furthermore, voltage source converter (VSC) technology based MTDC grids have been used here to facilitate the massive wind integration through the provision of ancillary services. This is achieved using a new control scheme named dual-droop embedded with the VSC based MTDC grids. The effectiveness of the dual-droop scheme to accommodate higher wind penetration and its impact on the AC/DC grid stability has been analysed through sensitivity studies and eigenvalue analysis.

Moreover, the performance of the dual-droop scheme in regulating the grid frequency is compared against conventional schemes through time-domain simulations in conjunction with experimental tests. Both through simulation and experimental work, the capabilities of this method are demonstrated. It is concluded that the use of dual-droop scheme could contribute to the large-scale deployment of wind power around the world by providing effective frequency regulation, stability and generation balancing.

7.3 Thesis Contributions

The main contributions of this thesis can be summarised as follows:

- **Analysis of interactions in-terms of SSR in AC/DC grids:** Evaluated the adequacy of linearised power system models, damping torque screening studies and EMT based time-domain analysis for AC/DC interaction studies such as SSR.
- **Design of SSR damping controllers:** The design and implementation of VSC HVDC supplementary SSR damping controllers such as:
 1. **Muti-modal damper:** A multi-modal damper scheme capable of damping multiple torsional modes using cascaded modal filters tuned at targeted SSF components.
 2. **Wideband damper:** A damping approach which is robust enough to stabilize multiple torsional modes associated with the HVDC connected series-compensated network, by acting upon the entire subsynchronous range.
 3. **Adaptive damper:** An adaptive SSFDC capable of estimating and damping SSF components regardless of the configuration of the power system. Due to its damping capabilities irrespective of the modes of oscillation being excited, its use is suitable to increase system resiliency against SSR events.
- **Experimental demonstration of SSR damping:** To prove the function and operational concept of the proposed SSRD schemes in the hybrid AC/DC network, an RT-HiL experimental test-rig was designed and developed to adopt to all the operating conditions of the 3GB test system.
- **Frequency regulation in a wind-thermal bundled AC/DC grid:** A control scheme to enhance the frequency regulation and stability of the AC grid operations with wind-thermal generations bundled with MTDC grids under high wind penetrations.

7.4 Publications reported in this thesis

7.4.1 Journal Papers

- (a) **T. Joseph**, C. E. Ugalde-Loo, S. Balasubramaniam and J. Liang " Real-Time Estimation and Damping of SSR in a VSC HVDC Connected Series-Compensated System" in *IEEE Transactions on Power Systems* (Second Round Review).
- (b) **T. Joseph**, C. E. Ugalde-Loo, S. Balasubramaniam and J. Liang " An Active Wideband SSR damping scheme for Series-Compensated AC/DC Networks" in *IEEE Transactions on Power Delivery* (Under Review).
- (c) **T. Joseph**, J. Goncalves, S. Balasubramaniam, C. E. Ugalde-Loo, and J. Liang, " Flexible Control Strategy in Wind-Thermal Hybrid AC/DC Systems for Higher Renewable Penetration" in *IEEE Transactions on Energy Conversion* (Under Review).
- (d) **T. Joseph**, C. E. Ugalde-Loo, S. Balasubramaniam and J. Liang " Real-time Hardware-in-the-loop Test-rig for Multimodal SSR damping in VSC HVDC connected Series-compensated AC System" in *IET Generation Transmission and Distribution* (Under Review).

7.4.2 Conference Papers

- (a) **T. Joseph**, C. E. Ugalde-Loo and J. Liang, "Subsynchronous oscillatory stability analysis of an AC/DC transmission system," *PowerTech, 2015 IEEE* Eindhoven pp. 1-6, 2015.
- (b) **T. Joseph**, C. E. Ugalde-Loo, J. Liang and P. Coventry, "Active filtering based current injection method for multi modal SSR damping in an AC/DC system," in *17th European Conf. on Power Electronics and Applications (EPE'15 ECCE-Europe)*, Geneva, Switzerland, pp. 1-10, 2015.
- (c) **T. Joseph**, J. Goncalves, C. E. Ugalde-Loo, and J. Liang, "Wind-thermal generation coordination in multi-terminal HVDC-connected AC systems for improved frequency support", in *13th IET Inter. Conf. on AC and DC Power Transm. (ACDC 2017)*, Manchester, UK, pp. 1-6, Feb. 2017.

7.5 Other publications during PhD

7.5.1 Journal Papers

- (a) **T. Joseph**, C. E. Ugalde-Loo, J. Liang and P. Coventry, "Asset management strategies for power electronic converters in transmission networks: Application to HVdc and FACTS devices" in *IEEE Access.*, vol. 6, pp. 21084-21102, 2018..
- (b) S. Balasubramaniam, C. E. Ugalde-Loo, J. Liang, **T. Joseph**, R. King and A. Adamczyk, "Experimental Validation of Dual H-Bridge Current Flow Controllers for Meshed HVdc Grids," in *IEEE Transactions on Power Delivery*, vol. 33, no. 1, pp. 381-392, Feb. 2018.
- (c) S. Balasubramaniam, C. E. Ugalde-Loo, J. Liang, and **T. Joseph**, "Power Flow Management in MTdc Grids using Series Current Flow Controllers," in *IEEE Transactions on Industrial Electronics*, (Under Review).
- (c) K. F. Jose, **T. Joseph**, J. Liang, and C. E. Ugalde-Loo, "An Auxiliary Dead-Band Controller for the Coordination of Fast Frequency Support from Multi-Terminal HVDC Grids," in *IET Renewable Power Generation* (Second Round Review).

7.5.2 Conference Papers

- (a) R. Zheng, **T. Joseph**, S. Wang and J. Liang, "A control strategy for TCSC to mitigate SSR with local measurements," 13th *IET Inter. Conf. on AC and DC Power Transm. (ACDC 2017)*, Manchester, UK, pp. 1-6, 2017.
- (b) **T. Joseph**, J. Liang, G. Li, A. Moon, K. Smith and J. Yu, "Dynamic Control of MVDC Link Embedded in Distribution Network: Case Study on ANGLE-DC," in 1st *IEEE Conf. on Energy Internet and Energy system Integration(EI² 2017)*, Beijing, China, pp. 1-6, 2017.
- (c) G. Li, J. Liang, S. Balasubramaniam, **T. Joseph**, C. E. Ugalde-Loo and K. F. Jose, "Frontiers of DC circuit breakers in HVDC and MVDC systems," in 1st *IEEE Conference on Energy Internet and Energy system Integration(EI² 2017)*, Beijing, China, pp. 1-6, 2017.

7.5.3 International Workshops and Colloquium Presentations

- (a) T. Joseph, " Dynamic interactions and modelling fidelity of AC/DC grids", Supergrid Symposia, Beijing, China, 2015.
- (b) T. Joseph, "AC/DC Interactions and Control," 6th HVDC Doctoral Colloquia, Copenhagen, Denmark, 2015.
- (c) T. Joseph, "Subsynchronous Resonance testing and damping in an AC/DC network using real-time hardware in-the-loop framework," RTDS 2016 European User's Group Meeting, Glasgow, UK, 2016.
- (d) T. Joseph, " Interactive AC/DC grids", special session on Offshore and HVDC grids in 2016 *IEEE International Energy Conference (ENERGYCON)*, Leuven, Belgium, 2016.
- (e) T. Joseph, C. E. Ugalde-Loo, and J. Liang, "Control of VSC-HVdc to Improve the Stability of AC System", poster on the special session on Offshore and HVDC grids in 2016 *IEEE International Energy Conference (ENERGYCON)*, Leuven, Belgium, 2016.
- (f) T. Joseph, "Dynamic performance of a three level NPC based MVDC link in ANGLE DC network," 8th HVDC Doctoral Colloquia, Cardiff, UK, 2017.
- (g) T. Joseph, J. Liang, A. Moon, K. Smith and J. Yu, "Operation and Control of Europe's First Bipolar MVDC link based on Neutral Point Clamped Converters: An ANGLE DC Perspective," in 2nd *IEEE Workshop on Electronic Power Transmission and Distribution (eT&D 2017)*, Aalborg, Denmark, 2017.

7.6 Future Research

The present research work has focussed on the analysis of AC/DC interactions using small-signal stability assessment and the use of that information to devise mitigation measures. This approach can be followed to create potential research avenues which are listed below:

- **AC/DC interaction studies related to other dynamic devices:** The small-signal models devised in Chapter 3, can be used to analyse and study other forms of SSOs in the power

systems. This includes SSCI, SSTI and the recently reported new forms of interactions. Moreover, the damping torque frame-work developed based on EMT platform can be expanded to larger and more complex AC/DC grids for screening negative interactions and resonances.

- **Suitability of the proposed SSRD schemes to damp other forms of SSO:** The SSRD schemes devised and embedded with VSC HVDC controllers in Chapter 4 could be integrated with other power electronic based controllers for damping purposes (for instance, with the service being provided by FACTS devices such as a static VAR compensator, TCSC, STATCOM or WPP converters).
- **Use of RT-HiL platform for interaction studies and control testing:** The RT-HiL platform devised in Chapter 5 could be used for testing the interactions between different power converter assets and the AC system. Moreover, such a platform can be used for testing different damping control schemes before their practical implementation. This includes SSO damping schemes, low-frequency oscillation damping controllers, harmonic mitigation measures etc.
- **Frequency regulation of future AC/DC grids:** The frequency regulation schemes reported in Chapter 6 for AC/DC grids can be integrated with other converters of the MTDC systems and/or offshore WPPs for fast frequency support. In addition, the coordination of WPPs and HVDC converters for frequency regulation in wind-thermal bundled AC/DC system is another research avenue which could be explored. Moreover, coordination of different frequency support schemes can be tested and implemented in the RT-HiL platform devised in Chapter 6.

Appendices

A Modelling of Generator, Multi-mass and Series-compensated Transmission Line

The corresponding detailed linearised state-space model of the synchronous machines is of sixth-order represented by the following state-space equation:

A.1 Generator Model

$$\Delta[\dot{X}_{GE}] = [A_{GE}][\Delta X_{GE}] \quad (\text{A.1})$$

$$\Delta X_{GE} = [\Delta i_d, \Delta i_q, \Delta i_f, \Delta i_{kd}, \Delta i_{kq1}, \Delta i_{kq2}]^T \quad (\text{A.2})$$

with X_{GE} contains the vector of state variables represented by 3.5 and A_{GE} , the state matrix represented by A.3.

$$[A_{GE}] = [L]^{-1}[R] \quad (\text{A.3})$$

Where $[L]$ and $[R]$ are represented as:

$$[L] = \omega_b \begin{bmatrix} -x_d & 0 & x_{md} & x_{md} & 0 & 0 \\ 0 & -x_q & 0 & 0 & x_{mq} & x_{mq} \\ -x_{md} & 0 & x_f & x_{md} & 0 & 0 \\ -x_{md} & 0 & x_{md} & x_{kd} & 0 & 0 \\ 0 & -x_{mq} & 0 & 0 & x_{kq1} & x_{mq} \\ 0 & -x_{mq} & 0 & 0 & x_{mq} & x_{kq2} \end{bmatrix} \quad (\text{A.4})$$

$$[R] = \begin{bmatrix} r_a & -x_q & 0 & 0 & x_{mq} & x_{mq} \\ x_d & r_a & -x_{md} & -x_{md} & 0 & 0 \\ 0 & 0 & -r_f & 0 & 0 & 0 \\ 0 & 0 & 0 & r_{kd} & 0 & 0 \\ 0 & 0 & 0 & 0 & r_{kq1} & 0 \\ 0 & 0 & 0 & 0 & 0 & r_{kq2} \end{bmatrix} \quad (A.5)$$

A.2 Multi-mass Turbine Model

The linearised shaft model consists of the rotor angle and speed of each masses as the state variables and is of 12th order represented by the following state-space equation:

$$\Delta[\dot{X}_{MM}] = [A_{MM}][\Delta X_{MM}] \quad (A.6)$$

$$\Delta X_{MM} = [\Delta\omega_{HP}, \Delta\theta_{HP}, \Delta\omega_{IP}, \Delta\theta_{IP}, \Delta\omega_{LPA}, \Delta\theta_{LPA}, \Delta\omega_{LPB}, \Delta\theta_{LPB}, \Delta\omega, \Delta\delta, \Delta\omega_{EX}, \Delta\theta_{EX}]^T \quad (A.7)$$

with X_{MM} contains the vector of state variables represented by 3.9 and A_{MM} , the state matrix represented by A.8.

$$[A_{MM}] = [M]^{-1}[T] \quad (A.8)$$

Where [M] and [T] are represented as:

$$[M] = \begin{bmatrix} 2H_{HP} & 0 & 0 & 0 & 0 & 0 & 0 & 0 & 0 & 0 & 0 \\ 0 & 2H_{IP} & 0 & 0 & 0 & 0 & 0 & 0 & 0 & 0 & 0 \\ 0 & 0 & 2H_{LPA} & 0 & 0 & 0 & 0 & 0 & 0 & 0 & 0 \\ 0 & 0 & 0 & 2H_{LPB} & 0 & 0 & 0 & 0 & 0 & 0 & 0 \\ 0 & 0 & 0 & 0 & 2H_{GE} & 0 & 0 & 0 & 0 & 0 & 0 \\ 0 & 0 & 0 & 0 & 0 & 2H_{EX} & 0 & 0 & 0 & 0 & 0 \\ 0 & 0 & 0 & 0 & 0 & 0 & 0 & 0 & 0 & 0 & 0 \\ 0 & 0 & 0 & 0 & 0 & 0 & 0 & 0 & 0 & 0 & 0 \\ 0 & 0 & 0 & 0 & 0 & 0 & 0 & 0 & 0 & 0 & 0 \\ 0 & 0 & 0 & 0 & 0 & 0 & 0 & 0 & 0 & 0 & 0 \\ 0 & 0 & 0 & 0 & 0 & 0 & 0 & 0 & 0 & 0 & 0 \\ 0 & 0 & 0 & 0 & 0 & 0 & 0 & 0 & 0 & 0 & 0 \end{bmatrix} \quad (A.9)$$

$$[T] = \begin{bmatrix} -D_{HP} & 0 & 0 & 0 & 0 & 0 & 0 & -K_{HI} & -K_{HI} & 0 & 0 & 0 & 0 \\ 0 & -D_{IP} & 0 & 0 & 0 & 0 & 0 & -K_{HI} & K_{HI} - K_{IA} & K_{IA} & 0 & 0 & 0 \\ 0 & 0 & -D_{LPA} & 0 & 0 & 0 & 0 & 0 & -K_{IA} & K_{IA} - K_{AB} & K_{AB} & 0 & 0 \\ 0 & 0 & 0 & -D_{LPB} & 0 & 0 & 0 & 0 & 0 & -K_{AB} & K_{AB} - K_{BG} & K_{BG} & 0 \\ 0 & 0 & 0 & 0 & -D_{GE} & 0 & 0 & 0 & 0 & 0 & K_{BG} & -K_{BG} - K_{GEX} & K_{GEX} \\ 0 & 0 & 0 & 0 & 0 & 0 & -D_{EX} & 0 & 0 & 0 & 0 & K_{GEX} & -K_{GEX} \\ \omega_b & 0 & 0 & 0 & 0 & 0 & 0 & 0 & 0 & 0 & 0 & 0 & 0 \\ 0 & \omega_b & 0 & 0 & 0 & 0 & 0 & 0 & 0 & 0 & 0 & 0 & 0 \\ 0 & 0 & \omega_b & 0 & 0 & 0 & 0 & 0 & 0 & 0 & 0 & 0 & 0 \\ 0 & 0 & 0 & \omega_b & 0 & 0 & 0 & 0 & 0 & 0 & 0 & 0 & 0 \\ 0 & 0 & 0 & 0 & \omega_b & 0 & 0 & 0 & 0 & 0 & 0 & 0 & 0 \\ 0 & 0 & 0 & 0 & 0 & \omega_b & 0 & 0 & 0 & 0 & 0 & 0 & 0 \\ 0 & 0 & 0 & 0 & 0 & 0 & \omega_b & 0 & 0 & 0 & 0 & 0 & 0 \end{bmatrix}$$

(A.10)

A.3 Series-compensated Transmission Line Model

The linearised transmission line model consists of the voltages and current as state variable and in state-space format it can be expressed as:

$$\Delta[\dot{X}_{TN}] = [A_{TN}][\Delta X_{TN}] \quad (A.11)$$

with X_{TN} contains the vector of state variables represented by 3.22 and A_{TN} , the state matrix represented by A.13.

$$\Delta X_{TN} = [\Delta i_{Ld}, \Delta i_{Lq}, \Delta V_{td}, \Delta V_{tq}, \Delta e_{cd}, \Delta e_{cq}]^T \quad (A.12)$$

$$[A_{TN}] = [W]^{-1}[Y] \quad (A.13)$$

Where, $[W]$ and $[Y]$ can be represented as:

$$[W] = \begin{bmatrix} X_L & 0 & 0 & 0 & 0 & 0 \\ 0 & X_L & 0 & 0 & 0 & 0 \\ 0 & 0 & X_{csh1} & 0 & 0 & 0 \\ 0 & 0 & 0 & X_{csh1} & 0 & 0 \\ 0 & 0 & 0 & 0 & X_C & 0 \\ 0 & 0 & 0 & 0 & 0 & X_C \end{bmatrix} \quad (A.14)$$

$$[Y] = \begin{bmatrix} -R_L & X_L & 1 & 0 & -1 & 0 \\ -X_L & -R_L & 0 & 1 & 0 & -1 \\ -1 & 0 & 0 & 0 & 0 & 0 \\ 0 & -1 & 0 & 0 & 0 & 0 \\ 0 & 0 & 0 & 0 & 0 & X_C \\ 0 & 0 & 0 & 0 & -X_C & X_C \end{bmatrix} \quad (A.15)$$

B Dynamic Modelling of VSC-HVDC Link

The final linearised relation of VSC-HVDC link in state-space format, including the converter controls and DC link can be written as:

$$\Delta[X_{HVDC}] = [A_{HVDC}][\Delta X_{HVDC}] \quad (B.1)$$

with ΔX_{HVDC} containing the vector of state variables represented by 3.36 and A_{HVDC} is the state matrix, represented by B.3 :

$$\Delta X_{HVDC} = [\Delta X_{PQ}, \Delta X_{DCt}, \Delta X_{DCQ}]^T \quad (B.2)$$

$$[A_{HVDC}] = \begin{bmatrix} [A_1] & [0] & [A_{DC31}] \\ [0] & [A_2] & [A_{DC32}] \\ [A_{DC13}] & [0] & [A_3] \end{bmatrix} \quad (B.3)$$

Each elements of the final $[A_{HVDC}]$ matrix can be represented as follows:

$$A_1 = \begin{bmatrix} [A_{1AC}] & [A_{1ACDC}] \\ [A_{1DCAC}] & [A_{1DC}] \end{bmatrix} \quad (B.4)$$

$$A_{1AC} = \begin{bmatrix} 0 & \omega_b & \omega_b/C_f & 0 \\ \omega_b & 0 & 0 & \omega_b/C_f \\ -\omega_b/L_f & 0 & \frac{\omega_b}{L_f}(k_{pp1} + R_g) & \omega_b \\ 0 & -\omega_b/L_f & \omega_b & \frac{\omega_b}{L_f}(k_{pp1} + R_g) \end{bmatrix} \quad (B.5)$$

$$A_{1ACDC} = \begin{bmatrix} & & [0]_{2 \times 4} & \\ \omega_b k_{iip1}/L_f & 0 & -\omega_b k_{iip1} k_{pp1}/L_f & 0 \\ 0 & \omega_b k_{iiq1}/L_f & 0 & \omega_b k_{iiq1} k_{pq1}/L_f \end{bmatrix} \quad (B.6)$$

$$A_{1DCAC} = \begin{bmatrix} & -1 & 0 \\ [0]_{4 \times 2} & 0 & -1 \\ & 0 & 0 \\ & 0 & 0 \end{bmatrix} \quad (B.7)$$

$$A_{1DCAC} = \begin{bmatrix} & k_{iip1} & 0 \\ [0]_{4 \times 2} & 0 & k_{iiq1} \\ & 0 & 0 \\ & 0 & 0 \end{bmatrix} \quad (B.8)$$

Elements of $[A_{HVDC}]$ related to the inverter (VSC2), e.g., A_2 , can be expressed in a similar way

as above. The DC line sub-matrix can be written as:

$$A_{DC13} = \frac{1}{C_{dc}V_{dc0}} \begin{bmatrix} I_{1d0}\omega_b & I_{1q0}\omega_b & K_1 & K_2 & 0 & 0 & -I_{1d0}\omega_b & -I_{1d0}\omega_b \\ 0 & 0 & 0 & 0 & 0 & 0 & 0 & 0 \\ 0 & 0 & 0 & 0 & 0 & 0 & 0 & 0 \end{bmatrix} \quad (B.9)$$

$$A_{DC13} = \frac{1}{C_{dc}V_{dc0}} \begin{bmatrix} I_{2d0}\omega_b & I_{2q0}\omega_b & K_3 & K_4 & 0 & 0 & -I_{2d0}\omega_b & -I_{2d0}\omega_b \\ 0 & 0 & 0 & 0 & 0 & 0 & 0 & 0 \\ 0 & 0 & 0 & 0 & 0 & 0 & 0 & 0 \end{bmatrix} \quad (B.10)$$

$$A_{DC31} = \begin{bmatrix} [0]_{2 \times 3} & & \\ \omega_b k_{ip1}/L_c & 0 & 0 \\ [0]_{5 \times 3} & & \end{bmatrix} \quad (B.11)$$

$$A_{DC32} = \begin{bmatrix} [0]_{2 \times 3} & & \\ \omega_b k_{idc}/L_c & 0 & 0 \\ [0]_{5 \times 3} & & \end{bmatrix} \quad (B.12)$$

$$A_{1AC} = \begin{bmatrix} K_5 & \omega_b/C_{dc} & \omega_b/C_{dc} \\ -\omega_b/L_c & \omega_b R_{dc}/L_c & \omega_b R_{dc}/L_c \\ \omega_b R_{dc}/L_c & -\omega_b/L_c & -\omega_b/L_c \end{bmatrix} \quad (B.13)$$

Appendix B. Dynamic Modelling of VSC-HVDC Link

where,

$$\begin{aligned}
 K_1 &= -2I_{1do}k_{pp1}\omega_b + V_{1d0}\omega_b + I_{1do}k_{ip1}\omega_b + k_{ip1}k_{pp1}\omega_b \\
 K_2 &= -2I_{1qo}k_{pq1}\omega_b + V_{1q0}\omega_b + I_{1qo}k_{iq1}\omega_b + k_{iq1}k_{pq1}\omega_b \\
 K_3 &= -2I_{1do}k_{pvd c}\omega_b + V_{1d0}\omega_b + I_{1do}k_{idc}\omega_b + k_{idc}k_{pdc}\omega_b \\
 K_4 &= -2I_{1qo}k_{pq1}\omega_b + V_{1q0}\omega_b + I_{1qo}k_{iiq1}\omega_b + k_{iiq1}k_{pq1}\omega_b \\
 K_5 &= \frac{1}{V_{dc0}}[-I_{1do}k_{pp1}\omega_b - (V_{1d0} + I_{1do}k_{ip1} + k_{pq1}k_{iiq1})I_{1do}] \\
 &\quad + \frac{1}{V_{dc0}}[I_{1qo}\omega_b(I_{1qo}k_{pdc} - k_{pq1}k_{iidc} - k_{iq1})I_{1qo}]
 \end{aligned}$$

The final linearised state matrices A_{sys1} and A_{sys2} to generate the eigenvalues suitable for screening SSR can be obtained by combining the matrix equations A.3 to B.13. Using these equations the final state-space format for the MFBM model can be derived as in B.14. The state matrix A_{sys1} is represented by the combination of matrices from the associated network. Similar procedure is followed to derive the state matrix A_{sys2} for the 3GB model.

$$\begin{bmatrix} \Delta[\dot{X}_{GE}] \\ \Delta[\dot{X}_{MM}] \\ \Delta[\dot{X}_{TN}] \\ \Delta[\dot{X}_{HVDC}] \end{bmatrix} = \begin{bmatrix} A_{GEGE} & A_{GEMM} & A_{GETN} & A_{GEHVDC} \\ A_{MG} & A_{MMMM} & A_{MMTN} & A_{MMHVDC} \\ A_{TNGE} & A_{TNMM} & A_{TNTN} & A_{TNHVDC} \\ A_{HVD CGE} & A_{HVD CMM} & A_{HVD CTN} & A_{HVD CHVDC} \end{bmatrix} \times \begin{bmatrix} \Delta X_{GE} \\ \Delta X_{MM} \\ \Delta X_{TN} \\ \Delta X_{HVDC} \end{bmatrix} \quad (B.14)$$

C Study System Parameters

Tables. C.1 and C.2 includes the both the AC and DC parameters of the two systems used in this thesis: Modified IEEE First Bench Mark Model (MFBM) [125] and the three machine Great Britain (3GB) Model [127]. The synchronous generator electrical parameters used for both systems are identical and are provided in Table. C.3. The mechanical mass turbine parameters: Inertias, self and mutual damping coefficients and torsional stiffness of the shaft are provided in Tables.C.4, C.5 and C.6 respectively.

C.1 Modified IEEE First Bench Mark Model

Table C.1: Modified IEEE First Bench Mark Model: System parameters

	Parameter	Value
AC System	AC transformer	539 kV/26 kV
	AC base Power (S_b)	500 MVA
	Frequency	60 Hz
	AC voltage	539 kV
	AC inductance and resistance	432.3 mH/6.08 m Ω
DC System	Converter transformer	539 kV/125 kV
	DC base Power (S_b)	500 MVA
	Converter f_{sw}	1650 Hz
	DC capacitance	600 μ F
	DC voltage	400 kV
	DC Phase inductance and resistance	40.89 mH/153.9 m Ω

C.2 Three GB Model

Table C.2: Three GB model: System parameters

	Parameter	Value
AC System	Southern Scotland	2800 MVA
	Northern Scotland	2400 MVA
	England and Wales	21000 MVA
	AC transformer	33 kV/400 kV
	AC base Power (S_b)	1000 MVA
	Frequency	50 Hz
	AC voltage	400 kV
	AC inductance and resistance	0.050 H/1.6 m Ω
DC System	Converter transformer	400 kV/230 kV
	DC base Power (S_b)	1000 MVA
	Converter f_{sw}	1650 Hz
	DC capacitance	600 μ F
	DC voltage	640 kV
	DC Phase inductance and resistance	40.89 mH/153.9 m Ω

Table C.3: Synchronous Generator: Electrical parameters

$R_a = 0.002$	$X_d = 0.17$	$X_q = 2.07$	$X'_q = 0.906$	$X''_q = 0.234$	$X'_d = 0.308$
$X''_d = 0.234$	$X_{mq} = 1.9$	$X_{md} = 1.96$	$\tau'_{do} = 6.08s$	$\tau''_{do} = 0.0526s$	$\tau''_{qo} = 0.0353s$

Table C.4: Multi-mass parameters:Inertias (in MWs/MVA)

$H_{HP} = 0.0928$	$H_{IPA} = 0.1555$	$H_{LA} = 0.8586$	$H_{LB} = 0.8842$	$H_G = 0.8684$	$H_{EX} = 0.0342$
-------------------	--------------------	-------------------	-------------------	----------------	-------------------

Table C.5: Multi-mass parameters:Self and mutual damping coefficients (in p.u. T/p.u. speed dev.)

$D_H = D_I = D_{LA} = D_{LB} = 0.1, D_G = D_X = 0$
$D_{HI} = D_{IA} = D_{AB} = D_{BG} = 0.2, D_{GX} = 0.005$

Table C.6: Multi-mass parameters:Torsional stiffness (in p.u. T/rad)

$K_{HI} = 19.303$	$K_{IA} = 34.929$	$K_{AB} = 52.038$	$K_{BG} = 70.852$	$K_{GX} = 2.822$
-------------------	-------------------	-------------------	-------------------	------------------

D Control Parameters

The proportional integral (PI) control parameters used for the VSC-HVDC link in both PSCAD time-domain simulations and experimental testes are provided in Tables. D.1 and D.2.

Where, the PI controllers are represented in the form: $K(s) = K_p + \frac{K_i}{s}$.

D.1 PSCAD Simulation

Table D.1: Controller Parameters: PSCAD SSR Simulations

Device	Controller	Parameters
VSC	Inner-current(dq)	$K_p = 50, K_i = 10000$
	DC voltage	$K_p = 0.2, K_i = 20$
	Active power	$K_p = 0.005, K_i = 0.1$
	Reactive power	$K_p = 0.2, K_i = 25$

D.2 RT-HiL Experiments

Table D.2: Controller Parameters: RT-HiL Tests

Device	Controller	Parameters
VSC	Inner-current(dq)	$K_p = 45, K_i = 45000$
	DC voltage	$K_p = 0.2, K_i = 20$
	Active power	$K_p = 0.2, K_i = 20$
	Reactive power	$K_p = 0.3, K_i = 10$

E Simulation and Experiment Models

This section details the simulation and experimental models used in this thesis.

E.1 Simulation Models

The modified FBM was implemented in PSCAD/EMTDC and is presented in Figure E.1, while the 3GB AC/DC model is depicted in Figure E.2. The control system implementation of the VSC HVDC link used for simulation tests in this thesis is shown in Figure E.3.

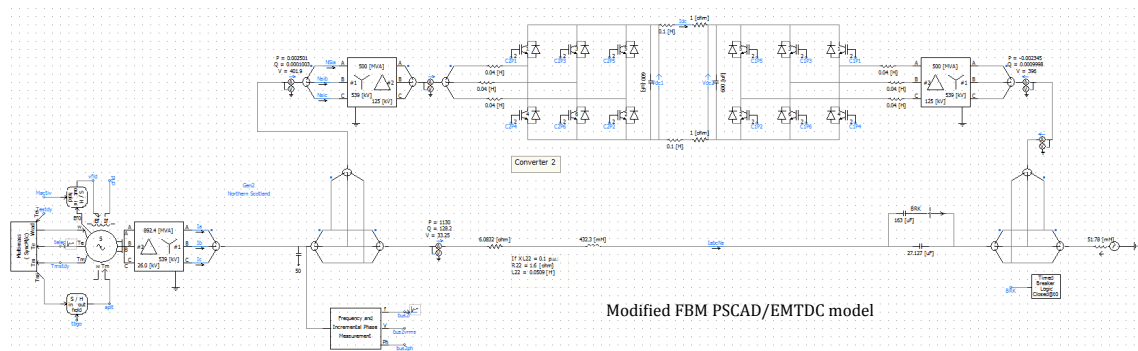


Figure E.1: MFBM AC/DC system model implemented in PSCAD/EMTDC.

Appendix E. Simulation and Experiment Models

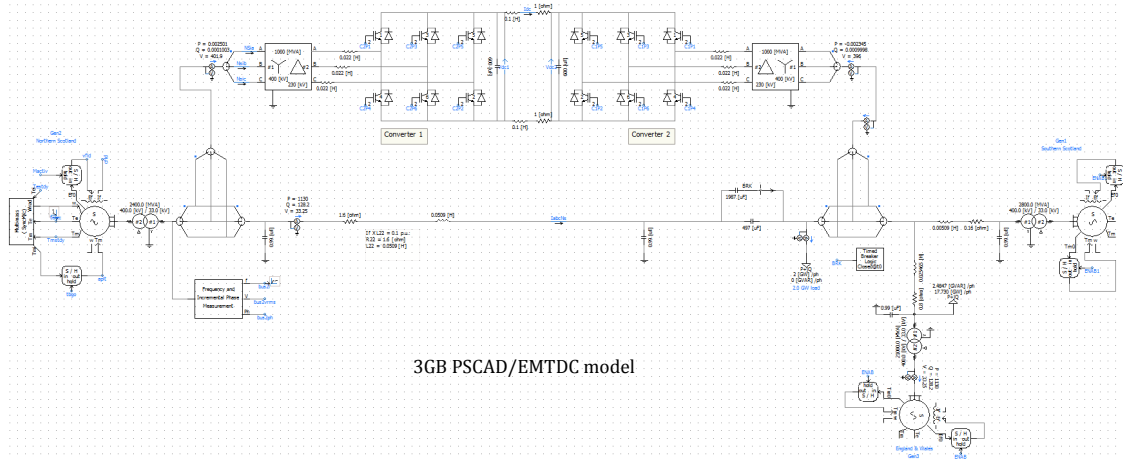
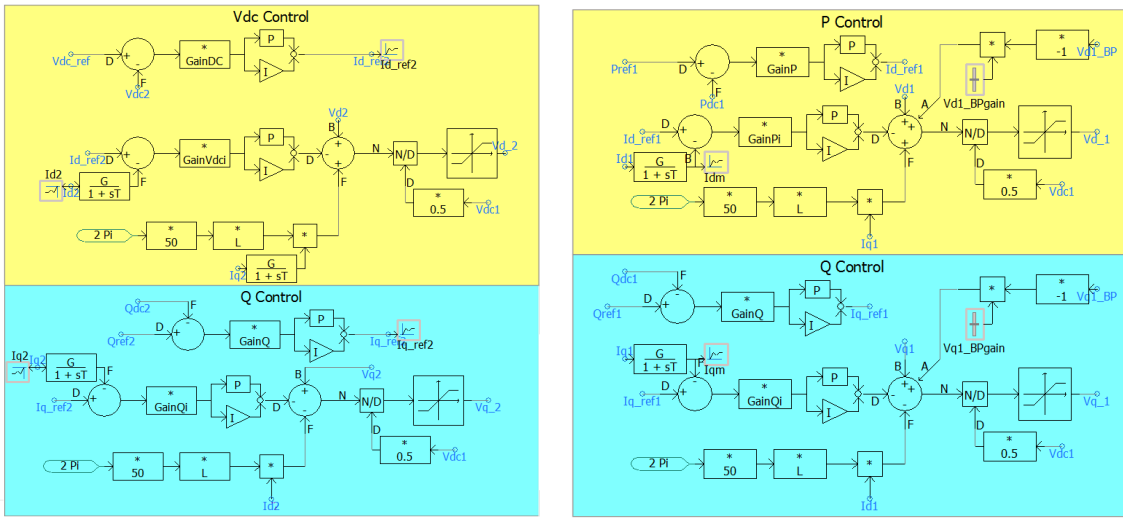


Figure E.2: 3GB AC/DC system model implemented in PSCAD/EMTDC.



(a) VSC 1 control system (VdcQ) in PSCAD/EMTDC

(a) VSC 2 control system (PQ) in PSCAD/EMTDC with SSR

Figure E.3: VSC HVDC control system implemented in PSCAD/EMTDC.

E.2 RSCAD Model

The 3GB AC system components implemented in RSCAD/RTDS for Rt-HiL test is presented in Figure E.4. The hardware outputs from the RSCAD model is shown in yellow colour, while the HiL closed loop implementation is shown as current source. The VSC HVDC with DC line has been implemented in physical test-rig and connected through a grid simulator to RTDS module (see Figure E.5).

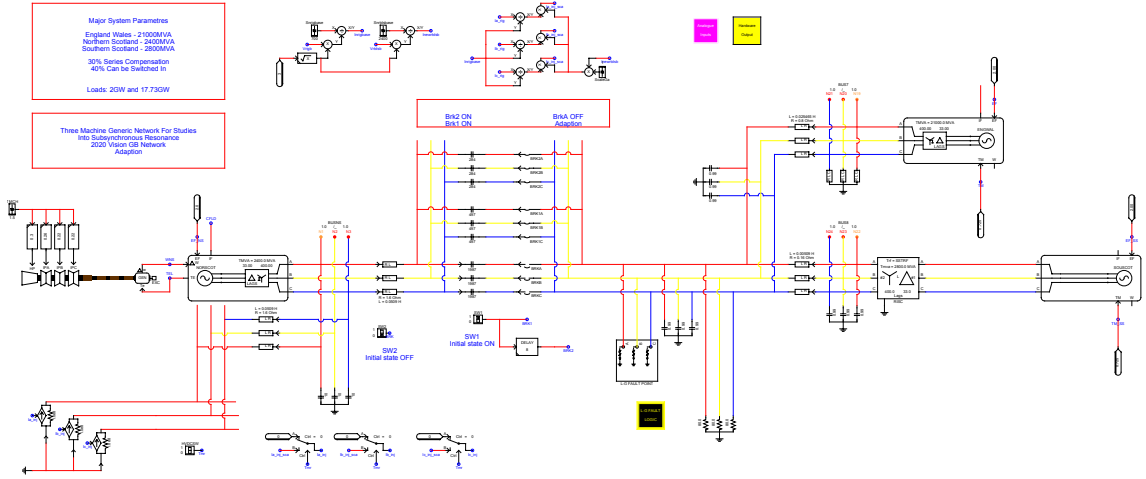


Figure E.4: 3GB AC system model implemented in RSCAD/RTDS.

E.3 High level RT-HiL configuration

A high-level Rt-HiL configuration and connection is outlined in this section. The full set-up as shown in Figure E.5 comprises of RSCAD/RTDS, where the 3GB AC system components (without VSC HVDC link) were implemented. The HVDC link comprising 2L VSC converters and DC network, controlled by dSPACE module together forms the VSC HVDC physical test-rig. The two platforms were connected through grid simulator whose input is from the RTDS and outputs 140 V(see Figure E.5).

The series-compensated transmission line is implemented in the RTDS which is connected to the multimass turbine-generator. The subsynchronous current component develops upon an SSR event is controlled to zero using the VSC converter connected close to the generator. This is achieved through controlled current injection from the VSC, which contains anti-phase current to cancel out the SSF component and prevent it from interacting with the torsional modes of the turbine-generator. The RT-HiL experimental test procedure can be summarised in three stages, as shown in Figure E.5.

- **Stage1:** The 3GB AC system with series-compensated transmission line and single and multi-mass enabled turbine-generators (without VSC HVDC link) is modelled in RSCAD platform of RTDS. The high-voltage measurements are scaled down to low voltage suitable for VSC test-rig operation and are fed to grid simulator (GS) (Stage 2) through the GTAO

port of RTDS firm ware.

- Stage2: The GS receives inputs from the AC system modelled in RTDS and the output is connected to the VSC physical set-up operating at 140 V AC. After receiving the signals from VSCs (Stage 3) the HiL loop is closed by measuring the currents at the VSC/GS output terminal, which are fed back to the RTDS AC system model through the GTAI port. The analogue input measurements are scaled-up from low voltage to high voltage suitable for the AC system model in the RSCAD. A controllable current source is used to emulate the VSC injection at the AC bus close to the generator where actual VSC HVDC link is connected.
- Stage3: This stage comprises the VSC HVDC link operation and control. The VSC HVDC link is operated from inputs for VSC 1 from GS and VSC 2 from lab grid connected through transformers. The control systems of both VSCs are embedded in dSPACE platform coded through Simulink. The HVDC link is established through a DC network connected between VSC 1 and 2. The connection of VSC1 to the AC system is made through the GS (stage 2) and controllable current source modelled in the RSCAD.

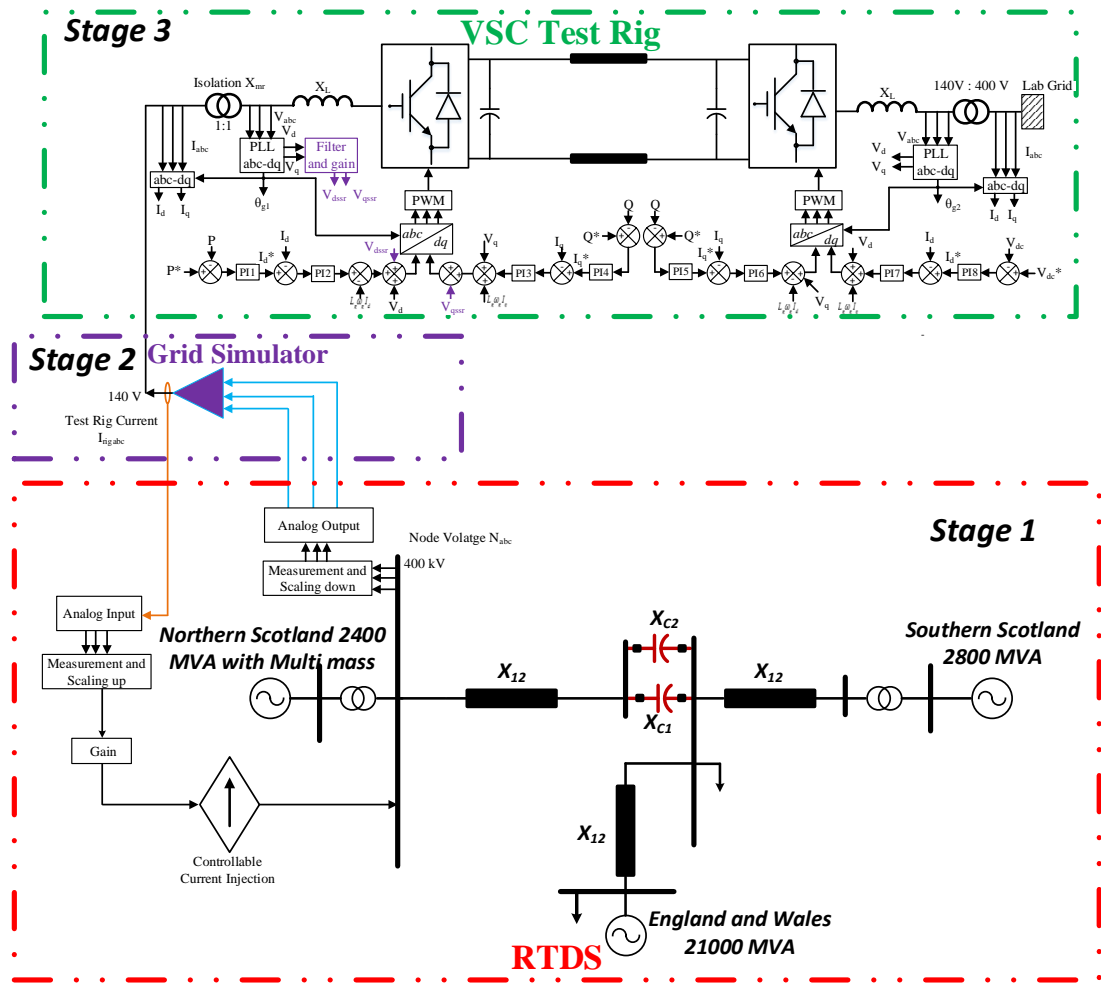


Figure E.5: High-level diagram of RT-HiL set-up for SSR damping.

Bibliography

- [1] "Renewable Energy Capacity Statistics", International Renewable Energy Agency (IRENA), March, 2017.
- [2] "Renewables 2017 - Global Status Report", Renewable Energy Policy Network for 21st century (REN21), May, 2017.
- [3] B. Kroposki, *et.al.*, "Achieving a 100% Renewable Grid: Operating Electric Power Systems with Extremely High Levels of Variable Renewable Energy", *IEEE Power & Energy Mag.*, vol. 15, no. 2, pp. 61-73, April, 2017.
- [4] "Wind Energy Scenarios for 2020," European Wind Energy Association (EWEA), July, 2014.
- [5] "Wind Energy Scenarios for 2030," European Wind Energy Association (EWEA), July, 2015.
- [6] D. van Hertem, O. Gomis-Bellmunt, and J. Liang (eds.), *HVDC Grids: For Offshore and Supergrid of the Future*. USA: Wiley, 2017.
- [7] Electricity Networks Strategy Group, "Our Electricity Transmission Network: A Vision for 2020," 2012.
Available:https://assets.publishing.service.gov.uk/government/uploads/system/uploads/attachment_data/file/48274/4263-ensgFull.pdf. [Accessed: 12-Feb-2014].
- [8] M. P. Bahrman and B. K. Johnson, "The ABCs of HVDC transmission technologies," *IEEE Power & Energy Mag.* 5 (2), pp 32-44, 2007.
- [9] D. Tiku, "dc Power Transmission: Mercury-Arc to Thyristor HVdc Valves [History]," *IEEE Power & Energy Mag.* 12 (2), pp 76 -96, 2014.

Bibliography

- [10] ENTSO-E, "Technologies for transmission systems", Ten-Year Network Development Plan (TYNDP), 2017. [Online], Available: <http://tyndp.entsoe.eu/2016/insight-reports/technology/>. [Accessed: 14-Jan-2017].
- [11] "Series Compensation (SC)," <http://www.energy.siemens.com/hq/en/powertransmission/facts/series-compensation/>, Siemens Energy, 2017. [Accessed: 22-Nov-2017].
- [12] P.M.Anderson and R.G.Farmer, *Series Compensation of Power Systems*: PBLSH Inc, 1996.
- [13] C. Hor, J. Finn, G. Thumm and S. Mortimer, "Introducing series compensation in the UK transmission network". 10th *IET Inter. Conf. on AC and DC Power Transm. (ACDC 2012)*, Birmingham, pp. 1-4, 2012.
- [14] National Grid, "Electricity Ten Year Statement 2014: UK electricity transmission," 2014. Available: <https://www.nationalgrid.com/sites/default/files/documents/37790-ETYS%202014.pdf>. [Accessed: 02-March-2016].
- [15] National Grid, "System Operability Framework 2015", Nov, 2015. Available: <https://www.nationalgrid.com/sites/default/files/documents/44046-SOF%202015%20Full%20Document.pdf>. [Accessed: 25-Jan-2016].
- [16] <https://www.gov.uk/government/policies/increasing-the-use-of-low-carbon-technologies>. [Online], [Accessed: 05-Aug-2017].
- [17] Department of Energy and Climate Change Gov of UK, "Renewable Energy Roadmap Update", 2013. <https://www.gov.uk/government/collections/uk-renewable-energy-roadmap>, [Accessed: 15-Sep-2017].
- [18] National Grid, "Future Energy Scenarios," 2017. <http://fes.nationalgrid.com/fes-document/fes-2017/> [Accessed: 15-Sep-2017].
- [19] S. Achenbach, V. Barry, C. H. Bayfield and P. F. Coventry, "Increasing the GB electricity transmission networks' power transfer capability between North and South — The Western HVDC Link," 10th *IET Inter. Conf. on AC and DC Power Transm. (ACDC 2012)*, Birmingham, pp. 1-4, 2012.

- [20] National Grid, "NETS security and quality of supply standard." 2014. [Online]. Available: <http://www2.nationalgrid.com/uk/industry-information/electricitycodes/sqss/the-sqss/> [Accessed: 22-April-2017].
- [21] Carlos Ugalde, Nick Jenkins, "Future GB Power System Stability Challenges and Modelling Requirements", IET, Aug 2017.
- [22] D. Van Hertem and M. Ghandhari, "Multi-terminal VSC HVDC for the European supergrid: Obstacles," *Renew. Sustain. Energy Rev.*, vol. 14, no. 9, pp. 3156–3163, Dec. 2010.
- [23] Anaya-Lara, O., Campos-Gaona, D., Moreno-Goytia, E., 'Offshore wind energy generation: control, protection, and integration to electrical systems' (John Wiley & Sons, Inc., Chichester, UK, 2014, 1st edn.).
- [24] N. Flourentzou, V. G. Agelidis and G. D. Demetriades, "VSC-Based HVDC Power Transmission Systems: An Overview," *IEEE Trans. Power Elec.*, vol. 24, no. 3, pp. 592-602, March 2009.
- [25] IEEE SSR Working Group, "Proposed Terms and Definitions for Subsynchronous Oscillations," *IEEE Trans. Power App. Syst.*, vol. 99, pp.506-511, 1980.
- [26] P. M. Anderson, B. L. Agrawal, and J. E. Van Ness, *Subsynchronous Resonance in Power Systems*. Piscataway, NJ, USA: IEEE Press, 1990.
- [27] K. R. Padiyar, *Analysis of Subsynchronous Resonance in Power Systems*. Boston, MA, USA: Kluwer, 1999.
- [28] L. C. Gross, "Sub-synchronous grid conditions: New event, new problem, and new solutions," in *Proc. Western Protective Relay Conf.*, 2010, pp. 1–5.
- [29] National Grid, "Network Options assessment report", 2017-18. <https://www.nationalgrid.com/uk/publications/network-options-assessment-noa>. [Accessed: 15-Nov-2017].
- [30] "NETS security and quality of supply standard GSR018/GC0077: Sub-Synchronous Oscillations" Report March 2017, <https://www.ofgem.gov.uk/publications-and-updates/gsr018gc0077-sub-synchronous-oscillations>. [Accessed: 07-October-2017].

Bibliography

- [31] National Grid, "System Operability Framework 2017", Nov, 2017.
<https://www.nationalgrid.com/uk/publications/system-operability-framework-sof>.
[Accessed: 21-Nov-2017].
- [32] "IET GB Power System Modelling Capability Reports", Aug 2017;
<http://www.theiet.org/sectors/energy/resources/modelling-reports/index.cfm>. [Accessed: 12-Nov-2017].
- [33] O. Daniel Adeuyi, "Grid Connection of Offshore Wind Farms through Multi-Terminal High Voltage Direct Current Networks," PhD Thesis, Cardiff Univeristy, 2016.
- [34] D. Gross and S. Bolognani and B.K. Poolla and F. Dörfler, "Increasing the Resilience of Low-inertia Power Systems by Virtual Inertia and Damping," *Bulk Power Systems Dynamics and Control Symposium (IREP)*, Portugal, Sep 2017.
- [35] F. D. Bianchi, J. L .Domínguez-Garcíaand and O. Gomis-Bellmunt, "Control of multi-terminal HVDC networks towards wind power integration: A review." *Renewable and Sustainable Energy Rev.* vol.55, pp. 1055-1068, 2016.
- [36] J. Jallad, M. Saad, and M. Hazlie, "Frequency Regulation Strategies in Grid Integrated Offshore Wind Turbines via VSC-HVDC Technology: A Review." *Energies* vol.10, no.9, pp. 12-44, 2017.
- [37] C. Luo and B. T. Ooi, "Frequency Deviation of Thermal Power Plants Due to Wind Farms", *IEEE Trans. on Energ. Conv.*, vol. 21, pp. 708-716, Aug. 2006.
- [38] M. R. Davidson, D. Zhang, W. Xiong, X. Zhang, and V.J. Karplus, "Modelling the potential for wind energy integration on China's coal-heavy electricity grid", *Nature Energy*, vol. 1 pp. 160-86, June 2016.
- [39] W. Pei, *et.al.*, "Temporal-spatial analysis and improvement measures of Chinese power system for wind power curtailment problem", *Renew. Sustain. Energy Rev.*, vol. 49, pp. 148-168, May 2015.
- [40] M. Barnes, D. Van Hertem, S. P. Teeuwssen and M. Callavik, "HVDC Systems in Smart Grids," *Proceedings of the IEEE*, vol. 105, no. 11, pp. 2082-2098, Nov. 2017.

-
- [41] Siemens data sheet, "AC/DC grids: Concepts and design for mixed AC/DC grids," 2011. <https://www.siemens.com/content/dam/webassetpool/mam/tag-siemens-com/smdb/energy-management/services-power-transmission-power-distribution-smart-grid/consulting-and-planning/power-systems-consulting/pti-psc-ac-dc-grids-datasheet.pdf>. [Accessed: 07-May-2016].
- [42] Siemens, "High Voltage Direct Current Transmission - Proven Technology for Power Exchange," 2010. <http://www.siemens.co.in/pool/>. [Accessed: 11-June-2017].
- [43] ABB, "Special Report 60 years of HVDC", 2014. <http://new.abb.com/grid/60-years-of-hvdc>. [Accessed: 11-June-2017].
- [44] National Grid, "High Voltage Direct Current Electricity – technical information", Fact sheet, 2010. <https://www.nationalgrid.com/sites/default/files/documents/13784-High%20Voltage%20Direct%20Current%20Electricity%20%E2%80%93%20technical%20information.pdf>. [Accessed: 18-July-2017].
- [45] J. Beerten, O. Gomis-Bellmunt, X. Guillaud, J. Rimez, A. van der Meer and D. Van Hertem, "Modeling and control of HVDC grids: a key challenge for the future power system." *Power Systems Computation Conference (PSCC), 2014. IEEE*, 2014.
- [46] A.G. Endegnanew, "Stability Analysis of High Voltage Hybrid AC/DC Power Systems," PhD Thesis, NTNU, 2017.
- [47] A. Adrees, "Risk Based Assessment of Subsynchronous Resonance in AC/DC Systems," PhD Thesis, University of Manchester, 2014.
- [48] M Benasla, T Allaoui, M Brahami, M Denai and V. K. Sood, "HVDC links between North Africa and Europe: Impacts and benefits on the dynamic performance of the European system", *Renew. Sustain. Energy Rev.*, vol. 82, no. 3, 2018, pp. 3981-3991, 2017.
- [49] L Liu, and C Liu, "VSCs-HVDC may improve the Electrical Grid Architecture in future world." *Renew. Sustain. Energy Rev.* 62 pp. 1162-1170, 2016.
- [50] P. Kundur, *et.al.*, "Definition and Classification of Power System Stability IEEE/CIGRE Joint Task Force on Stability Terms and Definitions," *IEEE Trans. Power Syst.*, vol. 19, pp. 1387-1401, 2004.

Bibliography

- [51] N. G. Hingorani, High-voltage DC transmission: A power electronics workhorse, *IEEE Spectrum*. vol. 33, no.4, pp. 63-72, 1996.
- [52] J. Arrillaga, *High Voltage Direct Current Transmission*., London, U.K. Inst. Elect. Eng., 1998.
- [53] W. Long and S. Nilsson, HVDC transmission: yesterday and today, *IEEE Power & Energy Mag.* vol. 5 no. 2, pp. 22-31, 2007.
- [54] J. Arrillaga, Y. H. Liu, and N. R. Watson, *Flexible Power Transmission: The HVDC Options*. Chichester: Jhon Wiley & Sons, 2007.
- [55] W. Wang, G. Wang, M. Andersson, "Development in UHVDC Multi-Terminal and VSC DC Grid," *International High Voltage Direct Current Conference (HVDC 2016)*, China.
- [56] M. Barnes and A. Beddard. "Voltage source converter HVDC links—the state of the art and issues going forward." *Energy Procedia* 24 108-122, 2012.
- [57] G. Reed, R. Pape, and M. Takeda, "Advantages of voltage sourced converter (VSC) based design concepts for FACTS and HVDC-link applications," *IEEE PES General Meeting*, vol. 3, p. 1821, 2003.
- [58] M. Yin, G. Li, H. Liang, and M. Zhou, "Modeling of VSC-HVDC and its active power control scheme," in *2004 International Conference on Power System Technology, 2004.PowerCon.*, vol.2, pp. 1351-1355, 2005.
- [59] S. Li, T. A. Haskew and L. Xu, "Control of HVDC light system using conventional and direct current vector control approaches." *IEEE Trans. Power Elec.* vol.25, no.12, pp: 3106-3118, 2010.
- [60] A. Nami, J. Liang, F. Dijkhuizen and G. D. Demetriades, "Modular Multilevel Converters for HVDC Applications: Review on Converter Cells and Functionalities," *IEEE Trans. Power Elec.*, vol. 30, no. 1, pp. 18-36, Jan. 2015.
- [61] ABB press releases, "ABB wins \$450 million order for Norway-UK HVDC interconnection", 2015. [Accessed: 18-July-2017]. <http://www.abb.co.uk/cawp/seitp202/992f3a8e32ca36c1c1257e8200234aa1.aspx>.

- [62] CIGRE WG Report, "Control Methodologies for Direct Voltage and Power Flow in a meshed HVDC Grid," *CIGRE report, WG B 4.58*. Paris, ISBN : 978-2-85873-402-3, Sep 2017.
- [63] R. L. Cresap, W. A. Mittelstadt, D. N. Scott and C. W. Taylor, "Operating experience with modulation of the pacific HVDC intertie," *IEEE Trans. Power App. Syst.*, vol. 97, no. 4, pp. 1053–1059, Jul. 1978.
- [64] Y. Pipelzadeh, B. Chaudhuri and T. C. Green, "Control Coordination Within a VSC HVDC Link for Power Oscillation Damping: A Robust Decentralized Approach Using Homotopy," *IEEE Trans. Control Sys. Tech.*, vol. 21, no. 4, pp. 1270-1279, July 2013.
- [65] T. Smed and G. Andersson, "Utilising HVDC to damp power oscillations," *IEEE Trans. Power Del.*, vol. 8, no. 2, pp. 620–627, 1993.
- [66] R. J. Piwko and E. Larsen, "HVDC System Control for Damping of Subsynchronous Oscillations," *IEEE Trans. Power App. Syst.*, no. 7, pp. 2203–2211, 1982.
- [67] V. A. Mete, "Contribution of high voltage direct current transmission systems to inter-area oscillation damping: A review." *Renew. Sustain. Energy Rev.*, vol. 57, pp. 892-915, 2016.
- [68] Y. Pipelzadeh, N. R. Chaudhuri, B. Chaudhuri and T. C. Green, "Coordinated Control of Offshore Wind Farm and Onshore HVDC Converter for Effective Power Oscillation Damping." *IEEE Trans. Power Syst.*, vol. 3, no. 32, pp. 1860-1872, 2017.
- [69] ENTSO-E, "Network Code on High Voltage Direct Current Connections," ed: ENTSO-E, 2016.
- [70] Siemens, "FACTS – Flexible AC Transmission Systems Series Compensation," 2010. <https://www.siemens.com/global/en/home/products/energy/high-voltage/facts.html>. [Accessed: 11-May-2016].
- [71] ABB, "Series Compensation Boosting Transmission Capacity," 2015. <https://library.e.abb.com/public/500e696d077796cf83257e0c0047d487/SC%20A02-0135E-E%20KorrI.pdf>. [Accessed: 11-May-2016].

Bibliography

- [72] M. Bahrman, E. V. Larsen, R. J. Piwko and H. S. Patel, "Experience with HVDC - Turbine-Generator Torsional Interaction at Square Butte," *IEEE Trans. Power App. Syst.*, vol. 99, no. 3, pp. 966-975, 1980.
- [73] IEEE Committee Report. "A bibliography for the study of subsynchronous resonance between rotating machines and power systems," *IEEE Trans. Power App. Syst.*, 1976, vol.95, no.1, pp.216-218. 1976.
- [74] IEEE Committee Report. "First supplement to a bibliography for the study of subsynchronous resonance between rotating machines and power systems." *IEEE Trans. Power Syst.*, vol. 98, no.6, pp.1872-1875, 1979.
- [75] IEEE Committee Report. "Second supplement to a bibliography for the study of subsynchronous resonance between rotating machines and power systems." *IEEE Trans. Power App. Syst.*, 1985,104(2):321-327.
- [76] IEEE Committee Report. "Third supplement to a bibliography for the study of subsynchronous resonance between rotating machines and power systems." *IEEE Trans. Power Syst.*, 1991, 6(2): 830-834.
- [77] M. R. Iravani; B. L. Agrawal; D. H. Baker, "Fourth supplement to a bibliography for the study of subsynchronous resonance between rotating machines and power systems." *IEEE Trans. Power Syst.*, 1997, 12(3): 1276-1282.
- [78] IEEE Subsynchronous Resonance Working Group of the System Dynamic Performance Subcommittee Power System Engineering Committee. Proposed Terms and Definitions for Subsynchronous Oscillations.*IEEE Trans. Power App. Syst.*, 1980, 99(2):506-511.
- [79] Subsynchronous Resonance Working Group of the System Dynamic Performance Subcommittee. Reader's guide to subsynchronous resonance. *IEEE Trans. Power Syst.*, 1992, 7(1):150-157.
- [80] G. D. Irwin, A. K. Jindal and A. L. Isaacs, "Sub-synchronous control interactions between type 3 wind turbines and series compensated AC transmission systems." *Power and Energy Society General Meeting.*, July, 2011.

-
- [81] V. B. Virulkar and G. V. Gotmare. "Sub-synchronous resonance in series compensated wind farm: A review." *Renew. Sustain. Energy Rev.* vol. 55, pp. 1010-1029, 2016.
- [82] W. Du, Q. Fu and H. Wang, "Method of Open-loop Modal Analysis for Examining the Sub-synchronous Interactions Introduced by VSC Control in a MTDC/AC System," *IEEE Trans. Power Del.*, vol. PP, no. 99, pp. 1-1.
- [83] W. Du, Q. Fu and H. Wang, "Sub-synchronous oscillations caused by open-loop modal resonance between VSC-based HVDC line and power system," *IEEE Trans. Power Syst.*, vol. PP, no. 99, pp. 1-1.
- [84] L. Wang, X. Xie, H. Liu, Y. Zhan, J. He and C. Wang, "A Review of Emerging SSR/SSO issues and their Classifications." *The Journal of Engineering* 1.1, 2017.
- [85] Brunet-Watson, Marc, Jed Leighfield, and PSC North America. "Review of Series Compensation for Transmission Lines." 2014.
- [86] M. H. Ali, "Transient stability enhancement of wind farms using power electronics and facts controllers". Diss. University of South Carolina, 2014.
- [87] B. L. Agrawal and R. G. Farmer, "Use of Frequency Scanning Techniques for Subsynchronous Resonance Analysis," *IEEE Trans. Power App. Syst.*, vol. PAS-98, pp. 341-349, 1979.
- [88] Electric Power Research Institute, "HVDC System Control for Damping of Subsynchronous Oscillations", EPRI EL-2708, Final Report, October 1982.
- [89] P. Pourbeik, A. Bostrom and B. Ray, "Modeling and application studies for a modern static VAr system installation," *IEEE Trans. Power Del.*, vol. 21, no. 1, pp. 368-377, Jan. 2006.
- [90] B. Badrzadeh, *et.al.*, "Sub-synchronous interaction in wind power plants—Part I: Study tools and techniques." *Power and Energy Society General Meeting*. July, 2012.
- [91] L. Wei, and X. Xiao. "Electromagnetic and electromechanical transient hybrid real-time simulation technology based on RTDS used in subsynchronous resonance research." *2010 International Conference on Power System Technology (POWERCON)*, IEEE, Hangzhou, China, 2010.

Bibliography

- [92] Y Gong, Y Xue, "Subsynchronous oscillation relay", Patent Publication, US9806690 B1, publication date: 31/10/2017.
- [93] J. Zhang *et.al.*, "Suppressing Intermittent Subsynchronous Oscillation via Subsynchronous Modulation of Reactive Current," *IEEE Trans. Power Del.*, vol. 30, no. 5, pp. 2321-2330, Oct. 2015.
- [94] L. Livermore, C. E. Ugalde-Loo, Q. Mu, J. Liang, J. B. Ekanayake and N. Jenkins, "Damping of subsynchronous resonance using a voltage source converter-based high-voltage direct-current link in a series compensated Great Britain transmission network," *IET Gen. Trans. & Distr.*, vol. 8, no. 3, pp. 542-551, 2014.
- [95] K. M. Alawasa and Y. A. R. I. Mohamed, "A simple approach to damp SSR in series-compensated systems via reshaping the output admittance of a nearby VSC-based system," *IEEE Trans. Indust. Electron.*, vol. 62, no. 5, pp. 2673-82, 2015.
- [96] W. Zhu, R. Spee, R. R. Mohler, G. C. Alexander, W. A. Mittelstadt and D. Maratukulam, "An EMTP study of SSR mitigation using the thyristor controlled series capacitor." *IEEE Trans. Power Del.* 10.3 1479-1485, 1995.
- [97] R. Zheng, T. Joseph, S. Wang and J. Liang, "A control strategy for TCSC to mitigate SSR with local measurements," 13th *IET Inter. Conf. on AC and DC Power Transm. (ACDC 2017)*, Manchester, pp. 1-6, 2017.
- [98] X. Xie, P. Liu, K. Bai and Y. Han, "Applying Improved Blocking Filters to the SSR Problem of the Tuoketuo Power System," *IEEE Trans. Power Syst.*, vol. 28, no. 1, pp. 227-235, Feb. 2013.
- [99] X. Xie, L. Wang, X. Guo, Q. Jiang, Q. Liu and Y. Zhao, "Development and Field Experiments of a Generator Terminal Subsynchronous Damper," *IEEE Trans. Power Elec.*, vol. 29, no. 4, pp. 1693-1701, April 2014.
- [100] X. Xie, H. Liu and Y. Han, "SEDC's Ability to Stabilize SSR: A Case Study on a Practical Series-Compensated Power System," *IEEE Trans. Power Syst.*, vol. 29, no. 6, pp. 3092-3101, Nov. 2014.
- [101] X. Xie, L. Wang and Y. Han, "Combined Application of SEDC and GTSDC for SSR Mitigation and Its Field Tests," *IEEE Trans. Power Syst.*, vol. 31, no. 1, pp. 769-776, Jan. 2016.

- [102] H. K. Nia, M. Sahni, N. Karnik, and H. Yin, "Power system sub-synchronous oscillation damper", Patent Publication, US9660449 B2, publication date: 23/05/2017.
- [103] GE Energy Consulting, "Subsynchronous Oscillations (SSO): Risk Analysis, Protection, and Mitigation Techniques", 2015
- [104] W. Ren and E. V. Larsen, "System and method for stabilizing sub-synchronous interaction of a wind turbine generator", Patent Publication, US20160254769 A1, publication date: 09/01/2016.
- [105] Ackermann, Thomas, ed. *Wind power in power systems*. John Wiley & Sons, 2005.
- [106] Savulescu, Savu, 2ed. *Real-time stability in power systems: techniques for early detection of the risk of blackout*. Springer, 2014.
- [107] National Grid, "Benefits of Interconnectors to GB Transmission System", December, 2014. <https://www.ofgem.gov.uk/ofgem-publications/93802/ngetreporttoofgem-qualitativeinterconnectorbenefits-pdf>. [Accessed: 18-July-2017].
- [108] ENTSOE, "High Penetration of Power Electronic Interfaced Power Sources (HPo-PEIPS)", Guidance document for national implementation for network codes on grid connection, March 2017.
- [109] C. E. Ugalde-Loo, *et al.*, "Open access simulation toolbox for the grid connection of offshore wind farms using multi-terminal HVDC networks", in *13th IET Inter. Conf. on AC and DC Power Transm. (ACDC 2017)*, Manchester, pp. 1-6, Feb 2017.
- [110] W. Lin, J. Wen, J. Liang, S. Cheng, M. Yao and N. Li, "A Three-Terminal HVDC System to Bundle Wind Farms With Conventional Power Plants", *IEEE Trans. Power Syst.*, vol. 28, pp. 2292-3000, Jan. 2013.
- [111] J. Liang, T. Jing, O. Gomis-Bellmunt, J. Ekanayake and N. Jenkins, "Operation and Control of Multiterminal HVDC Transmission for Offshore Wind Farms", *IEEE Trans. Power Del.*, vol. 26, pp. 2596-2604, June 2011.

Bibliography

- [112] Z. Y. Xu, H. N. Qu, W. H. Shao and W. S. Xu, "Virtual Power Plant-Based Pricing Control for Wind/Thermal Cooperated Generation in China", *IEEE Trans. on Syst., Man, and Cybernetics: Syst.*, vol. 46, pp. 706-712, May 2016.
- [113] K. F. Jose, O. D. Adeuyi, J. Liang and C. E. Ugalde-Loo, "Inertial contribution from large scale variable-speed wind turbines connected to the GB grid." *13th IET Inter. Conf. on AC and DC Power Transm. (ACDC 2017)*, Manchester, pp. 1-6, Feb 2017.
- [114] J. Fradley, R. Preece and M. Barnes, "VSC-HVDC for frequency support (a review)," *13th IET Inter. Conf. on AC and DC Power Transm. (ACDC 2017)*, Manchester, pp. 1-6, Feb 2017.
- [115] L. Jiang, *et.al.*, "Wind Energy in China", *IEEE Power & Energy Mag.*, vol. 9, pp. 36-46, Oct. 2011.
- [116] L. Xu, L. Yao, and C. Sasse, "Grid Integration of Large DFIG-Based Wind Farms Using VSC Transmission", *IEEE Trans. Power Syst.*, vol. 22, pp. 976-984, July 2007.
- [117] H. Yin, L. Fan, and Z. Miao, "Fast Power Routing Through HVDC", *IEEE Trans. Power Del.*, 27, pp. 1432-1441, July 2012.
- [118] Z. Miao, L. Fan, D. Osborn and S. Yuvarajan, "Wind Farms With HVDC Delivery in Inertial Response and Primary Frequency Control", *IEEE Trans. on Energ. Conv.*, vol. 25, pp. 1171-1177, Dec. 2010.
- [119] P. Kundur, *Power System Stability and Control*. McGraw-Hill, NewYork, pages 17-40, 1994.
- [120] C. Karawita, HVDC interaction studies using small signal stability assessment, PhD thesis, Univ. Manitoba, 2009.
- [121] N.G.Hingorani, *Understanding FACTS: concepts and technology of flexible AC transmission systems*. Vol. 2. New York: IEEE press, pages 1-15, 2000.
- [122] G. O. Kalcon, G. P. Adam, O. Anaya-Lara, S. Lo and K. Uhlen, "Small-Signal Stability Analysis of Multi-Terminal VSC-Based DC Transmission Systems", *IEEE Trans. Power Syst.*, vol. 27, no. 4, pp. 1818-1830, Nov. 2012.
- [123] S. Cole, J. Beerten, and R. Belmans, "Generalized Dynamic VSC MTDC Model for Power System Stability Studies," *IEEE Trans. Power Syst.*, vol. 25, no. 3, pp. 1655-1662, Aug. 2010.

-
- [124] J. Beerten, S. D'Arco and J. A. Suul, "Frequency-dependent cable modelling for small-signal stability analysis of VSC-HVDC systems," *IET Gen. Trans. & Distr.*, vol. 10, no. 6, pp. 1370-1381, 2016.
- [125] "First Bench Mark Model for computer simulation of subsynchronous resonance", *IEEE Trans. Power App. Syst.*, vol. 96, no. 5, pp. 1565-1572, 1977.
- [126] "Second Benchmark Model for Computer Simulation of Subsynchronous Resonance," *IEEE Trans. Power App. Syst.*, vol. 104, no. 5, pp. 1057-1066, May 1985.
- [127] O. Anaya-Lara, N. Jenkins, J. Ekanayake, P. Cartwright, and M. Hughes, *Wind energy generation: modelling and control*. John Wiley & Sons. USA: Wiley, pages 149-151, 2011.
- [128] R. Thirumalaivasan, M. Janaki and N. Prabhu, "Damping of SSR Using Subsynchronous Current Suppressor With SSSC," *IEEE Trans. Power Syst.*, vol. 28, no. 1, pp. 64-74, 2013.
- [129] C. E. Ugalde-Loo, J. B. Ekanayake and N. Jenkins, "Subsynchronous resonance in a series-compensated Great Britain transmission network," *IET Gen. Trans. & Distr.*, vol. 7, no. 3, pp. 209-17, 2013.
- [130] C.E. Ugalde-Loo, J.B. Ekanayake and N. Jenkins. "Subsynchronous resonance on series compensated transmission lines with quadrature boosters." *PowerTech, 2011 IEEE Trondheim. IEEE*, Netherlands, 2011.
- [131] N. Prabhu and K. R. Padiyar, "Investigation of subsynchronous resonance with VSC based HVDC transmission systems," *IEEE Trans. Power Del.*, vol. 24, no. 1, pp. 433-440, 2009.
- [132] D. Sun, X. Xie, Y. Liu, K. Wang and M. Ye, "Investigation of SSTI Between Practical MMC-based VSC-HVDC and Adjacent Turbogenerators through Modal Signal Injection Test," *IEEE Trans. Power Del.* vol. 32, no. 6, pp. 2432-2441, Dec. 2017.
- [133] L. Harnefors, "Analysis of subsynchronous torsional interaction with power electronic converters," *IEEE Trans. Power Syst.*, vol. 22, no. 1, pp. 305-313, 2007.
- [134] Y. C. Choo, A. P. Agalgaonkar, K. M. Muttaqi, S. Perera and M. Negnevitsky, "Analysis of Subsynchronous Torsional Interaction of HVDC System Integrated Hydro Units With Small

Bibliography

- Generator-to-Turbine Inertia Ratios," *IEEE Trans. Power Syst.*, vol. 29, no. 3, pp. 1064-1076, May 2014.
- [135] L. Wang, X. Xie, Q. Jiang and H. R. Pota, "Mitigation of Multi-modal Subsynchronous Resonance Via Controlled Injection of Supersynchronous and Subsynchronous Currents," *IEEE Trans. Power Syst.*, vol. 29, no. 3, pp. 1335-1344, 2014.
- [136] M. Bongiorno, J. Svensson and L. Angquist, "On control of static synchronous series compensator for SSR mitigation," *IEEE Trans. Power Electron.*, vol. 23, no. 2, pp. 735-43, 2008.
- [137] T. Bengtsson, S. Roxenborg, M. M. Saha, P. O. Lindström, H. Eriksson and M. Lindström, "Case studies and experiences with Sub-synchronous resonance (SSR) detection technique," *2016 Power Systems Computation Conference (PSCC)*, Genoa, pp. 1-6, 2016.
- [138] W. Wang, Y. Li, Y. Cao, U. Häger and C. Rehtanz, "Adaptive Droop Control of MTDC System for Frequency Support and Power Sharing", *IEEE Trans. Power Syst.*, vol. 33, no. 2, pp. 1264-1274, March 2018.
- [139] N. R. Chaudhuri and B. Chaudhuri, "Adaptive Droop Control for Effective Power Sharing in Multi-Terminal DC (MTDC) Grids", *IEEE Trans. Power Syst.*, vol. 28, no. 1, pp. 21-29, Feb. 2013.
- [140] J. Beerten and R. Belmans, "Analysis of power sharing and voltage deviations in droop-controlled DC grids", *IEEE Trans. Power Syst.*, vol. 28, no. 4, 4588-4597, Nov. 2013.
- [141] T. M. Haileselassie and K. Uhlen, "Impact of DC Line Voltage Drops on Power Flow of VSC-MTDC Using Droop Control", *IEEE Trans. Power Syst.*, vol. 27, no. 3, pp. 1441-1449, Aug. 2012.
- [142] E. Prieto-Araujo, F. D. Bianchi, A. Junyent-Ferre and O. Gomis-Bellmunt, "Methodology for Droop Control Dynamic Analysis of Multiterminal VSC-HVDC Grids for Offshore Wind Farms," *IEEE Trans. Power Del.*, vol. 26, no. 4, pp. 2476-2485, Oct. 2011.
- [143] H. Liu and Z. Chen, "Contribution of VSC-HVDC to Frequency Regulation of Power Systems With Offshore Wind Generation", *IEEE Trans. on Energ. Conv.*, vol. 30, pp. 918-926, Sept. 2015.

- [144] S. Akkari, J. Dai, M. Petit and X. Guillaud, "Interaction between the voltage-droop and the frequency-droop control for multi-terminal HVDC systems", *IET Gen. Trans. & Distr.*, vol. 10, pp. 1345-1352, May 2016.